Conceptualization, Analysis, and Design of Miniaturized EBG Surfaces and Antenna for WBAN Applications

by

Dinesh Rano

Under the Supervision of Dr. Mohammad S. Hashmi

Indraprastha Institute of Information Technology Delhi

June 2020

Conceptualization, Analysis, and Design of Miniaturized EBG Surfaces and Antenna for WBAN Applications

by

Dinesh Rano

Submitted

in partial fulfillment of the requirements for the degree of Doctor of Philosophy

to the

Indraprastha Institute of Information Technology Delhi

June 2020

Certificate

This is to certify that the thesis titled "**Conceptualization, Analysis, and Design of Miniaturized EBG Surfaces and Antenna for WBAN Applications**" being submitted by **Mr. Dinesh Rano** to the Indraprastha Institute of Information Technology Delhi, for the award of the degree of Doctor of Philosophy, is an original research work carried out by him under my supervision. In my opinion, the thesis has reached the standards fulfilling the requirements of the regulations relating to the degree.

The results contained in this thesis have not been submitted in part or full to any other university or institute for the award of any degree/diploma.

June 2020

Dr. Mohammad S. Hashmi

Indraprastha Institute of Information Technology Delhi

New Delhi 110 020

Dedicated to my Family and Friends ……

Acknowledgements

First and foremost, I would like to express my deepest gratitude to my supervisor Dr. Mohammad Hashmi for his tremendous support, guidance, and encouragement throughout these five years. I have been indeed lucky to have the opportunity to work with Dr. Hashmi. He has always pushed me for independent research, problem-solving, and collaboration with other esteemed professors. It has helped me a lot to pursue independent research and excel in my research career. I am looking forward to continuing research with him in the future.

My family's support has been enormous throughout this journey. It was my mother who insisted on pursuing research and be away from home for such a long time. Her love and support were phenomenal throughout my bad times in these five years. What can I say about my father, simply, he is the backbone of my life. Thank you, maa and baba, we did it together. Last but not least, my wife, Piu. She was very kind to help me during my measurements and tolerating my anger for two and a half years. She has been very patient and loving for allowing me to go ahead with my research and not to focus on anything else. A special thanks to her.

A special mention for my doctoral committee members Dr. Sobha S. Ram and Dr. Vivek Bohra, for their feedback and comments. I would like to thank Dr. Muhammad A. Chaudhary for active collaboration and providing support. A special thanks to all Administrative Staff for all kinds of infrastructure and financial support.

Any journey is incomplete without friends. I would like to thank all my friends Dr. Hemanta Mondal, Deepayan (Deepa), Amit Chauhan, Rahul Gangopadhyay, and Nalla Anandkumar, for being a support and help throughout these years. I will always miss the time when all of us were together, especially the Friday party. Once again, thank you, friends. A special mention for my two other friends, Parmesh Yadav (Pamme) and Sagar, for their contribution as well.

List of Abbreviations

1D	One Dimension
2D	Two Dimension
3D	Three Dimension
AGSW	Array Guided Surface Wave
AOA	Angle-of-Arrival
BG	Band-gap
CM	Conformal Mapping
CMA	Conformal Mapping Approach
CPW	Co-planar Waveguide
CST	Computer Simulation Tool
DUT	Device Under Test
EBG	Electromagnetic Band-gap
ECG	Electrocardiography
ECC	Edge Coupling Capacitance
EIA	EBG Integrated Antenna
EIRP	Effective Isotropic Radiate Power
EM	Electromagnetic
FCC	Federal Communications Commission
FDS	Frequency Domain Solver
FDTD	Finite Difference Time Domain
GI	Gastro-Intestinal

HIS	High Impedance Surface
ISM	Industrial Scientific Medical
LUT	Liquid Under Test
MBAN	Medical Body Area Network
ME-BC	Magnetic Electric Boundary Condition
MPA	Microstrip Patch Antenna
PIFA	Planar Inverted F Antenna
PBC	Periodic Boundary Condition
PCB	Printed Circuit Board
PEC	Perfect Electric Conductor
PTFE	Polytetrafluoroethylene
RAM	Random Access Memory
RSSI	Received Signal Strength Indicator
SAR	Specific Absorption Rate
SMA	Sub Miniature Version A
SW	Surface Wave
TDS	Time Domain Solver
TE	Transverse Electric
TEM	Transverse Electromagnetic
TM	Transverse Magnetic
UC-BC	Unit Cell Boundary Condition
VNA	Vector Network Analyser
WBAN	Wireless Body Area Network
WCE	Wireless Capsule Endoscopy
WSN	Wireless Sensor Network

Abstract

A network of wearable, implantable, and body-worn devices are collectively known as Wireless Body Area Network (WBAN). These networked devices comprising the WBANs are frequently used in the monitoring and tracking of the body's essential physiological parameters such as glucose content, temperature, blood pressure, ligament pressure (round ligament), heart rate, etc. remotely. In the WBANs, antennas essentially play the roles of sensors in a variety of scenarios for link establishment between the base stations and the concerned patient. For example, there are situations requiring placement of antennas on different body parts, and in such a scenario, it is called on-body to on-body communication. Then there are often requirements of communication between sensors on patients' bodies and base station and this situation is called on-body to off-body communication. Finally, sometimes antennas in WBANs form in-body to on-body communication links. Overall, this area has been extensively studied in the past few years still issues such as large antenna size at medical body area network (MBAN), a quintessential WBAN band, and Wi-Fi bands, significant radiation towards the body, and shift in their corresponding resonant frequencies in the presence of multiple textile layers require further investigations. Moreover, body-worn antenna exhibits sound detuning (coupling) in the presence of a body that also degrades antenna performance.

The critical issues of antenna size and radiation towards the body in the body-worn sensors are often addressed by utilizing Electromagnetic Band-gap (EBG) surfaces. It is achieved by integrating the EBG with the body-worn antenna sensors. This has shown great promise in enhancing the performance in terms of gain and efficiency due to the exciting in-phase reflection features of EBG cells. Besides, the surface wave rejection ability of an EBG surface reduces the diffraction of surface currents at the edges of the PCB and hence minimizes the specific absorption rate (SAR). However, the periodic arrangement of these EBG cells is often not compatible with any of the WBAN frequency standards due to the dimension constraints imposed by these cells. Besides, WBAN requires bending and conforming of antenna sensors for ease of usage and for keeping the actual practical scenario in perspectives to seamlessly place on corresponding body parts such as arms, biceps, and legs. It essentially means that the conforming of EBG surfaces is required but, in turn, leads

to a shift in the in-phase reflection frequency. As a consequence, there is degradation in the performance of the proposed and designed antenna sensors. Furthermore, WBAN requires testing of SAR on a real phantom, but these are full of challenges such as the existing technologies and tools that are sophisticated, costly, and beyond access to many labs.

It is thus apparent that there is plenty of scope for innovations and inventions within the broad regime of WBAN. Therefore, to advance the tools and technologies for the WBAN infrastructure, we have to pursue multi-pronged research work. Firstly, we explored, investigated, and proposed the design and analysis of miniaturized and conformal EBG integrated low profile body-worn antenna. It has been shown that the proposed EBG integrated antenna possesses dimensions that are compatible to fit in the existing smart-watches and associated gadgets. The developed EBG cells demonstrate excellent phase stability to polarization change of incident TE-TM and TEM waves. We have also identified that the surface wave rejection ability of the proposed EBG cells and arrays can be readily comprehended using the dispersion diagram and transmission characteristics. It plays a vital role in reducing SAR values in the eventual body-worn designed antenna and antenna arrays. To assess the features and characteristics of the proposed designs for WBAN compliance, the measurements have been carried out in both inside an anechoic chamber and the ambiance environments.

During this research work, we were able to observe a significant problem with the shifts in the in-phase reflection frequency of EBG unit cells and corresponding arrays due to conforming for making them suitable for placement on various body parts. To address this problem, as part of our second contribution in this thesis work, we have proposed analytical formulations to determine the shift in the in-phase reflection frequency of the conformed EBG unit cell and array. We were able to develop the formulations through analysis and experimental investigation on three distinct EBG unit cells and arrays. The proposed approach is scalable, as has been demonstrated through its implementation on various shapes and radii of the conformed surfaces.

It is well known that the body-worn antennas suffer from a shift in their resonance frequencies in the presence of protective layers in the form of textiles or other dielectrics. In our third contribution, therefore, we have proposed a unique iterative model to determine the effective dielectric constant and resonant frequency of an MPA covered with multiple textile layers. We have also developed closed-form expressions to determine the effective

dielectric constant of such an arrangement based on the conformal mapping approach. The demonstration of excellent consonance between the theoretically obtained results and the simulation, as well as measurement results, is a testament to the effectiveness of the proposed approach. An extremely important feature of the proposed analytical model and the formulations are that they can be readily implemented using any commercial mathematical processing tool.

It is pertinent to note that the applications of the design of antennas and antenna systems in the WBAN require tests and evaluations within a realistic scenario. As a first step, it is a standard practice to carry out such evaluations using phantoms, which are rarely available with academic labs. To circumvent this challenge, and as part of the last and fourth contribution of this thesis work, we proposed a cost-effective and straightforward approach to develop liquid phantoms utilizing common materials such as salt, sugar, glycerine, and water to mimic the human tissue behavior. We have also proposed a simple and cost-effective measurement setup to characterize the developed phantom. Finally, we used the developed phantom also to propose a point SAR measurement technique that proves effective in assessing the SAR performance of the proposed antennas.

List of Publications

Journal Articles

1. **D. Rano**, M.S. Hashmi, and M.A. Chaudhary "A Geometrical Approach to Determine Shift in Reflection Phase of Conformal Electromagnetic Band Gap/High Impedance Surface for an Oblique Incident EM Wave," *IET Microwaves, Antennas & Propagation* (Accepted for publication).

2. **D. Rano**, M.A. Chaudhary, and M.S. Hashmi, "Determination of Effective Permittivity and Resonant Frequency of Patch Antenna Covered with Same and Mixed Type Dielectric Superstrates," *IEEE Access*, vol. 8, pp. 34418-34430, February 2020.

3. **D. Rano** and M.S. Hashmi, "Extremely Compact EBG-Backed Antenna for Smart-Watch Applications in Medical Body Area Network," *IET Microwave. Antennas Propag*. vol. 13, pp. 1031-1040, December 2019.

4. **D. Rano** and M.S. Hashmi, "A Modified Interdigital EBG Reflector for Wireless Body Area Network Applications," in *Wiley Microwave Optical Technology Letter*, vol. 61, 912–919, December 2019.

Conferences Articles

1. **D. Rano** and M. S. Hashmi, "Determination of Effective Dielectric Constant and Resonant Frequency of Microstrip Patch Antenna with Multilayered Superstrate Structures," *IEEE European Microwave Conference*, 2019, pp. 81-84.

2. **D. Rano** and M. S. Hashmi, "A New Miniaturized Slot-loaded EBG Cell for Cancelling Surface Waves in PCBs," *IEEE Asia-Pacific Conference on Antenna and Propagation*, 2018, pp. 349 – 350.

3. **D. Rano** and M. S. Hashmi, "A New Lumped Circuit Modelling Technique for EBG Based on Surface Current Flow," *IEEE Asia-Pacific Conference on Antenna and Propagation*, 2018, pp. 351 – 352.

4. **D. Rano** and M. S. Hashmi, "Interdigital Based EBG: Compact and Polarization Stable for MBAN and Wi-Fi," *IEEE European Conference on Antenna and Propagation*, 2018, pp. 1 – 5.

5. **D. Rano**, D. Banerjee, and M.S. Hashmi, "A Miniaturized Three-Stage Dual-Frequency Matching Network," *IEEE International Microwave and RF Conf.*, 2017, pp. 1 – 5.

6. **D. Rano**, and M.S. Hashmi, "Design and Analysis of Wearable Patch Antenna Array for MBAN Applications," *IEEE National Conference on Comm.*, 2016, pp. 1 – 6.

Other Contributions

1. S. Verma, **D. Rano**, and M. S. Hashmi, "A Novel RF Based Impedance Matching Technique for Near Field Wireless Power Transfer Systems," *IET Microwaves, Antennas & Propagation*, 2020. (Accepted for publication).

2. Zere Iman, Amanzhol Shungeyev, **D. Rano** and M. S. Hashmi, "A Planar End-fire Antenna for Wireless Body Area Network," *The International Workshop on Antenna Technology*, 2020, Romania (Presented).

3. S. Verma, **D. Rano**, and M. S. Hashmi, "A Novel Dual Band Defected Ground Structure for Short Range Wireless Power Transfer Applications," *IEEE Wireless Power Transfer Conference*, 2019, pp.188 – 191.

4. A. Kafizov, **D. Rano**, and M. S. Hashmi, "End-fire Yagi Antenna with DGS for

WBAN Applications," *IEEE Asia-Pacific Conference on Antenna and Propagation*, 2019. (Presented).

5. S. Verma, **D. Rano**, and M. S. Hashmi, "A Novel Miniaturized Band Stop Filter Using Fractal Type Defected Ground Structure," *IEEE Asia Pacific Microwave Conference*, 2017, pp. 799 – 802.

6. W. Akaram, **D. Rano**, M. S. Hashmi, and A. Q. Ansari, "Design of a New UC-Planar EBG Cell and its Application in Performance Enhancement of Microstrip Patch Antenna /Antenna Array," *IEEE Asia Pacific Microwave Conference*, 2016, pp. 1 – 4.

Contents

List of Figures

List of Tables

Chapter 1

Introduction

A network of wearable, implantable, and body-worn devices are collectively known as *Wireless Body Area Network* (WBAN). Several bands such as ***M**edical **B**ody **A**rea **N**etwork* (MBAN 2.36 – 2.4 GHz), ***I**ndustrial, **S**cientific and **M**edical* band (ISM), and others operate in WBAN. It provides a flexible platform to connect the sensor nodes wirelessly, measuring, and recording the *physiological parameters* of the body. Recent advances in integrated technology have brought a revolution in miniaturization in electronic devices. The use of ultra low power sensors in wearable applications has enabled many nodes to be placed on the body [1] – [3]. The overall idea behind the use of such devices is to monitor patient healthcare seamlessly and to increase patients' mobility substantially [4] – [6]. In this context, these devices could be further categorized as body-worn devices or implanted devices [4] – [11]. Body temperature sensors, blood pressure sensors, hearing aids, and smartwatches are a few examples of body-worn devices. Whereas pacemakers, retinal prosthesis, and capsule endoscopy are examples of implanted devices [7] – [11]. A depiction of such a network can be seen in Figure 1.1.

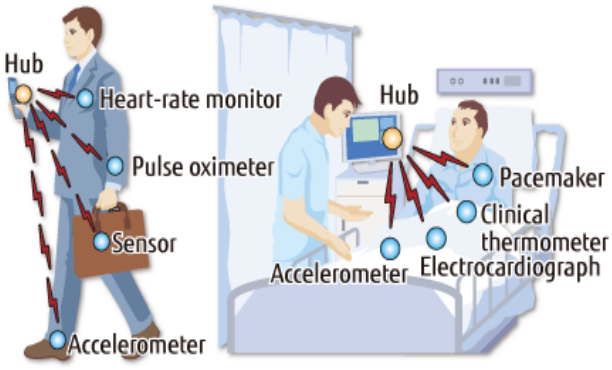

Figure 1.1 Network of sensors known as WBAN (left) and deployment of these sensors on the body for a moving body and a patient resting on a bed (right) [12]

There has been a recent emphasis on wireless health monitoring owing to the aging world population [13]. Its importance can be deduced from the fact that the Federal Communications Commission (FCC) has allocated a separate low-power band for personal communication, known as MBAN, covering a band of 2.36 – 2.4 GHz [14]. This band is being frequently utilized in applications such as monitoring of vital parameters like temperature, blood pressure, ligament pressure (round ligament), and many more. The need for ultra low power devices emanates from the fact that all these sensors and devices rely on batteries for operation. Therefore, to establish a link between an on-body node and an external node with limited power, the performance of an antenna has to be optimum in terms of gain and efficiency. Furthermore, power emitted in the form of EM (electromagnetic) radiation tends to heat dielectric (body) present nearby and therefore requires these wearable and implanted devices to operate within a safe level. FCC has restricted equivalent radiated isotropic power (EIRP) norms for MBAN as 1 mW and medical implants 25 μW [14] – [16].

1.1 Scenarios of WBAN

As a general categorization, the successful realization of holistic WBAN includes three types of scenario named as 1) On-body – off-body 2) On-body – on-body and 3) In-body – on/off-body communication.

On-body to off-body communication consists of sensors located on the body communicating with external devices, commonly known as a base station. A typical on-body to off-body communication scenario is shown in Figure 1.2 (a) where a wireless sensor network (WSN) located on shoulders and waist communicates with an external device. In this scenario, the antenna should radiate away from the body, and also, its polarization should be vertical, considering that the losses for the horizontally polarized antenna are higher [17] – [19]. It, however, leads to protrusion from the surface of the antenna, which is not desirable from the WBAN perspective. Therefore, a low profile patch antenna with horizontal polarization is a viable option [20] – [22]. Typically, the range for this type of communication lies from 20 to 30 m (approximately size of a standard room).

The on-body to on-body communication consists of sensors or antennas communicating with each other located on-body itself. Figure 1.2(b) depicts such a scenario in which WSN located on the legs, waist, and shoulders of an athlete communicates with each other [23] – [24]. These sensors, in turn, send physiological data to an external node for further monitoring and processing. Antenna for this scenario should radiate towards the body, and minimum radiation should take place away from the body [24] – [29]. Since communication among the sensors happens mostly through the body, which has much higher attenuation than the free space, therefore the design of antenna for this scenario is very critical.

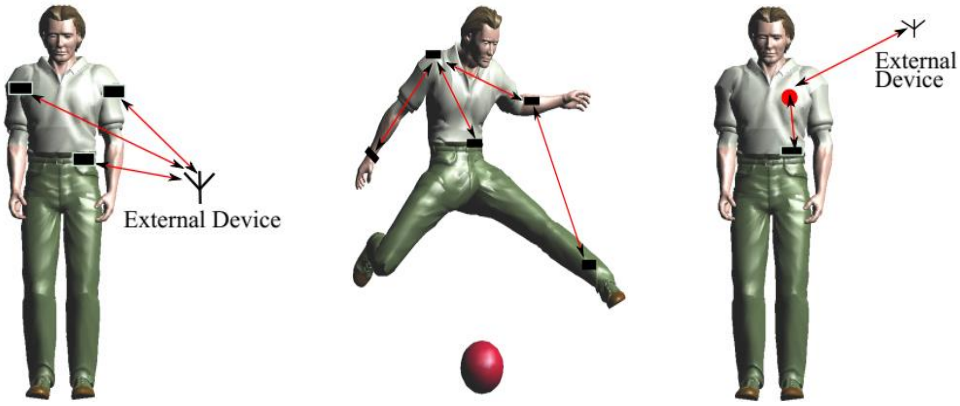

(a) (b) (c)

Figure 1.2 Communication scenario in a typical WBAN (a) On-body to off-body, (b) On-body to on-body (c) In-body to on/off-body [24]

In-body to on-/off-body communication consists of medical implants communicating with an external device or sensor placed on the body [7] – [11], [30] – [32]. For example, Figure 1.2(c) shows communication between a pacemaker and an external or an on-body node [24]. Similarly, an implant in wireless capsule endoscopy (WCE) when swallowed an external device is placed on the body to receive images of the inside of the body [7] – [11]. Such a scenario is an example of in-body to on-body communication. Since the communication in this scenario happens through lossy tissues, the attenuation of the EM wave is higher than the on-body to the on-body case. Moreover, the implant devices operate on shallow power, are compact, and

in some cases, conformal as well. It places a strict requirement on the size and performance of an implanted antenna [9].

In this dissertation, we have focused on on-body to off-body communications from the WBAN perspective. The comprehensive study of various aspects of this scenario provides sufficient clues that there is a need to address several aspects to incorporate the technological advancements in such a system. The doctoral research being pursued here intends to address some of the concerns outlined below:

1.1.1 Antenna Design:

The antenna is an integral part of WBAN devices and plays a vital role in establishing a link between a wearable and base station (remote location away from the body). Although this area has been extensively studied in the past few years still issues like large antenna size at medical body area network (MBAN) and Wi-Fi bands, significant radiation towards the body, non-conformability, and reduction in performance in the presence of body requires further investigations. Often patch antennas used in WBAN applications are limited by its operational bandwidth, size, reduced efficiency, strong coupling with the body, and high specific absorption rate (SAR). *Electromagnetic band-gap* (EBG) surfaces in this regard have shown a significant improvement in radiation properties and miniaturization of antenna used in WBAN [33] – [50].

EBG is the artificially engineered structures that exhibit *in-phase reflection* for an *incident EM wave* (through reflection phase diagram) and *band-gap* property (through dispersion diagram) [42] – [43], [48]. The band-gap characteristics of an EBG surface, suppress surface wave propagation in that region established by dispersion curve and transmission property [42] – [43]. It can lead to the rejection of surface currents propagating on the metal surface and cancel diffraction at the edges of the ground plane. Consequently, this reduces back lobe radiation, and improves gain, reduces SAR, and improves front to back ratio of an antenna [48]. It implies that sound isolation can be achieved between the EBG incorporated antenna and the human body in the absence of surface current throughout the band-gap region.

Besides, EBG surfaces also exhibit in-phase reflection for an incident electric field rather than out of phase response from a typical PEC surface [46] – [48]. It leads to constructive interference of reflected and direct electric field from a horizontally polarized monopole antenna, which improves the radiation properties [48]. Nevertheless, EBG surfaces have a disadvantage that only periodic repetition of the unit cells can contribute to the band-gap and in-phase reflection characteristics [42] – [43]. Therefore, antennas with such an arrangement result in increased overall size and become incompatible for the use in WBAN applications such as smart-watch.

1.1.2 Conformability of Body-worn Antenna:

An essential feature of wearable devices is *conformability* for the comfort of users. It necessitates the design of conformal antennas suitable for placement on shoulders, biceps, wrists, and legs [35] – [39]. The fundamental challenge in the design of conformal EBG structures is that the bending leads to alteration of the in-phase property and hence changes in the performance of the conformed antenna [38] – [39]. Therefore, either unit cell of larger width is required so that even after bending, the desired band is covered [38] – [39], or appropriate prior analysis is carried out for phase compensated design [51] – [52]. However, increased cell width is often not feasible, considering that wearable applications require miniaturization.

Furthermore, the determination of in-phase property in simulation is a complex process as the meshing of conformal EBG unit cell, or EBG array is critical. The discontinuity in the edges might appear while conforming to a unit cell or array, and hence increase in the number of mesh cells is needed to smoothen the computational area [53]. It, in turn, increases the simulation time and space requirement. Moreover, the existing analytical solutions in this direction to determine the in-phase property of a conformal EBG unit cell/array are sophisticated and available for higher frequencies, e.g., 5.8 and 10 GHz [51] – [52]. Besides, these solutions are applicable for a large array size of EBG unit cells that might not be appropriate from the WBAN perspective.

1.1.3 Communication Through Multiple Textile Layers:

Another essential facet of WBAN is reliable communication between the on-body transmitter and receiver located externally, such that essential physiological parameters are not lost. However, this is challenged by *multi-layered communication* of antenna covered underneath (either in the form of *textiles* or plastic cover) for protection from environmental hazards. Such an arrangement of an antenna covered by single or multiple layers of dielectric (in form *textiles*) alters the resonant frequency as the effective dielectric constant of the whole structure gets changed [54] – [69]. The present works in literature exhibit more than 3% of the shift in resonant frequency for superstrate of height 1 mm having dielectric constant lesser than 2.32 [54] – [56]. However, antenna designed on substrates such as Polyamide lossy (Nylon-6), Kapton (Dupont), Latex, polyester sheet, and RO4350B having dielectric constants of 3.6, 3.5, 3.31, 2.8 and 3.66 are in general very common in WBAN [70]. Therefore, a high percentage of shift is not desirable as patch antennas used in WBAN itself has *narrow fractional bandwidth* of 2 – 3% [58]. The *Conformal mapping approach* (CMA) with modified expressions to determine the effective dielectric constant of such an arrangement can reduce the error considerably. It makes the whole system much more reliable.

1.1.4 Development of Phantom and SAR Measurement:

As wearable devices operate very close to the body, a close check on keeping SAR under alarming levels becomes essential [33]–[40]. Hence, body-worn devices must be tested in real scenarios, apriori the design, and manufacturing. In this regard, test and evaluation using a *physical phantom* have become very popular to avoid the risks of exposing body parts to persistent EM radiation exposure and avoiding any damage [33]–[40]. *Thermographic imaging* and *electric field probe scanning* are the two most popular methods of reliable and accurate SAR testing [71] – [81]. However, these methods are very complex, highly expensive, and most of the labs have no access to it. Moreover, the preparation of physical phantoms in the form of *solid*/*semi-solid* or *liquid* itself is a complex process and employs expensive setup of the *dielectric*

probe tool kit, which is also not easily available in labs [82] – [86]. In this regard, a lesser expensive technique employing two antenna arrangements shows promising results in the development of liquid phantoms. Besides, point SAR measurement of developed phantoms can provide a good comparative analysis w.r.t. complex mass averaging techniques [33] – [40].

1.2 Problem Statement

After an extensive research survey of antenna design in WBAN (on-body to off-body), it was identified that the existing designs have severe limitations in most of the performance metrics, namely *compactness*, *desired gain*, and *ease of conformability* [33] – [40], [87] – [91]. With a compact size of the antenna and low-profile nature, gain and efficiency drop considerably. It is because the gain of an antenna is directly proportional to *effective aperture* and with smaller aperture gain falls [58] – [60]. Improvement in radiation and compactness can be achieved by incorporating EBG surfaces with standalone antennas. However, the design of such surfaces at MBAN and Wi-Fi bands is still a challenge. For example, the *in-phase reflection frequency* of the EBG unit cell is susceptible to *the mode of polarization* [92] – [93]. Furthermore, the polarization sensitivity of the UC to obliquely incident *TE* and *TM* wave further poses a challenge to the designers.

Moreover, the compactness (at MBAN band) and ease of conformability of the EBG unit cells is another big challenge [38] – [39]. The current state-of-the-art designs achieve conformability in design. However, they lack from the large footprint, sensitivity to incident TE and TM modes either normally or obliquely, and ease of conformability as well.

In summary, Table 1.1 lists a detailed analysis of previous works and their shortcomings. As apparent from the Table that EBG unit cells reported in [38] – [39], [87], [89] – [90] indeed achieves a high level of miniaturization when compared with [34], [36], [88], and [91], however, most of the previously reported works have not included the analysis of polarization sensitivity and surface wave propagation.

Moreover, bandgap analysis is only reported in a few works. Suppression of surface wave propagation along the substrate is very important to reduce SAR values as WBAN antennas operate very close to the body. Besides, the presence of surface waves also tends to reduce the gain of the antenna in the main lobe. Therefore, a detailed analysis of surface wave propagation of the EBG ground plane ([34], [38] – [39], [87] – [91]) through a suspended transmission line or microstrip line is very important to extract the required bandgap or stopband range.

Table 1.1 State-of-the-Art Works Working at MBAN and Wi-Fi bands

Ref.	Size (lxb) (mm^2)	*g* (mm)	*h* (mm)	Band-gap (GHz)	Sensitivity analysis	Surface wave propagation analysis
[34]	48.0*48.0	2.00	1.00	-	No	No
[91]	34.0*34.0	0.40	0.10	-	No	No
[36]	31.0*31.0	-	1.52	-	No	No
[88]	27.6*27.6	1.20	0.70	.07	No	No
[39]	25.3*27.8	2.50	5.00	-	No	No
[87]	22.7*22.7	1.00	1.52	.02	No	Yes (2.395 – 2.405)
[38]	27.0*16.0	2.15	2.00	-	No	No
[89]	20.0*20.0	1.00	2.00	-	Yes (Unstable)	No
[90]	20.0*18.0	1.50	3.00	-	No	No

Therefore, based on the above discussion it is apparent that there is plenty of room for improvement of the performance EBG unit cell. Moreover, polarization sensitivity of EBG unit cell for an incident TE, TM and TEM wave, bandgap extraction, and surface wave suppression also needs to be included in a study.

Measurement of SAR on-body is another challenge faced in WBAN. Instead of human testing, which involves the risk of exposing a part of the body to persistent exposure of EM radiation, two other ways, i.e., *physical phantom* and *numerical phantom* (simulation) have become very popular [37] – [39], [92] – [93], [72] – [74]. Physical phantom is an accurate model of the body. However, development and testing

of SAR require costly setup, which is not easily assessable. Furthermore, a numerical phantom is a *simulated biological body* which consists of homogeneous tissues of average electrical property [92] – [93]. It can also be a more complex and accurate phantom having different tissues of a human body such as Emma, Gustav, Hugo, and Laura in CST [53]. The numerical phantoms are indeed accurate but require considerable simulation time and memory for the generation of results. Most works to date rely on *simulated values* of SAR for either 1g/10g of averaging mass [33] – [40], [92] – [93]. Moreover, the simulated SAR values are obtained only for a *finite duration* until the steady-state is achieved. However, this might not be the case for a typical wearable device worn on-body for a 24/7 basis.

Another most significant challenge faced in this direction is *the shift in the resonant frequency* of the on-body antenna covered by *multiple textile layers*. For communication taking place through multiple layers of textiles depending on terrain, it becomes essential to develop accurate formulas to determine *the resonant frequency* of antenna and *effective dielectric constant* so that the communication between on-body sensors with externally located receiver does not go out of the band. Present research predicts the resonant frequency with a relative percentage error of more than *3%* between the *theoretical* and *measured* values in case of permittivity of substrate and superstrate is less than 2.32 [54]-[57]. For a patch antenna, this much shift in resonant frequency may lead to out of band communication with the receiver due to its *narrow fractional bandwidth* [58] – [60]. Moreover, the existing methods fail to predict the resonant frequency and effective dielectric constant of an antenna covered by multiple layers of the dielectric or textiles as well.

1.3 Major Contributions

This thesis has been pursued to contribute in this direction and to address most of the concerns. These are the design of *highly efficient antennas* for WBAN, provide conformability analysis of EBG surfaces. Development of a *cost-effective and straightforward* approach to model liquid phantoms. Determination of *effective permittivity* and *the resonant frequency* of patch antenna covered with single or

multiple *dielectric layers* in the form of textiles.

1.3.1 EBG Incorporated Antenna Design

We have proposed different EBG surfaces for improving the performance of *a low profile antenna*. In this regard, design, development, and analysis of two major types of EBG surfaces have been carried out in the context of WBAN. The first one is *via-less* and compact interdigital–EBG (IDE) surface ideally suited for smartwatch applications. The second is compact, conformal, and via-less *Blocking type EBG* with the smallest dimension to date. The *polarization stability* of the EBG cells under oblique incident TE and TM waves have been thoroughly analyzed.

Furthermore, the *surface wave rejection* ability of all the EBGs is also analyzed with the help of *dispersion* and *transmission diagram*. Performance metrics of these designs have been presented and compared to state-of-the-art EBGs. Enhancement in the performance of a monopole antenna has been obtained by incorporating both the EBG surfaces. Once again, performance metrics of the designed antenna like gain (in body and air), bandwidth, efficiency, and SAR have been presented. The proposed EBG incorporated antennas make it attractive for use in WBAN applications.

1.3.2 Development of Liquid Phantoms and SAR Testing

We have developed highly *reliable*, *cost-effective*, and *accurate* distinct approaches for the determination of *permittivity* ε_r and *conductivity* σ_d of a liquid phantom using a standard VNA. It essentially requires the design of a microstrip patch antenna (MPA) operating at the center of MBAN frequency, i.e., 2.38GHz. At first, the resonant frequency of the antenna covered by a plastic container (to contain liquid under test) and water is measured. Based on the percentage variation in resonant frequency through simulation and measured results, an approximation is made to determine ε_r of sample liquids.

Furthermore, for the determination of σ_d, *two antenna arrangement* is

employed. The antennas are dipped inside liquid under test (LUT), and the received power is calculated from the measured values of S_{21}, S_{11}, and transmitted power. The power received, in turn, gives the attenuation constant, which is then used in the calculation of σ_d by using a standard expression. The measured values are in good agreement with that of data given in [83]. Next, SAR of the liquid phantoms exposed to EM radiation has been determined through simulation and measurement.

1.3.3 Determination of Effective Dielectric Constant

We have developed new empirical relations based on *Conformal Mapping* and equivalent capacitance between the metallic plates, partially covered by dielectric layers, to determine effective permittivity (ε_{eff}) of MPA covered with superstrate layer. Furthermore, we also proposed a *unique iterative model* to determine ε_{eff} and f_r of MPA covered with either single or multiple layers of dielectric. The method uses modified relation in each iteration to determine ε_{eff} of the overall geometry. It is unlike all previous approaches where ε_{eff} is evaluated by substituting the total thickness of the superstrate in the expression. The proposed formulations and model exhibits superior performance w.r.t. previously reported works based on the same technique [55] – [56]. Besides, the proposed model can also be integrated with any technical computing software with ease.

1.3.4 Conformability Analysis of Conformal EBG Surfaces

We have proposed a simple geometrical approach for the determination of *a shift in the in-phase reflection frequency* of conformal EBG surfaces. The presented technique is evaluated by employing it on three distinct conformal-EBG surfaces operating at relatively lower frequencies, i.e., ISM and MBAN band. For this purpose, the planar unit cells are drawn on a circle of radius (***r***) along *x*- and *y*-axes to geometrically determine the shift in the in-phase property. It has been shown that the extra path delay due to reflected wave, together with the incident wave, results in maximum phase lag, an EM wave experiences while interacting with a conformal EBG surface. The presented theory is validated with the use of CST (computer simulation

tool) and prototyping array consisting of the third UC proposed by us.

1.4 Dissertation Outline

The rest of the dissertation is divided into 6 chapters. In this section, we discuss the contents of each chapter briefly.

Chapter 2: The inability of the existing approaches to predict the resonant frequency (f_r) of an MPA covered with multiple dielectric layers has led to the proposal of an iterative model that efficiently computes the f_r of an MPA with multiple layers of dielectric over it. The proposed model in this chapter is straightforward and can be conveniently implemented using technical computing software like MATLAB. Furthermore, we have also developed modified empirical expressions based on the CMA to determine the effective dielectric constant (ε_{eff}) of MPA covered with single or multiple superstrate layers. We have done extensive analysis of the proposed formulation and model on three different combinations of PCBs (RO5880B, RO4350, and FR4) and six textile fabrics namely Jeans cotton, Pure cotton, Rayon, Polyester, Wool, and Felt. The theoretically obtained resonant frequencies agree well with that of measured and simulated results.

Chapter 3: In this chapter, we discuss another two crucial aspects of WBAN that are SAR measurement and liquid phantom development. The existing tools to measure SAR values and dielectric properties are not cost-effective and also not readily available in most of the labs. Hence, it led to propose two cost-effective and straightforward approaches to emulate tissue-equivalent liquid (phantom) operating at the MBAN band. We have realized the two most common categories of the liquid phantom, i.e., homogeneous and heterogeneous (skin) models in this chapter. We determined one of the critical parameters that are the ε_r of the liquid phantom through approximation using CST. The other crucial parameter, α_d or σ_d, is determined with the help of a two-antenna arrangement dipped inside LUT. From the developed phantoms, we measured the thermal SAR values of an MPA operating in the MBAN band. For this, we measured the temperature rise of the liquids exposed to EM wave (antenna) for a given time. We validated our proposed theory with simulation by

keeping the conditions identical to measurement.

Chapter 4: The current-state-of-the-arts EBG integrated antennas are compact and have proved to be efficient in improving the performance. However, the designs require further miniaturization, improved on-body gain, and efficiency. Moreover, the polarization stability and surface wave rejection ability has not been considered, which is of prime importance for a compact and low-profile antenna in WBAN applications. In this chapter, therefore, we propose a design of a compact and via-less interdigital EBG unit cell (IDE) for wearable applications in the MBAN band. The uniqueness of the proposed cell is in its ability to achieve lower resonant frequency despite the very compact size of 14.3mm x 14.5mm. We have validated the polarization stability of the proposed EBG unit cell under TE-TM and TEM mode of incidence with the help of the reflection phase diagram. We also have demonstrated the polarization stability of the unit cells under obliquely incident TE-TM modes at 0^o, 15^o, 30^o, 45^o, and 60^o. Subsequently, we have designed an array of 2x2 IDE unit cells for enhancing the radiation feature of a monopole antenna. The size of the proposed IDE based EBG array integrated monopole antenna is 36mm x 38mm x 3.12 mm and is compatible with commercially available wristwatches. Although of its compact size, the EBG incorporated antenna can provide gain and efficiency of 5.3 dBi and 85% respectively at the MBAN frequency. Moreover, the incorporated antenna demonstrates measured on-body gain and efficiency of 3.7dBi and 50%, which is better than the present works.

Chapter 5: The conformability analysis of an EBG cell or array is critical for its effective operation when integrated with an antenna. For this, the exact determination of the in-phase frequency of conformal EBG surfaces becomes essential. The existing analytical approaches are efficient in the calculation of the in-phase points. However, these are predominantly for large arrays and hence impractical from the WBAN perspective. Besides, these techniques are sophisticated and are available for higher frequencies. In this chapter, therefore, we present a simple approach to determine the shift in in-phase reflection frequency of three standard conformal EBG/HIS. Then the unit cells are bent along *x*- and *y*-axes under radii (*r*) of 40, 50, and 60 mm. In our approach when an EBG unit cell of a given dimension is

drawn on a circle of desired radius (r), the new path traveled by the reflected and incident EM wave at the edges in terms of an electrical length (βl) results in a maximum shift in reflection phase. We have also extended the proposed theory to analyze three conformal EBG arrays consisting of 2x2 and 3x3 unit cells. For the validation of our approach, we simulated three conformal EBG unit cells for unit cell boundary condition (UC-BC) under TE^z-TM^z wave incidence and as well as for magnetic-electric BC (ME-BC) under TEM wave. Finally, an array of 3x3 unit cells is prototyped, and the reflection phase under TEM wave incidence for the array bent along x-and y-axes is recorded**.** The close agreement between the theoretical, simulated, and measured results justifies the significance of the proposed work.

Chapter 6: It is apparent that various body parts such as arms, wrists, torso, legs, and many more necessitates innovative conformed designs for both placement and enhanced performance of antenna (gain and efficiency) on-body. Therefore, in this work, we propose a design of a conformal, low-profile, and compact EBG backed monopole antenna operating at the MBAN band. The respective dimensions of the antenna and the unit cells are 44.36 x 42.8 x 0.832 mm^3 and 13.8 x 13.4 x 0.381 mm^3. We have also presented the polarization stability of the proposed unit cell to the incident TE and TM modes at angles 15^o, 30^o, 45^o, 60^o, and 75^o. We have also designed an array of unit cells arranged in a 3x3 pattern, acting as an antenna reflector. We then incorporated the developed EBG array to the low-profile monopole antenna for performance improvement. The low profile nature of the standalone antenna and the EBG array provides the conformability feature, and it is demonstrated by bending it for three distinct radii (r) of 40, 50 and 60mm. We measured the performance of the EBG incorporated conformal antenna on the body at the wrist and shoulders. The design exhibits excellent agreement between the measured and simulated results, whereby it achieves band-gap, gain, and efficiency of 2.34 – 2.65 GHz, 5.5dB, and 72%, respectively.

Chapter 7: In the last chapter of this dissertation, we conclude our present research work and have listed the future research in this direction.

Chapter 2

Effective Dielectric Constant of an MPA with Multiple Dielectric Layers

This chapter is based on the following research papers:

- D. Rano, M.A. Chaudhary, and M.S. Hashmi, "Determination of Effective Permittivity and Resonant Frequency of Patch Antenna Covered with Same and Mixed Type Dielectric Superstrates," *IEEE Access*, vol. 8, pp. 34418-34430, February 2020.
- D. Rano and M. S. Hashmi, "Determination of Effective Dielectric Constant and Resonant Frequency of Microstrip Patch Antenna with Multi-layered Superstrate Structures," *IEEE European Microwave Conference*, 2019, pp. 81-84.

In this chapter, we propose an iterative model to determine the resonant frequency (f_r) of MPA with multiple layers of dielectric over it. The proposed model is simple and can be conveniently implemented using a technical computing software like MATLAB. Furthermore, we have also developed modified empirical expressions based on the CMA to determine the effective dielectric constant (ε_{eff}) of MPA covered with single or multiple superstrate layers. We have done extensive analysis of the proposed formulation and model on three different combinations of PCBs (RO5880B, RO4350, and FR4) and six textile fabrics namely Jeans cotton, Pure cotton, Rayon, Polyester, Wool, and Felt.

Firstly, the proposed model and formulations are applied to MPA designed and

covered with PCB substrate and superstrates. Next, the applicability of the model and the formulations are carried out on MPA covered with textile layers. In the first part of the chapter, the model and the proposed formulations determine ε_{eff} and f_r of MPA covered with a single superstrate layer in the form of PCBs and textiles. In the next part of the chapter, the model and the formulations determine ε_{eff} of MPA with two superstrate layers like RO4350B and RO5880, pure cotton and wool, pure cotton, and felt fabric and many more combinations. Lastly, the effectiveness of the proposed model and formulations has been shown for a combination of three textiles layers, namely polyester, foam, and polyester. The theoretically obtained resonant frequencies have been verified through measurements with the help of the VNA.

2.1 Background and Related work

An MPA covered with single or multiple dielectric layers tends to resonate at a different frequency than the original one [54] – [60]. It is because of the effective dielectric constant of the overall arrangement changes [54]. From the WBAN perspective, WSN is widely used in the medical realm. WSN attached to the body (on-body wearables) can record and transfer vital physiological parameters of the body like heartbeat rate (Electrocardiogram, ECG), body temperature, blood pressure, respiratory rate, ligament pressure (round ligament), and many more [1] – [5]. Often, these sensors are placed on the body for accurate monitoring. Therefore, the communication between the on-body sensor and external BTS happens through single or multiple layers of textiles. ZigBee, Z-wave, and X-Bee are ubiquitous transmit and receive modules in WSN deployed on- and off-body. These modules operate in either 800 MHz – 900 MHz (Z-wave) or 2.4 GHz – 2.4835 GHz (ZigBee and X-Bee) unlicensed bands. Out of the entire band (100MHz) allocated to Z-wave, only a part of it is used in various parts of the world. For example, Z-wave in India, US, Russia, Europe, and Japan operate at 862.5 MHz, 908.4 MHz, 869 MHz, 868.4 – 868.42 MHz, 922 – 926 MHz respectively. Since the fractional bandwidth of these devices is less than 3% and any deviation from the original band (in the presence of textile layers) leads to out of band communication, and the essential body parameters are lost. Hence,

it is of utmost importance to accurately determine ε_{eff} and f_r for reliable and error-free communication between sensors.

Communication of an MPA through multiple dielectric layers has been a challenge for a long time and has not been given importance [23], [54] – [57]. In this dissertation, we have followed approaches based on conformal mapping (CM) because they are simple and can be easily integrated with technical computing software like MATLAB [54] – [57]. Techniques based on CM, however, relying on approximation, predict f_r of superstrate covered MPA with good accuracy w.r.t. measured values that, too, with simpler closed-form expressions.

Svacina in [54] presented an analysis of the dielectric covered microstrip line by CMA. In this method, a three-layered structure (substrate – superstrate – air) is conformally mapped on the flux-potential plane (*w*-plane). During the transformation of the physical plane to the complex plane, the angle of refraction at the interfaces (air – superstrate, substrate – superstrate) has been retained. Based on the fractional area occupied by the respective dielectrics, a filling fraction is assigned, which was further used to determine ε_{eff}. Furthermore, *Svacina* in [57] further extended the analysis to the microstrip and co-planar line covered with multiple layers. It was, however, a theoretical work, and no experimental results have been presented. *Zhong* in [55], proposed a closed-form expression to predict f_r of MPA with multi-dielectric layers. The proposed expressions further added fringing effects at the open-end of the MPA, which improved the theoretically determined f_r w.r.t—measured one. *Bernard* in [56], made further modifications in the formulations proposed by *Zhong* due to the presence of inconsistency in the superstrate thickness (discussed in detail in section 2.2). But, the method had a drawback of assuming a superstrate layer of infinite thickness. Since the possibility of such a scenario is very less in practice, therefore the proposed formula has to be modified to take into account the finite thickness of the superstrate layer. *Guha* in [94], used the formulations in [54], to predict ε_{eff} and f_r of circular patch antenna operating at fundamental and other higher modes. The values of the dielectric constant of substrate and superstrate considered in this work were also identical to that in [55] – [56]. Therefore, it does not provide any significant advancement. *Li* in [95], varied the superstrate dielectric constant from 1 to 10.2 and successfully predicted the

f_r with reasonable accuracy for considerable thickness (10.5 mm). However, all the analyses were carried on a foam substrate of dielectric constant 1.046. Since foam has particular use in antenna design (low loss and conformal), therefore the variation in theoretical and measured results may be different for any other substrate of higher dielectric constant. *Banik* in [96], defined a new relative permittivity below the patch to encounter the surface wave losses due to fringing. However, once again, the dielectric constant of the substrate and superstrate used in the analysis was limited to values used in [55] and [56]. Moreover, the analysis was limited to superstrates of the thickness of 2.345 mm, which is much lesser than that of [55] and [56].

A thorough literature review, therefore, reveals that the work presented in [55] and [56] are most standard in this direction. Therefore, in this dissertation, we have compared results obtained by our proposed model with [55] and [56]. We also present here the following unsolved issues in this domain that require urgent attention considering the evolving biomedical and e-health related applications.

a) Lack of analysis in the determination of f_r of superstrate covered MPA for a substrate with permittivity greater than 2.2, 2.32, and 2.47. Since many antennas from WBAN perspective are designed on Polyamide lossy (Nylon-6), Kapton (Dupont), Latex, polyester sheet, and RO4350B having dielectric constants of 3.6, 3.5, 3.31, 2.8 and 3.66 respectively [38], [50], [70], therefore, modification in the current state is required to determine the shift in f_r of such antennas covered by textile layers.

b) Unavailability of formulation of ε_{eff} and analysis of f_r of MPA covered with multiple dielectric layers, i.e., $\varepsilon_1, \varepsilon_2, \varepsilon_3 \ldots \varepsilon_n$ (here $\varepsilon_1, \varepsilon_2, \varepsilon_3$ are dielectric constants of subsequent superstrate layers over an MPA). For example, CM based technique in [57] provides formulations based on a quasi-static model to determine ε_{eff} for a microstrip line covered with multi-layers of superstrate. However, these are not scalable to determine ε_{eff} and f_r of MPA covered with multiple dielectric layers. From the WBAN perspective, the communication of WSN can happen through multiple textile layers depending on terrain. Therefore, it becomes essential to determine all possible scenarios of frequency shift that may happen in such

conditions.

c) For an MPA covered with a spaced superstrate, an existing analysis ignores the material present above the air gap for the determination of ε_{eff} and f_r [56]. It essentially means that the MPA is radiating into the infinitely thick spaced superstrate rather than the free space. However, the possibility of such a scenario is negligible, hence the height of subsequent superstrate layers must be taken into account in the determination of ε_{eff} and the eventual f_r.

Therefore, this work addresses most of the concerns and advances the current state-of-the-art by following way.

1) Development of new empirical relations based on CM and equivalent capacitance between metallic layers of ground plane and patch of an MPA. The dielectric layers present above the patch (superstrate - air), and the substrate is conformed on an imaginary flux-potential plane, and respective filling fractions are calculated. For the obtained filling fractions, capacitances per unit area of air, substrate, and superstrate layers are determined to result in ε_{eff} and f_r. We have validated our approach to MPAs designed on the substrate of dielectric constant higher than the previous works. For example, in this dissertation, we used dielectric constants of 3.66 and 4.7 to design the MPAs and subsequently cover it by textiles as well as with PCBs.

2) Development of a unique iterative model to use the formulations derived in (1) and predict the resonant frequency of MPA covered with single or multiple layers of dielectric. Unlike previous approaches, the proposed model allows fragmentation of multiple superstrate layers over the MPA such that ε_{eff} and f_r are determined separately for each layer.

3) The proposed technique avoids the presence of an infinite superstrate layer over the MPA, unlike [56].

4) Restoration of the original f_r of the MPA covered with multiple superstrates by modifying the physical parameters (mostly length).

2.2 Formulation of effective dielectric constant

In this section, we derive formulations to determine ε_{eff} of MPA covered with a single superstrate layer by using CMA. For this, an MPA designed on a substrate (shaded in brown) with dielectric constant ε_1 and thickness h is shown in Figure 2.1 (a). The physical parameters of the MPA, width W and length L are determined through standard expressions in [58]. The MPA is covered by a superstrate layer (shaded in red) of thickness $h_2 - h$ and dielectric constant ε_2.

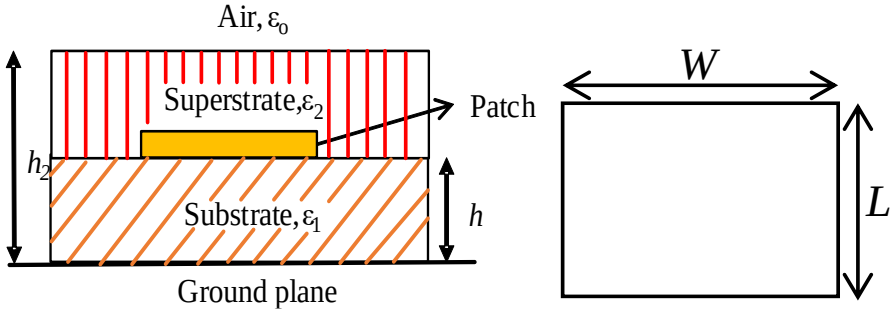

Figure 2.1 MPA with dimensions *W* and *L* covered with a single superstrate layer

For $W/h > 1$ (low profile MPA, mostly in WBAN), CM is then applied at the interface of a substrate (ε_1) – superstrate (ε_2) and superstrate (ε_2) – air (ε_o) using Wheeler's transformation [67] – [68]. The conformed dielectric boundaries on the flux-potential plane are shown in Figure 2.2 (a). Here, W_{ef} is the effective width of the patch accounting to fringing at the edges, V_ε is the extent of the superstrate layer in the imaginary axis of w-plane, q_o, q_1, and q_2 are the effective filling fractions of air, substrate, and superstrate boundaries defined by the ratio of the area occupied by a given dielectric by total area [54]. For example, assume the specific area occupied by air, substrate, and superstrate are $S_{\varepsilon o}$, $S_{\varepsilon 1}$, and $S_{\varepsilon 2}$ respectively, whereas the total area is S. Therefore, filling fractions q_o, q_1, and q_2 are given by (2.1). The overall filling fraction, q is the summation of q_o, q_1, and q_2 and is expressed in (2.2). Apparently, from (2.2) q reduces to unity. As a necessary condition of Wheeler's transformation, the angle of refraction at the interfaces ($x - y$, physical plane) must be retained while conforming the dielectric boundaries to w – plane, as shown in Figures 2.2 (a)–(b). It

essentially means that for an EM wave while traveling from substrate to superstrate or superstrate to air, angle of refraction at these interfaces shall be retained while conforming physical planes to imaginary ones (*w*-plane).

$$q_o = \frac{S_{\varepsilon o}}{S}; q_1 = \frac{S_{\varepsilon 1}}{S}; q_2 = \frac{S_{\varepsilon 2}}{S} \tag{2.1}$$

$$q = \frac{S_{\varepsilon o}}{S} + \frac{S_{\varepsilon 1}}{S} + \frac{S_{\varepsilon 2}}{S} = \frac{S_{\varepsilon 0} + S_{\varepsilon 1} + S_{\varepsilon 2}}{S} \tag{2.2}$$

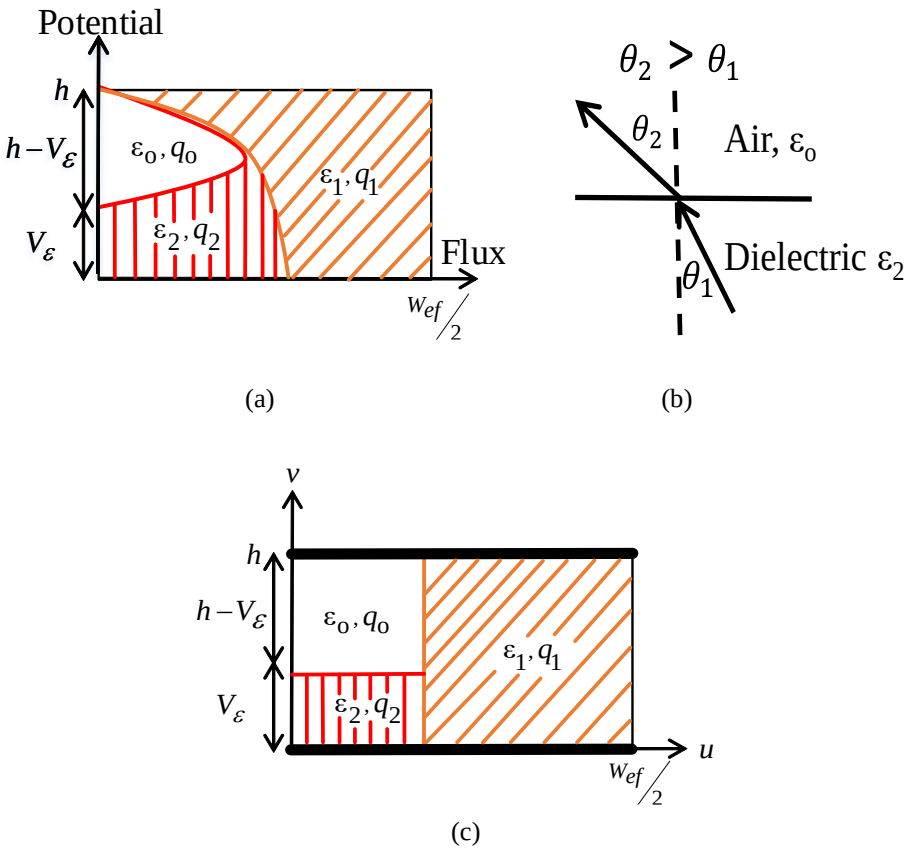

Figure 2.2 (a) Refraction of EM wave traveling from a dielectric medium to air (Snell's law) [θ_1 and θ_2 are incident and refracted angles of EM wave] (b) Conformed dielectric boundaries in the flux-potential plane (*w*-plane) (Shaded portions indicate: red–superstrate, brown–substrate, and white-air), (c) Approximation of dielectric boundaries q_0 and q_2 with associated permittivities

Figure 2.2 (c) is an approximation of dielectric boundaries similar to the works of Javina, Zhong, and Bernard [54] – [56]. For an MPA with width, W fringing at the edges results in W_{ef} given in (2.3), and the point of intersection V_ε in Figure 2.2 (a) is given by (2.4). The filling fractions q_o, q_1, and q_2 can be determined from W_{ef}, V_ε, h_2, and h and given by (2.5) – (2.7). In the absence of the superstrate layer, i.e., $h_2 = h$, V_ε, and q_2 must go to zero. However, Bernard found out that even in the absence of the superstrate layer, q_2 does not reach zero, as evident from (2.5) – (2.7). This inconsistency found in q_2 by Bernard has resulted in a modified expression of $q_2 \rightarrow q_{2new}$ as given (2.8). Now, we can see that the dielectric layers in Figure 2.2 (c) are either in series or in parallel. It implies that $S_{\varepsilon o}$ is in series with $S_{\varepsilon 2}$, and the combination of them is in parallel to $S_{\varepsilon 1}$. These dielectric regions form capacitances between the metallic layers of the MPA and ground plane, which is utilized here to derive the expression of ε_{eff}.

$$W_{ef} = W + \frac{2h}{\pi}\ln\left[17.08\left(\frac{W}{2h}+0.92\right)\right] \tag{2.3}$$

$$V_\varepsilon = \frac{2h}{\pi}\tan^{-1}\left[\frac{\pi}{\frac{\pi}{2}\frac{W_{ef}}{h}-2}\left(\frac{h_2}{h}-1\right)\right] \tag{2.4}$$

$$q_o = \frac{1}{2}\cdot\frac{h-V_\varepsilon}{W_{ef}}\cdot\ln\left[\pi\frac{W_{ef}}{h}\cdot\frac{\cos\left(\frac{\pi}{h}\cdot\frac{V_\varepsilon}{2}\right)}{\pi\left(\frac{h_2}{h}-\frac{1}{2}\right)+\frac{V_\varepsilon}{2}\cdot\frac{\pi}{h}}+\sin\left(\frac{V_\varepsilon}{2}\cdot\frac{\pi}{h}\right)\right] \tag{2.5}$$

$$q_1 = 1-\frac{h}{2W_{ef}}\cdot\ln\left(\pi\frac{W_{ef}}{h}-1\right) \tag{2.6}$$

$$q_2 = 1 - q_1 - q_o \tag{2.7}$$

$$q_{2new} = 1 - q_1 - q_0 - \frac{h}{2W_{ef}} \ln\left[\frac{\pi}{2} - \frac{h}{2W_{ef}}\right] \tag{2.8}$$

The capacitance per unit area of the substrate C_1, air C_o, and superstrate C_2 regions is given by (2.9) – (2.11), respectively. Here, $h_1 = h - V_\varepsilon$ (from Figure 2.2(a)). Now, we derive the equivalent series capacitances C_{eqs} between the C_o, and C_2, which is expressed in (2.12). Next, we can see from Figure 2.2 (c) that C_{eqs} is in parallel with C_1, and effective capacitance C_{eff} of both of them is expressed in (2.13). After the substitution of (2.9) and (2.12) in (2.13), C_{eff} is given by (2.14). From Figure 2.1, we can write this effective capacitance in terms of the overall dielectric constant of the arrangement ε_{eff}, the overall filling fraction, q, and the total height of the arrangement, h_2 as expressed in (2.15). Substituting (2.15) in (2.14), ε_{eff} is given by (2.16). When we further simplify the expression of ε_{eff} given in (2.16) to (2.17), it has a term ε_{eqs}, which is essentially (2.18). Now we can say that from the known values of ε_o, ε_1, ε_2, h, h_2 and the determined values of W_{ef}, V_ε, q_o, q_1, q_{2new} can enable determination of ε_{eff} of the arrangement of layers shown in Figure 2.1. Interestingly, the formula of ε_{eff} proposed in this chapter takes into account the height of the superstrate layer, unlike that proposed in [54] – [56].

$$C_1 = \frac{(\varepsilon_1 q_1)}{h} \tag{2.9}$$

$$C_o = \frac{(\varepsilon_o q_o)}{h_1} \tag{2.10}$$

$$C_2 = \frac{(\varepsilon_2 q_{2new})}{V_\varepsilon} \tag{2.11}$$

$$C_{\text{eqs}} = \frac{\varepsilon_2 q_{2\text{new}} \varepsilon_0 q_0}{\varepsilon_2 q_{2\text{new}} h_1 + \varepsilon_0 q_0 V_\varepsilon} \tag{2.12}$$

$$C_{\text{eff}} = C_{\text{eqs}} + C_1 \tag{2.13}$$

$$C_{\text{eff}} = \frac{\varepsilon_2 q_{2\text{new}} \varepsilon_0 q_0}{\varepsilon_2 q_{2\text{new}} h_1 + \varepsilon_0 q_0 V_\varepsilon} + \frac{\varepsilon_1 q_1}{h} \tag{2.14}$$

$$C_{\text{eff}} = \frac{\varepsilon_{\text{eff}} q}{h_2} \tag{2.15}$$

$$\varepsilon_{\text{eff}} = \frac{\varepsilon_1 q_1 h_2}{h} + \frac{\varepsilon_2 q_{2\text{new}} \varepsilon_0 q_0 h_2}{\varepsilon_2 q_{2\text{new}} h_1 + \varepsilon_0 q_0 V_\varepsilon} \tag{2.16}$$

$$\varepsilon_{\text{eff}} = \frac{\varepsilon_1 q_1 h_2}{h} + \varepsilon_{\text{eqs}} \tag{2.17}$$

$$\varepsilon_{\text{eqs}} = \frac{\varepsilon_2 q_{2\text{new}} \varepsilon_0 q_0 h_2}{\varepsilon_2 q_{2\text{new}} h_1 + \varepsilon_0 q_0 V_\varepsilon} \tag{2.18}$$

2.3 Proposed Iterative Model

In this section, we propose a unique iterative model to determine ε_{eff} and f_r at each iteration. The model is iterative because, at the end of each step, the dielectric constant of the substrate, ε_1, gets updated with the newly computed ε_{eff}. We implemented the model in MATLAB. However, following the steps mentioned below, it can be implemented in any technical computing software. Unlike the previous approaches [55] – [57], the proposed model does not take into account the theoretically obtained length of the MPA; instead, it considers the optimized simulated values in CST. We did this because the standard expression to determine physical parameters of

MPA operating at some f_r assumes the ground plane is of infinite extent. It, however, is not the case in simulation and measurement, therefore often, there is a noticeable shift in f_r from the original one obtained from the theoretical values. We would like to mention here that the design of MPA is the first step, and then a layer of superstrate is added over it. Therefore, parameters of MPA (width, length, and impedance) are independent of the superstrate. The detailed flow chart of the proposed model to determine ε_{eff} and f_r is shown in Figure 2.3.

W: Width of the patch (mm)

L: Length of the patch (mm)

h : Height of the substrate (mm)

h_2: Actual total height of the superstrate

h_2' : Total height of the substrate and superstrate assumed in this model

Δh : ($h_2 - h$) mm

ε_2 : Permittivity of the superstrate

ε_1 : Initial permittivity of the substrate

W_{ef} : Effective width of the patch (mm)

V_ε : Extent of superstrate in w – plane (mm)

N: Number of steps = round ($\Delta h/n$)

n : Resolution of the model

q_o, q_1 and q_{2new} : Filling fraction of air, substrate and superstrate respectively

ε_i : Permittivity of the substrate for i^{th} step which gets updated to ε_i for every i = i+1

ε_{eqs} : Permittivity of air and superstrate given by 2.18

%variation = [f_r (Sim.) – f_r (Theory)]/f_r (Sim.)

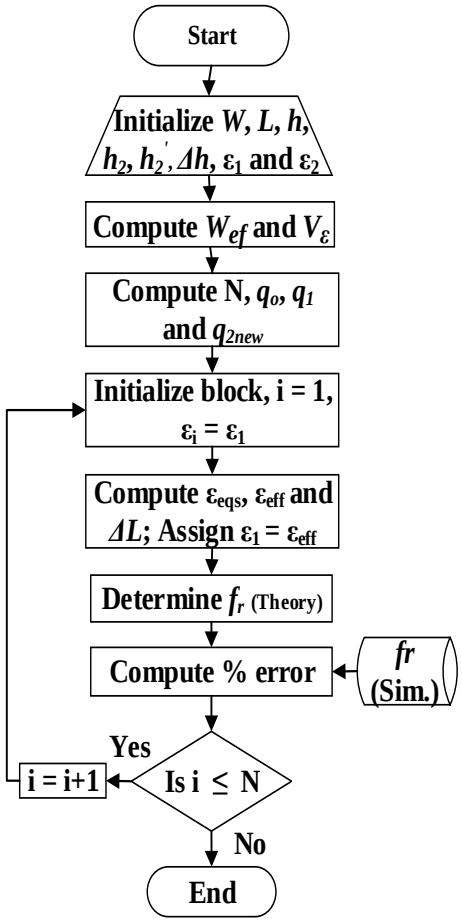

Figure 2.3 Proposed model to determine the effective dielectric constant of MPA covered with single superstrate layer (The model is implemented in MATLAB)

The following steps explain the implemented model.

***Step 1*:** We choose the antenna's parameters, substrate, superstrate, and such as length, width, height, and dielectric constant. Here, the actual superstrate's height is $\Delta h = h_2 - h$ from Figure 2.1. However, the total height of the substrate and the superstrate is taken as h_2' rather than h_2 in this model, which is given by $h_2' = h + n$. Therefore, h_2 in (2.4) – (2.5), (2.15) – (2.18) is replaced by h_2'.

We have divided the total superstrate layer into 'N' smaller blocks of thickness 'n' each. The selection of n is explained here with the help of an example, whereas the selection of N is included in step 3. Consider an MPA designed on substrate RO4350B of dielectric constant and height of 3.66 and 1.524mm, respectively. It is covered by a superstrate layer identical to the substrate. Therefore, h_2' becomes 1.524 + n mm. Putting the value of n = 0.1mm in (2.4), (2.5), (2.15) – (2.18) ε_{eff} comes out to be 3.679. For any other values of n lesser than 0.1 mm say 0.09 or 0.08 mm, ε_{eff} is smaller than ε_1 of 3.66. Therefore, n assumes the limiting value for which ε_{eff} is just greater than ε_1. It is obvious that for larger n, say 0.11 or any higher value, the ε_{eff} becomes greater than ε_1, but due to iterative nature of the model, the value of ε_{eff} becomes impractically larger for thicker superstrates. As a good assumption, we chose the starting value of n = 0.01, and it ends at the value for which $\varepsilon_{eff} > \varepsilon_1$ with a step increment of 0.01.

***Step 2*:** Next, we determine the values of W_{ef} and V_ε from the parameters chosen in step 1 using (2.3)–(2.4).

***Step 3*:** In this step, from the chosen and obtained parameters in steps 1 and 2, we compute the filling fractions q_o, q_1, and q_{2new} with the help of (2.5) – (2.6), (2.8). Subsequently, we determine the number of steps N using round ($\Delta h/n$) in MATLAB to find the maximum iterations (no. of blocks) required to calculate ε_{eff}. The process of determination of N is explained here with the help of two examples. For Δh = 1.524 mm and n = 0.1mm, gives N = 15 and this implies that the loop in Figure 2.3 run 15 times. It also implies that the modified Δh for which the model calculates ε_{eff} now becomes 0.1*15 = 1.5mm instead of 1.524mm. Similarly, for Δh = 1.575 mm and n = 0.1mm, N equals 16, and modified Δh for which ε_{eff} is determined becomes 1.6 mm. We can see that the model may underestimate or overestimate the value of ε_{eff} based

on the value of Δh. However, we show in section 2.4 that this difference is very less and does not have a significant impact.

***Step 4*:** In this step, we initialize a counter, i. The dielectric constant of the substrate, ε_1, gets updated in each loop. As a starting $\varepsilon_i = \varepsilon_1$.

(**Note:** ε_i for i = 1, 2 … N should not be confused with permittivities of substrate and superstrates).

Step 5: We compute ε_{eqs} and ε_{eff} from (2.16) – (2.18) in this step. Then, the newly computed ε_{eff} is assigned to ε_1. We also calculate the open-end extension of the patch ΔL due to the fringing field with the help of [97] in this step.

Step 6: Next, we determine the f_r of the MPA given by (2.19) using the values ε_{eff}, ΔL, and L from steps 1 and 5.

$$f_r = \frac{c}{2\left(L + 2\Delta L\right)\sqrt{\varepsilon_{\text{eff}}}} \tag{2.19}$$

Step 7: Determine the percentage variation in resonant frequencies between the simulated and theoretical values with the help of (2.20).

$$\%\,\text{variation} = \frac{\left| f_r\,(\text{Sim.}) - f_r\ (\text{Th.}) \right|}{f_r\,(\text{Sim.})} \tag{2.20}$$

Step 8: Finally, we use a conditional check, such that if i ≤ N, then the counter is incremented by i = i+1 else the loops breaks, which indicates completion of all steps.

(**Note:** Since frequency dispersion generally decreases for the wider conductor (W/h >1), hence it has not been considered in this model).

2.4 Theoretical and Simulated Results

In this section, we compare the theoretically obtained f_r with the simulated values in CST for an MPA covered with a single superstrate layer. We have divided this section into two parts. In the first part, we have analyzed the formulations and

model on PCB, whereas in the second part, we do the same for the textile layers. We first design an MPA on RO4350B board with dielectric constant and thicknesses of 3.66 and 1.524mm, respectively, in CST. The optimized physical parameters of an MPA operating at 2.38 GHz in CST are mentioned in Table 2.1. The reason for choosing 2.38 GHz as f_r here is because FCC in 2014 has allocated a dedicated band for medical applications, and it operates from 2.36 – 2.4 GHz with center frequency at 2.38 GHz. We used here a quarter-wave matching to feed the patch of the MPA with a primary feed line of 50Ω. The electrical and physical parameters of the line and MPA are also given in Table 1.

Table 2.1 Physical and electrical parameters of the MPA, and feed line designed on RO4350B

Antenna para.	Value	Antenna para.	Value	Antenna para.	Value
Length *L* (mm)	31.5	Patch Impedance	283 Ω	Length of λ/4 line (mm)	17
Width W (mm)	41.3	Quarter-wave transformer (λ/4) impedance	119 Ω	Width of primary feed (50 Ω) line (mm)	3.6
Effective dielectric constant	3.34	Width of λ/4 line (mm)	0.5	Length of 50Ω line (mm)	6

2.4.1 Single Layer of PCB Over MPA

We covered the designed MPA by superstrate layers, RO4350B, RO5880 (ε_2 = 2.2) and FR4 (ε_2 = 4.7) in such a way that all the conditions $\varepsilon_1 = \varepsilon_2$ (case 1), $\varepsilon_1 > \varepsilon_2$ (case 2), and $\varepsilon_1 < \varepsilon_2$ (case 3) are met. The reason for choosing these substrates is due to availability for in-house fabrication in our institute. Tables 2.2 – 2.4 list the theoretical and simulated results for all the three cases up to the superstrate height of 4.5mm. The table also compares the results obtained with the proposed technique with that of [55] – [56], which are considered most standard in this direction.

We can make the following inferences from Tables 2.2 – 2.4.

a) Even in the absence of frequency dispersion, our proposed formulation and model

performs better than [54] – [56].

b) It is apparent from case 2 that the % variation is higher in the case of Δh = 4.5 mm w.r.t. [55]. Apparently, for a superstrate of $\varepsilon_2 \leq 2.2$ and smaller heights (1mm–3mm), the proposed model and the formulation determine ε_{eff} and f_r with high accuracy, but accuracy decreases for more significant height.

c) It is apparent from the first and second rows of Tables 2.2 and 2.4 that % variation of the presented work goes slightly out of trend. But careful observation of (2.20) and the values in Tables 2.2 and 2.4 agrees to the fact that % variation increases from a more negative value to a more positive.

Table 2.2 Comparison of simulated and theoretically obtained resonant frequencies of the MPA in this work with [55] and [56] for superstrate of dielectric constant ε_2 = 3.66 (Case 1: $\varepsilon_1 = \varepsilon_2$) [$\Delta h = h_2 - h$, L = 31.5 mm, W = 41.3 mm, ε_1 = 3.66, h_1 = 1.524 mm at 2.38] (%var signifies % variation)

Δh (mm)	ε_{eff} [55]	ε_{eff} [56]	ε_{eff} [This]	Sim. Freq. (GHz) (CST)	Th. Freq. (GHz) [55]	Th. Freq. (GHz) [56]	Th. Freq. (GHz) [This]	% var [55]	% var [56]	% var [This]
1.0	3.60	3.50	3.83	2.317	2.401	2.434	2.338	3.61	5.05	0.91
1.5	3.62	3.51	3.92	2.305	2.392	2.429	2.312	3.80	5.40	0.30
3.0	3.69	3.54	4.13	2.284	2.372	2.421	2.268	3.86	5.95	0.70
4.5	3.74	3.56	4.30	2.270	2.358	2.414	2.230	3.88	6.34	1.76

Table 2.3 (Case 2: $\varepsilon_1 > \varepsilon_2$, where ε_1 = 3.66, and ε_2 = 2.2 RO5880)

Δh (mm)	ε_{eff} [55]	ε_{eff} [56]	ε_{eff} [This]	Sim. Freq. (GHz) (CST)	Th. Freq. (GHz) [55]	Th. Freq. (GHz) [56]	Th. Freq. (GHz) [This]	% var [55]	% var [56]	% var [This]
1.0	3.59	3.47	3.83	2.347	2.403	2.443	2.336	2.40	4.10	0.45
1.5	3.62	3.48	3.91	2.341	2.395	2.441	2.320	2.32	4.27	1.20
3.0	3.67	3.49	3.98	2.330	2.377	2.437	2.292	2.06	4.62	1.58
4.5	3.72	3.50	4.17	2.316	2.362	2.434	2.243	1.82	4.90	3.15

Table 2.4 (Case 3: $\varepsilon_1 < \varepsilon_2$, where $\varepsilon 1 = 3.66$, and $\varepsilon_2 = 4.7$ FR4)

Δh (mm)	ε_{eff} [55]	ε_{eff} [56]	ε_{eff} [This]	Sim. Freq. (GHz) (CST)	Th. Freq. (GHz) [55]	Th. Freq. (GHz) [56]	Th. Freq. (GHz) [This]	% var [55]	% var [56]	% var [This]
1.0	3.60	3.52	3.83	2.305	2.400	2.428	2.328	4.12	5.34	1.00
1.5	3.63	3.53	3.92	2.287	2.391	2.422	2.305	4.57	5.89	0.77
3.0	3.67	3.57	4.13	2.260	2.370	2.409	2.250	4.87	6.60	0.44
4.5	3.76	3.60	4.30	2.242	2.352	2.401	2.210	4.92	7.10	1.43

2.4.2 Single Layer of Textile Over MPA

Next, we show the effectiveness of the presented model and the formulations on the designed MPA (on RO4350B) covered with textiles layers as the superstrate. From the WBAN perspective, the antenna in WSN has to send data through multiple layers of textiles such as cotton, Rayon, polyester, wool, and many more. Often there may be a combination of textiles such as woolen jacket over cotton, felt jacket over polyester and, many more. Therefore, we divide our analysis with textile layers into two sets. In the first set, we see the performance of our technique on textile layers, which are immediately next to MPA, such as cotton, Rayon, and polyester. In the second set combination of two textile layers like wool and felt fabric (hoodie) and many more have been used to carry out the analysis. This section limits the analysis until MPA covered with a single layer, whereas a combination of two layers is discussed in section 2.5.2. Table 2.5 lists f_r for the MPA covered with some conventional textiles obtained from the proposed model and CM based models [55]–[56].

We took the thickness of the textile layers mentioned in Table 2.5 from the previous researches [98] – [99]. We can conclude from the results that for thinner superstrate (0.2–0.3 mm), the % variation obtained from this work is superior to [55]–[56]. However, for the thicker superstrates (1–1.5 mm), the %variation increases when compared to [55]. Both the results agree with the trend in Table 2.3. We can also infer

from the Tables 2.3 and 2.5 that for superstrates with $\varepsilon_2 = 2.2$, and lesser height the % variation for the proposed model is better when compared to [55]–[56]. However, for superstrates with similar dielectric constant and more considerable heights, the %variation increases when compared to [55]. This inference is very useful and is used in the next section, where the MPA covered with many textiles is analyzed.

Table 2.5 Comparison of simulated and theoretically obtained resonant frequencies of the MPA covered by different textile layers as superstrate in this work with [55] and [56] (Mat. signifies material, 1 – Polyester, 2 – Jeans cotton, 3 – Pure cotton, 4 – Rayon, 5 – Felt fabric, 6 – Terry wool, 7 - Leather)

Mat.	Δh (mm)	ε_{eff} [55]	ε_{eff} [56]	ε_{eff} This	Sim. Freq. (GHz) (CST)	Th. Freq. (GHz) [55]	Th. Freq. (GHz) [56]	Th. Freq. (GHz) [This]	%var [55]	%var [56]	%var This
1	0.3	3.56	3.45	3.71	2.372	2.408	2.442	2.3655	1.52	3.00	0.27
2	0.3	3.56	3.46	3.71	2.373	2.407	2.442	2.3620	1.50	2.91	0.46
3	0.2	3.55	3.45	3.70	2.374	2.409	2.442	2.3670	1.48	2.86	0.29
4	0.2	3.56	3.46	3.70	2.365	2.408	2.438	2.3635	1.82	3.09	0.06
5	1.5	3.60	3.45	3.91	2.363	2.397	2.442	2.3007	1.46	3.35	2.64
6	1.5	3.61	3.46	3.91	2.358	2.392	2.441	2.3005	1.45	3.54	2.44
7	1.5	3.61	3.47	3.91	2.353	2.390	2.438	2.3000	1.58	3.62	2.25

2.5 Proposed Model for Two Superstrate Layers

In this section, we extend our analysis from a single superstrate layer to two layers over the MPA. Figure 2.4 (a) depicts a scenario of MPA covered by two dielectric layers, namely superstrate#1 (shaded in red) and 2 (shaded in blue). Here, the height and dielectric constant of the additional dielectric layer is $\Delta h_1 = h_3 - h_2$ and ε_3, respectively. Once again, we have divided our analysis into two parts. In the first part, we prove the effectiveness of the proposed model for a combination of two PCBs layers, and in the next part, we repeat it for textile layers.

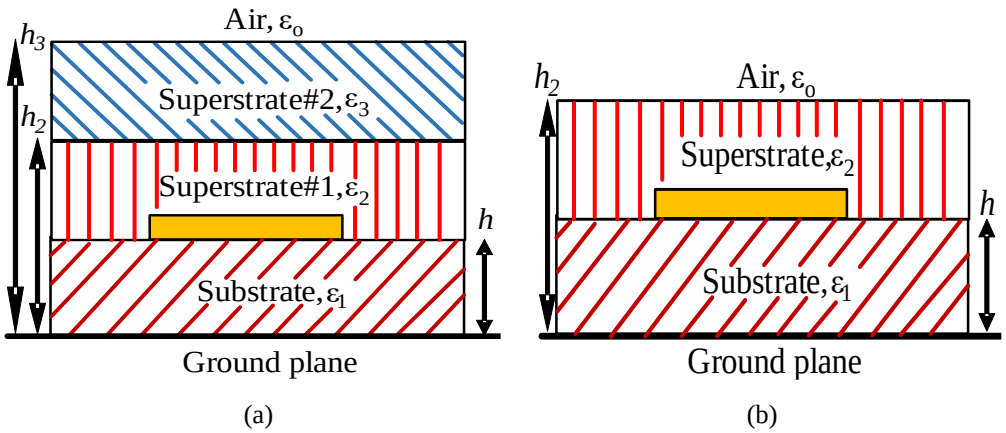

Figure 2.4 (a) MPA covered with two superstrate layers, (b) Fragmentation of the MPA covered by two dielectric layers to one layer

2.5.1 Two Layers of PCB Over MPA

The determination of ε_{eff} of the structure in Figure 2.4(a) consists of two steps. In the first step, we fragment two superstrate layers to one layer over the MPA, as depicted in Figure 2.4(b). Then $\varepsilon_{eff}(h_2)$ is computed using the model proposed in section 2.3. In the second step, the fragmented dielectric layer is restored over the MPA, as shown in Figure 2.5(a), and then the $\varepsilon_{eff}(h_3)$ is computed similarly to the first step. The idea is to replace ε_1 by $\varepsilon_{eff}(h_2)$, the scenario depicted in Figure 2.5(b), before using the single-layer formulations. Essentially it means that ε_{eff} of the first superstrate layer becomes the dielectric constant of the substrate in the second step, as evident from Figure 2.4 – 2.5(a).

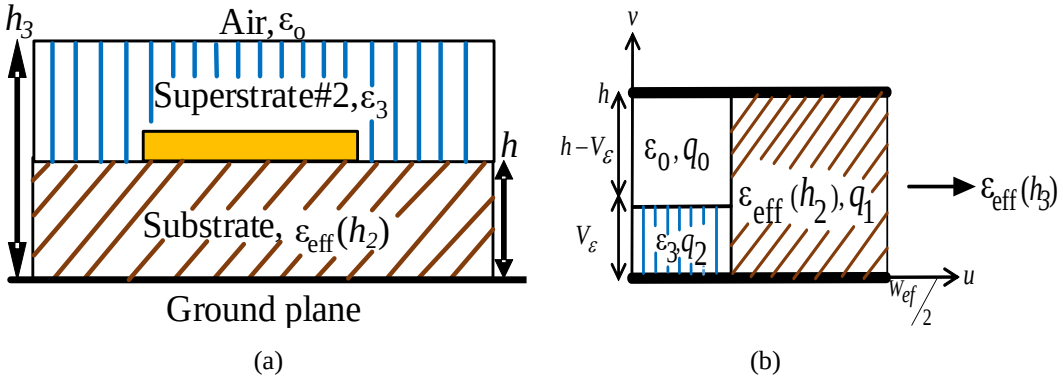

Figure 2.5 (a) MPA covered with the second superstrate layer, (b) Approx. of dielectric boundaries with modified permittivities

We have added the following additional steps in the flowchart in Figure 2.3 for the determination of ε_{eff} (h_3) in Figure 2.5(b). It is important to note here that these steps are followed only after the determination of ε_{eff} (h_2) of the single-superstrate layer.

1) Add the values of Δh_1 and ε_3 of the second superstrate layer. Determine new '*n*' for the addition of the second superstrate layer. It was observed during our analysis that if the values of permittivities of the first and second superstrates are close, then the results don't show significant variation in f_r, and therefore, *n* can be kept identical to that used for superstrate 1.
2) Determine the number of steps M similar to N given by M = round ($\Delta h_1/n$) in MATLAB required to calculate ε_{eff} (h_3).
3) Initialize another loop with counter j after the complete execution of the condition $i \leq N$. Initially assign $\varepsilon_j = \varepsilon_{eff}$ (h_2) similar to *step 3* in Figure 2.3. In this way, the substrate in the i^{th} loop gets updated with the new value ε_{eff} (h_2), as depicted in Figure 2.5(b). Furthermore, equations 2.4 – 2.18 also gets modified by replacing h_2, ε_1, and ε_2 by h_3, ε_{eff} (h_2), and ε_3, respectively.
4) Finally, a conditional check of $j \leq M$ is performed at the end of the loop to increment the counter by j+1. If $j \leq M$, the loop continues else the loop breaks and results in ε_{eff} (h_3).

The above mentioned additional steps in the model of section 2.3 enable the determination of ε_{eff} and f_r of MPA covered with two superstrate layers. Next, we have done a rigorous analysis of the proposed two-layer model on combination of dielectric layers such as $\varepsilon_1 = \varepsilon_2 > \varepsilon_3$, $\varepsilon_1 = \varepsilon_2 < \varepsilon_3$, $\varepsilon_1 < \varepsilon_2 > \varepsilon_3$, $\varepsilon_1 > \varepsilon_2 < \varepsilon_3$ (case 1 – 4), and $\varepsilon_1 > \varepsilon_2 > \varepsilon_3$ (case 5). These combinations include all the possible dielectric constant of substrate and superstrate. For the cases, 1–4, the substrate is fixed as RO4350B (ε_1) while the superstrate layer varies. Therefore, dimensions of the MPA remain unaltered, as mentioned in Table 2.1. However, for case 5, the MPA is designed on FR4, and a new set of physical and electrical parameters of the patch and feedline were determined, as mentioned in Table 2.6. Tables 2.7 – 2.11 lists all cases of ε_1, ε_2, and ε_3.

Table 2.6 Physical and electrical parameters of the MPA, and feed line designed on FR4

Antenna para.	Value	Antenna para.	Value	Antenna para.	Value
L (mm)	27.7	Patch Impedance	281 Ω	Length of λ/4 line (mm)	15.8
W (mm)	38.5	Quarter-wave transformer (λ/4) impedance	118 Ω	Width of primary feed (50 Ω) line (mm)	2.8
Effective permittivity	3.946	Width of λ/4 line (mm)	0.37	Length of 50Ω line (mm)	5.6

Table 2.7 Comparison of simulated and theoretically obtained resonant frequencies of the MPA covered by two superstrate layers in this work with [57] (Case 1: $\varepsilon_1 = \varepsilon_2 < \varepsilon_3$, where $\varepsilon_1 = \varepsilon_2 = 3.66$, and $\varepsilon_3 = 4.7$) [$\Delta h_1 = h_3 - h_2$, $\Delta h = h_2 - h_1$, L = 31.5 mm, W = 41.3 mm]

Δh_1 (mm)	Δh (mm)	ε_{eff} [57]	ε_{eff} (h_2) [This]	ε_{eff} (h_3) [This]	Sim. Freq. (GHz) (CST)	Th. Freq. (GHz) [57]	Th. Freq. (GHz) [This]	%var [57]	%var [This]
1.0	1.0	3.53	3.838	3.995	2.302	2.393	2.300	3.95	0.08
		3.54		4.056	2.296	2.387	2.280	3.96	0.70
		3.58		4.191	2.283	2.376	2.245	4.07	1.66
1.5		3.53		4.044	2.290	2.391	2.288	4.41	0.09
	1.5	3.55	3.919	4.120	2.285	2.385	2.267	4.47	0.78
	2.5	3.59	4.064	4.240	2.272	2.373	2.234	4.49	1.67
2.5		3.54		4.140	2.270	2.387	2.260	5.15	0.44
		3.56		4.222	2.262	2.381	2.240	5.26	0.97
		3.60		4.343	2.250	2.368	2.210	5.43	1.70

Table 2.8 (Case 2: $\varepsilon_1 = \varepsilon_2 > \varepsilon_3$, where $\varepsilon_1 = \varepsilon_2 = 3.66$, and $\varepsilon_3 = 2.2$)

Δh_1 (mm)	Δh (mm)	ε_{eff} [57]	ε_{eff} (h_2) [This]	ε_{eff} (h_3) [This]	Sim. Freq. (GHz) (CST)	Th. Freq. (GHz) [57]	Th. Freq. (GHz) [This]	%var [57]	%var [This]
1.0	1.0 1.5 2.5	3.51	3.838 3.919 4.064	3.988	2.314	2.400	2.305	3.72	0.40
		3.52		4.058	2.305	2.396	2.286	3.94	0.82
		3.54		4.170	2.284	2.390	2.255	4.64	1.27
1.5		3.51		4.038	2.311	2.398	2.291	3.77	0.87
		3.52		4.120	2.300	2.395	2.270	4.13	1.30
		3.54		4.211	2.282	2.388	2.243	4.70	1.70
2.5		3.52		4.152	2.300	2.396	2.264	4.17	1.70
		3.53		4.225	2.286	2.393	2.246	4.68	1.75
		3.54		4.301	2.262	2.386	2.222	5.48	1.80

Table 2.9 (Case 3: $\varepsilon_1 < \varepsilon_2 > \varepsilon_3$, where $\varepsilon_1 = 3.66$, $\varepsilon_2 = 4.7$ and $\varepsilon_3 = 2.2$)

Δh_1 (mm)	Δh (mm)	ε_{eff} [57]	ε_{eff} (h_2) [This]	ε_{eff} (h_3) [This]	Sim. Freq. (GHz) (CST)	Th. Freq. (GHz) [57]	Th. Freq. (GHz) [This]	%var [57]	%var [This]
1.0	1.0 1.5 2.5	3.51	3.840 3.921 4.067	3.990	2.295	2.398	2.302	4.50	0.35
		3.52		4.055	2.285	2.394	2.284	4.77	0.04
		3.54		4.190	2.264	2.387	2.250	5.43	0.62
1.5		3.51		4.058	2.294	2.397	2.284	4.50	0.44
		3.52		4.120	2.282	2.393	2.270	4.86	0.53
		3.55		4.244	2.262	2.385	2.235	5.44	1.20
2.5		3.52		4.160	2.285	2.395	2.258	4.81	1.18
		3.53		4.211	2.276	2.391	2.244	5.05	1.41
		3.55		4.330	2.253	2.383	2.215	5.77	1.68

Table 2.10 (Case 4: $\varepsilon_1 > \varepsilon_2 < \varepsilon_3$, where $\varepsilon_1 = 3.66$, $\varepsilon_2 = 2.2$ and $\varepsilon_3 = 4.7$)

Δh_1 (mm)	Δh (mm)	ε_{eff} [57]	ε_{eff} (h_2) [This]	ε_{eff} (h_3) [This]	Sim. Freq. (GHz) (CST)	Th. Freq. (GHz) [57]	Th. Freq. (GHz) [This]	%var [57]	%var [This]
1.0	1.0 1.5 2.5	3.51	3.833 3.925 4.053	3.987	2.332	2.397	2.330	2.80	0.09
		3.52		4.068	2.323	2.393	2.306	3.01	0.73
		3.55		4.160	2.312	2.385	2.280	3.16	1.38
1.5		3.52		4.056	2.320	2.395	2.310	3.23	0.43
		3.53		4.135	2.315	2.391	2.287	3.28	1.18
		3.55		4.230	2.305	2.383	2.267	3.38	1.60
2.5		3.53		4.172	2.311	2.392	2.288	3.50	1.00
		3.54		4.251	2.302	2.388	2.266	3.73	1.55
		3.57		4.324	2.292	2.380	2.250	3.84	1.80

Table 2.11 (Case 5: $\varepsilon_1 > \varepsilon_2 > \varepsilon_3$, where $\varepsilon_1 = 4.7$, $\varepsilon_2 = 3.66$ and $\varepsilon_3 = 2.2$) (L = 27.7 mm, W = 38.5 mm)

Δh_1 (mm)	Δh (mm)	ε_{eff} [57]	ε_{eff} (h_2) [This]	ε_{eff} (h_3) [This]	Sim. Freq. (GHz) (CST)	Th. Freq. (GHz) [57]	Th. Freq. (GHz) [This]	%var [57]	%var [This]
1.0	1.0 1.5 2.5	4.47	4.803 4.850 4.938	4.895	2.317	2.391	2.330	3.20	0.56
		4.48		4.937	2.308	2.388	2.320	3.47	0.52
		4.50		5.021	2.292	2.383	2.300	4.00	0.35
1.5		4.47		4.942	2.312	2.390	2.318	3.37	0.26
		4.48		4.976	2.305	2.387	2.311	3.56	0.25
		4.51		5.056	2.290	2.382	2.293	4.02	0.13
2.5		4.48		5.003	2.310	2.388	2.298	3.38	0.52
		4.49		5.050	2.300	2.386	2.288	3.74	0.53
		4.51		5.124	2.285	2.380	2.269	4.16	0.70

We now analyze the results obtained in Tables 2.7 – 2.11 in the following points.

a) The obtained results from the proposed model demonstrate %variation of less than 1% for most of the cases than the Svacina's work in [57] the only work in this direction.

b) Each table determines ε_{eff} and f_r for three different heights of substrate and superstrate. For example, MPA covered with a second superstrate layer of thickness 1mm; the model determines ε_{eff} and f_r for Δh (thickness of the first superstrate) of 1, 1.5, and 2.5mm, respectively.

c) The variation in theoretical and simulated f_r gradually increases for the proposed model for a given Δh and Δh_1. However, it may appear in Tables 2.9 and 2.11 that the % variation goes out of trend. But, careful observation of (2.20) agrees to the fact that %variation increases from a more negative value to a more positive one.

2.5.2 Two Layers of Textile Over MPA

Now we apply the proposed theory on the practical situation of WBAN in which the MPA on-body is covered with two layers of the textile, as discussed in section 2.4.2. Once again, the previously designed MPA on RO4350B is taken as a source of EM wave. It is then covered with a combination of textile layers, as mentioned in section 2.4.2. Table 2.12 lists a few such combinations of two textiles. Layer 1, like cotton, polyester, and Rayon, essentially forms the layer which is adjacent to the patch of the MPA, whereas layer 2 consists of textile that is worn over layer 1 in practical such as woolen jackets and hoodies made of felt.

For the determination of f_r and ε_{eff} of two layers of textiles over an MPA, we amalgamated the technique presented in this chapter with the approach reported in [55]. We did this to overcome the specific limitation of our proposed technique in which the % error is higher when compared to the approach in [55] for covers like wool and felt (layer 2), as evident from Table 2.5. The idea here is first to determine ε_{eff} (h_2) that constitutes layer 1 over an MPA using the proposed technique outlined in the flowchart in Figure 2.3. Then the arrangement over the MPA reduces to one

superstrate layer shown in Fig. 2.5(a). Subsequently, in the next step, we replaced ε_1 with ε_{eff} (h_2) and determined ε_{eff} (h_3) for a given Δh_1 by employing the technique in [55]. This combined approach has been used to compute f_r and ε_{eff} for various practical scenarios, and the obtained results are given in Table 2.12. It is essential to note that the thicknesses of layer 1 in Tables 2.5 and 2.12 are limited to 0.2–0.4 mm, considering the practical scenarios/applications. However, woolen and felt jackets are in general thick. Therefore, for layer 2, we took a thickness of 1–1.5 mm in our analysis.

Table 2.12 Comparison of simulated and theoretically obtained resonant frequencies of the MPA covered by two textile layers as superstrate layers in this work with [57] (Material, 1 – polyester and terry wool, 2 – Jeans cotton and terry wool, 3 – Pure cotton and felt fabric, 4 – Rayon and felt fabric)

Mat.	Δh (mm)	Δh_1 (mm)	ε_{eff} [57]	ε_{eff} (h_2) [This]	ε_{eff} (h_3) [This]	Sim. Freq. (GHz)	Th. Freq. (GHz) [57]	Th. Freq. (GHz) [This]	%var [57]	%var [This]
1	0.2	1.0	3.47	3.696	3.622	2.368	2.4119	2.387	1.85	0.80
		1.5	3.47		3.642	2.367	2.4116	2.381	1.88	0.60
	0.3	1.0	3.47	3.714	3.640	2.365	2.4116	2.382	1.97	0.72
		1.5	2.47		3.660	2.364	2.4113	2.375	2.00	0.46
2	0.3	1.0	2.47	3.716	3.641	2.365	2.4112	2.381	1.95	0.68
		1.5	3.47		3.663	2.362	2.4109	2.375	2.06	0.55
	0.4	1.0	3.47	3.732	3.660	2.362	2.4109	2.376	2.06	0.60
		1.5	3.47		3.678	2.360	2.4105	2.370	2.14	0.42
3	0.2	1.0	3.47	3.697	3.622	2.368	2.4118	2.387	1.85	0.80
		1.5	3.47		3.642	2.365	2.4115	2.381	1.97	0.68
	0.3	1.0	3.47	3.715	3.640	2.365	2.4115	2.381	1.97	0.68
		1.5	3.47		3.660	2.362	2.4112	2.375	2.08	0.55
4	0.2	1.0	3.47	3.700	3.623	2.362	2.4104	2.387	2.05	1.06
		1.5	3.47		3.644	2.358	2.4102	2.380	2.21	0.93
	0.3	1.0	3.47	3.726	3.641	2.356	2.410	2.381	2.30	1.06
		1.5	2.47		3.670	2.350	2.4096	2.375	2.54	1.05

It is apparent from Table 2.12 that the %variation demonstrated by the combined technique is significantly lower when compared to the approach reported in [57]. In the last section of this chapter, we present the analysis of the combined technique to

three layers of textiles (Windcheater).

2.6 Measured Results

In this section, we demonstrate the effectiveness of the proposed technique by prototyping two MPAs operating at 2.38 GHz with parameters given in Tables 2.1 and 2.6. The prototyped MPA on the substrates RO4350B and FR4 are shown in Figures 2.6(a) and (b). For PCB superstrates, we fabricated the dielectric layers RO4350B, RO5880, and FR4 of identical size to the MPA. The measurements were done in VNA by calibrating the device from 1 GHz to 3.8 GHz with center frequency at 2.4 GHz. The successive layers of dielectrics were attached with the help of low permittivity adhesive RTV coating ($\varepsilon_r = 1.22$). The purpose of using adhesive of low permittivity is to nullify the effect of dielectric loading on MPA and cause frequency shift due to change in dielectric constant. For the MPA covered with textiles, the measurement of f_r in VNA is carried out by placing either single or multiple layers over it. Proper care was taken while performing measurements with textiles such that the formation of the gap doesn't take place between the MPA and layers.

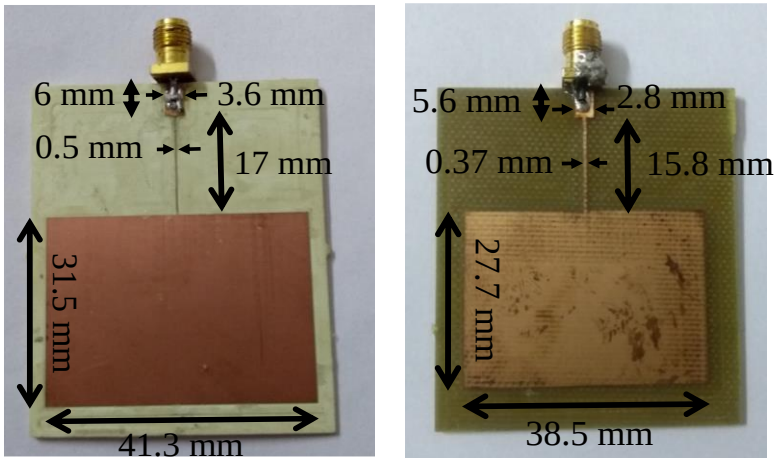

(a) (b)

Figure 2.6 (a) Prototyped MPA on RO4350B (b) Prototyped MPA on FR4

2.6.1 Single PCB and Textile Over MPA

At first, we verify the cases given in Tables 2.2–2.4 through measurement. Figures 2.7(a) and (b) depict the measurement setup of covered with single and two layers of RO4350B of h = 1.524mm and 3.048mm. We have taken proper care to apply the adhesive (RTV coating) on the dielectric layer such that no air gap is formed at the interface. Moreover, we have left sufficient space at the feed location of the MPA to suitably place the dielectric layers over the MPA in the presence of SMA connector, as evident from Figures 2.7(a) and (b). The plot of S_{11} vs. frequency in Figure 2.8 depicts measured f_r of the stand-alone MPA along with MPA covered with RO4350B for all thicknesses mentioned in Table 2.13. For the other two cases, measurement results are listed in Tables 2.14–2.15. We selected the values of Δh as given in Tables 13–15 due to availability for in-house fabrication.

(a) (b)

Figure 2.7 (a) Measurement setup of fabricated prototype on RO4350 substrate and superstrate for Δh = 1.524mm exhibiting f_r of 2.302 GHz (b) Δh = 3.048mm exhibiting f_r of 2.29 GHz

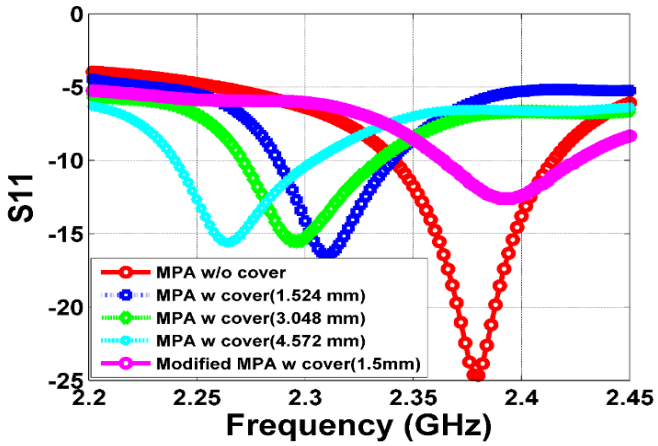

Figure 2.8 Measured return losses of MPA on RO4350B with and without the cover of Δh = 1.524, 3.048, and 4.572 mm

Table 2.13 Comparison of measured and theoretically obtained resonant frequencies of the MPA for superstrate of dielectric constant $\varepsilon_2 = 3.66$ (case 1: $\varepsilon_1 = \varepsilon_2$)

Δh (mm)	Δh (mm) (theoretical)	Meas. Freq. (GHz)	Th. Freq. (GHz) [55]	Th. Freq. (GHz) [56]	Th. Freq. (GHz) [This]	% var [55]	% var [56]	% var [This]
1.524	1.5	2.302	2.392	2.429	2.312	3.55	5.15	0.43
3.048	3.0	2.290	2.372	2.421	2.268	3.42	5.50	0.96
4.572	4.6 (4.5)	2.262	2.358 (2.358)	2.416 (2.414)	2.220 (2.23)	4.25 (4.24)	6.80 (6.72)	1.85 (1.41)

Table 2.14 Comparison of measured and theoretically obtained resonant frequencies of the MPA for superstrate of dielectric constant $\varepsilon_2 = 2.2$ (case 2: $\varepsilon_1 > \varepsilon_2$)

Δh (mm)	Δh (mm) (theoretical)	Meas. Freq. (GHz)	Th. Freq. (GHz) [55]	Th. Freq. (GHz) [56]	Th. Freq. (GHz) [This]	% var [55]	% var [56]	% var [This]
1.575	1.6 (1.5)	2.338	2.394 (2.395)	2.441 (2.441)	2.310 (2.320)	2.40 (2.32)	4.40 (4.27)	1.25 (1.20)
3.150	3.2 (3.0)	2.327	2.375 (2.377)	2.436 (2.437)	2.285 (2.292)	2.06 (2.06)	4.70 (4.62)	1.80 (1.60)
4.725	4.7 (4.5)	2.312	2.358 (2.362)	2.432 (2.434)	2.237 (2.243)	2.00 (1.82)	5.23 (4.90)	3.24 (31.5)

Table 2.15 Comparison of measured and theoretically obtained resonant frequencies of the MPA for superstrate of dielectric constant $\varepsilon_2 = 4.7$ (case 3: $\varepsilon_1 < \varepsilon_2$)

Δh (mm)	Meas. Freq. (GHz)	Th. Freq. (GHz) [55]	Th. Freq. (GHz) [56]	Th. Freq. (GHz) [This]	% var [55]	% var [56]	% var [This]
1.5	2.290	2.391	2.422	2.305	4.41	5.76	0.66
3.0	2.262	2.370	2.409	2.250	4.80	6.50	0.53
4.5	2.245	2.352	2.401	2.210	4.80	6.95	1.56

It is apparent from Tables 2.13 and 2.14 that Δh for which f_r is measured may differ from the values used for the determination of theoretical f_r in Tables 2.2 and 2.3. For example, Δh of 1.524mm becomes Δh = 1.5mm following *step 3* of the proposed model in Figure 2.3. Similarly, for superstrate heights Δh = 3.048 mm, 4.572 mm, 1.575 mm, 3.15 mm, 4.725mm, the modified Δh following *step 3* becomes 3 mm, 4.6 mm, 1.6 mm, 3.2 mm and 4.7mm respectively. Therefore, we can conclude that the proposed model tends to under/overestimate the value of ε_{eff}. Moreover, we have theoretically determined the f_r for new Δh as given in Tables 2.13 and 2.14 in brackets. Interestingly, the %variation with and without modified Δh is very less. Hence, we can say that measured/simulated and theoretical results show excellent agreement despite the presence of inconsistency in the selection of Δh.

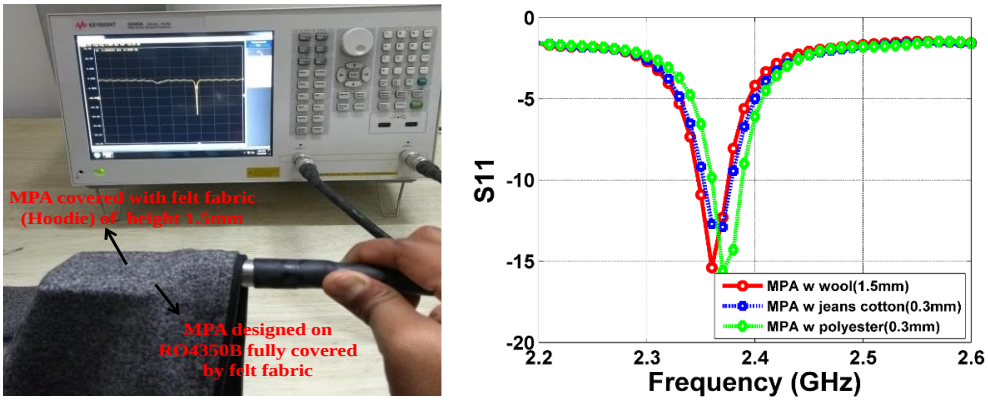

(a) (b)

Figure 2.9 (a) Measurement setup of MPA covered with felt fabric (hoodie) (b) Return loss of MPA covered with wool, jeans cotton and polyester with Δh = 1.5, 0.3, and 0.3 mm

Next, we validate the theoretically obtained f_r of MPA covered with a single textile layer with those of measured results. For this, the prototyped MPA in Figure 6(a) is again used as an RF source. The measurement setup of MPA covered with a textile layer (here felt fabric) is shown in Figure 2.9(a). During the measurement with textiles, we have taken proper care to avoid the formation of an air gap between its layer and MPA. However, due to the presence of the SMA connector at the top, a bulge appears as evident from Figure 2.9(a). For this, a layer of textile was pressed over the MPA with considerable force applied at the bottom. As radiation is taking place near the patch, which is well covered by the textile layer, therefore, this air gap can be avoided. The S_{11} plot in Figure 2.9(b) depicts the measured f_r of MPA covered with wool, jeans, cotton, and polyester with respective Δh of 1.5, 0.3, and 0.3 mm. Interestingly, we can find an excellent resemblance to the shift of f_r with that of theoretical values. Therefore, the work presented in this dissertation restricts its analysis to textiles over MPA without an air gap. Tables 2.16 lists the measured values of f_r for the cases listed in Table 2.5. The measured results are in excellent agreement with that of the theoretical values.

Table 2.16 Comparison of measured and theoretically obtained resonant frequencies of the MPA covered with single textile superstrates [Material (ε_2): 1 – Polyester (1.4), Jean cotton (1.6), Pure cotton (1.7), Rayon (3.2), Felt fabric (1.22), Terry wool (1.3), Leather (1.66)]

Mat.	Δh (mm)	Meas. Freq. (GHz)	Th. Freq. (GHz) [55]	Th. Freq. (GHz) [56]	Th. Freq. (GHz) [This]	% var [55]	% var [56]	% var [present]
1	0.3	2.375	2.408	2.442	2.3655	1.46	2.84	0.40
2	0.3	2.373	2.407	2.442	2.3620	1.50	2.91	0.46
3	0.2	2.371	2.409	2.442	2.3670	1.61	3.00	0.17
4	0.2	2.367	2.408	2.438	2.3635	1.73	3.00	0.15
5	1.5	2.363	2.397	2.442	2.3007	1.46	3.35	2.64
6	1.5	2.358	2.392	2.441	2.3005	1.45	3.54	2.44
7	1.5	2.359	2.390	2.438	2.3000	1.32	3.36	2.50

2.6.2 Restoration of Original Frequency

In this sub-section, we restore the original f_r of an MPA covered by a dielectric layer by altering the physical parameters based on new ε_{eff}. This analysis is critical to proving the effectiveness of the proposed formulation and model from the WBAN perspective. In the first step, we determine of ε_{eff} of an MPA covered with a dielectric layer (PCB/textile) following the model and steps in section 2.3. Next, the new physical and electrical parameters of the MPA are recalculated by replacing ε_1 of the substrate with new ε_{eff}. Lastly, the modified MPA is either simulated or measured to check the operation. The condition in row 3 of Table 2.2 is used to elaborate on this aspect. For the given parameters in Table 2.2, the ε_{eff} comes out to be 3.69, 3.54, and 4.13 for [55], [56], and this work, respectively. To restore the original f_r of the MPA, i.e., 2.38 GHz, the modified length is obtained with the help of (2.21).

$$f_r = \frac{c}{2\left(L^m + 2\Delta L\right)\sqrt{\varepsilon_{\text{eff}}}} \tag{2.21}$$

Here, L^m is the modified length of the MPA. The substitution of the known and determined values f_r = 2.38 GHz, c = 3e8, ε_{eff} = 3.69, 3.54 and 4.13, and ΔL = 0.34mm in (2.21) results in L^m of 32.46 mm, 33.15 mm, and 29.37 mm. Consequently, for these modified values of length, the MPA resonates at 2.352 GHz, 2.34 GHz, and 2.392 GHz, respectively, for the techniques given in [55], [56], and this work. It becomes apparent from the calculated values that only proposed predicts f_r closest to desired resonance. The measured f_r of the modified MPA for this work is depicted in Figure 2.8. A slight shift in f_r from the original one can be attributed to the overestimation of ε_{eff} by the model (Δh = 4.6mm was used in the calculation instead of actual thickness 4.572mm). It implies that for the given case study, the obtained f_r from the model is lower than the simulated, and this has resulted in L^m that is smaller than the desired length to bring resonance at 2.38 GHz. Therefore, the lesser %variation leads to higher accuracy in the determination of L^m, and that, in turn, leads to better accuracy in the restoration of the original f_r even with the cover. Since we only varied the length of the MPA, keeping the width as it is this leads to the poor return loss, as evident from

Figure 2.8.

2.6.3 Dual PCB and Textile Over MPA

Next f_r of the prototyped MPA is measured for a combination of PCBs and textiles as given in Table 2.7 – 2.12. For case 5 in Table 2.11, we prototyped another MPA on FR4 from the parameters given in Table 2.6, as shown in Figure 2.6(b). The measurement setup with successive layers of superstrates over the MPA is similar to Figure 2.7(a). The measurement results for some of the Δh_1 and Δh covering all five cases in section 2.5 are given in Table 2.17. %variations are in good agreement with the predicted values in section 2.5. It validates the effectiveness of the proposed model for two dielectric layers over the MPA as well.

Subsequently, we cover the MPA with the combination of textile layers mentioned in Table 2.12, and the values of f_r are measured using the setup shown in Figure 2.9(a). Table 2.18 includes the measured f_r for some of the combinations. The chosen thickness of the textile layers in this work is the average of many samples. It is clear that the measured % variation entirely agrees with the predicted values in Table 2.12 and demonstrates the scalability of the proposed model to two superstrates (PCB/textile) layers.

Table 2.17 Comparison of measured and theoretically obtained resonant frequencies of the MPA covered with two superstrate layers

Case	Δh_1 (mm)	Δh (mm)	Meas. Freq. (GHz)	% var [57]	% var [This]
$\varepsilon_1 = \varepsilon_2 < \varepsilon_3$	1.500	1.524	2.286	4.33	0.83
$\varepsilon_1 = \varepsilon_2 > \varepsilon_3$	1.575	1.524	2.302	4.04	1.40
$\varepsilon_1 < \varepsilon_2 > \varepsilon_3$	1.575	1.500	2.290	4.50	0.87
$\varepsilon_1 > \varepsilon_2 < \varepsilon_3$	1.500	1.575	2.318	3.15	1.34
$\varepsilon_1 > \varepsilon_2 > \varepsilon_3$	1.575	1.524	2.307	3.47	0.17

Table 2.18 Comparison of measured and theoretically obtained resonant frequencies of the MPA covered with two textile layers

Layer 1	Layer 2	Δh (mm)	Δh_1 (mm)	Meas. Freq. (GHz)	%var [57]	%var [This]
Polyester	**Wool**	0.3	1.5	2.3708	1.71	0.18
Jeans cotton	**Wool**	0.3	1.5	2.3628	2.04	0.52
Pure cotton	**Felt**	0.2	1.5	2.3668	1.85	0.60
Rayon	**Felt**	0.2	1.5	2.3547	2.33	1.07

2.6.4 Multiple Textile Layers Over MPA

Next, we have shown the effectiveness of the proposed theory for two superstrate layers for multi-layered superstrate structures over the MPA. For this, the MPA in Figure 2.6(a) is covered by a combination of polyester, foam, and polyester (typically a windcheater). The polyester forms layer 1 and 3, whereas layer 2 consists of foam. No air gap between the successive layers in simulation as well as in measurement has been considered here. The measurement setup is identical to that shown in Figure 2.9(a). The thickness of foam and polyester considered here is 1.2mm and 0.3mm, while the corresponding permittivities are 1.13 and 1.4 in both the simulation and measurement scenarios. The presence of the third superstrate layer of thickness h_4 brings the parameter Δh_2 given by $h_4 - h_3$ in Figure 2.4(a). Then the steps mentioned in sections 2.3 and 2.5 are followed to determine f_r for the combination mentioned in Table 2.19. The comparison between the theoretical, simulated, and measured f_r for this work shows remarkable similarity. Besides, the %variation for the proposed model is substantially smaller when compared to results obtained using the technique in [57]. The obtained results also convey that the presented model and formulations in this work are scalable to determine ε_{eff} and f_r of MPA covered with multiple layers on it with excellent accuracy and therefore advances the existing state-of-the-art significantly.

Table 2.19 Comparison of simulated, measured and theoretically obtained resonant frequencies of the MPA covered by three textile layers as superstrate (Wind Cheater) in this work with [57] (Lay signify layer: 1 – Polyester (Δh = 0.3mm), 2 – Foam (Δh = 1.2mm), 3 – Polyester (Δh = 0.3mm))

Lay	Sim. Freq. (GHz)	Meas. Freq. (GHz)	Th. Freq. (GHz) [57]	Th. Freq. (GHz) [This]	%error [57] (Sim.)	%error [This] (Sim.)	%error [57] (Mea.)	%error [This] (Mea.)
1, 2, 3	2.374	2.375	2.410	2.381	1.52	0.30	1.47	0.25

2.7 Conclusion

In this chapter, we propose new empirical relations based on CM and series-parallel combination of dielectric-loaded capacitors between the metallic patch and the ground plane to determine the effective dielectric constant of an MPA covered with either PCB or textile layers. The chapter also presents a unique iterative model that fragments a superstrate layer into multiple sub-layers and then computes ε_{eff} and f_r of the whole arrangement. This chapter finds its usefulness from the WBAN scenario, where sensor networks operate beneath multiple layers of protective clothing. The presented model determines f_r of MPA covered with single superstrate layer for the three cases of $\varepsilon_1 = \varepsilon_2$, $\varepsilon_1 > \varepsilon_2$, and $\varepsilon_1 < \varepsilon_2$. The variation in f_r obtained from the proposed model w.r.t. measured or simulated results for the three cases suggest that the model is perfect for the dielectric cover of $\varepsilon_2 > 2.2$. Furthermore, the proposed model, when tested on MPA covered with textile layers, shows excellent performance (%variation less than 0.5%) for thinner heights and a slightly weaker performance for thicker superstrates (>2%). The application of the proposed model on MPA covered with two superstrate layers for the conditions of $\varepsilon_1 = \varepsilon_2 > \varepsilon_3$, $\varepsilon_1 = \varepsilon_2 < \varepsilon_3$, $\varepsilon_1 < \varepsilon_2 > \varepsilon_3$, $\varepsilon_1 > \varepsilon_2 < \varepsilon_3$, and $\varepsilon_1 > \varepsilon_2 > \varepsilon_3$ respectively exhibits %variation less than 1.5%. Therefore, we can conclude that the proposed model, when applied with an existing technique, significantly advances the state-of-the-art for the determination of f_r for two and three textile layers over MPA. Besides, the presented model has lower complexity and therefore has the potential to be easily integrated with any technical computing software.

Chapter 3

Development of Liquid Phantom and Measurement of SAR

This chapter is based on the following research paper:

D. Rano, M.S. Hashmi, and M.A. Chaudhary, "Design, Development and Measurement Technique for Simple and Cost Effective Liquid Phantoms," *IEEE Transaction on Instrumentation and measurement*. (Under review)

In this chapter, we discuss another two crucial aspects of WBAN, SAR measurement, and liquid phantom development. For this, we propose two simple and cost-effective approaches to emulate tissue-equivalent liquid (phantom) operating at the MBAN band (2.36 – 2.4 GHz). We have realized the two most common categories of the liquid phantom, i.e., homogeneous and heterogeneous (skin) models in this chapter. We determined one of the critical parameters that are the relative permittivity (ε_r) of the liquid phantom through approximation using CST. The other crucial parameter, attenuation constant (α_d) or dielectric conductivity (σ_d), is determined with the help of a two-antenna arrangement dipped inside liquid under test (LUT). For the determination of dielectric constant, we put LUT on PTFE container above an MPA and measured S_{11} in VNA. Next, we performed a parametric variation in the dielectric constant of the designed MPA in CST. We chose the value of the dielectric constant of LUT for which the simulated S_{11} agrees closest to the measured S_{11}. We determined α_d from the received signal strength, S_{21}, and return loss S_{11} of the two-antenna arrangement dipped inside LUT. Finally, resulting in σ_d from the regular expressions of EM wave traveling through a lossy medium. In this chapter, we used deionized

water, salt, sugar, glycerine in the preparation of both the liquid phantoms. We have validated all our results in this chapter with a standard work presented in [82].

Finally, from the developed phantoms, we measured the thermal SAR values of an MPA operating in the MBAN band. For this, we measured the temperature rise of the liquids exposed to EM wave (antenna) for a given time. We validated our proposed theory with simulation by keeping the conditions identical to measurement.

3.1 Background and Related work

In this section, we introduce a different type of phantoms and SAR measurement techniques. We also provide limitations of existing works and our efforts to advance the current state-of-the-art.

3.1.1 Determination of SAR

SAR is the amount of radiation absorbed near the adjacent tissues in the presence of EM sources such as antennas. It is the mass-normalized rate at which the body absorbs EM energy at any specific location [74]. Since the human body mostly consists of water, which tends to excessive dielectric heating due to vibrational motion of molecules exposed to a high-frequency wave, therefore, SAR is a crucial parameter in WBAN used as protection guidelines. It is always essential to keep the radiated power levels such that the thermo-regulatory mechanism of the body can cope with the temperature rise at a specific location of the body. In general, SAR is related to the electric field radiated from an EM source (like antennas) as given by (3.1).

$$\mathrm{SAR} = \frac{\sigma_{\mathrm{e}}}{\rho}\left|\mathbf{E}\right|^2 \tag{3.1}$$

Here, ρ is the density of tissue (Kg/m^3), σ_e is the conductivity of tissue used for SAR averaging, and $|\mathbf{E}|^2$ is root-mean-square (RMS) magnitude of the electric field absorbed by the tissue. Typically, SAR is determined either for 1g or 10g of averaging

mass. FCC has a strict guideline on SAR regulation and radiated power from an EM device. For example, peak SAR limitations in Europe and the USA are 2 W/Kg and 1 W/Kg for 10g and 1g of average mass, respectively. We present here the two most popular SAR measurement techniques that are widely used all over the globe and their limitation. In general, these techniques are very accurate in predicting the actual absorption of EM energy. However, they are highly expensive, very detailed, not easily assessable, and require a professional while measurements.

Electric Field Probe Scanning Method:

This method calculates SAR (mass averaging of either 1g or 10g) by recording the spatial distribution of actual electric field with the help of a probe scanner when a conducting liquid or solid phantom is exposed to a radiating device like mobile handset, WSN, wearables and many more. A configuration of an electric field scanning probe method for SAR measurement is shown in Figure 3.1. Moreover, a practical system DASY5 by SPEAG is also shown in Figure 3.2 for reviewers understanding [72].

The following elements in the system constitute the measurement setup of the field probe method.

1) *Phantom*: Characterized homogeneous liquid phantom of the body is filled in the container, as shown in Figures 3.1 and 3.2. The outer shell of the phantom is in the form of solid or semi-solid to hold the LUT. Mass averaging is explained here with the help of an example. Suppose the density of LUT used here is 3600 Kg/m^3. We know that mass (m) is any object is the product of density (ρ) and volume (V) as given by (3.2).

$$m = \rho \cdot V \tag{3.2}$$

For an average mass of 10g, substituting the values of m and ρ in (3.2), V comes out to be 2.78e-6 m^3. Now, from Figure 3.1, the side length of the averaging cube equals 14.06mm. Therefore, field probes must record the

RMS electric field at these positions to determine SAR for a mass average of 10g.

2) *Electric field probe*: It consists of three mutually orthogonal dipoles along *x*-, *y*- and *z*-axes. The width of the dipoles must be much smaller than the width of the averaging volume's side length. Commercial probes come with minute dipoles of 2~4mm dimension.

3) *Robot*: A robot arm attached to the electric field sensor probe moves it with a precision of 0.02mm.

4) *WBAN or Cellular holder*: This unit holds the wearable to a specified position and location for SAR measurement. The placement of the device must be precise such that it reads accurate SAR value.

Note: The measurement setup is automated with the help of a robotic arm. Therefore, SAR reading is taken inside an anechoic chamber, as shown in Figure 3.2.

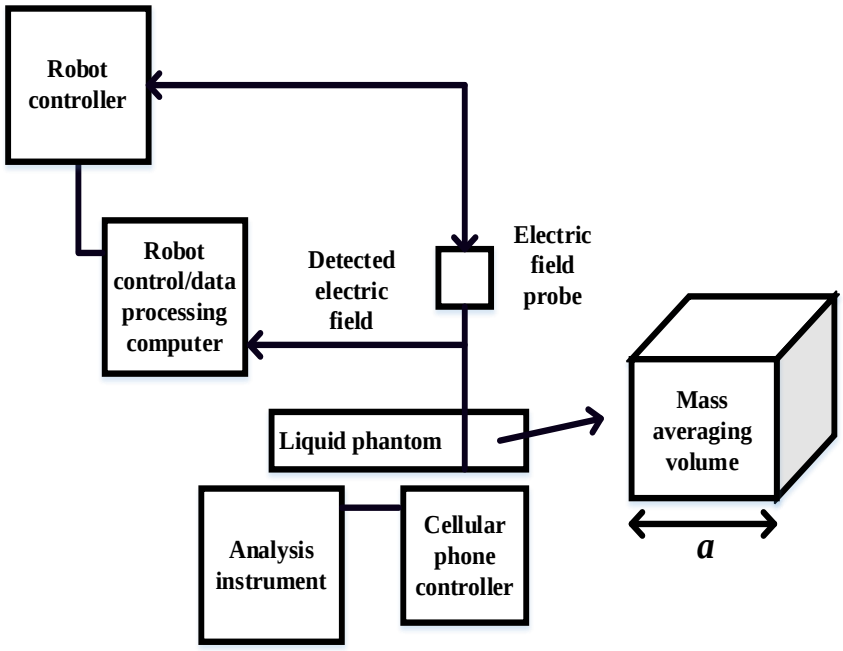

Figure 3.1 Spatial electric field probe scanning method for the determination of SAR

Figure 3.2 Practical electric field probe scanning method for the determination of SAR (DASY 6 by SPEAG) [72]

Most of the works in this direction involve SAR measurement with the help of the DASY system by SPEAG [73] – [74], [78]. For example, in [73], a technique is presented to measure 3D SAR, employing the 2D measurement setup explained above at 2.45 GHz. The numerically obtained results agree well with the measured results with %error less than 2%. Another work in [74], employing field probe method measures, SAR of 9.1 W/Kg for 10g average mass of a lightweight liquid phantom when exposed to a PIFA antenna. The SAR values obtained from the proposed method in [74] and the measured one demonstrates the error of 5.8%. In [100], a multi-antenna system to predict SAR also uses the field probe method for validation. The technique in [100] predicts theoretical SAR with a %error of 3% w.r.t. measured result. In [71], a comparison is made between the DASY systems and thermal SAR (to be discussed next), which exhibits an error of 2% between them.

In general, the field probe scanning method is prevalent in the scientific community to measure SAR due to accurateness. However, the cost of the whole setup is USD 44,000, which is very expensive, and very few labs have access to it. Moreover, this value does not include the costs of the anechoic chamber and the liquid phantom. It is also apparent from the setup shown in Figures 3.1 and 3.2 that the method is complicated and has to be performed by a professional only.

Temperature Rise and Thermographic Method:

SAR can also be determined by the increase of temperature on the tissue exposed to EM source for a given time. SAR is directly proportional to the rise in temperature due to the presence of EM source, as given by (3.3) [71]. Here, C (J/ Kg. C^o) is the specific heat capacity of the solution; ΔT (C^o) is a rise in temperature, and Δt (s) is the exposure duration of EM source.

$$\text{SAR} = C\frac{\Delta T}{\Delta t}\ [\text{W/Kg}] \tag{3.3}$$

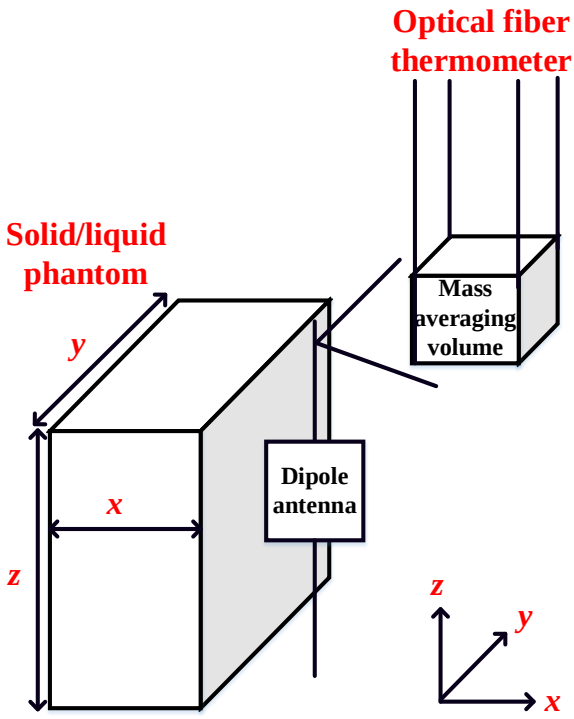

Figure 3.3 Thermal SAR measurement setup [71]

The measurement setup of thermal SAR is shown in Figure 3.3. It consists of a container holding the liquid/solid phantom of dimension x, y, and z mm along x-, y-, and z-axes. A dipole antenna acting as a source of EM wave is positioned close enough to the container to replicate a WBAN device/mobile handset accurately. A four-

channel optical fiber thermometer is used to measure the temperature rise of the solution in the presence of an EM source. The optical fiber is positioned in such a way that it encloses averaging mass of either 10g or 1g. The procedure of the same is explained in the electric field probe scanning method.

Now, the working of the thermal SAR measurement setup is explained here in the following steps.

a) The EM energy is exposed (radiating out of a dipole antenna) to the phantom for a short time (*t* seconds).

b) The rise in temperature of the solution is measured with the help of optical fiber thermometers.

c) Lastly, the substitution of the values in expression (3.3) to determine SAR.

Note: When the phantom gets heated by the EM wave, thermal diffusion may take place with the liquid. However, its effect can be nullified if the rate of heat diffusion is constant such as homogeneous phantom.

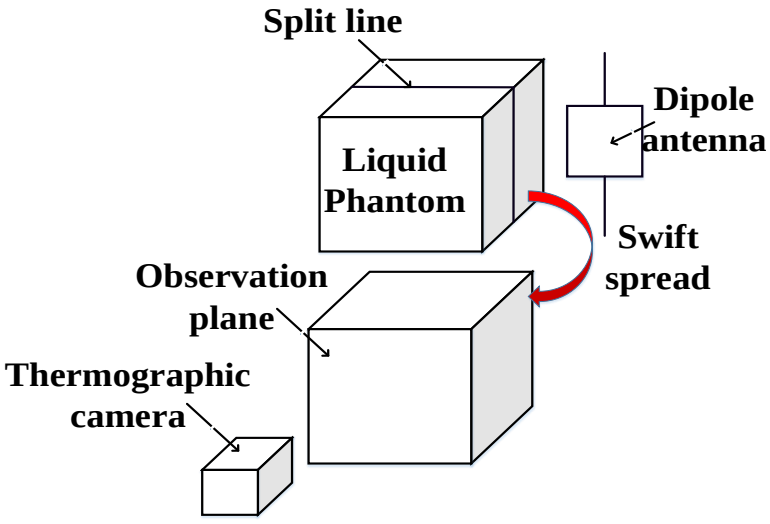

Figure 3.4 Thermographic SAR measurement setup [81]

The thermographic method, as shown in Figure 3.4, consists of a container

holding the liquid phantom, a thermographic camera, and a dipole antenna acting as an RF source. At first, a phantom is placed inside a radio anechoic chamber. The phantom is split (through the *split line*, as shown in Figure 3.4), and the thermographic view is recorded with the help of a thermographic camera (infrared camera). Then, a high power RF device is used to irradiate the phantom for a minute or two. In general, the exposure is maintained until the time the temperature of the phantom increases by 1K. Subsequently, the phantom is reopened (the process is fast, so it is called the *swift spread*) and put in front of a thermographic camera to capture the temperature profile.

Drawbacks of Temperature Rise and Thermographic Method:

Although both the methods are extensively used in [71], [75] – [81], [100] to calculate SAR. However, the techniques suffer from these drawbacks.

1) Both systems use an RF source of very high power nearly 100W. Since mobile handset and WBAN devices operate from 1mW – 1 W, therefore, these methods are not suitable for RF devices.

2) For such high power, the exposure duration is merely 10s – 30s. It is very less duration in comparison to a typical wearable device worn on the body for a 24/7 basis.

3) Once again, both the techniques are expensive as the components involved in the measurement like the infrared camera, anechoic chamber, multi-channel optical fiber, high power generating device are itself costly.

4) The SAR images obtained from the thermographic method are limited to 2D only [80] – [81]. It is because when the phantom is opened and put in front of a thermographic camera is only records the SAR profile of the surface. For example, if we assume the coordinate axes shown in Figure 3.3, applies to Figure 3.4 as well, then the thermographic camera shows the SAR profile of the surface along *xz*-axes. However, it fails to generate the SAR profile of the phantom along the *y*-axis. For this, the phantom needs to be split along *yz*-axes.

5) The mass averaging involved in the temperature rise method again requires a precise probe scanning approach. The only difference here is the probes (optical fiber) measures the temperature instead of the electric field that is controlled (or positioned) by a robotic arm in a way such it encloses 10g or 1g of mass for SAR measurement. Therefore, the inclusion of a robotic arm adds to the overall cost.

6) The swift spread process involved in the thermographic method is time taking because no one is allowed to stay in the anechoic chamber due to the use of high power sources. Therefore, after switching off the RF source and safe radiation level inside the anechoic chamber, one can enter and reopen the phantom to capture the SAR profile. It may induce an error in peak SAR measurement.

3.1.2 Phantoms

As WBAN devices operate very close to the human body, therefore, amount of EM wave absorbed by the adjacent tissues (SAR) has to be kept low such that no damage can happen [33] – [40]. It generally occurs due to dielectric heating at the specific location exposed to EM wave generated from WBAN devices like an antenna. Test and evaluation using numerical phantom (in simulation) or physical phantom have become very popular to avoid the risks of exposing body parts to persistent EM radiation and avoiding any damage [33]–[40]. In this section, we discuss three types of numerical phantoms used by antenna designers to emulate a section of a body and measure SAR, when a WBAN device is placed nearby. We have also discussed the characterization of physical phantoms (liquid only) with the help of two techniques.

The numerical phantom is a simulated biological body which consists of heterogeneous tissues of average electrical property [33] – [40]. It can also be a more complex and accurate phantom having different tissues of a human body such as Emma, Gustav, Hugo, and Laura in CST [53], [92] – [93]. Figure 3.5(a) shows a flat heterogeneous model of the wrist. In general, the heterogeneous model consists of four

layers, namely skin, fat, muscle, and bone [92] – [93]. The electrical parameters and thickness of the individual layers are also given in Figure 3.5(a). For a better understanding of the working of the numerical phantom, we have placed an MPA over the model. SAR value of the overall arrangement can be obtained by simulating the design for an input power of desired value and mass averaging of either 1g or 10g. This process is further discussed in detail in Chapter 4. Another type of numerical phantom that is more realistic and accurate is shown in Figure 3.5(b). It shows a realistic model of a wrist in CST known as Gustav [92]. Once again, for understanding, we have placed an MPA over the wrist model to simulate the SAR values for the desired input power and mass averaging.

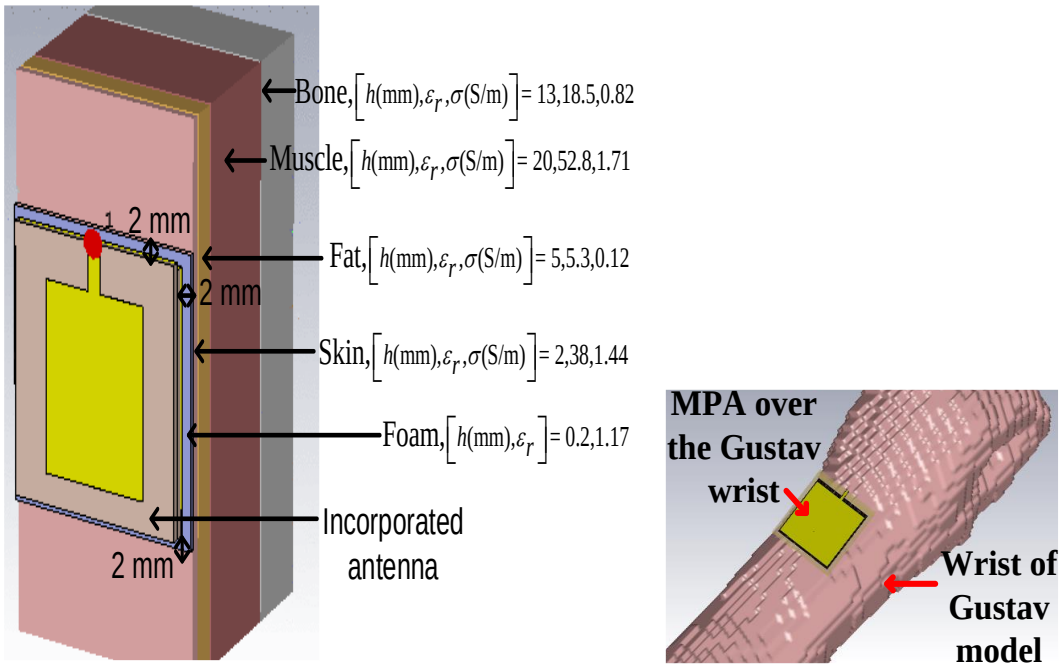

(a) (b)

Figure 3.5 Numerical phantoms (a) Heterogeneous model of the flat wrist, (b) Gustav model of the wrist in CST

The numerical phantoms are accurate but require considerable simulation time and memory for the generation of results. For instance, simulation of an MPA operating between 1–3.8 GHz over the wrist in the Gustav model, as shown in Figure

3.5(b), generates mesh cells of approximately 2,600,000 for a resolution of 2.08*2.08*2 mm^3. It takes a total simulation time of approximately 3 hours and 20 GB of memory for the i5 processor and 8 GB RAM [53], [92]. In Chapters 4 and 6, we have shown simulated SAR values on both heterogeneous and realistic models in CST.

The physical phantoms, on the other hand, consist of homogenous or heterogeneous tissues mimicked by a liquid, semi-solid (gel), and solid materials [82]–[86], [101] – [103]. They are indeed accurate in the generation of SAR values, but their characterization is a complicated and expensive process. We have discussed here two very known techniques to measure the dielectric properties of a phantom.

1) **Transmission line method:** In the transmission line method, a sample under test is inserted in a sample holder and then connected to two ports of the VNA with the help of coaxial cable to measure S_{11} and S_{21}. The obtained S_{11} and S_{21} are then converted to dielectric properties (real and complex permittivity) with the help of Nicolson-Ross-Weir (NRW) or NIST method [104] – [106]. Both the conversion methods have their advantages and disadvantages. For example, NRW is a fast and non-iterative process and is applicable for both coaxial line and waveguide. However, this method can only be used for short samples as divergence occurs at the frequencies integer multiple of half-wavelength [104] – [105]. NIST method, on the other hand, is accurate and can be used for samples of arbitrary size; however, it suffers from the need for an initial guess of permittivity value of the sample [106].

2) **Open-ended coaxial probe method:** This method is most common among the designers to measure the permittivity of a specimen. In this method, one end of a cable is connected to an open-ended coaxial probe and the other to a VNA. Then the probe is immersed into a liquid, and S_{11} is measured in VNA. A mismatch in impedance between the probe and the medium (tissue) results in reflected signals in VNA. These reflected waves when converted with the help of an in-built program in VNA or NRW/NIST, give the

permittivity of the sample [107] – [110].

Limitations: After an extensive literature review of the works employing both the methods mentioned above, the following limitations have been found.

a) The accuracy of both methods is limited by the formation of air-gap. For example, during the placement of the sample inside the sample holder in the transmission line method, often create air bubbles [101]. It limits the accuracy of the method. Whereas, the accuracy of the open-ended coaxial probe method is limited by the heterogeneous sample, the precision of the probe and calibration of the VNA.

b) The open-ended probe mechanism to measure permittivity of a sample consists of an expensive dielectric probe tool kit, as shown in Figure 3.6. The price of such an experimental setup shown in Figure 3.6 is approximately 13,500USD, and only a few labs have access to it.

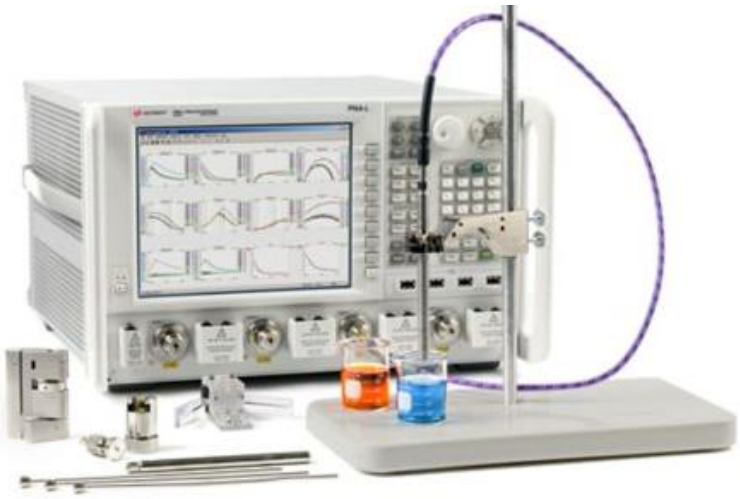

Figure 3.6 N1501A dielectric probe kit from Keysight technologies [111]

Therefore, the motivation of this chapter is to addresses some of the concerns and advance the current state-of-the-art by following way.

a) We propose two different techniques to measure ε_r and σ_d of a liquid phantom. The proposed techniques are least inexpensive and can be performed in any microwave laboratory with the help of a VNA.

b) We have validated the liquid phantoms developed in this chapter with a point SAR measurement method. The results obtained from the proposed method, when compared with the simulated one, possess good resemblance. The proposed method employs a weighing scale, a digital thermometer of very less response time (typically lesser than 2s), and an arrangement of VNA and an MPA as a source of EM wave. Once again, the SAR measurement method proposed in this chapter can be performed in any microwave laboratory without any professional help.

3.2 Determination of Dielectric Constant

For the determination of ε_r of LUT, we have first designed an MPA operating in the MBAN band on FR4 with dielectric constant and thickness of 4.7 and 1.5mm, respectively. The physical and electrical parameters of the MPA and feed line (quarter-wave transformer) are given in Table 3.1. The prototyped antenna on FR4 with all the parameters listed in Table 3.1 is shown in Figure 3.7. Then we covered the MPA with PTFE container of dielectric constant and thickness of 2.1 and 1.2 mm, respectively, as shown in Figure 3.8(a). For the proper placement of the container on the radiating patch of the MPA, we took a container of the flat bottom, as evident from Figure 3.8(a). We also exercised proper care while placing PTFE over the MPA to avoid the formation of an air gap. For this, we kept a spacing of 4 mm between the SMA connector and patch of the MPA.

The simulation setup of MPA covered with PTFE container in CST is shown in Figure 3.8(b). The PTFE container designed in the simulation setup is identical in dimension and electrical property to the measurement step. A gap of 4 mm between the feed line and the container is left in simulation as well. The simulated and measured

plots of S_{11} vs. frequency, depicting f_r of the MPA in air and covered with PTFE, are shown in Figure 3.9 (a)–(b). We determined the percentage variation between the measured and simulated f_r using 3.4, and it comes out to be 0.17%.

Table 3.1 Physical and electrical parameters of the MPA, and feed line designed on FR4

Antenna para.	Value	Antenna para.	Value	Antenna para.	Value
L (mm)	27.7	Patch Impedance	281 Ω	Length of λ/4 line (mm)	15.8
W (mm)	38.5	Quarter-wave transformer (λ/4) impedance	118 Ω	Width of primary feed (50 Ω) line (mm)	2.8
Effective permittivity	3.946	Width of λ/4 line (mm)	0.37	Length of 50Ω line (mm)	5.6

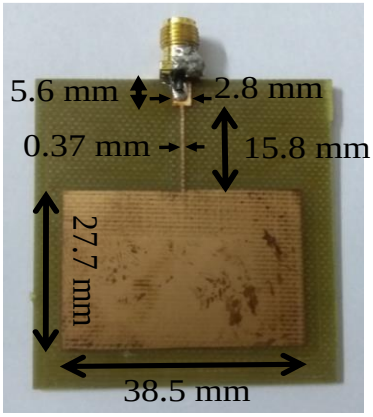

Figure 3.7 MPA with all physical dimensions. The substrate and ground plane length and width are 49.75mm and 42.5mm

$$\%\text{variation} = \frac{f_r\,(\text{sim.}) - f_r\ (\text{meas.})}{f_r\,(\text{meas.})} \tag{3.4}$$

In the next step, we spread a layer of water of h = 1.2mm uniformly over the container and measure f_r plotted in Figure 3.9(b). Then we simulated the MPA covered

water with an assumption that the ε_r of deionized water at room temperature is 78. Figure 3.9(a) depicts the simulated f_r of MPA covered with layer water of height 1.2mm over the PTFE container. The percentage variation, in this case, using (3.4), comes out to be 0.1%. Therefore, we can say that choosing the appropriate value of ε_r in the simulation environment demonstrates excellent agreement in the f_r with that of the measured value. It is also known from standard works and previous chapter that f_r of an MPA or MPA covered with dielectric layers depends primarily on the real value of permittivity ($\varepsilon_c = \varepsilon' - j\varepsilon''$), i.e., $\varepsilon_0\varepsilon_r$ [58] – [60]. We used this concept to predict ε_r of any LUT over an MPA by altering its value in simulation such that percentage variation w.r.t. is in agreement.

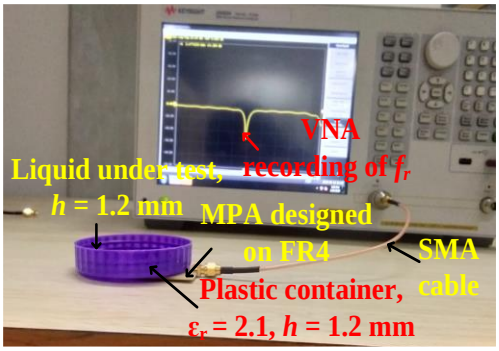

(a)

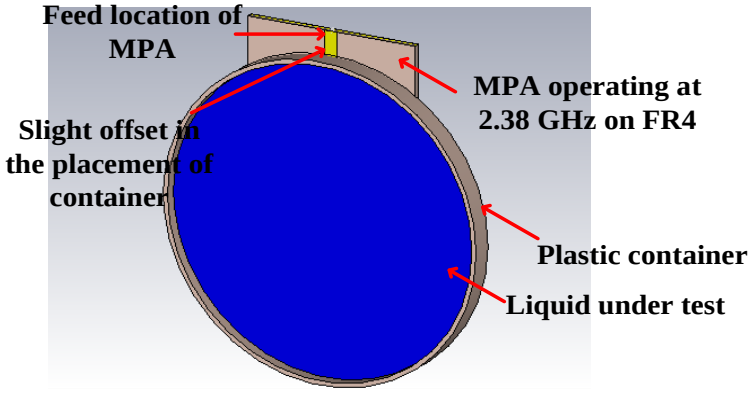

(b)

Figure 3.8 (a) Measurement setup of MPA covered with PTFE container holding LUT (b) Simulation setup of MPA covered with PTFE container holding LUT

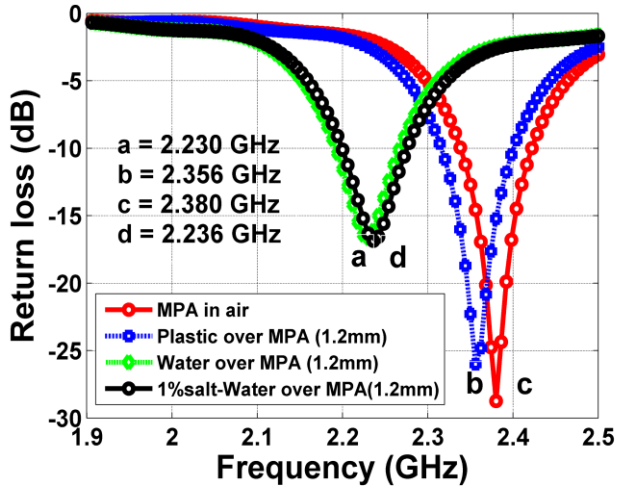

(a)

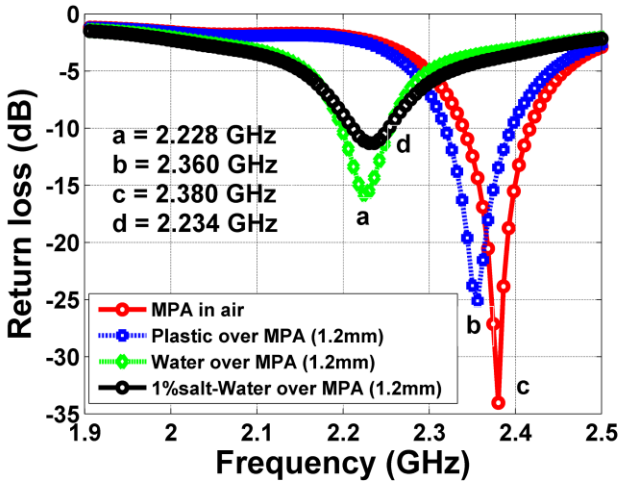

(b)

Figure 3.9 Resonant frequencies of MPA in air and covered with PTFE, water, 1% wt. NaCl in water (a) Simulated (b) Measured

We now explain the theory mentioned above here with the help of an example. We made a solution of 1% salt (in weight = 2.5g) in 250g of water. Then the solution is evenly spread on PTFE such that h = 1.2 mm, and the f_r of the arrangement is measured in VNA is shown in Figure 3.9(b). The MPA loaded with PTFE and LUT resonates at 2.236 GHz. When we substituted the previously determined %variation

of 0.1% and f_r (meas.) in (3.4), f_r (sim.) comes out to be 2.234 GHz. It implies that ε_r of LUT for this case must be smaller than that of water (since f_r (meas._water) > f_r (meas._salt in water)), as evident from (3.5). Next, a parametric variation is carried out from $\varepsilon_r = 78$ to $\varepsilon_r = 70$ in simulation and desired resonance is achieved at 2.234 GHz for $\varepsilon_r = 72$. We took a step width of 0.1 while varying ε_r from 78 to 70. It allowed us to get the exact resonance in simulation w.r.t. measurement. The simulated f_r of MPA covered with PTFE and LUT of $\varepsilon_r = 72$ is shown in Figure 3.9(a). Interestingly, ε_r obtained for the given %weight of salt in this experiment matches with that of [82]. It justifies the appropriateness of the proposed approach.

$$f_r \propto \frac{1}{\sqrt{\varepsilon_r}} \tag{3.5}$$

3.3 Determination of Dielectric Conductivity

In this section, we determine attenuation constant α_d and dielectric conductivity σ_d of the LUT for which we determined ε_r in the previous section. In general, EM wave while propagating through a lossy dielectric medium (here LUT) attenuates. The extent of attenuation can provide α_d and after some calculation using regular expressions σ_d as well [58] – [60]. For this purpose, we used two antenna measurement setup, as shown in Figure 3.10(a). The MPAs are of identical dimension to that listed in Table 3.1. We dipped the MPAs only partially inside the LUT such that liquid does not touch the SMA connector. One end of the SMA cables is connected to the VNA and the other end to the MPA, as shown in Figure 3.10(a).

We have performed the following steps for the determination of α_d and σ_d.

Step 1: The S_{21} and S_{11} of the two antenna systems are measured using VNA. Usually, the values are in dB; therefore, we converted the values to natural ones. For accurate measurement of S_{21}, the MPAs are kept at an optimum distance from the sides and base of the container to minimize the reflections. Since the MPAs are dipped inside

the liquid, the value of S_{11} used here is different from that in the previous section in which liquid is placed over an MPA and PTFE container.

Step 2: Evaluate power received P_r at the receiver antenna by using S_{21} and S_{11} in (3.6). Here, P_t is the transmitted power. In this chapter, we have kept P_t to 0dBm (1mW) for all the measurements.

$$P_r = \frac{\left|S_{21}\right|^2}{1-\left|S_{11}\right|^2} P_t \tag{3.6}$$

Step 3: We can also express P_r by (3.7). Here, 'z' is the distance of separation between the two MPAs. Therefore, we can determine the α_d of the LUT using (3.8) by substituting z, P_r, and P_t. In this chapter, we have kept z = 30mm for all the experiments.

$$P_r = P_t e^{-2\alpha_d z} \tag{3.7}$$

$$\alpha_d = \frac{1}{2z} \ln \frac{P_t}{P_r} \tag{3.8}$$

Step 4: Compute of σ_d from α_d using 3.9. Here, ω is the angular frequency at f_r, μ_o, and μ_r are the permeability of free space and the LUT, whereas, ε_o is the permittivity of free space and ε_r is the permittivity of the LUT (determined in the previous section). In general, α_d obtained in *step 3* is in dB/m; therefore, we converted it to Np/m by dividing it by 8.686 before its use in 3.9.

$$\alpha_d = \omega \sqrt{\frac{\mu_o \mu_r \varepsilon_o \varepsilon_r}{2} \left[\sqrt{1 + \left[\frac{\sigma_d}{\omega \varepsilon_o \varepsilon_r} \right]^2} - 1 \right]} \tag{3.9}$$

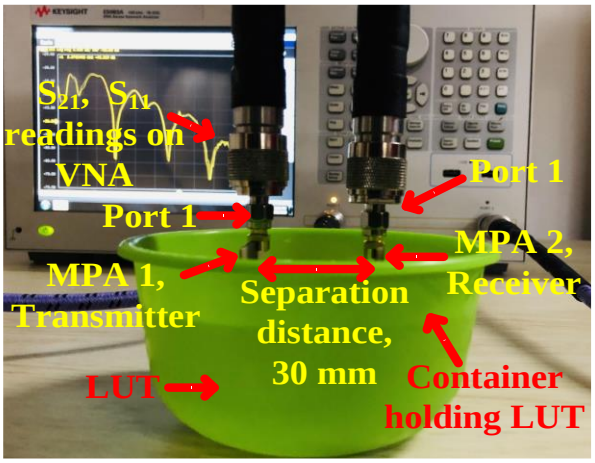

(a)

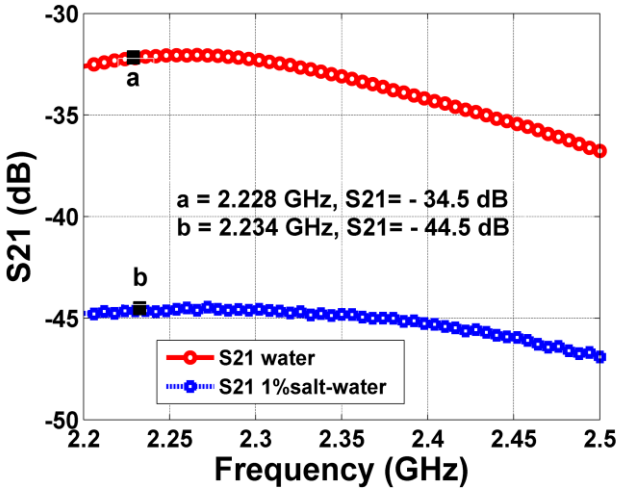

(b)

Figure 3.10 (a) Measurement setup of MPA dipped inside LUT with SMA Cables (z = 30 mm) (b) Measured S_{21} of water and salt solution at the receiver antenna

Now, we present a case study of LUT modeled in the previous section. The σ_d of the LUT is determined by following the steps mentioned above. The essential parameters to determine α_d and σ_d, along with their values, are mentioned in Table 3.2 and Figure 3.10(b). Here, we took z = 30 mm and P_t = 0dBm for calculations. Therefore, at the end of this section, we can say that techniques presented in sections 3.2 and 3.3 together can provide two key parameters ε_r and σ_d in the design of liquid

phantom. We can also conclude from Table 3.2 that as the concentration of salt in water increases, ε_r tends to reduce, whereas σ_d tends to increase. This inference is crucial and is used extensively throughout this chapter.

Table 3.2 Parameters to Determine σ_d and ε_r of LUT for Two Antenna Setup

LUT	S_{21} (dB)	S_{11} (dB)	P_r (μW)	α_d (Np/m)	f_r (GHz)	ε_r	σ_d (S/m)
Water	- 33.3	- 9.67	0.52	29.00	2.228	78	1.36
1% salt-water	-44.1	-10.11	0.06	37.51	2.234	72	1.70

3.4 Development of Homogeneous Liquid Phantom

In this section, we developed the homogenous tissue-equivalent model of the body having ε_r and σ_d of 52.7 and 1.95 S/m, respectively [92] – [93]. Since ε_r and σ_d for the LUT given in Table 3.2 does not match with that of the homogenous model, therefore, we have done further investigation in this section. To achieve the electrical properties of a homogeneous phantom, we prepared and tested solutions of different concentrations of salt and sugar in water in this section.

3.4.1 2% and 10% Salt Solution in Water

At first, we have added a salt concentration of 1% weight to the solution prepared in the previous section. In this way, the total weight of salt becomes 5g in 250g of water, which has 2% salt concentration. We spread a layer of LUT of thickness mentioned in section 3.2 over PTFE and MPA and measured the f_r as depicted in Figure 3.11(a). Once again, we substituted the initially obtained %variation of 0.1% (for water) along with f_r = 2.24 GHz (Figure 3.11(a)) in (3.4) to determine f_r (sim.), which comes out to be 2.242 GHz. Then we performed variation in ε_r in CST that

satisfies the %variation that results in a value of 69. In this case, a percentage variation of 0.1% is chosen since water has a more significant concentration in the salt solution. The simulated f_r of MPA covered with LUT of ε_r = 69 is shown in Figure 3.11(a).

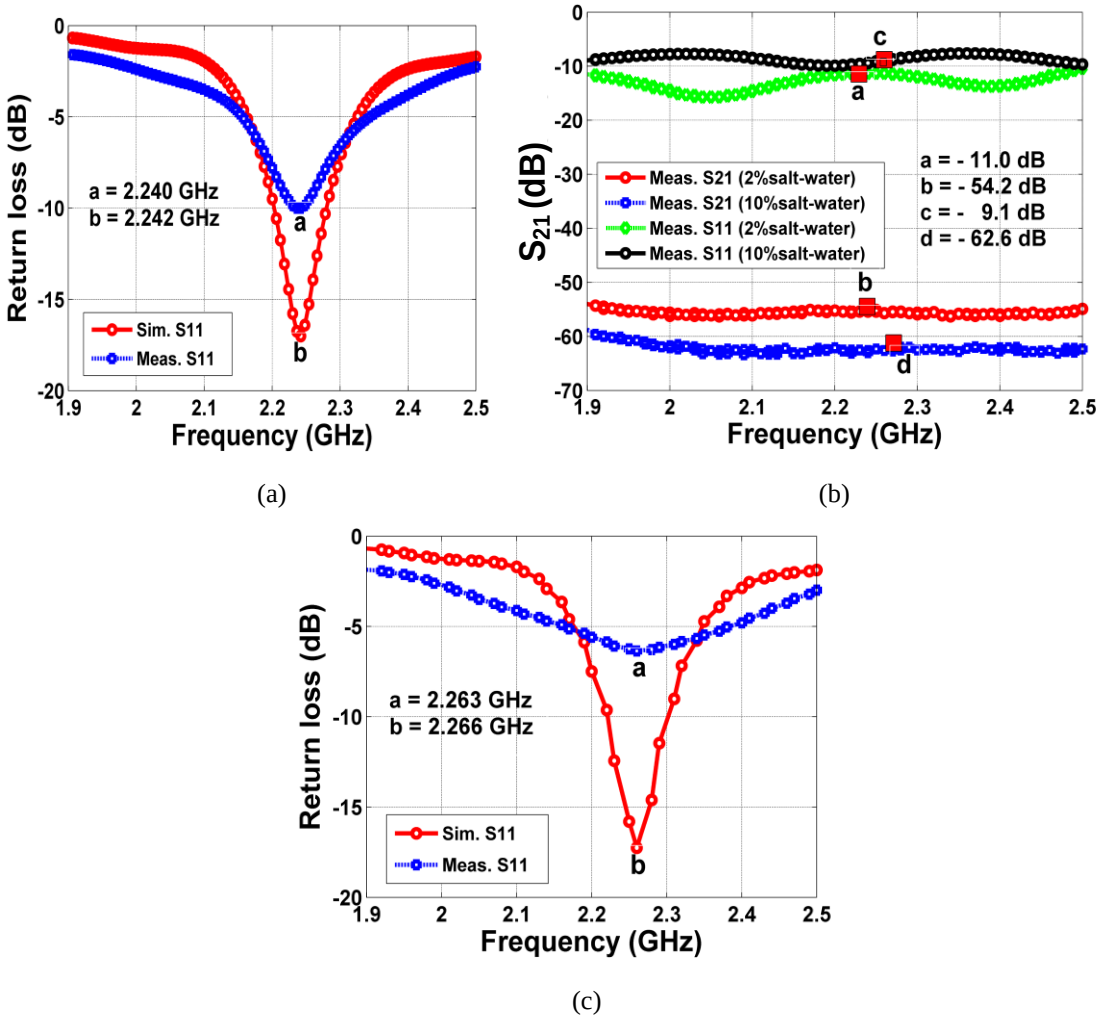

(a) (b)

(c)

Figure 3.11 (a) Simulated and measured f_r of MPA covered with 2% wt. NaCl in water (b) Measured S_{21} and S_{11} of MPA inside the salts solutions, (c) Simulated and measured f_r of MPA covered with 10% wt. NaCl in water

Furthermore, to determine α_d and σ_d of this solution, we followed the steps mentioned in 3.3. The measured S_{21} and S_{11} plots of the MPA dipped inside the LUT are depicted in Figure 3.11(b). To obtain the highest accuracy while measuring S_{21} and

S_{11} has been MPAs dried before getting dipped inside LUT for every measurement. The list of all essential parameters, along with the values of α_d and σ_d, are given in Table 3.3. Once again, the solution is unable to achieve the desired ε_r and σ_d.

Next, a salt concentration of 8% by weight is added to the 2% solution. In this way, the total concentration of salt in water becomes 10%. The measured f_r = 2.263 GHz of the LUT over PTFE is shown in Figure 3.11(c). Once again, the substitution of the values of percentage variation, and f_r (meas.) in (3.4) results in f_r (sim.) of 2.266 GHz. Next, we follow the steps given in section 3.3, to determine α_d and σ_d of the solution. The obtained values of ε_r, α_d, and σ_d are mentioned in Table 3.3. Once again, the new solution is unable to match the desired characteristic of the liquid phantom. The deterioration of the measured return loss of both the solutions in comparison to the simulated ones is because the only real component of ε_c (ε_r) is varied in simulation. However, the imaginary term (loss component) remains as it is. Since losses (α_d) increase due to the addition of salt, as evident from Tables 3.2 and 3.3, the measured results are more unsatisfactory than the simulated ones.

3.4.2 10% and 30% Sugar Solution in Water

In this sub-section, we prepared and tested solutions made of 10% and 30% weight of sugar (25g and 75g) in water (250g) to achieve the desired ε_r and σ_d of a homogeneous phantom. For both the solutions, we obtained measured f_r = 2.233 GHz and 2.245 GHz of the MPA with PTFE container at the top, as depicted in Figure 3.12(a). Next, we followed the steps given in section 3.2, ε_r for which the percentage variation agrees to results in 74 and 60, respectively, for 10% and 30% sugar in water in simulation. Moreover, the measured S_{21} and S_{11} of the MPA inside the solutions are shown in Figure 3.12(b). Once again, we follow the steps mentioned in sections 3.2 and 3.3 to determine ε_r, α_d, and σ_d, as listed in Table 3.3. Interestingly, the values of ε_r and σ_d for a 30% sugar solution approach to that of the homogeneous phantom. Therefore, this solution is appropriate for the further modification of the characteristics as described in the next sub-section.

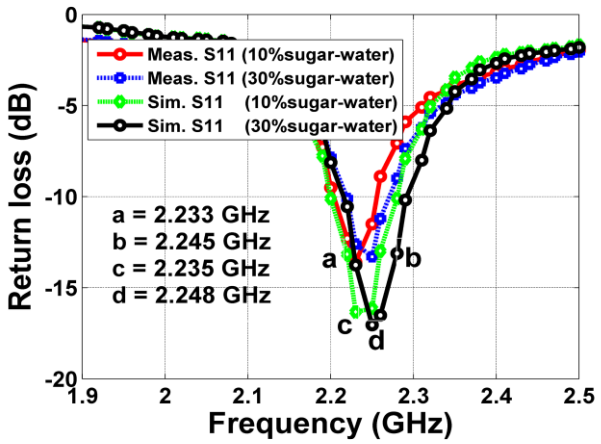

(a)

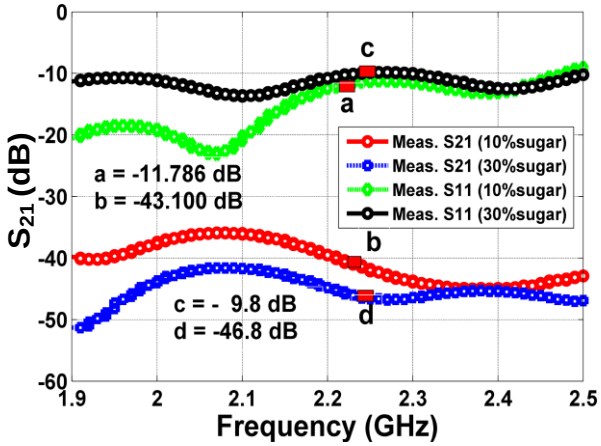

(b)

Figure 3.12 (a) Simulated and measured f_r of MPA covered with 10% and 30%wt. sugar in water (b) Measured S_{21} and S_{11} of MPA inside the sugar solutions

3.4.3 1% and 2% Salt in 30% Sugar Solution in Water

We saw in the last sub-section that 30%sugar in 250g of water is closest to all the solutions still prepared to achieve the electrical properties of a homogeneous phantom. In this sub-section, we add 1% and 2% of salt to the 30% sugar solution to reduce the ε_r further and increase σ_d. The measured f_r of the MPA covered with both the LUTs and PTFE are shown in Figure 3.13(a). When we follow the technique proposed in section 3.2, ε_r of LUTs that satisfy the percentage variation of 0.1 comes out to be 58 and 52.7, respectively, for both the LUTs. The simulated f_r of the MPA

with these values is also shown in Figure 3.13(a). Table 3.3 list the values of σ_d obtained from the measured S_{21} and S_{11} plots of both the solutions, as shown in Figure 3.13(b). We can conclude from the results given in Table 3.3 that 2% of salt in 30% of sugar in 250g of water approximately matches the desired ε_r and σ_d of a homogeneous phantom. Once again, the obtained values of ε_r and σ_d are validated with the graphical data presented in [82], and they possess a perfect resemblance.

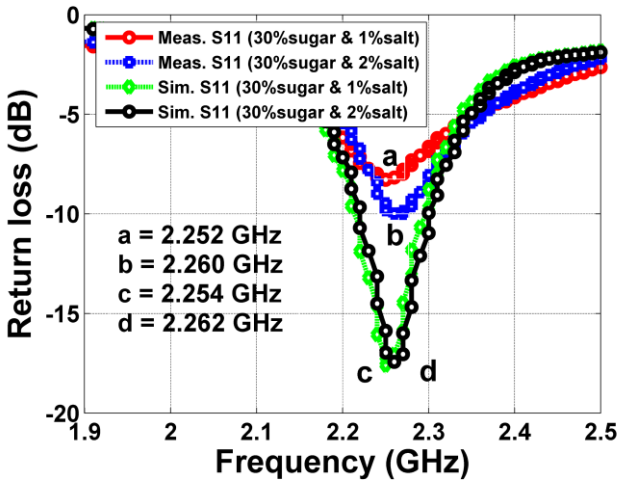

(a)

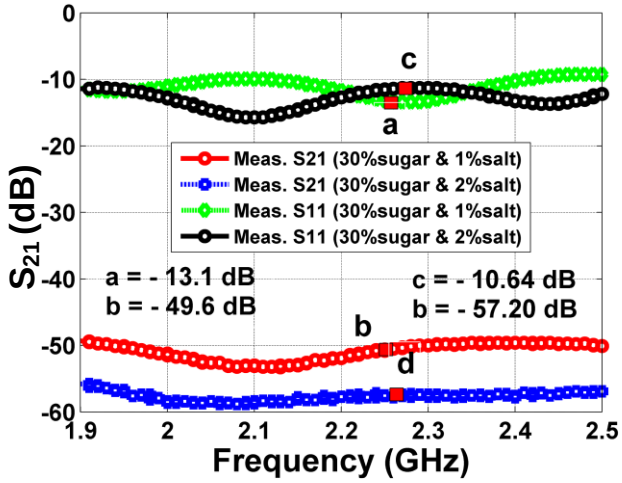

(b)

Figure 3.13 (a) Simulated and measured f_r of MPA covered with 1 and 2% salt in 30% sugar in water (b) Measured S_{21} and S_{11} of MPA inside the sugar solutions

We now analyze the results given in Tables 3.2 and 3.3 in the following points.

a) Both salt and sugar are capable in the reduction of ε_r and increment of σ_d.

b) The increase in the concentration of salt has a more considerable impact on increasing σ_d than sugar. For example, when the concentration of salt increases from 2% to 10% (increment of 8%), the σ_d increases from 2.11 to 2.34. It implies an increment of 0.02875 S/m for each 1% increment in concentration. However, for sugar, this value is 0.0195S/m.

Table 3.3 Parameters to Determine σ_d and ε_r of LUT for Two Antenna Setup

LUT (in water)	S_{21} (dB)	S_{11} (dB)	P_r (μW)	α_d (Np/m)	ε_r	σ_d (S/m)
2%_salt	- 54.2	- 10.8	0.0042	47.51	69	2.11
10%_salt	- 62.6	- 9.1	0.0006	37.51	55	2.34
10%_sugar	- 43.1	- 11.8	0.0690	27.60	74	1.26
30%_sugar	- 46.8	- 9.8	0.0308	39.86	60	1.65
1%_salt in 30%_sugar	- 49.6	- 13.1	0.0132	43.10	58	1.75
2%_salt in 30%_sugar	- 57.5	- 10.6	0.0028	46.40	52.7	1.92

3.5 Development of Heterogeneous Liquid Phantom

In this section, we prepare a solution, mimicking the skin layer with glycerine in water, having ε_r and σ_d of 38.5 and 1.4 S/m, respectively [92] – [93].

3.5.1 Pure and 1% Water in Glycerine

In the first step, pure glycerine of $\varepsilon_r = 13.5$ and $h = 1.2$ mm is spread over a PTFE container. Then we measured $f_r = 2.319$ GHz of the arrangement in VNA, as shown in Figure 3.14(a). The measurement setup is identical to Figure 3.8(a). Next, using the simulation setup, as shown in Figure 3.8(b) and feeding the parameters of pure glycerine, we obtained the simulated $f_r = 2.320$ GHz of the arrangement, as depicted in Figure 3.14(a). The percentage variation between the simulated and measured results using (3.4) comes out to be 0.086%.

Since we know only one key parameter (ε_r) of the liquid under observation here, therefore, to determine the other important parameter (σ_d), the arrangement of two MPAs is dipped inside the container holding the glycerine. We measured the S_{21} and S_{11} of the MPAs, as shown in Figure 3.14(b). Next, from the measured S_{21} and S_{11} values, we obtained α_d and σ_d following the steps given in section 3.3. Table 3.4 list the values of all essential parameters along with ε_r and σ_d.

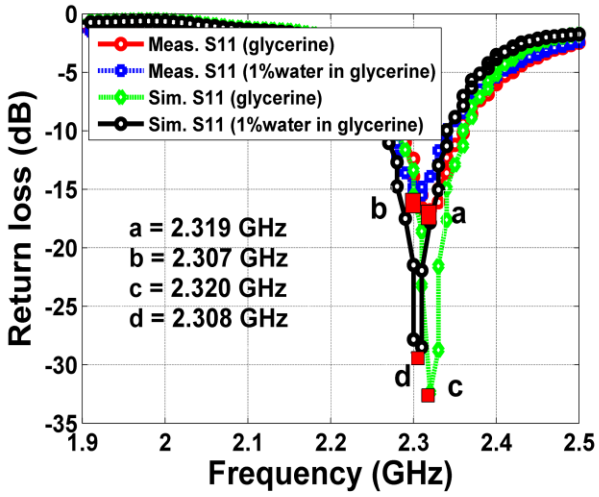

(a)

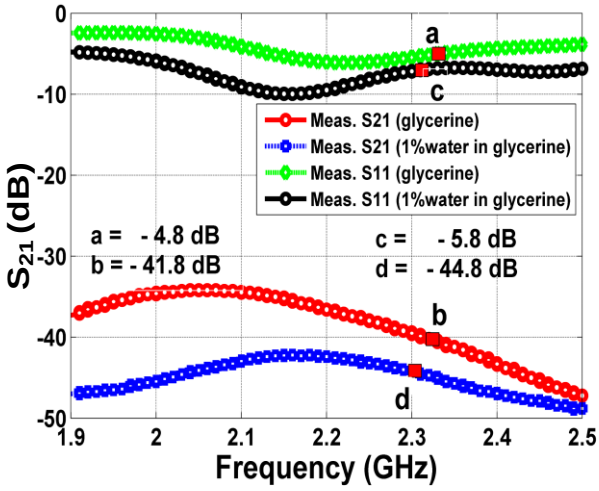

(b)

Figure 3.14 (a) Simulated and measured f_r of MPA covered with glycerine and 1%water in glycerine (b) Measured S_{21} and S_{11} of MPA inside the solutions

It is apparent from the results that ε_r and σ_d are far away from the desired values of a heterogeneous phantom. We know from the previous section that the addition of salt or sugar tends to increase σ_d; however, this can also reduce ε_r. Interestingly, we observed that adding water to glycerine increases the ε_r as well as the σ_d. Therefore, in the second step, we added 1% of water by weight (2.5g) in 250g of glycerine. Since glycerine has a more significant concentration than the water, hence %variation = 0.086 is used to determine simulated f_r and subsequently ε_r. This step is identical to section 3.2, where we used the percentage variation of 0.1% due to a higher concentration of water than the other constituent (salt and sugar) to determine ε_r through simulation. The measured f_r of MPA covered with pure glycerine of h = 1.2mm and PTFE is shown in Figure 3.14(a). The value of ε_r = 23 satisfies the %variation of 0.086 in simulation with simulated f_r at 2.308GHz. The measured S_{21} and S_{11} of the two-antenna arrangement dipped inside the LUT shown in Figure 3.14(b). We then determined the σ_d of the LUT listed in Table 3.4 following the steps given in section 3.3. It is clear from the result that both ε_r and σ_d increases after adding water in glycerine. Therefore, we can conclude that we are in the right direction, and in the next sub-section, suitable modifications are made to obtain the desired electrical characteristics of the heterogeneous phantom.

3.5.2 5% and 7% of Water in Glycerine

In the previous sub-section, we found out that the addition of water in pure glycerine can help us to achieve the properties of a heterogeneous phantom, therefore in this section, the concentration of water in glycerine is increased to 5% and 7% by weight which is equivalent to 12.5g and 17.5g. The measured f_r of both the solutions with PTFE containers are depicted in Figure 3.15(a). For the %variation = 0.086, ε_r = 33 and 38.5 satisfies the simulated f_r of 5% and 7% of water as shown in Figure 3.15(a). Subsequently, we measured the S_{21} and S_{11} of the two antenna arrangements for both the solutions, as depicted in Figure 3.15(b). Then we followed the steps given in section 3.3 to determine σ_d of LUTs, which comes out to be 1.1 and 1.4 S/m, as listed in Table 3.4. It is apparent from the Table that the solution with 7% water in glycerine matches the desired characteristics of the skin phantom.

At the end of this section, we now have both homogeneous and skin liquid phantoms ready for SAR measurements. When we compared our obtained values with that of [82], the results are in excellent agreement.

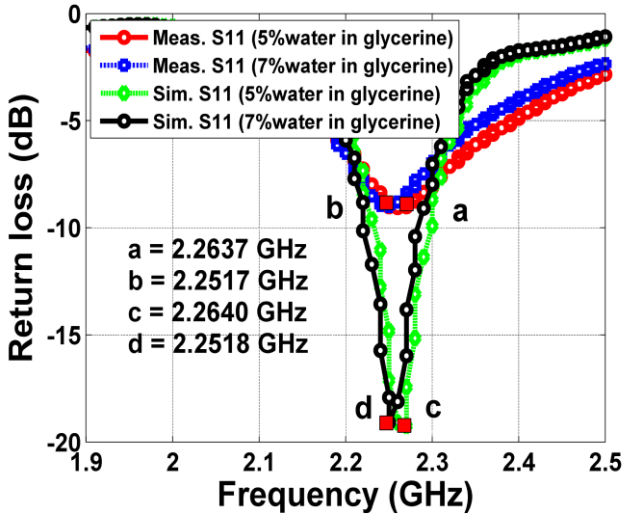

(a)

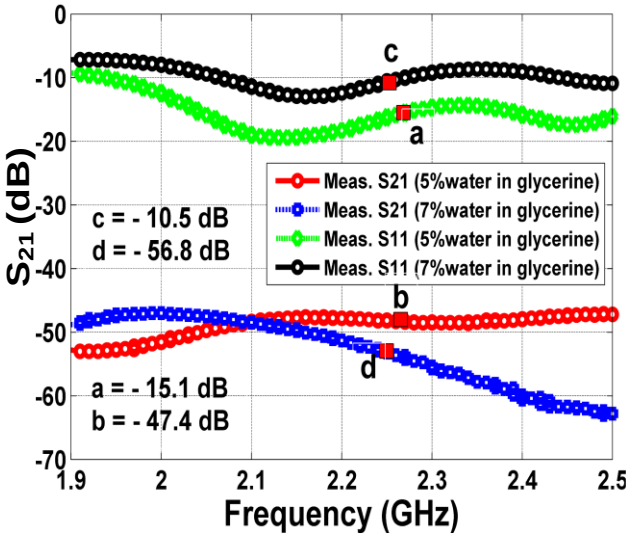

(b)

Figure 3.15 (a) Simulated and measured f_r of MPA covered with 5 and 7% water by weight in glycerine (b) Measured S_{21} and S_{11} of MPA inside the solutions

Table 3.4 Parameters to Determine σ_d and ε_r of LUT for Two Antenna Setup

LUT (Glycerine + water)	S_{21} (dB)	S_{11} (dB)	P_r (μW)	α_d (Np/m)	ε_r	σ_d (S/m)
Glycerine	- 41.8	- 4.8	0.13	25.75	13.5	0.51
1% water -	- 44.8	- 5.8	0.06	31.60	23	0.81
5% water	- 47.4	-15.1	0.02	34.75	33	1.10
7% water	- 56.8	-10.5	0.003	41.80	38.5	1.4

The determination of dielectric constant with a resonant cavity in the form of a dielectric resonator is quite popular among researchers. For example, work done in [112] – [114], are based on cavity perturbation of dielectric resonator. These works are successful in predicting the dielectric constant of material/chemical of the lower values. However, for chemicals with higher dielectric constant (like water, and liquid phantoms designed in this chapter), the variation of actual and estimated value is high. For example, Table 3.5 shows a comparison of our work with the most recent one [112]. The proposed work in this thesis predicts the ε_r of water and glycerine with substantially lesser error than [112]. This justifies the effectiveness of the proposed work.

Table 3.5 Comparison of Proposed Work and [112]

Specimen	Reference value (ε_r)	This work (ε_r)	[112] (ε_r)	% error [This]	% error [112]
Water	80.0	78.5	75.96	1.8	5.05
Glycerine	13.5	13.5	13.23	0	2.00

3.6 SAR Measurement and Simulation

In this section, we measure the SAR values of the developed phantoms by exposing it to a radiating device, a typical scenario in WBAN. We also performed a

simulation to validate it with measured SAR values.

3.6.1 SAR Measurement Due to Rise in Temperature

We know from previous works that in the absence of heat diffusion (or uniform distribution), SAR is directly proportional to the rise in temperature due to the presence of an EM source in the form of a body-worn antenna as given by (3.10) [80] – [81].

$$\text{SAR} = C\frac{\Delta T}{\Delta t}\ \text{[W/Kg]} \tag{3.10}$$

Here, C (J/ Kg. C^{o}) is the specific heat capacity of the solution,

ΔT (C^{o}) is the rise in temperature and

Δt (s) is the total exposure time of EM radiation.

The measurement setup to determine ΔT is shown in Figure 3.16. We took an elliptical cylinder of height h = 100mm and radii along x– (semi-major) and y–axes (semi-minor) of 25mm and 15mm respectively in our experiment to hold the phantoms. The container is of polyethylene that has thickness t and ε_r of 0.2mm and 1.6, respectively. The MPA designed in Figure 3.7 is used as an RF source for measurements carried out in this work, as shown in Figure 3.16. The MPA is attached to the body of the container with the help of low permittivity RTV coating (ε_r = 1.22). The open surface of the container is covered with a skinny adhesive tape to avoid the spilling of phantoms while experiments. We placed the antenna at the top of the container, as evident from Figure 3.16, because the SMA connector soldered to the feed line of the MPA creates an unnecessary gap. However, in our experiments, no gap between the MPA and the container is left to model the scenario of wireless body sensors accurately. The MPA is driven by a VNA with an input power of 0dBm.

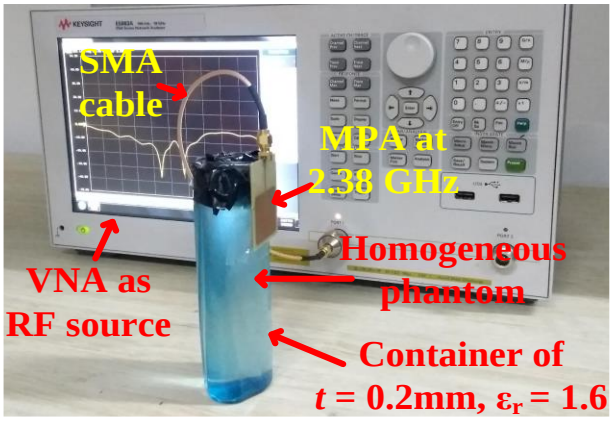

Figure 3.16 Measurement setup of SAR determination with MPA backed by elliptical cylinder

Now following steps are followed for the determination of C, ΔT, Δt, and subsequently thermal SAR.

Step 1: The LUT is poured inside the container and, initial temperature T_i is noted with the help of a digital thermometer, as shown in Figure 3.17(a).

Step 2: RF source is turned on, and a stopwatch is started.

Step 3: RF source is turned off, and the stopwatch is stopped. Subsequently, the final temperature of the LUT T_f is noted, as shown in Figure 3.17(b), and ΔT is determined as given by $T_f - T_i$. Next, the reading in stopwatch indicates Δt in s.

Step 4: The specific heat capacity of the LUT is determined, as explained here, with the help of an example. For a given mass m of LUT, T_i is measured, as shown in Figure 3.18. Subsequently, LUT is heated with the help of an induction oven, and equivalent heat transfer Q (in J) is calculated as given by (3.11).

$$Q = P \cdot t \quad \text{(J)} \tag{3.11}$$

$$Q = mC(\Delta T) = mC\left(T_f - T_i\right) \tag{3.12}$$

Here, P is the power supplied (in W), and t (s) is duration. Next, T_f is noted after

heating of 10s, and C is evaluated by substituting Q, m, T_f, and T_i in (3.12).

[We have kept, t and m to 10s and 200g respectively in this dissertation.

Note: T_i and T_f in *step 4* are different from that of *steps 1* and *3*]

Step 5: SAR is computed by the substitution of C, ΔT, and Δt in (3.10).

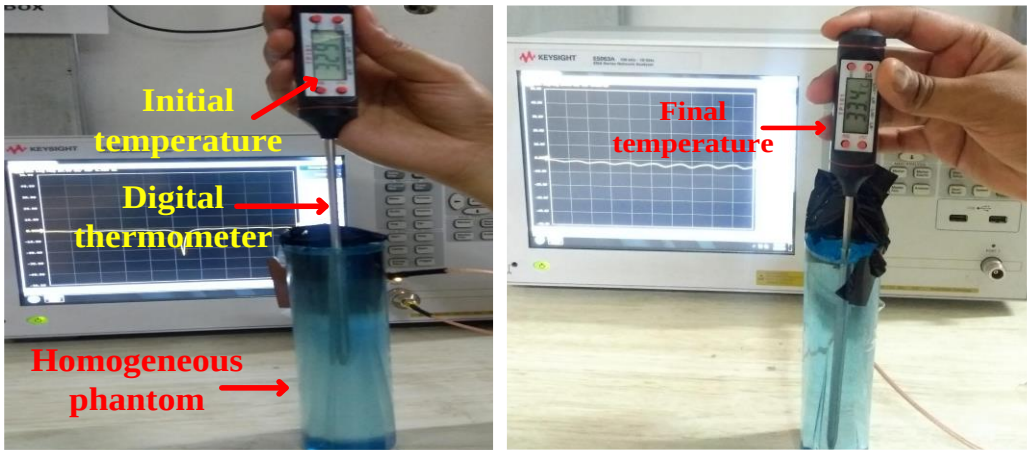

(a) (b)

Figure 3.17 Digital thermometer measuring temperature of LUTS (a) Initial (b) Final

Figure 3.18 Weighing machine for the measurement of weight of phantom to be used in the determination of specific heat capacity (weight of empty container = 18g, total weight = 200 g (phantom) + 16 = 218g)

Now we follow the steps mentioned above to determine SAR for homogeneous (2% salt in 30% sugar solution in water) and skin (7% of the water in glycerine) phantoms called here as LUT 1 and LUT 2 respectively. The measurement setup for both the LUTs is depicted in Figures 3.16 and 3.17. All parameters, along with the SAR values, are given in Table 3.5. We have fixed the parameters like P, m, Δt, and t for both the LUTs to 400W, 200g, 3600s, and 10s. The final and initial temperature readings are carried out at an arbitrary position. It is because both the liquids have a uniform composition of constituents on contrary to four and five-layer models [70], [92]. Moreover, due to uniform composition, the heat diffusion would be constant throughout the sample, and the final temperature reads the same value at other points as well. Therefore, for SAR determination in this dissertation, no averaging sample of mass is considered, instead of the proposed technique predicts the point SAR.

Table 3.5 SAR Values of LUT 1 and LUT 2

LUT	SAR meas.		C meas. (J/ Kg. C^o)				SAR (W/Kg)
	T_i (^{o}C)	T_f (^{o}C)	T_i (^{o}C)	T_f (^{o}C)	Q (J)	C	
LUT 1	32.9	33.5	30.8	36.5	4000	3500	0.583
LUT 2	32.8	33.4	31.3	38.3	4000	2857	0.476

3.6.2 SAR Simulation on Homo- and Heterogeneous models

Next, we performed SAR simulations on LUT 1 and LUT 2 discussed in section 3.6.1. For this, we have designed an elliptical cylinder of height h = 100mm and radii along x– (r_x) and y–axes (r_y) of 25mm and 15mm, respectively, in CST as shown in Fig. 3.19 (a). The radii of the elliptical cylinder are chosen to mimic a human wrist which has a larger dimension along the major axis than the minor one. The outer layer of the cylinder is modeled as polyethylene of thickness t = 0.2 mm and ε_r = 1.6 identical to measurement. The inner layer consists of homogeneous and skin liquid phantoms, as shown in Figures 3.19 (b) and (c). The electrical parameters of the homogeneous and heterogeneous (skin) liquid phantoms are fed into the CST model based on the obtained values of ε_r and α_d. The simulated model of the MPA prototyped in Figure 3.7 acts as an RF source for the simulations, as shown in Figure 3.19(a). We have left

no gap between the MPA and the cylinder in simulation as identical to the measurement setup.

In the simulation setup, we fed the power of 0dBm to the MPA at the feed location (identical to measurement), as shown in Figure 3.19a. Then we performed a simulation in transient domain solver (CST) with a power loss monitor fixed at 2.38 GHz (operating frequency of the MPA). The total duration of the 3600s is set for simulating the MPA backed by the container holding the phantom. The simulated SAR values for the LUTs are shown in Figure 3.20 (a) and (b). For a valid comparison and proving the effectiveness of the proposed techniques in section 3.2 and 3.3, we took the in-built electrical properties of homogeneous and skin phantom in CST simulation also given in [92] – [93]. The simulations indicate the maximum point SAR (no averaging mass) of 0.528W/kg and 0.432W/kg, respectively, for homogeneous and skin liquids. Therefore it is apparent that the measured SAR in section 3.6.1 is in excellent agreement with that of simulated values. It justifies the liquid models developed in this work are suitable for the use of SAR measurements in commercial scale in WBAN scenarios.

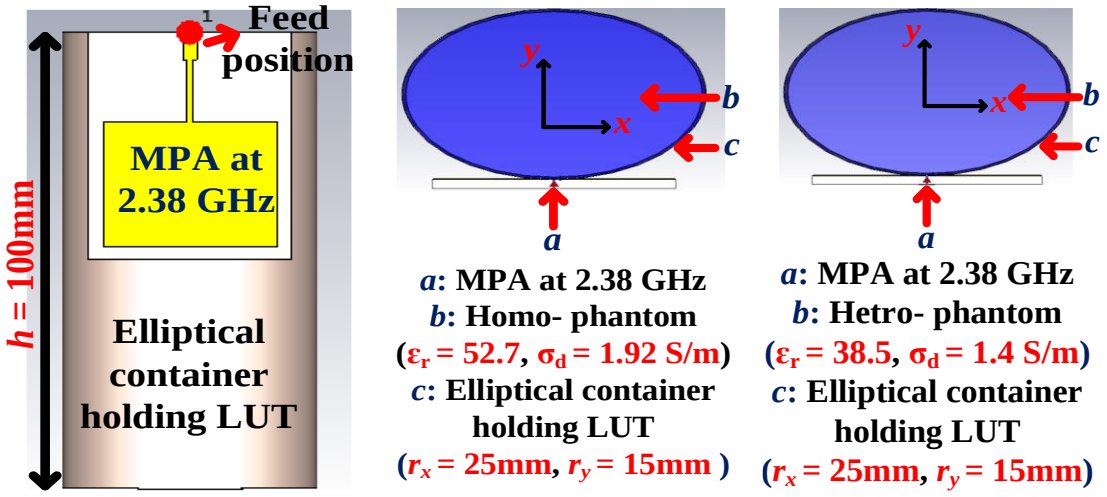

(a) (b) (c)

Figure 3.19 (a) Front view of MPA backed by an elliptical cylinder of *h* = 100mm containing liquid phantoms, Top view of MPA backed by an elliptical cylinder with liquid phantoms (b) homogeneous (c) skin layer

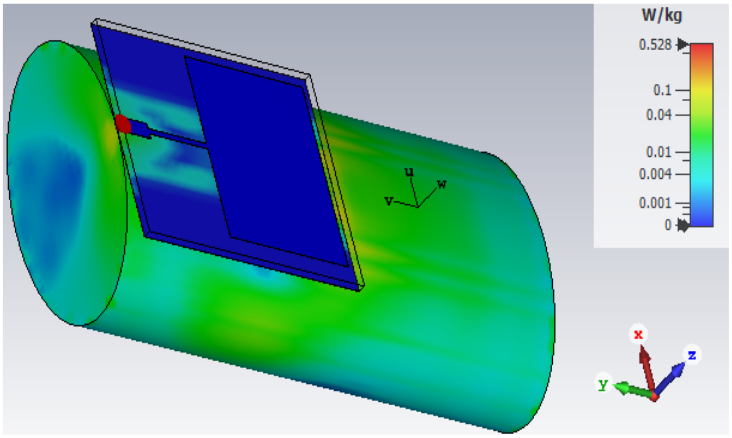

(a)

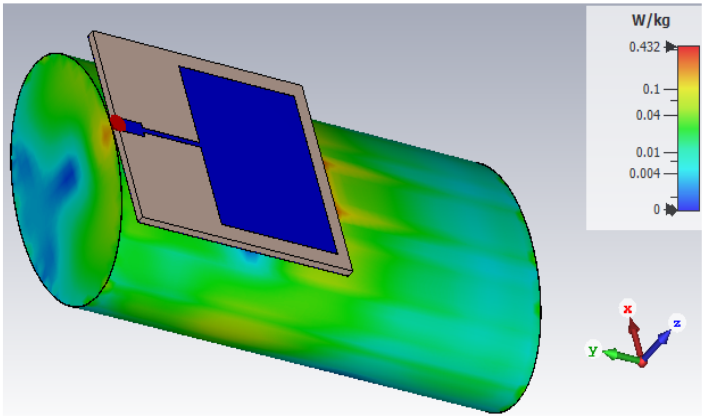

(b)

Figure 3.20 SAR simulation indicating point SAR values on (a) homogeneous model (b) skin model

3.7 Conclusion

In this chapter, we developed a homogeneous and skin equivalent liquid phantoms with the help of low-cost materials such as salt, sugar, glycerine, and water. We have presented two different techniques to determine the crucial parameters of the phantom ε_r and σ_d with the use of just VNA. Therefore, no complicated and expensive

setup, such as a dielectric probe tool kit, is necessary to do the measurements. The prepared homogeneous phantom consists of 2%weight of salt in 30%weight of sugar in 250g of water. Whereas, the heterogeneous model mimicking skin layer comprises of 7%weight of water in 250g of glycerine. We verified the effectiveness of the presented approaches by simulating, and measurement of point SAR on liquid phantoms developed. A drawback of the SAR measurement setup proposed in this work is that some heat is absorbed by the polyethylene container, which is undesired. However, we observed excellent agreement between the simulated and measured SAR values, and this justifies the appropriateness of the presented approach.

Chapter 4

Compact EBG Based Antenna for Smart-watch Applications

This chapter is based on the following research papers:

- D. Rano and M.S. Hashmi, "Extremely Compact EBG-Backed Antenna for Smart-Watch Applications in Medical Body Area Network," *IET Microwave. Antennas Propag*. vol. 13, pp. 1031-1040, December 2019.

- D. Rano and M.S. Hashmi, "A Modified Interdigital EBG Reflector for Wireless Body Area Network Applications," in *Wiley Microwave Optical Technology Letter*, vol. 61, pp. 912–919, December 2019.

- D. Rano and M. S. Hashmi, "A New Lumped Circuit Modelling Technique for EBG Based on Surface Current Flow," *IEEE Asia-Pacific Conference on Antenna and Propagation*, 2018, pp. 351 – 352.

In this chapter, we propose a design of a compact and via-less interdigital EBG unit cell (IDE) for wearable applications in the medical body area network (MBAN) band covering 2.36 - 2.40 GHz. The uniqueness of the proposed cell is in its ability to achieve lower resonant frequency despite the very compact size of 14.3mm x 14.5mm. The cell has adjacent fingers connected in such a way that the net inductance contributed by the metallic strips increases and this aids in the reduction of the resonant frequency. We have provided an analysis of the proposed cell with the help of an equivalent lumped circuit model developed using a surface current flow through the

metal strips. The evaluation of the developed model is assessed by comparing the reflection phase response obtained from the circuit model and full-wave analysis, which show remarkable resemblance. Furthermore, we have validated the polarization stability of the proposed unit EBG cell under TE-TM and TEM mode of incidence with the help of the reflection phase diagram. We also have demonstrated the polarization stability of the unit cells under obliquely incident TE-TM modes at 0^o, 15^o, 30^o, 45^o, and 60^o.

Subsequently, we design an array of 2x2 IDE unit cells for enhancing the radiation feature of a monopole antenna. The size of the proposed IDE based EBG array integrated monopole antenna is 36mm x 38mm x 3.12 mm and is compatible with commercially available wristwatches. The design exhibits an excellent agreement between the experimental and the simulated results, whereby it can provide gain and efficiency of 5.3 dB and 85% respectively at the MBAN frequency. Moreover, the incorporated antenna demonstrates measured on-body gain and efficiency of 3.7dBi and 50%.

4.1 Background and Related work

Wireless health monitoring has drawn significant attention in the past few years because as it enables regular monitoring, a patient's mobility, and is non-invasive in the case of explants [1]-[3], [115]. In this context, smart-watches have contributed significantly [116]-[122]. Such devices are body-worn and therefore need to be very compact and operate at a shallow power level. It necessitates antenna used in such applications to be miniature in size, lightweight, low in profile, optimum gain (required to establish a link between an external node), and with low levels of specific absorption rate (SAR) [115]. It has been widely reported that patch antennas exhibit low profile and can be designed in smaller sizes and is appropriate for these situations [58] – [60], [115]. However, it suffers from reduced gain, and efficiency reduces with miniaturization. Besides, a smaller ground plane in such antennas increases the back lobe radiation and hence increases SAR in adjacent tissues [70]. Furthermore, the

placement of an antenna close to the body disturbs impedance matching and frequency shift. It makes the design of antennas for smart-watches a real challenge.

Earlier reported designs of antennas for smart-watches were successful in achieving compact size and low profile, however radiation efficiency, gain, and SAR level deteriorates in the presence of the human body in the vicinity [123]-[127]. A monopole antenna seems appropriate for wearable applications such as smart-watches owing to its compact size with a low profile but exhibits high SAR, which can damage human tissues [127]. These issues can be addressed, and antenna performance can be improved through the incorporation of electromagnetic band-gap structures (EBG) in the ground plane of the antenna substrate [37]-[39].

In this section, we introduce EBG surfaces and their application in the enhancement of radiation properties of body-worn antennas. We have explained the terms lumped circuit model, reflection phase, dispersion diagram, and transmission characteristics commonly used to characterize an EBG unit cell or surface. We have also presented a convenient technique to model an EBG unit cell with the help of surface current flow.

4.1.1 Introduction to EBG

EBG structures are a particular type of material that is non-existent but can be made by a periodic arrangement of unit cells along with 1D, 2D, or 3D axes [43]. The periodicity of the unit cell must be very small than the operating wavelength. These unique materials at resonance conditions show infinite impedance (HIS), and thus surface impedance tends to be infinity. Surface impedance in terms of the electric and magnetic field can be given by (4.1). Here, Z_S is the surface impedance of the EBG, E_x is the electric field along the x-axis, and H_y is the magnetic field along the y-axis. We can express the magnetic field in terms of current density J_x from Ampere's law given by (4.2). Furthermore, (4.2) can also be written as (4.3) (Ohm's law). Here, σ is the conductivity of the surface. We can express the electric field of a surface wave as given in (4.4). Here, α is the attenuation constant of the medium.

$$Z_S = \frac{E_x}{H_y} \tag{4.1}$$

$$\nabla \times H_y = J_x \tag{4.2}$$

$$J_x(z) = \sigma E_x(z) \tag{4.3}$$

$$J_x(z) = \sigma E_o e^{-\alpha z} \tag{4.4}$$

For high impedance surface Z_s becomes infinity. It implies the magnetic field to be zero from (4.1). Substituting this in (4.2) results in a surface current of zero value. Hence, EBG prohibits the flow of surface current along with the metal, and this further stops diffraction at the discontinuity of the patch of an MPA and also sides of PCB. Consequently, it reduces back lobes, enhances gain, and improves efficiency.

A typical EBG unit cell is shown in Figure 4.1. It has a dimension of *W* * *W* along *x*- and *y*-axes. A via of radius *r* connects the patch at the top to the ground plane. Periodic repletion of the unit cells along *x*- and *y*-axes with a gap of *g* among the adjacent cells leads to the generation of an EBG surface. The unit cell shown in Figure 4.1 is commonly known as a mushroom cell. In general, EBG surfaces are characterized by *in-phase reflection frequency* and *band-gap* property. *In-phase reflection* is demonstrated by a reflection phase diagram and a lumped circuit model. Whereas, the *band-gap* property is shown with the help of the dispersion diagram of a unit cell and transmission characteristics of an array of EBG unit cells.

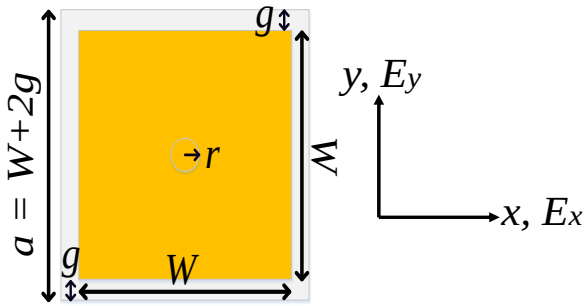

Figure 4.1 Mushroom EBG unit cell [*W*: width of the patch, *g*: gap on either side of the patch, *r*: radius of the via, *a*: period of the unit cell]

4.1.2 Lumped Circuit Model

For an EBG unit cell, if the operating wavelength is more significant than the periodicity, as shown in Figure 4.1 (Where $W+g$ is the periodicity of the EBG cell), then the operating mechanism can be explained with the help of equivalent lumped element circuit model. The equivalent circuit model of the mushroom for a *y*-polarized EM wave is shown in Figure 4.2. The capacitor C_{C1} and C_{C2} represent the capacitance developed between the adjacent patches due to the charge accumulated. Whereas, the inductor L_v is due to the via that connects the top patch with the ground plane. For an *x*-polarized EM wave, the circuit model remains the same. However, the capacitance develops along the *x*-axis.

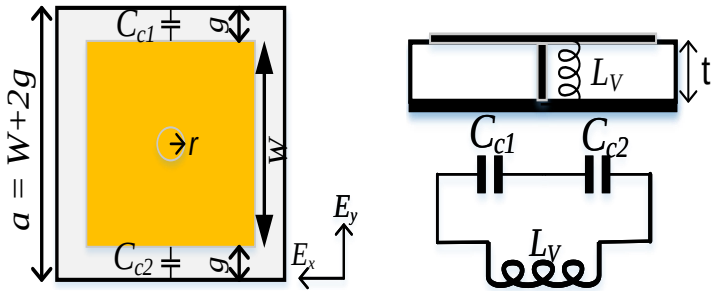

Figure 4.2 Mushroom EBG unit cell with edge coupling capacitance C_{c1} *and* C_{c2} for E_y polarized wave (left)], Equivalent circuit Model [L_v: inductance of the via] (right)

The net impedance of the parallel combination of two lumped components, as shown in Figure 4.2, can be written as given in (4.5). Here, L is the net inductance and capacitance, which is L_v, C_{C1}, and C_{C2} for the present case. Further simplifying (4.5), we can write impedance as given in (4.6). Since this is a parallel resonant circuit, therefore the impedance at resonance becomes infinity. Equating the denominator of (4.6) to zero, the resonant frequency of the circuit is given in (4.7).

$$Z_S = j\omega L_V \square \frac{1}{j\omega C_C} \tag{4.5}$$

$$Z_S = \frac{j\omega L_V}{1-\omega^2 L_V C_C} \tag{4.6}$$

$$f_r = \frac{1}{2\pi\sqrt{L_V C_C}} \tag{4.7}$$

The resonant frequency suggests that at resonance, the circuit behaves as a stop band, thus not allowing any surface current to flow. Hence, this type of surface is also known as a high impedance surface.

Our contribution: We have developed a new approach of lumped circuit modeling for a standard cell in [127]. Our approach is based on surface current flow through the metallic strips when an *x*- or *y*- polarized EM wave is incident on an EBG.

A fork-shaped EBG cell from [127] has been shown in Figure 4.3(a) with repetition along *x*- and *y*- axes. For a fair comparison, we kept the original dimensions of the unit cells in this chapter. For a *y*-polarized EM wave incident normally, the unit cell is bisected along the *x*-axis, as shown in Figure 4.3(b). The edge coupling capacitances (ECCs) develops along the *y*-axis between the adjacent metallic strips, as depicted in Figure 4.3(b) and given by (4.8). Here, C_c is coupling capacitance, W is the width of the strip, g is the gap between the adjacent cells, ε_o and ε_r are the permittivities of the air and substrate, respectively. It results in the formation of three ECCs at the top and the bottom. Due to different widths of the strip, the values of the ECCs vary, as can be inferred from Figure 4.3(b).

According to Maxwell's equation for an electric field incident on a PEC/metal plate, surface current (AC) gets induced in it. This induced surface current on the patch grounds through the via taking the path, as shown in Figure 4.3(b). The metal surface through which the surface current flow forms the inductor. The value of grid/strip inductance L_g is given by (4.9). The idea here is, in the calculation of L_g through (4.9), the length of a strip l_s is the dimension along the electric field, whereas the width of a strip w_s is the dimension orthogonal to the electric field. For example, the dimensions L_s and D in Figure 4.3(a) forms length (l_s) and width (w_s), respectively, for the bottom strip. Here, k_g is the correction factor in the presence of a full ground plane given by (4.10). The distribution of all strip inductances and ECCs in the unit cell using the concept given above is depicted in Figure 4.3(c).

$$C_C = \frac{17 \times W \times \varepsilon_O \times (\varepsilon_r + 1)}{\pi} \times \cosh^{-1}\left(\frac{W+g}{g}\right) \quad (4.8)$$

$$L_g = 0.25 \times 10^{-7} \times l_s \left(\ln \frac{l_s}{w_s} + 1.193 + 0.25 \frac{w_s}{l_s} \right) k_g \quad (4.9)$$

$$k_g = 0.57 - 0.145 \ln \frac{w_{s1}}{t} \quad (4.10)$$

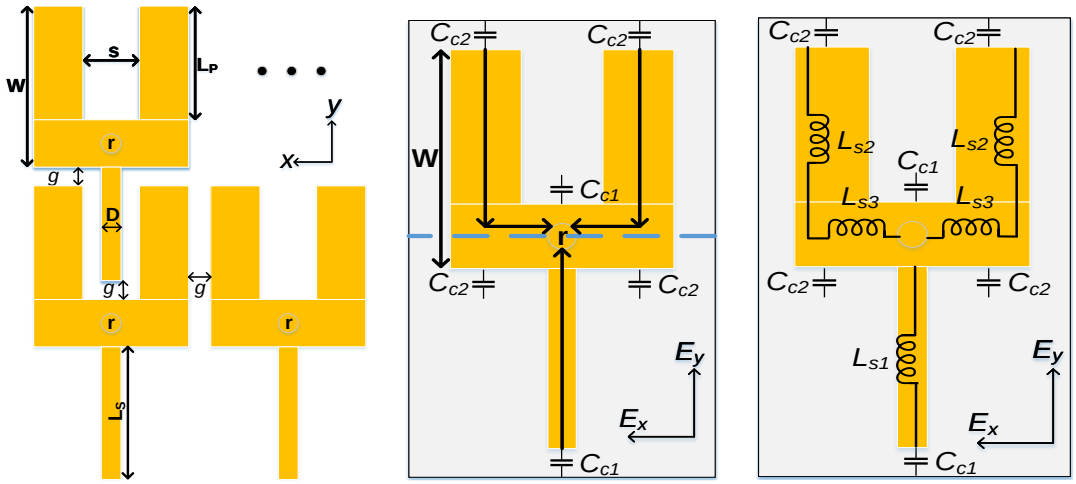

(a) (b) (c)

Figure 4.3 (a) Fork shaped EBG cell [*W*: width of the patch, *g*: gap on either side of the patch, *r*: radius of the via, *s*: slot width, L_s and L_p: length of strips at the top and bottom, *D*: width of the bottom strip]; (b) Surface current flow through the cell for EM wave polarized along *y*-axis [C_{c1} *and* C_{c2}: edge coupling capacitances]; (c) Formation of inductances along the path of surface current flow [L_{s1}, L_{s2}, and L_{s3} are strip inductances]

On the same note, for an *x*-polarized EM wave, the unit cell is bisected along the *y*-axis, as shown in Figure 4.4(a). ECCs develop along the *x*-axis between the adjacent strips, as shown in Figure 4.4(a). The flow of induced surface current through the unit cell is similar to the approach mentioned above. However, due to the orthogonal polarization of EM wave in the present case, the calculation of grid inductance by (4.9)

results in swapping of the values of length and width. The distribution of inductances and ECCs on the unit cell are depicted in Figure 4.4(b).

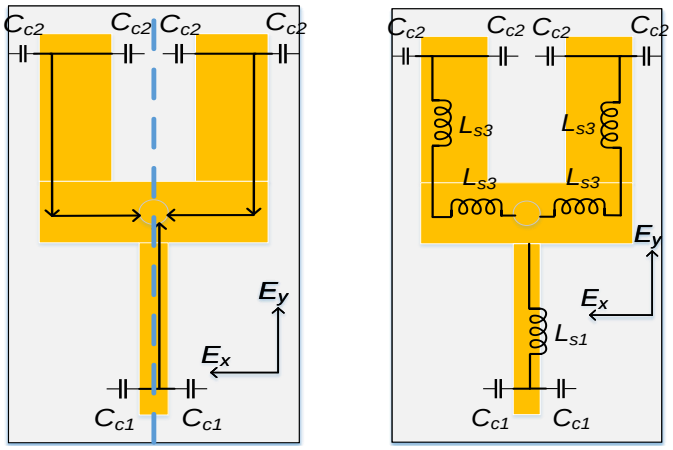

(a) (b)

Figure 4.4 (a) Surface current flow through the cell and grounded through via for EM wave polarized along *x*-axis [C_{c1} *and* C_{c2}: edge coupling capacitances] (b) Formation of inductances along the path

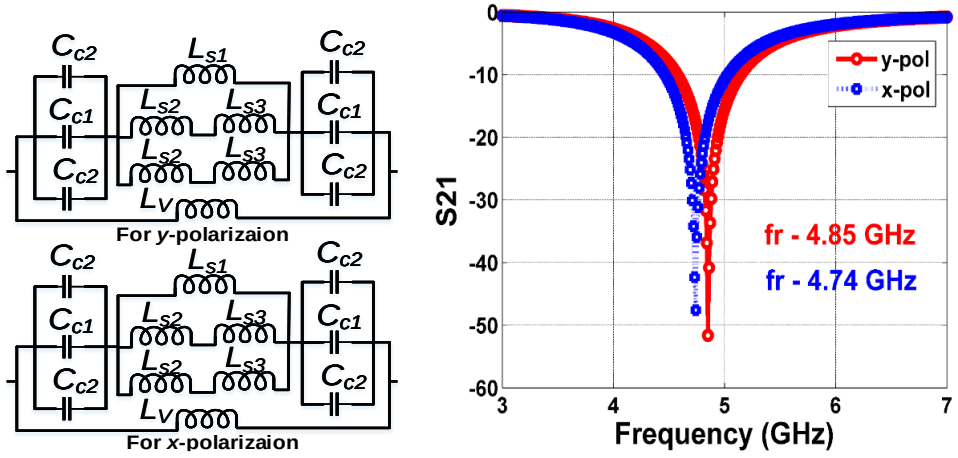

(a) (b)

Figure 4.5 (a) Simulation model for *y*- and *x*- polarized EM wave; (b) Transmission parameter from a simulation model of fork-shaped EBG unit cell

The simulation models of the unit cell for both the polarizations are extracted from Figure 4.3(c) and 4.4(b) and are depicted in Figure 4.5(a). It can be inferred that

model is simply a parallel resonant circuit. L_v in Figure 4.5(a) can be expressed in terms of r, and t is given by (4.11). We have performed circuit-level simulation in ADS to obtain the resonant/stop-band frequency, as shown in Figure 4.5(b).

$$L_v = 2\times10^{-7} t\left[\ln\frac{4t}{2r} + 0.5\left(\frac{2r}{t}\right) - 0.75\right] \tag{4.11}$$

To prove the effectiveness of the proposed technique, we have validated the results obtained from the circuit model with that of full-wave analysis in the next sub-section.

4.1.3 Reflection Phase

It is another property of EBG cells that can be utilized by radiating structures like antennas to strengthen the electric field intensity at the far-field [43] – [48]. In general, for an incident EM wave on an EBG surface, the reflected wave exhibit in-phase (0^o) property. It implies that both incident and reflected electric fields are in-phase. To further explain it mathematically, we have used the expression of the reflection coefficient of EM wave at the interface of two mediums as given in (4.12). Here, Γ is the reflection coefficient, η_2, and η_1 are the intrinsic impedances of the EBG surface and air. Since EBG surfaces show very high impedance, ideally infinity at the resonant frequency, therefore, $\eta_2 \rightarrow$ infinity. Modification of (4.12) results in $\Gamma = 1$. On the contrary, a normal PEC plane (copper or silver as a ground plane in most of the antenna) exhibit $\eta_2 = 0$. Therefore, (4.12) results in $\Gamma = -1$.

$$\Gamma = \frac{\eta_2 - \eta_1}{\eta_2 - \eta_1} \tag{4.12}$$

It has further implications on the improvement of the far-field property of an MPA. Figure 4.6 shows a patch of an MPA is separated from a ground plane by a substrate of given parameters. At the far-field, the electric field is a combination of direct wave E_1 and reflected wave from the ground plane E_2 as given in (4.13). Moreover, E_1 can be expressed as given in (4.14). Here, r is the radial distance from the patch to the observation point P, k is the phase constant, and E_0 is constant. Since

E_2 is a reflected version of E_1, it can be expressed as (4.15). The initial phase difference between E_1 and E_2 should be zero as both originate from the same source (patch). However, reflected wave experiences an additional phase shift of $2\beta h$ due to reflection at the ground plane, as shown in Figure 4.6. Now, using this fact and substituting (4.14) and (4.15) in (4.13) results in the net electric field as expressed in (4.16). Next, the substitution of $\Gamma = 1$ in (4.16) results in constructive interference of both the electric fields, whereas $\Gamma = -1$ results in destructive interference. Therefore, we can conclude from the above theory that an EBG surface assists in enhancing the radiation properties of an MPA than a PEC plane. This property is widely used by the antenna designers to improve the performance of the antenna from the WBAN perspective.

$$E_{net} = E_1 + E_2 \tag{4.13}$$

$$E_1 = E_o e^{-j(kr)} \tag{4.14}$$

$$E_2 = \Gamma E_1 \tag{4.15}$$

$$E_{net} = E_o e^{-j(kr)} + \Gamma E_o e^{-j(kr+2\beta h)} \tag{4.16}$$

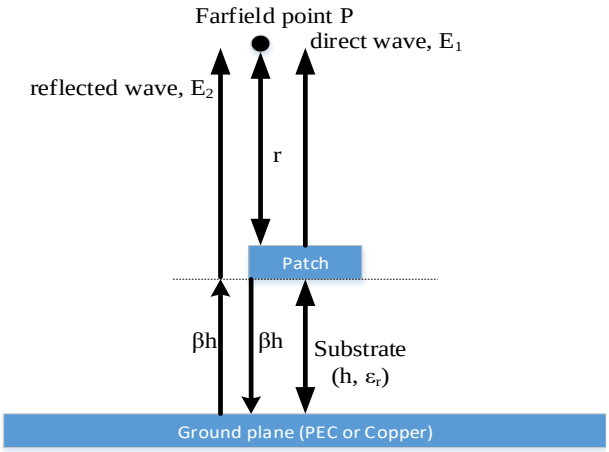

Figure 4.6 Electric field from patch antenna resolved into a direct wave and reflected wave due to ground plane [βh is the electrical length from the patch to the ground plane, E_1 and E_2 represents direct and reflected electric fields]

An FDTD setup to get, reflection phase of an EBG cell is shown in Figure 4.7. The boundaries of the EBG cell is terminated with unit cell boundary condition (UC-BC), and TE/TM wave is incident on the surface of the cell. The reflected wave is collected in the observation plane and plotted against frequency to obtain the reflection phase. In this dissertation, we have kept the excitation plane at a height, equal to the separation distance of the EBG surface and an antenna.

The reflection phase plot of the mushroom cell in Figure 4.1 with dimension 14.8*14.8 mm^2 and designed on a substrate RO4350B of h = 1.524mm and ε_r = 3.66 is shown in Figure 4.8(a). The point 'a' in the plot signify in-phase reflection frequency. In general, the bandwidth of an EBG unit cell in the reflection phase diagram is the range of frequency covered between ±90^o represented by points 'b,' and 'c' in Figure 4.8 (a). Moreover, Figure 4.8(b) shows the reflection phase plots for the EBG unit cell in Figure 4.3(a) under x- and y-polarized EM wave. It is evident from the plots in Figures 4.5(b) and 4.8(b) that they possess remarkable resemblance. It proves the appropriateness of our proposed lumped model. We can also conclude from the lumped model and reflection phase plot that in-phase frequency and stop-band frequencies are equivalent.

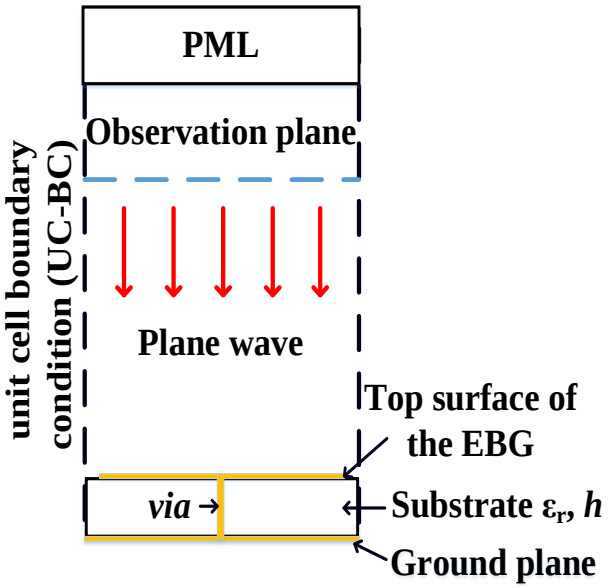

Figure 4.7 FDTD model to get a dispersion diagram of a unit mushroom cell

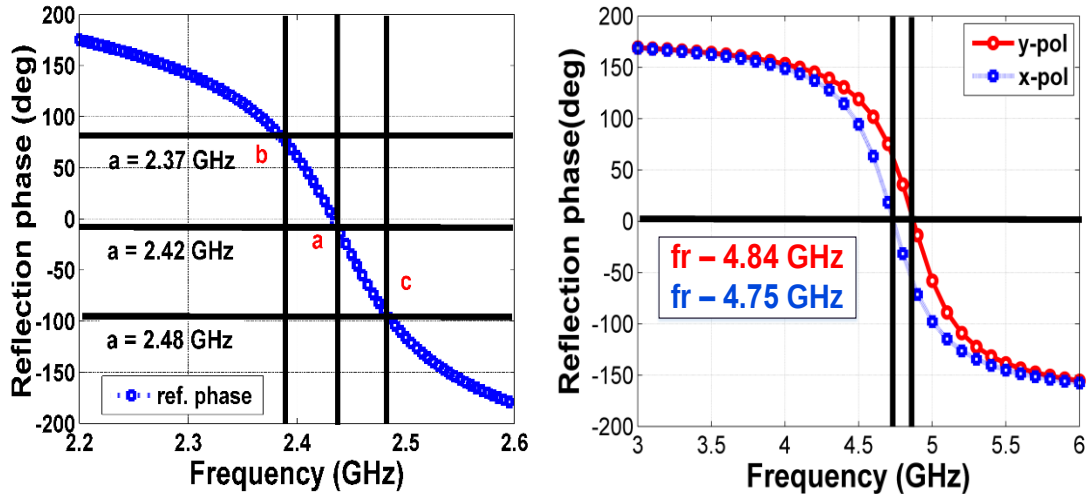

(a) (b)

Figure 4.8 Reflection phase diagrams (a) mushroom EBG cell (b) Fork-shaped EBG cell

4.1.4 Dispersion Model

A graphical plot between the wave number in a periodic structure and frequency is known as the dispersion model [48]. The dispersion diagram displays a band-gap of a periodic structure. In general, the FDTD model shown in Figure 4.7 is used to extract the dispersion diagram. The only difference is that instead of UC-BC, periodic boundary condition (PBC) is used. Besides, the computation domain is truncated by periodic boundaries given by (4.17).

$$k_{xn} = k_x + n\frac{2\pi}{p} \tag{4.17}$$

Here k_{xn} is the propagation constant along the x-axis in a periodic structure, k_x is the propagation constant of the unit cell, and p is the periodicity of the unit cell. Instead of simulating a vast number of EBG cells to display band gap periodic boundaries along x-and y-axes, these can be achieved through Brillouin's irreducible triangle [48] shown in Figure 4.9(a). It has a more significant implication as it reduces the time consumed and also space requirements primarily. The computation domain is truncated by PML boundaries such that no waves are scattered and alters the result.

Figure 4.9(b) depicts the dispersion diagram for a mushroom cell for the dimensions and substrate parameters given in section 4.1.3. The band-gap for mushroom exists at 2.35 GHz to 4.5 GHz.

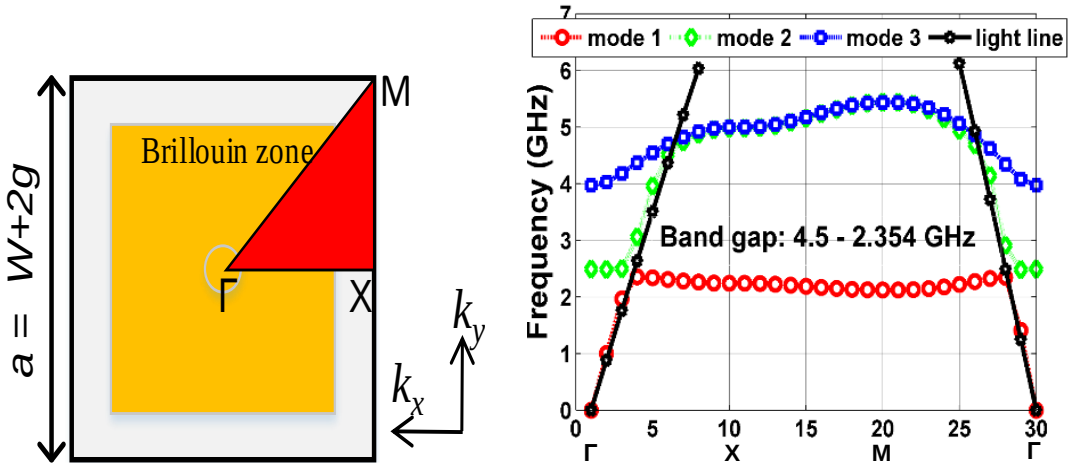

(a) (b)

Figure 4.9 (a) Brillouin irreducible triangle in a mushroom unit cell with propagation constants k_x and k_y (b) Dispersion diagram of a mushroom cell (Γ, X, and M represents the Brillouin zone)

4.1.5 Transmission Characteristics

It is another method (more practical) to obtain a band-gap of an EBG surface. The physical realization of the band-gap of an EBG unit cell can be done by designing an array at the bottom and transmission line of 50Ω at the top. The band-gap region is exhibited by transmission characteristic, S_{21}, of the fabricated prototypes. For this, the device under test (DUT, an array of EBG unit cells) is connected to two ports of a VNA. For an arbitrary power fed to any of the ports, the measured S_{21} at the other port results in the band-gap of an EBG array. If the measured and the simulated S_{21} of the EBG array matches with the band-gap of the unit cell, it justifies the design. Moreover, the band-gap in the desired range also suggests that no or very less propagation of surface waves along the substrate. It implies less diffraction at the edges of a PCB and reduced back lobes.

A prototyped array of 3x5 unit cells of mushroom is shown in Figure 4.10(a).

The dimensions used here are identical to those used in section 4.1.3. The back of the PCB is printed with a 50Ω transmission line and soldered with two SMA connectors, as shown in Figure 4.10(b). The simulation setup is identical to the measurement one with the only difference of waveguide port used to feed the array. The simulated and measured results of the array are shown in Figure 4.10(c). In general, the suppression level of -20dB is considered very good for eradicating surface waves. It is apparent from the plots in Figures 4.9(b) and 4.10(c) that the band-gap of the array is smaller than the individual unit cell. It is since the band-gap obtained in previous sections assumed periodic boundary conditions of the unit cell till infinity. However, validation of band-gap is performed with a limited number of cells (here 3x5). It leads to an eventual reduction in the band-gap.

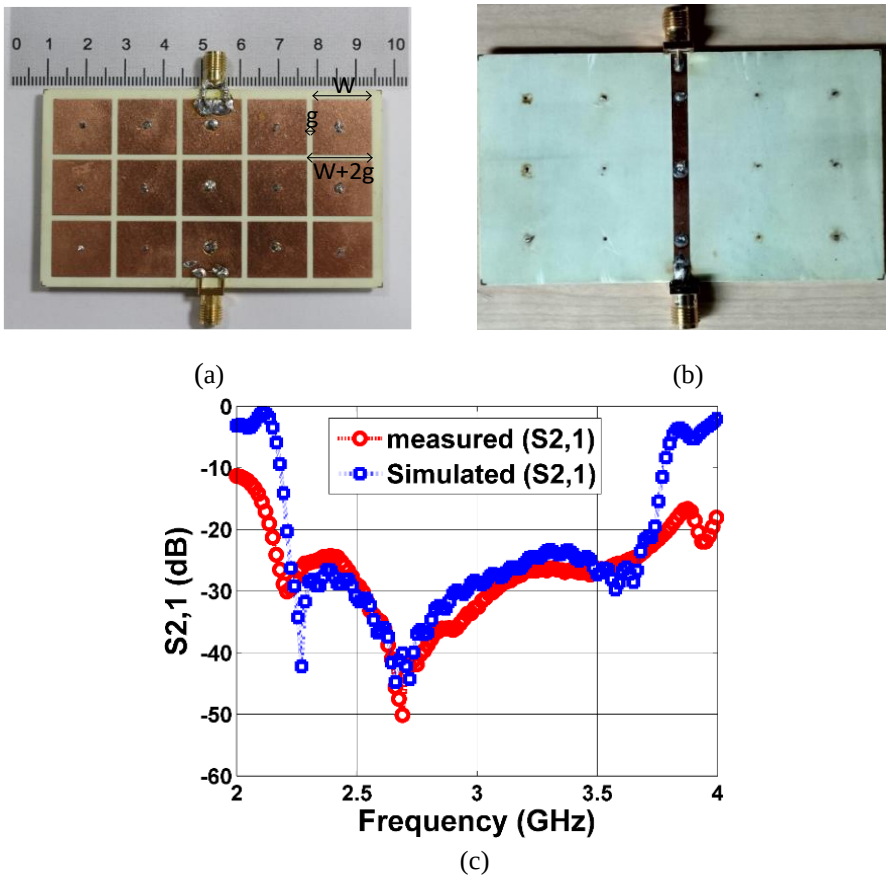

Figure 4.10 (a) Fabricated prototypes of 3x5 EBG unit cells on 1.524 mm thick Roger (b) A 50Ω transmission line at the bottom (c) Measured and simulated S_{21} of mushroom array

The existence of band-gap in the presence of the EBG surface indicates no or very less propagation of surface waves along the substrate. It further leads to very less diffraction of surface waves at the edges of the PCB. From the WBAN perspective, this scenario helps to reduce back lobes from an antenna due to a smaller ground plane. Ultimately, the absorption of EM waves (SAR) by the body in the presence of a body-worn antenna nearby reduces.

In this context, several antennae for smart-watch application has been proposed. For example, in [116], a compact and low profile inverted F antenna has been designed at 2 GHz, to study the SAR performance on a flat and wrist phantom filled with homogenous equivalent body tissue. The SAR value on flat phantom is more than 1W/kg, and because the antenna resonates at 2 GHz, the SAR value must increase at higher frequencies such as Wi-Fi and medical body area network (MBAN). A compact ultra-wideband diversity antenna designed in [117] shows promising results in terms of isolation among the antenna elements. However, this design has a disadvantage that return loss and gain have been simulated for antenna placed at the height of 15 mm that too in the air from the human equivalent flat phantom of the wrist, which is impractical in general use. Copper tapes on the rubber belt of a smart-watch used to design an antenna for cellular communication in [118] have a large footprint, and the radiating surface is exposed to the environment that makes it prone to change in performance with external force. Moreover, the radiation efficiency of a mere 23% can be achieved for on-body simulation with such an arrangement. An antenna integrated into the metal frame in [119] has a compact size and low profile due to a longer resonant path at 2.4 GHz. Nevertheless, the gain and efficiency of the antenna degrade substantially to -0.89 dBi and 26% respectively on flat wrist phantom. It shows the detuning effect of the body is prominent in this design and can't be employed in practice. Moreover, the simulations have been performed, keeping a space of 3 mm to separate the antenna from the skin in air. In [120], a monopole antenna for smart-watch has been designed to study SAR distribution on flat and wrist phantoms. The SAR value at these locations at 2.45 GHz is as high as to damage the adjacent cells in general. It is apparent from the reports given above that though

compactness and low profile nature can be achieved by monopole antennas to be fit into smart-watches. However, a strong detuning effect in the presence of the body worsens radiation efficiency, gain, and SAR values. Therefore, sound isolation is needed to overcome body effects for the proper functioning of the antenna in smart-watches. These parameters can be improved significantly by incorporating EBG surfaces in the ground plane of the antenna substrate [50], [93], [129]-[130].

A circular EBG incorporated PIFA operating at the Wi-Fi band in [129] has a compact shape suitable to fit into a smart-watch. However, simulation results for antenna placed on flat wrist phantom show that gain and radiation efficiency of just 2 dBi and 40% respectively can be obtained from the design. A low-profile Meta surface backed monopole antenna designed in [38] shows a better gain and SAR values of 5.9 dBi and 0.8 W/kg, respectively for on body simulation. However, the unit cell of EBG itself has a dimension of 27 x 16 mm^2 and having an array of 2x2 cells as a reflector, the overall size at 2.45 GHz becomes 62 x 42 $mm^{2,}$ which is inconsistent with the smart-watch dimension. Till this point, the smallest antenna operating at 2.45 GHz with EBG backing is 38 x 38 mm^2 [130] with a unit cell dimension of 15.5 x 15.5 mm^2. Though the proposed antenna has a directivity of 6.1 dBi, the design suffers from low efficiency and gain of 45% and 2.7 dBi, respectively.

In this chapter, therefore, we propose the designs of miniaturized EBG backed monopole antenna with excellent performance operating at the MBAN band, to advance the state-of-the-art significantly. The overall dimension of 36 x 38 x 3.12 mm^3 for the proposed antenna with a unit cell dimension of 14.3 x 14.5 mm^2 is consistent with the dimension of most of the smart-watches present today. The proposed design is a threefold step, namely miniaturization of state-of-the-art EBG unit cell, design of array reflector consisting of 2x2 unit cells, and incorporation of monopole antenna with the proposed EBG reflector for performance enhancements.

4.2 IDE Unit Cell

In this section, we present an interdigital EBG (IDE) unit cell, as shown in Figure 4.11. Unlike the conventional interdigital geometry, it consists of interconnection among the adjacent fingers marked by blue and red boxes in Figure 4.11. The dimensional parameters of the unit cell are *W*: width of the unit cell, *g/2*: gap on either side of the patch, l_f, and w_f : length and width of the fingers in the middle, g_f : gap among the fingers and also gap among the fingers and base strip = 0.4 mm, $l_f + g_f$: length of the finger from the base strip, l_b, and w_b: length and width of the base strip, l_a, and w_a : length and width of the additional strip for interconnection, l_{bf} : length of the strip from the base to the bottom of the strip for interconnection on either side. We have kept a gap g_f of 0.4 mm due to in-house fabrication tolerance.

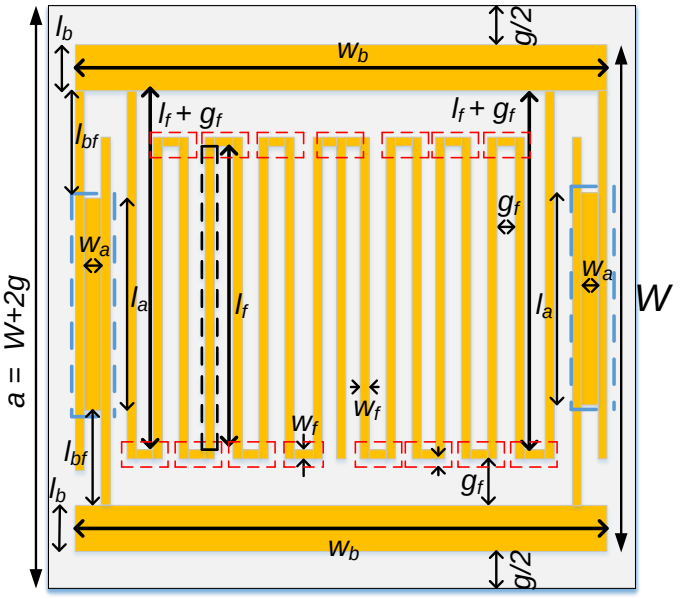

Figure 4.11 The geometry of the IDE unit cell with interconnects shown in colored boxes

4.2.1 Lumped (LC) Circuit Modelling

The circuit modeling approach adopted here makes use of the surface waves generated on a metal surface for an incident EM wave (polarized along either *x*- or *y*-

axes), as discussed in section 4.1. Surface waves are surface currents (AC) at high frequencies and flow through the metallic strip [42] – [43]. Therefore, the strips through which the surface current flows imitate as an inductor in the lumped circuit model. The gap among the adjacent cells along *x*-and *y*-axes forms edge coupling capacitors (ECCs) dependent on the polarization of the EM wave. For example, the flow of surface current along with the fingers of the IDE unit cell for a *y*-polarized incident EM wave is shown in Figure 4.12(a). Due to the symmetrical nature of the unit cell about the *y*-axis, the surface current divides equally at the base strip and flows until reaching the strip in the middle. The surface current flows in series, leading to an increase in the overall inductance of the unit cell. It is due to the interconnection of the adjacent strips and last fingers on either side shown in dotted red and blue boxes in Figure 4.11.

In this design, the whole arrangement of inductors is connected in series with ECCs to complete the equivalent circuit model of the unit cell. In the proposed approach of equivalent circuit modeling, the dimension parallel to the electric field forms the length, i.e., l_{s1}, l_{s2}, ... l_{s7} and the dimension orthogonal to the electric field form width, i.e., w_{s1}, w_{s2} ... w_{s6}. For a *y*-polarized EM wave, the modified dimension of the unit cell, considering the above aspect is depicted in Figure 4.12(b). Subsequently, the distribution of strip inductances L_{s1}, L_{s2} ... L_{s7} distributed all along the fingers of the unit cell is shown in Figure 4.12(c). Equation (4.18) relates L_{s1} formed by the metal surface of the respective length and width of l_{s1} and w_{s1} [25]. Here, k_g is the correction factor given by (4.19). Here, h is the height of the substrate. Subsequently, inductances L_{s2} ... L_{s7} can be evaluated by substituting corresponding lengths and widths of the strips in (4.18) and (4.19).

$$L_{s1} = 0.25\times10^{-7}\times l_{s1}\left(\ln\frac{l_{s1}}{w_{s1}} + 1.193 + 0.25\frac{w_{s1}}{l_{s1}}\right)k_g \tag{4.18}$$

$$k_g = 0.57 - 0.145\ln\frac{w_{s1}}{h} \tag{4.19}$$

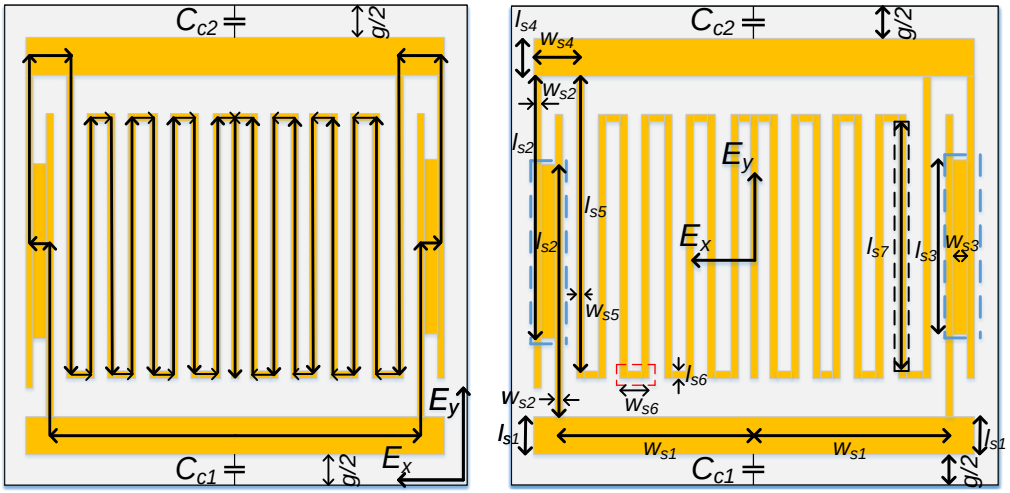

(a) (b)

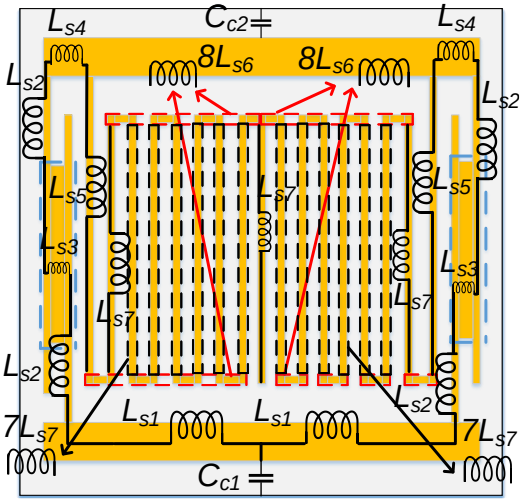

(c)

Figure 4.12 (a) Flow of surface current along the strips for a *y*-polarized EM wave [C_{c1} and C_{c2} are two edge coupling capacitance], (b) Modified dimension of the unit cell based on the polarization of EM wave, (c) Formation of inductances and coupling capacitances in the unit cell

Unlike the geometry of [93] that results in the formation of static capacitances between the fingers and the base strip, here, the continuity in surface current through the strips discards the formation of static capacitances. The inductances formed by red and black boxes, L_{s6} and L_{s7}, add eight and seven times, respectively, as shown in

Figures 4.12 (b) and (c). The resulting inductors are connected in series with coupling capacitors, as shown in Figure 4.13. Moreover, the top (patch) and bottom surfaces (ground) of the EBG cell are metal separated by a dielectric layer and thus form capacitance C_{pg}, as shown in the circuit model.

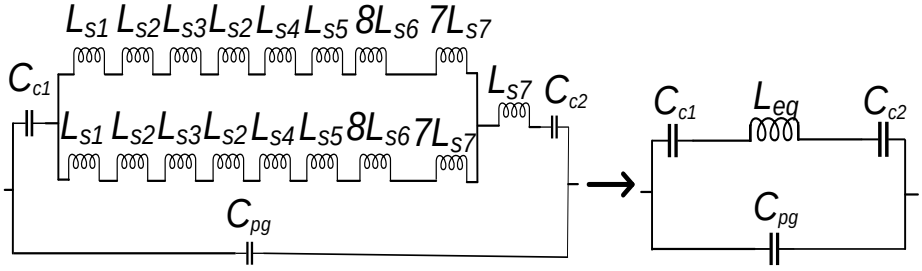

Figure 4.13 Equivalent circuit model of the unit cell consisting of strip inductances connected in series with two ECCs [L_{eq} is the net inductance of the circuit]

Subsequently, the total inductance L_{eq} in Figure 4.13 can be used to express the net impedance of the equivalent circuit Z_{eq} in (4.20). Then we deduced the stop-band or resonant frequency of the equivalent circuit, in (4.21), by equating the denominator of (4.20) to 0. It is important to note that only C_{c1} is mentioned in the expressions because both the capacitances are equal, and the use of any one of them is acceptable. Furthermore, the capacitance C_{pg} between patch and ground can be given by (4.22). Here, h and ε_r are the height and dielectric constant of the substrate, and A is the area of the unit cell.

$$Z_{eq} = \frac{2 - \omega^2 L_{eq} C_{c1}}{j\omega\left(2C_{pg} + C_{c1} - \omega^2 L_{eq} C_{c1} C_{pg}\right)} \tag{4.20}$$

$$f_r = \frac{1}{2\pi}\sqrt{\frac{\left(2C_{pg} + C_{c1}\right)}{L_{eq} C_{c1} C_{pg}}} \tag{4.21}$$

$$C_{pg} = \varepsilon_o \varepsilon_r \frac{A}{h} \tag{4.22}$$

As a design example, an IDE unit cell is designed on Roger 4350B with a dielectric constant of 3.66 and a height of 1.524 mm. The optimized dimension of the unit cell to get the desired resonant frequency at 2.4 GHz is 14.3 mm x 14.5 mm. The ECCs play a crucial role in controlling the resonant frequency of the unit cell and is given by (4.6) [128]. Table 4.1 lists all the circuit parameters and their corresponding strip inductances and coupling capacitances for the gaps of 0.4mm. However, as evident from (4.23), for a fixed width of the unit, cell ECC depends only on *g* between the adjacent cells; therefore, three other widths 0.5, 0.6, and 0.7 mm has also been used to obtain the resonant frequency of the unit cell keeping all other parameters intact.

$$C_{c1} = C_{c2} = \frac{17 \times W \times \varepsilon_O \times (\varepsilon_r + 1)}{\pi} \times \cosh^{-1}\left(\frac{W+g}{g}\right) \qquad (4.23)$$

Table 4.1 IDE Unit Cell Parameters

Parameter	Value (mm)	Parameter	Value
l_{s1}	1.05	L_{s1}	0.01 nH
w_{s1}	6.10	L_{s2}	1.00 nH
l_{s2}	10.9	L_{s3}	0.75 nH
w_{s2}	0.30	L_{s4}	0.02 nH
l_{s3}	10.0	L_{s5}	1.28 nH
w_{s3}	0.40	L_{s6}	3.8e-3 nH
l_{s4}	1.05	L_{s7}	1.00 nH
w_{s4}	1.70	$C_{c1} = C_{c2}$ (g = 0.4mm)	1.63 pF
l_{s5}	11.7	$C_{c1} = C_{c2}$ (g = 0.5mm)	1.53 pF
w_{s5}	0.30	$C_{c1} = C_{c2}$ (g = 0.6mm)	1.47 pF
l_{s6}	0.30	$C_{c1} = C_{c2}$ (g = 0.7mm)	1.40 pF
w_{s6}	0.40	f_0 (g = 0.4mm)	2.40 GHz
l_{s7}	10.9	f_0 (g = 0.5mm)	2.46 GHz
w_{s7}	0.30	f_0 (g = 0.6mm)	2.51 GHz
		f_0 (g = 0.6mm)	2.55 GHz

The values of strip inductances and coupling capacitances can be determined from (4.18), (4.19), and (4.23). Moreover, expression (4.22) results in capacitance, C_{pg} of 4.4 pF. The listed values of dimensions and L and C in Table 4.1 are optimized for achieving resonance at 2.4GHz. These values might change slightly during full-wave analysis, and if they do not, then this proves the accuracy of our proposed equivalent circuit model. The plot in Figure 4.14 depicts resonant/stop-band frequencies of the unit cell for varying gaps listed in Table 4.1. Only a gap width of 0.4 mm among the unit cells is capable of achieving desired resonance in the MBAN band.

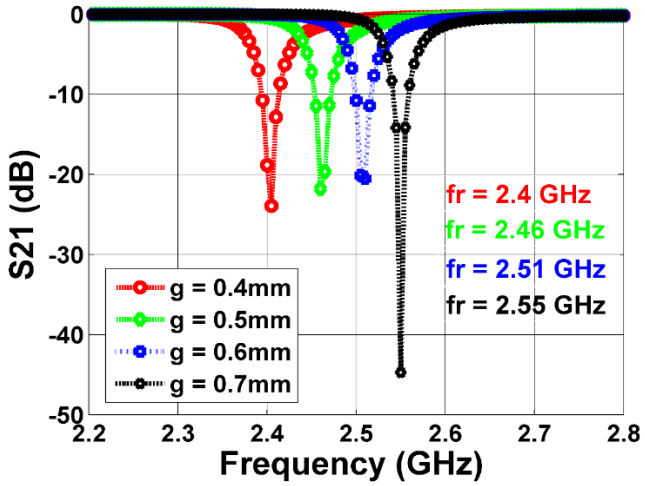

Figure 4.14 The resonant frequencies of the IDE unit cell for the proposed equivalent circuit model (Figure 4.13) and the dimensions in Table 4.1

It appears from the above theory that the influence of the gap among the interdigital elements on resonant frequency is negligible. However, it does vary substantially because the number of fingers varies if the gap between the fingers is varied for a fixed dimension of the unit cell. For example, in the present case, if the gap is more significant than 0.4 mm, say 0.55 mm, the number of fingers to be accommodated on either side change to 6 ($7L_{s7} \rightarrow 6L_{s7}$). While most of the circuit parameters in the equivalent circuit remain, the same, L_{s4} and L_{s6} (3.2e-3 nH) vary slightly. The plot in Figure 4.15 shows the significance of interconnection and the number of adjacent fingers on the resonant frequency. It can be inferred that the

resonance frequency increases by 120 MHz, with the reduction of finger counts from 7 to 6.

Furthermore, the opposite effect can be expected if the *g* between the fingers is reduced. It explains the selection of an optimum number of fingers for any dimension to obtain a stop band in the MBAN range is tricky. It is essential to note that the *g* has been kept at 0.4mm due to the limitation of our in-house fabrication facility.

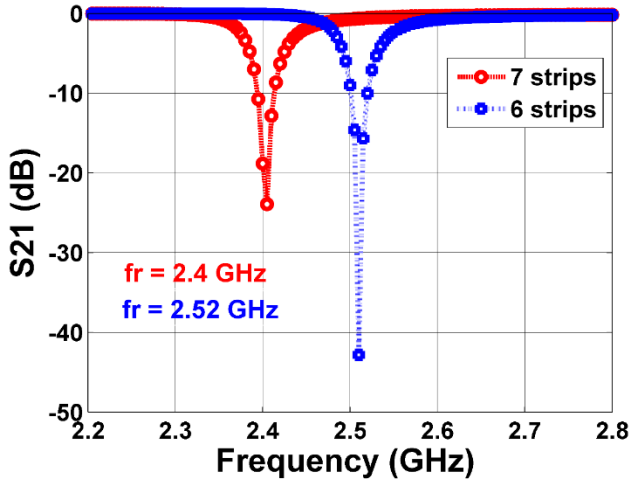

Figure 4.15 Resonant frequency of the unit cell for 7 and 6 connected strips/fingers

4.2.2 Reflection Phase, Band-gap, and Polarization Stability

The reflection phase ϕ in terms of Z_{eq} and intrinsic impedance of space (η) are related as given by (4.24) [45]. Now we plot the reflection phase diagram of the unit cell for the parameters in Table 1 and (4.24), as shown in Figure 4.16 (a). Furthermore, to validate the proposed technique of modeling the IDE unit cell, the resonant frequencies for different gap widths in Table 1 are plotted by full-wave analysis using CST and is depicted in Figure 4.16 (b). The unit cell's dimension and substrate details are identical to that in section 4.2.1.

$$\phi = \mathrm{Im}\left\{\ln\left(\frac{Z_{eq}-\eta}{Z_{eq}+\eta}\right)\right\} \tag{4.24}$$

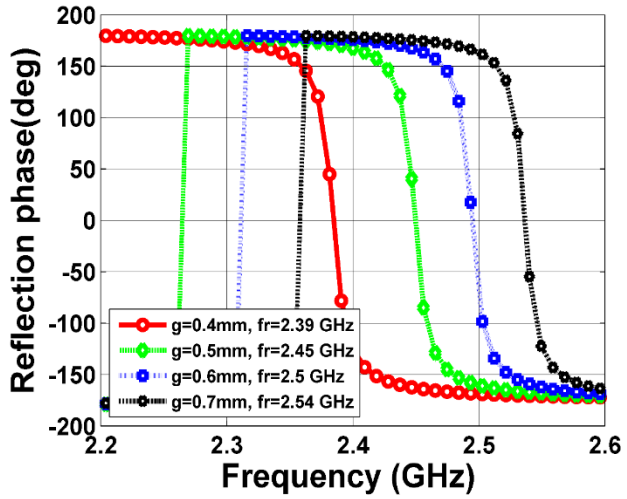

(a)

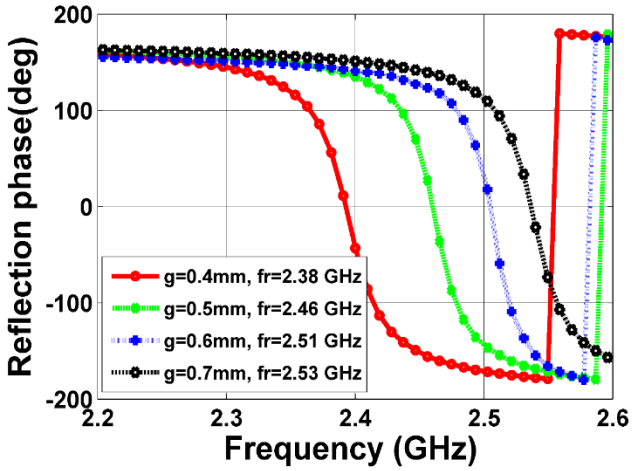

(b)

Figure 4.16 Reflection phase results of the unit cell (a) Obtained from the equivalent circuit model (b) Obtained from CST transient solver

It is apparent from the plots in Figures 4.16 (a) and (*b*) that they possess good resemblance between them, and this proves the appropriateness of the proposed model. Once again, the only *g* of 0.4mm satisfies the desired stop-band frequency at 2.4 GHz. It is also important to mention that the excitation plane for the plane wave incidence is set at a height of 1.524 mm above the unit cell's surface to record the reflection phase data. It is because the height of the antenna above the EBG base is 1.524 mm,

as discussed in section 4.1. For the effective operation of an EBG surface, the bandwidth is measured between ± 90^{o} of the reflection phase plot, as we discussed in section 4.1 [26]. Evidently from the plots in Figures, 4.16 (a) and (b) *g* of 0.4mm essentially covers the MBAN region here. It is apparent from Figure 4.16(b) that the bandwidth of the IDE unit cell obtained from the full-wave analysis is smaller than that proposed in [39]. It is because the bandwidth is inversely proportional to the capacitance developed between the patch and ground plane, as we saw in section 4.1. Capacitance, in turn, depends on PCB thickness, which is 1.524mm for the present case and 5mm in [39]. Therefore, due to the smaller thickness, the capacitance of the proposed IDE cell is more considerable than the [39], and consequently, the bandwidth is smaller. It has been shown later in the chapter that the proposed unit cell, when incorporated with a monopole antenna, can enhance its performance in this range.

Although we have maintained the uniformity in the dimension of the unit cell while achieving the desired result, still symmetricity is slightly compromised along the longitudinal dimension to adjust the resonant frequency. It introduces a slight asymmetry in the design of the unit cell. Hence to test the polarization stability of the IDE unit cell, it is excited by an *x*- and *y*-polarized TEM wave, and reflection phase data are recorded as shown in Figure 4.17 while keeping all other parameters intact for the *g* of 0.4 mm. It is clear from the plots that the unit cell shows excellent resistance to phase change for polarization variation even in the presence of asymmetry.

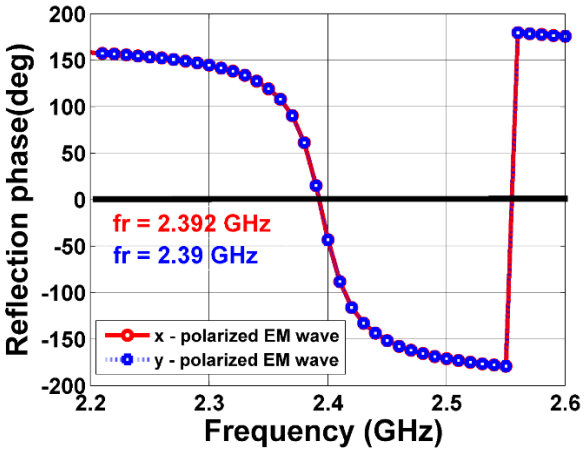

Figure 4.17 Reflection phases of the IDE unit cell for an *x*-and *y*-polarized EM wave

Furthermore, we have also checked the polarization sensitivity of the unit cell to obliquely incident TM and TE wave. For this, TM and TE wave at 0^o, 15^o, 30^o, 45^o, and 60^o is incident on the IDE unit cell, and reflection phase data are plotted in Figures 4.18 and 4.19. The need for such an investigation is because TM waves are the fundamental mode of propagation, and the distance by which the antenna is separated from the EBG base is minimal that might induce TE modes as well. Moreover, separation of the EBG base of 1.524 mm from the antenna does not lie in the far-field region. It implies that the angle at which the TM and TE waves are falling on the EBG base, originating from a patch antenna, may not be 0^o. It is pertinent to mention that the *g* among the unit cells is kept the same at 0.4mm for all the incidence angles. The results in Figures 4.18 and 4.19 convey that the IDE unit cell demonstrates a stable phase relationship for all incident angles of TM and TE wave with complete MBAN coverage with some Wi-Fi band as well.

An important aspect to note is the seemingly distinct look of the reflection phase plots in Figures 4.16(b), 4.18, and 4.19, even though they are for the same unit cell. The difference is natural as the former is for transient domain solver (TDS), the latter is for the frequency-domain solver (FDS), and the boundary conditions for both the techniques are different. For example, the TDS uses magnetic and electric boundaries along *x*-and *y*-axes, whereas, under FDS, the unit cell is simulated under unit cell conditions along *x*-and *y*-axes. The bandwidth, frequency range between $\pm 90^o$ in the reflection phase plot, in both the plots are different. The FDS gives bandwidth for an infinite series of unit cells, whereas TDS gives a bandwidth of a finite dimension unit cell, which is more general.

In addition, the reflection phase of the circuit model does not incorporate the surface wave propagation as it assumes an ideal scenario in which EBG cell acts as a perfect band-stop filter. However, frequency and transient domain solver incorporates the accurate boundaries in case of an infinitely long unit cell or unit cell with finite counts. Due to the presence of surface waves (although less), mutual coupling among the unit cells comes into the effect. The mutual coupling among the unit cells results in a relatively slower change in reflection band than the circuit model which completely ignores it.

To qualify the proposed interdigital structure as a band-gap surface, the dispersion diagram depicted in Figure 4.20 for the given dimension and *g* in Table 4.1 of the unit cell has been obtained through CST solver. Three consecutive modes, mode 1, mode 2, and mode 3, along with the corresponding band-gap, suggest that there is a specific region of surface wave suppression between fundamental (mode 1) and next to fundamental mode (mode 2) effectively covering the MBAN. In the absence of surface waves along the substrate, the diffraction at the edges is minimal. Therefore, it reduces back lobes of an antenna and improves the front to back ratio.

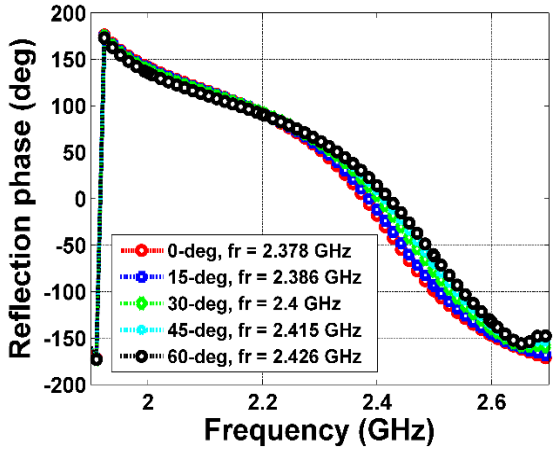

Figure 4.18 Reflection phases of the unit cell for TM wave incidence at 0º, 15º, 30º, 45º, and 60º

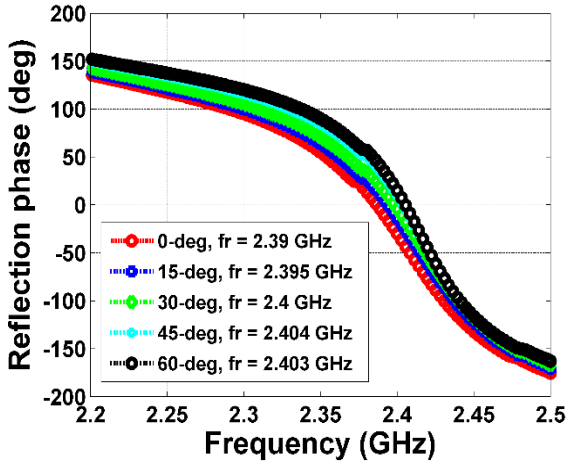

Figure 4.19 Reflection phases of the unit cell for TE wave incidence at 0º, 15º, 30º, 45º, and 60º

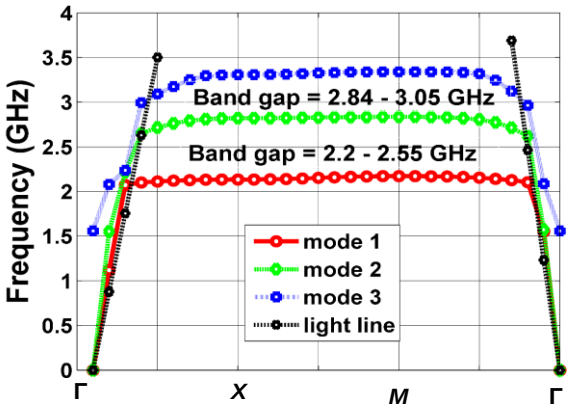

Figure 4.20 Band-gap diagram of the IDE unit cell [Γ, X, and M are points in the Brillouin zone]

We have presented a comparison between the proposed IDE unit cell and the current state-of-the-art in Table 4.2. It is apparent that the IDE cell significantly advances the current state-of-the-art. The size of the proposed unit cell is the smallest of the known works. Besides, the via-less structure also reduces the design complexity when compared to [93].

Table 4.2 Comparison of the Proposed IDE-EBG Cell with State-of-the-Art EBG Cells at MBAN and ISM band

Ref.	Frequency (GHz)	Footprint (lxb) (λ_o^2)	gap (mm)	ε_r	Band-gap (GHz)
[34]	2.45	0.153	2.00	1.70	-
[36]	2.43	0.065	-	3.00	-
[131]	2.45	0.047	2.50	2.20	-
[39]	2.45	0.044	2.53	3.20	-
[38]	2.45	0.028	2.15	3.00	0.10
[89]	2.46	0.027	1.00	2.00	-
[37]	2.45	0.025	1.80	2.50	-
[90]	2.45	0.024	1.50	3.00	-
[130]	2.44	0.024	0.20	4.40	-
Prop. IDE cell	2.38	0.013	0.40	3.66	0.35

4.3 Array of 2x2 unit cells

In this section, we design an array of 2x2 IDE unit cells, as shown in Figure 4.21, to act as a reflector for an antenna and enhance its performance. The unit cells are arranged periodically in a way such that the desired reflection phase and surface wave rejection can be achieved in the MBAN frequency range. The reason for limiting the array size is that the overall size of the incorporated antenna has been chosen as 38 x 38 mm^2 [130]. The unit cells are placed symmetrically over the substrate while keeping an identical distance from the substrate edges, keeping the spacing amongst the unit cells (g) of 0.4 mm. A parametric study is performed on gap g_2 while keeping gap g_1 fixed to 4.3 mm to obtain a reflection phase diagram covering the entire MBAN. The optimum parameters of the array for the desired reflection phase are g_1 = 4.3 mm, and g_2 = 3.5 mm. Therefore, the array along the x-axis can be reduced by 2 mm, and then the overall dimension becomes 36x38 mm^2.

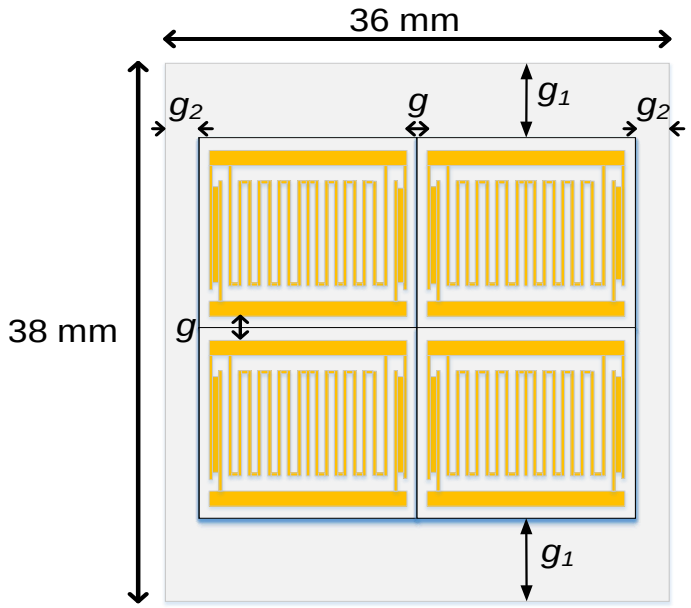

Figure 4.21 Array of 2x2 EBG unit cells [g_1 = 4.3 mm, g_2 = 3.5 mm, g = 0.4 mm]

For a y-polarized TEM wave incident from a height of 1.524 mm above the EBG surface, the reflection phase is plotted in Figure 4.22. It can be seen that the reflection

phase plot for the array mentioned above size covers the MBAN region for a gap, *g*, of 0.4 mm under the condition mentioned in section 4.2.2.

The surface wave rejection ability of the array is an essential facet in terms of demonstrating band-gap. For this, we have used the setup explained in section 4.1 to obtain transmission characteristics. A 50 Ω line has been printed in the ground plane without altering the top layer. In this case, the width of 50 Ω feed comes out to be 3.2 mm for the substrate; we chose to design the unit cell in section 4.2. For an input power of 0dBm fed into any of the ports, the transmitted power in the form of S_{21} is recorded at the other port. In the simulation setup, we have used waveguide port, the properties of which are determined through the inbuilt calculator in CST. The simulated received power is shown in Fig 4.23.

Furthermore, to validate, the array shown in Figure 4.21 is prototyped, and the measured result is also depicted in Figure 4.23. A perfect agreement can be seen between the measured and simulated results, and the surface rejection of -15dB can be obtained in the MBAN range. It proves the utility of the unit cell in the rejection of surface waves. The band-gap obtained in Figure 4.23 is not in agreement with the result in Figure 4.20. It is because Figure 4.20 depicts the band-gap diagram of the unit cell with periodic boundary conditions along *x*-and *y*-axes, whereas the extent of band-gap reduces substantially in practice due to the limited size of the unit cells. Simulation results for 3x2 and 4x2 array configurations are added in Figure 4.23 to highlight this aspect. Hence, it can be expected that with larger array size and more unit cells, the band-gap obtained through this phenomenon can be in perfect agreement with that of Figure 4.20. Also, Figure 4.23 includes the transmission characteristic of a single EBG unit cell. Apparently, the unit cell is unable to suppress the propagation of surface waves and hence, we need to opt for a higher configuration of unit cells like 2x2, 3x2 or 4x2 (array), etc to achieve desired surface wave suppression.

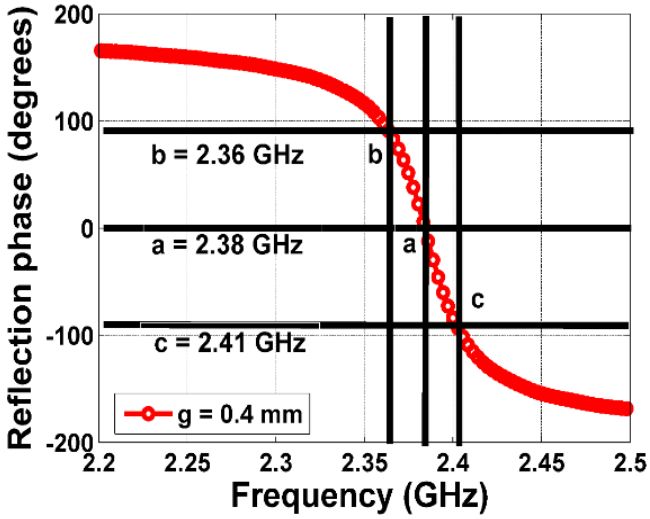

Figure 4.22 Reflection phase results of 2x2 array

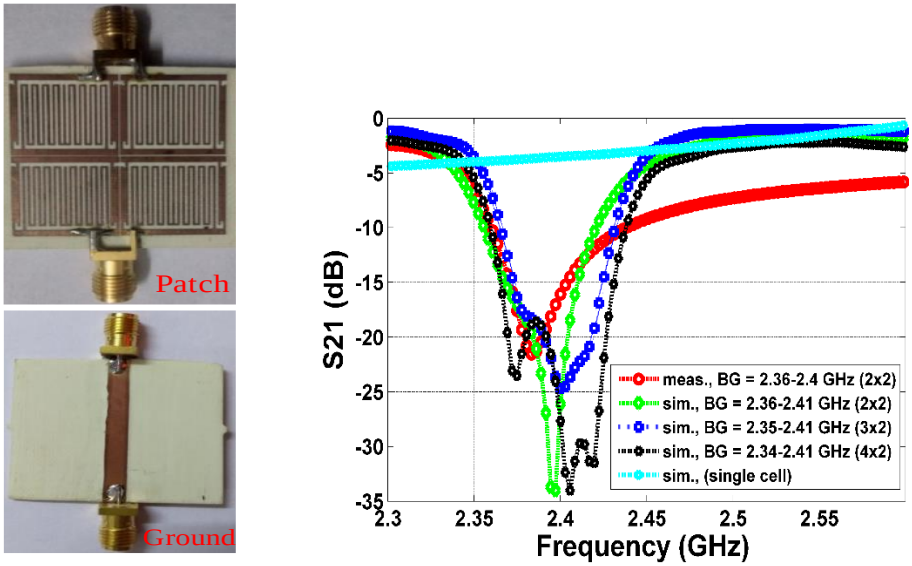

Figure 4.23 Measured and simulated transmission result of the IDE array along with the prototyped array (BG signifies Band-gap)

4.4 Integrated Monopole Antenna with EBG Array

In this section, we design an EBG array integrated antenna. For this, at first, a simple monopole antenna, as shown in Figure 4.24, is designed on the substrate RO4350B of height 1.524 mm, having a dielectric constant of 3.66. The optimized design parameters L_P, W_P, L_{gnd}, L_F, and W_F of the monopole are given in Table 4.3. We prototyped the antenna for the given dimensions in Table 4.1, as shown in Figure 4.25(a). The simulated and measured return losses are depicted in Figures 4.26. We have simulated the design in CST's transient domain solver with open-boundary conditions and frequency of operation from 1 GHz to 3.8 GHz.

Table 4.3 Design parameters (in mm) of the EBG integrated monopole antenna

L_P	W_P	L_F	W_F	L_{gnd}	L_{gap}
27.6	22	6	3	3	0.55

Subsequently, the EBG array is incorporated with the monopole antenna, as shown in Fig 4.24, to improve its performance. The prototyped EBG incorporated antenna is shown in Figures 4.25(b) and (c). We have left no gap between the array and the monopole, unlike designs [38] – [39]. For this, both the individual surfaces (monopole and the EBG array) have been attached with the help of adhesive RTV coating having a dielectric constant of 1.22. However, this leads to the formation of a gap between the layers while soldering SMA connector during fabrication. Therefore, for suitable placement of the SMA connector to the monopole antenna, it has been shifted slightly upwards by 1.5 mm. A slight shift in monopole antenna relative to the array can be observed from Figure 4.25(c).

The design parameter L_{gap} plays a crucial role in getting a good match in such a scenario. It was observed during the design process that the matching improves with decreasing L_{gap}, but the resonant frequency increases and vice-versa. Therefore, care has been taken in regulating L_{gap} to get a proper match (below -10dB) as well as desired resonance at 2.4 GHz. The optimum L_{gap} is mentioned in Table 4.3.

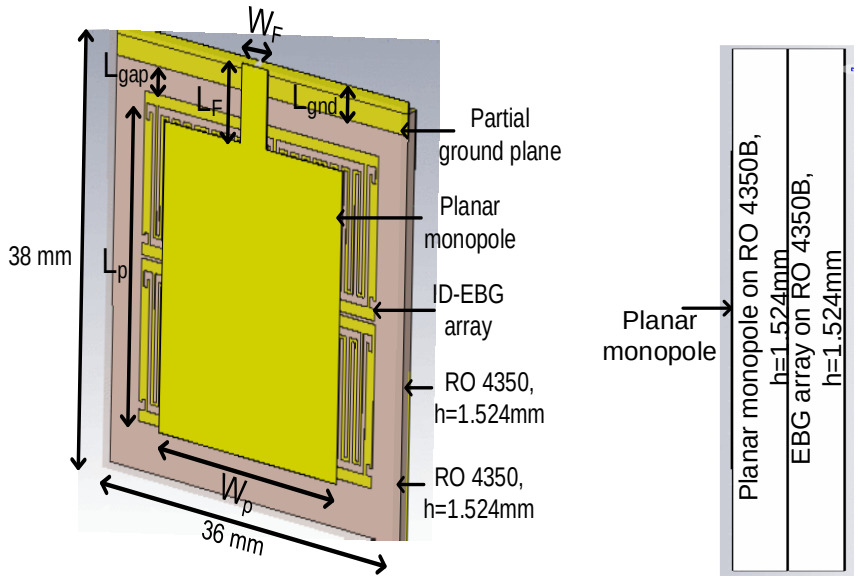

Figure 4.24 Planar monopole antenna at the top integrated with 2x2 EBG array on RO4350 B substrate

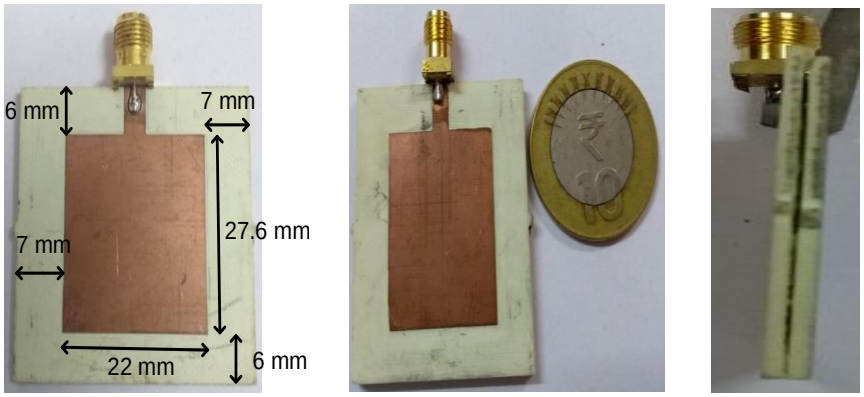

(a) (b) (c)

Figure 4.25 Fabricated IDE incorporated antenna (a) Simple monopole (b) Incorporated antenna (front view) (c) Incorporated antenna (side view)

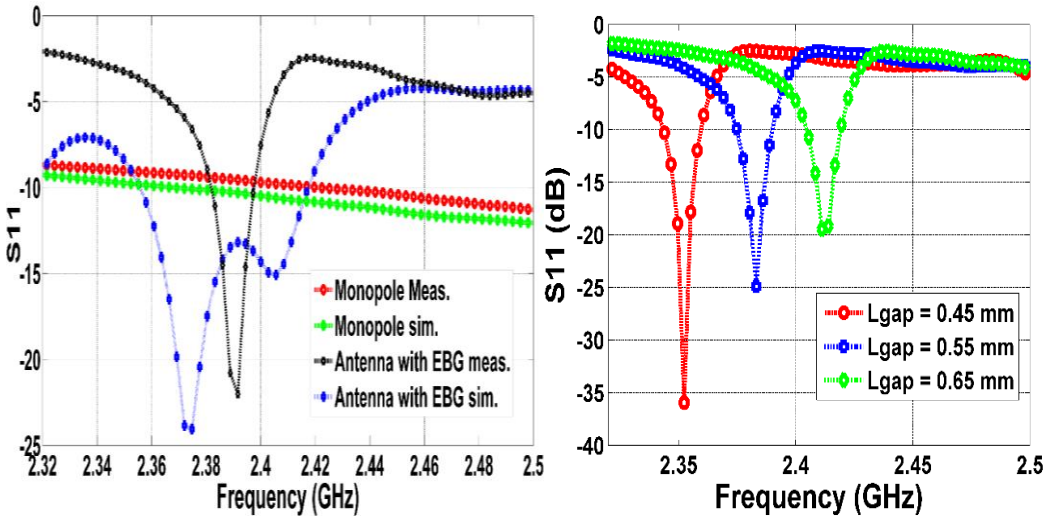

(a) (b)

Figure 4.26 (a) Simulated and measured return losses for simple and EBG incorporated monopole antenna (b) Simulated return losses of EBG incorporated antenna with variation in L_{gap}

We then simulated and measured return losses of the EBG incorporated antenna, as shown in Figure 4.26 (a). The measured return loss of the EBG incorporated monopole antenna shows better results in terms of matching and desired band coverage. It is due to the reduction in the overall quality factor of the structure from the ohmic losses in the SMA connector [38]. Figure 4.26 (b) depicts simulated return loss (dB) of the EBG incorporated antenna for three different L_{gap}. Evidently, as L_{gap} decreases the matching improves but resonance shifts to lower frequency and vice versa. The far-field radiation pattern of the integrated antenna is measured inside the anechoic chamber, as shown in Figure 4.27(a). The simulated and measured radiation patterns of the integrated antenna along *xz* and *yz* planes are shown in Figures 4.27(b) and (c). The simulation shows the possibility of a gain of 5.3 dB and the measured gains are well-matched with gains of 5.1 dB in both the planes.

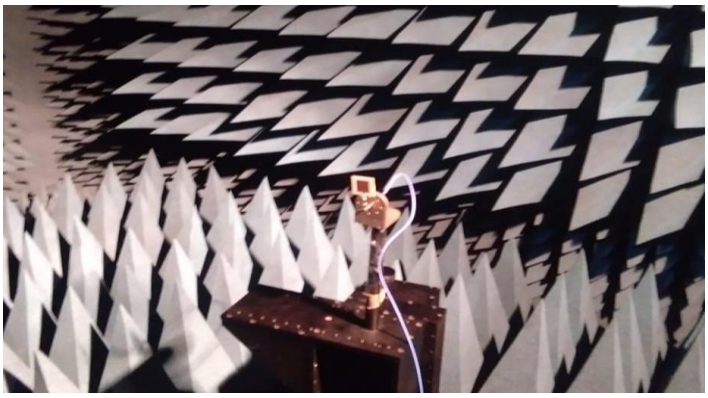

(a)

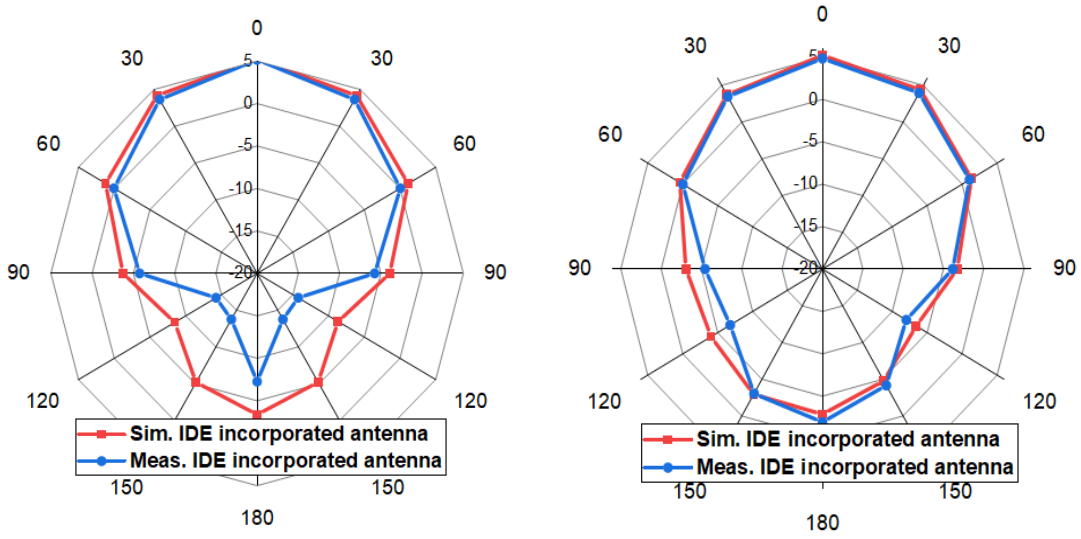

(b) (c)

Figure 4.27 (a) Radiation pattern measurement setup inside the anechoic chamber, far-field results of the incorporated antenna (b) *xz* plane (c) *yz* plane

The presence of back lobes in both simulated and measured results is due to the surface waves diffracted at the edges of the substrate of the monopole antenna. It is since the upper radiating edge of the monopole antenna is closer to the top edge by 1.5mm when compared to the bottom edge in the overall geometry, as can be seen in Figure 4.24. This anomaly eventually leads to the enhanced diffraction at the edge and hence the increased back lobe radiation. Besides, the EBG array tends to suppress

surface wave propagation through the substrate; however, due to the low level of rejection level (-15dB), surface waves still exist. It leads to diffraction at the edges and enhances the back lobes. Still, the accuracy of the radiation pattern measured in both the planes and gain enhancement fully justifies the analysis in section 4.2 and the array design in section 4.3. It is imperative to know that the proposed antenna is relatively small and achieves an improvement of gain from 2.3 dB to 5.3 dB in free space when compared to [130].

4.5 On-body Performance and SAR Analysis

In this section, we assess the performance of the EBG incorporated antenna when operated close to the body. In this context, a simulation environment consisting of partial (bottom) and a full cover of foam on EBG incorporated antenna along with the subsequent layers of the wrist phantom has been created, as depicted in Figures 4.28(a) and (b). Figure 4.28(a) mentions the electrical property and height of the respective body layers and the foam at the bottom. The overall dimension of the wrist phantom is 40 x 80 x 40 mm^3. We have left a spacing of 2 mm from the antenna edges to the foam for both the designs, as evident from Figure 4.28(a). The thickness of the foam at the bottom of the antenna is just 0.2 mm. It makes the total height of the design with full-foam cover to be 5.2 mm, as depicted in Figure 4.28(b).

The measurement setup for both scenarios is given in Figures 4.29(a) and (b). The respective sides of foam are attached, and the whole design is tied to the wrist with the help of adhesive RTV coating. The simulated and measured results for both the scenarios are given in Figure 4.30. It can be inferred that though there is a slight shift in the resonant frequency of simulated and measured results due to body loading, still, the plots are similar to that in Figure 4.26. The results convey the uniqueness of the proposed design in getting sound isolation from the body.

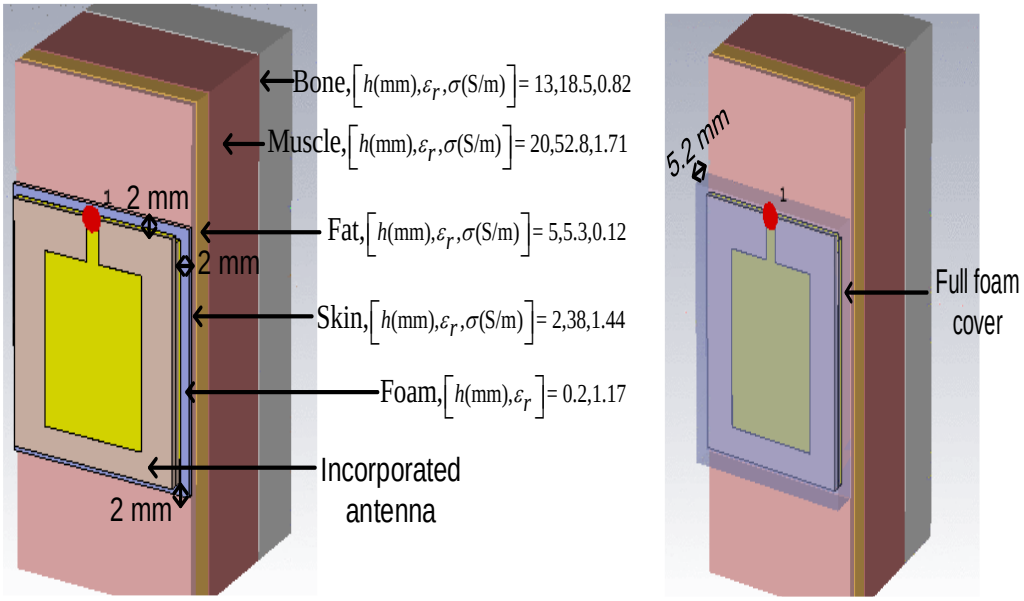

(a) (b)

Figure 4.28 A simulation environment for on-body performance analysis with flat four-layer design of the wrist (a) Partial cover of foam at the bottom of the incorporated antenna (b) Full cover of foam over the antenna

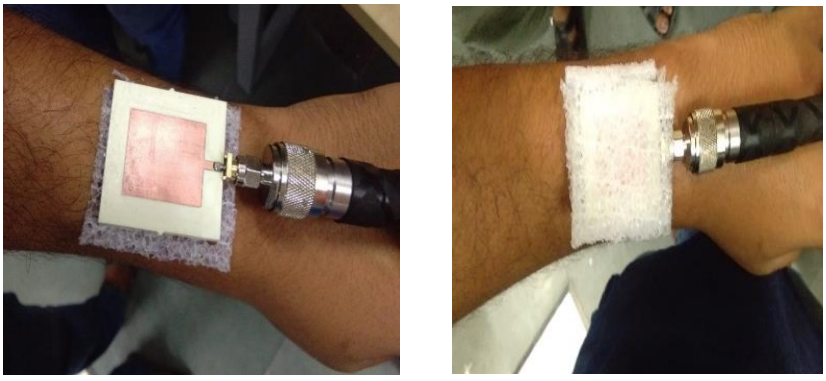

(a) (b)

Figure 4.29 Measurement setup for evaluating the return loss of the incorporated antenna (a) With foam at the bottom (b) Fully covered with foam

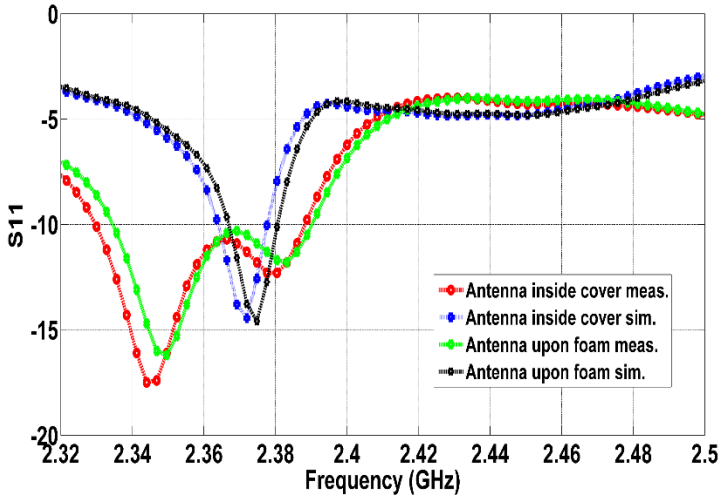

Figure 4.30 Simulated and measured return losses of the antenna with partial and full coverage on the wrist model

Next, the gain and efficiency of the foam-backed EBG integrated antenna are measured. The measurement setup inside the anechoic chamber is shown in Figure 4.31 (a). The wrist is perfectly aligned with that of a receiver antenna ($\theta = 0^o$ – co-pol), and gain is plotted between 2.3 to 2.5 GHz in Figure 4.31(b). The antenna gives a maximum measured gain of 3.7 dB at 2.4 GHz with a measured gain of 3 dB at 2.38 GHz, which is substantially higher when compared to design proposed in the literature as tabulated in Table 4.4.

Subsequently, the simulated and measured on-body efficiency of the foam-backed IDE antenna inside the anechoic chamber is depicted in Figure 4.31(c). Slight variation in simulated and measured on-body gain and efficiency of foam-backed antenna suggests that the electrical parameters, along with the respective thickness of the heterogeneous model developed for the simulation is not exact at a higher frequency. The data used for simulation are mere approximations at 2.4 GHz. However, the measured results clearly show that the proposed design with foam backing can achieve an efficiency of more than 50% for on-body measurements, and these are again a significant improvement over the reported designs. Furthermore, to compare the performance, the simulated efficiency of the simple IDE backed antenna in the air has also been shown in Figure 4.31(c). The simulated efficiencies of simple

IDE and foam-backed IDE antennas compare much more favorable than recently reported designs [38], [125]-[128], [130]. It is imperative to note that the measured efficiencies of the simple IDE antenna and the foam-backed IDE antennas follow a similar pattern.

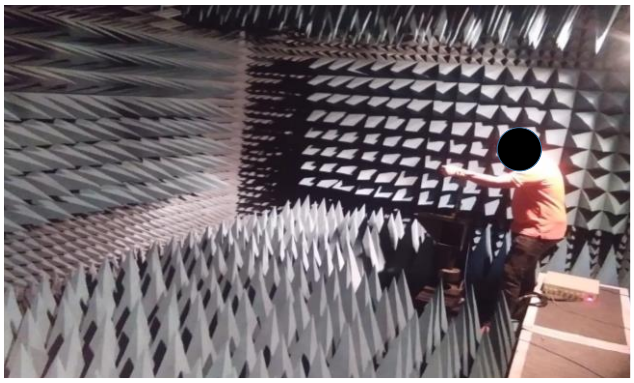

(a)

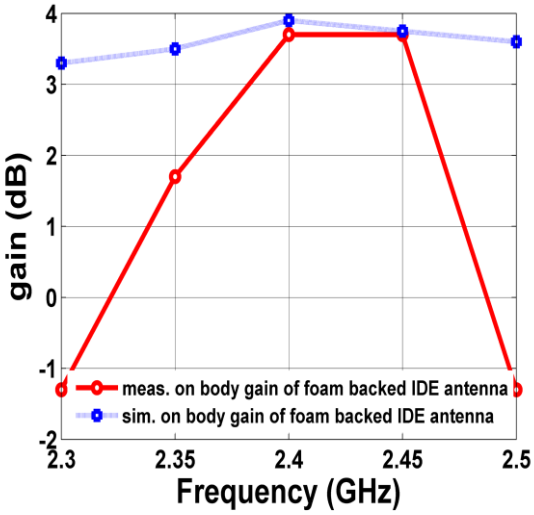

(b)

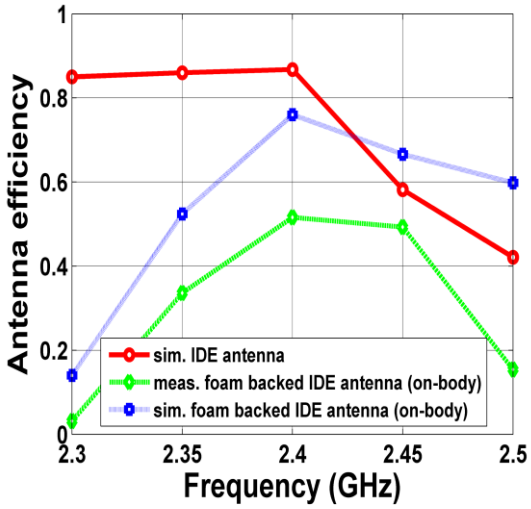

(c)

Figure 4.31(a) Setup inside the anechoic chamber for the on-body measurement of gain and efficiency of the antenna (b) Simulated and measured gain of the foam-backed incorporated antenna (c) Simulated and measured on-body efficiency of the foam-backed IDE antenna measured inside an anechoic chamber

Measurement setup: The far-field pattern measurements so far have been inside the anechoic chamber, but the antenna in the wearable device has to operate in ambient applications. Therefore, we present an analysis here that is more realistic. The measurement setup consists of a receiver antenna of gain 5 dBi at the height of 150 cm from the ground and is connected to one of the ports of a vector network analyzer (VNA). The other port of the VNA is connected to the transmitter antenna that consists of foam-backed IDE on the wrist, as shown in Figure 4.29(a). The name transmitter and receiver could be misleading as both the antennas are connected to VNA that sends equal power to both the ports per 0.2 ms. Therefore, terms port 1 for T_x (transmitter) and port 2 for R_x (receiver) is adopted. For simplicity, the height of both port 1 and port 2 is kept identical, and both radiate and receive in co-pol.

For the first set of measurements, both the antennas are perfectly aligned with each other, i.e., the broadside beam of both the antennas point towards each other and make an angle of 0^o. For an input power of -10 dBm from the VNA, the power received in the other port at four different locations 75cm, 150cm, 225cm, and 300cm of the port1 is shown in Figure 4.32. For obvious reasons, the received power gradually decreases with the increase in separation between port 1 and port 2. It can also be seen that the power received in the MBAN frequency range is maximum when compared to other frequencies, and this result is in perfect agreement with the measured result obtained in the anechoic chamber, given in Figure 4.31(b). One point to be kept in mind is that these results are obtained from the VNA that gives relative power received concerning power fed. The absolute power can be determined by adding the power input to the relative power. For example, the relative power of about -38 dBm is received at 2.4 GHz for separation of 75 cm. It results in the absolute power of -48 dBm. Hence, absolute power for all other cases can be determined by adding -10 dBm power to the plots obtained in Figure 4.32.

In the second set of the experiment, port 1, along with the wrist, is rotated by ± 45^o about its normal axis (main beam). The half-power beamwidth of the IDE incorporated antenna in both the planes is approximately $92^{o,}$ as can be deduced from the polar plots given in Figures 4.27(b) and (c). Thus rotating the T_x antenna by ± 45^o

gives a total angle of 90º that still lies in the central lobe of the radiation pattern. For an input power of -10dBm, the received power at four different locations are depicted in Figure 4.33. The power received is reduced from the previous case but still shows optimum performance in the MBAN frequency range.

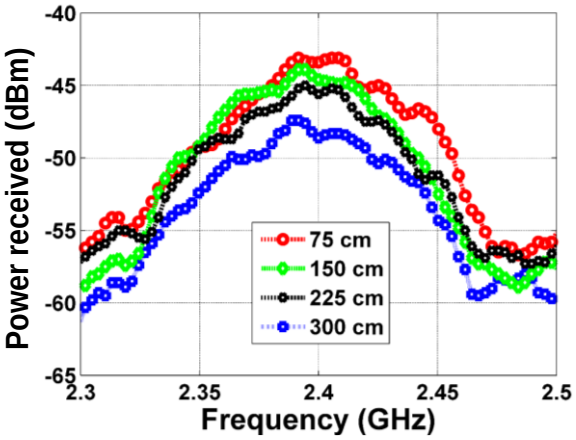

Figure 4.32 Power received in dBm vs. frequency at four different locations of foam-backed IDE incorporated antenna when antennas are perfectly inclined

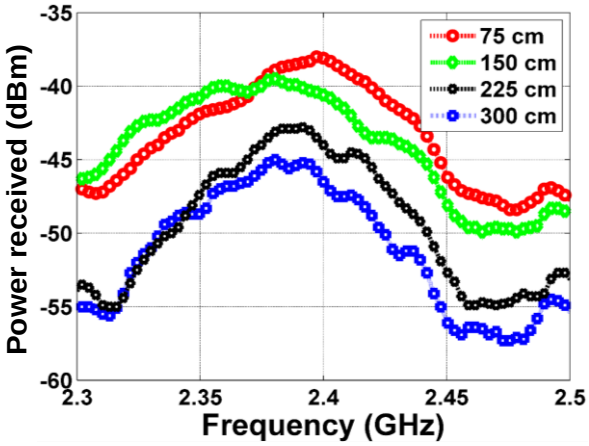

Figure 4.33 Power received in dBm vs. frequency at four different locations of foam-backed IDE incorporated antenna when IDE antenna aligned at ±45º w.r.t. receiver (port-2)

SAR gives the amount of radiation absorbed near the adjacent tissues in the presence of EM sources such as an antenna. As the proposed antenna has been

designed from the perspective of the smart-watch application, therefore SAR analysis is carried out to get some understanding. For this, the simulations were performed on two different models of the flat wrist, namely homogeneous and heterogeneous phantoms. The heterogeneous model of the wrist with its composition, properties, and height is given in Figure 4.28(a) and (b). On the contrary, the homogenous model consists of a single layer of body equivalent tissue shown in Figure 4.34(a) [93]. Then the simple, foam backed, and fully foam covered IDE incorporated antenna is simulated over both the phantoms. The input power of 0.1 W and 1g of averaging mass is considered for SAR analysis. The SAR results for both the models of the phantom are plotted in Figures 4.34(b) and (c). It can be seen in Figures 4.34(b) and (c) that the maximum SAR are 0.22 and 0.25 W/kg for the simple IDE, 0.12 and 0.09 W/kg for foam-backed IDE, and 0.115 and 0.085 W/kg for entirely foam covered IDE antenna for the heterogeneous and homogenous phantom models respectively.

The obtained SAR values are much smaller than any reported designs in literature so far. The design and analysis demonstrate that the proposed design significantly improves the state-of-the-art, as tabulated in Table 4.4. Besides, SAR analysis on the human phantom model, Gustav, for similar power and averaging mass are shown in Figures 4.35(a), (b), and (a). The simulated SAR values on a more realistic phantom agree with the data provided in Figures 4.34(b) and (c). The SAR results of the detailed numerical phantom are even lower than the approximate models used in this work.

In summary, it is safe to convey that the proposed antenna demonstrates enhanced performance in terms of gain, radiation efficiency, and SAR values with a comparatively smaller dimension than the earlier designs. Lastly, Table 4.4 lists a comparison of recent works with the proposed design. It is clear that when a monopole antenna is incorporated with the proposed IDE unit cell in this chapter, it significantly improves the gain, efficiency, and SAR values from the previous standard works. Therefore, the proposed antenna proves to be an excellent candidate for the present smart-watches.

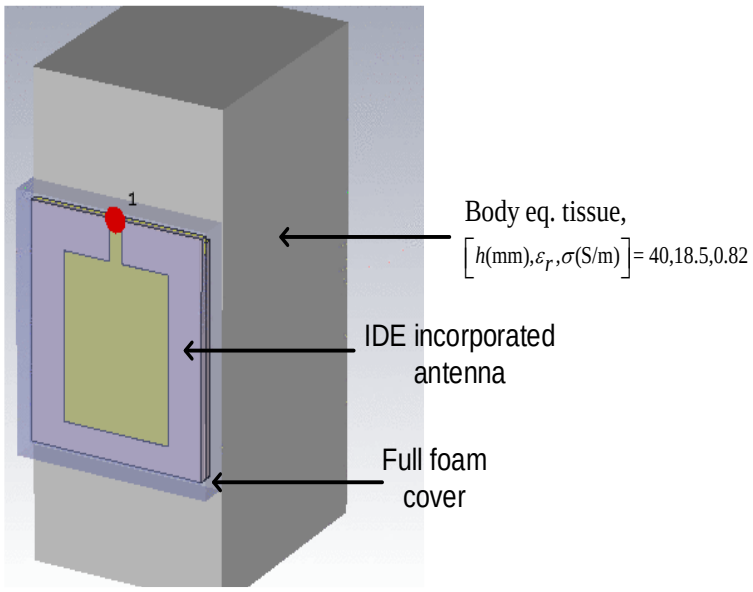

(a)

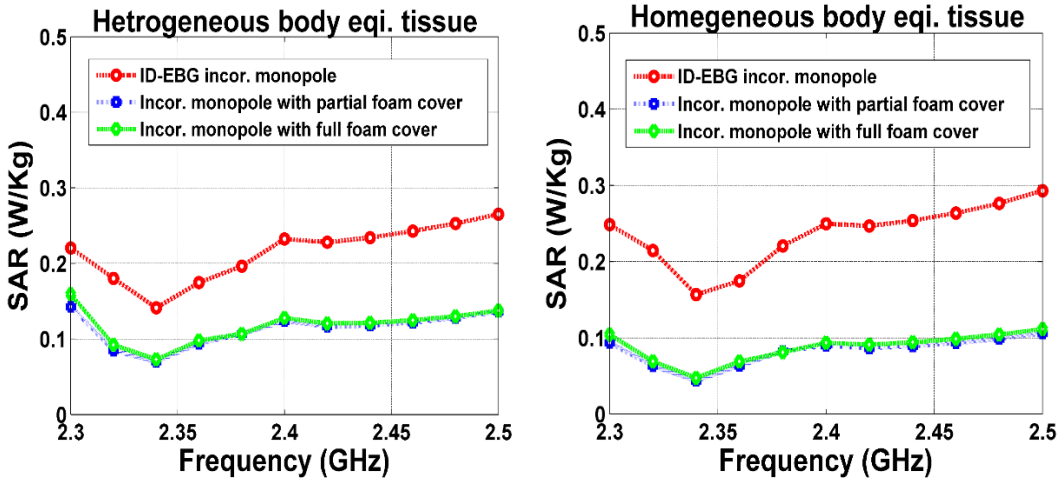

(b)

(c)

Figure 4.34 Homogenous model of wrist and SAR results (a) Homogenous flat wrist phantom (b) SAR results for homogeneous and (c) Heterogeneous model

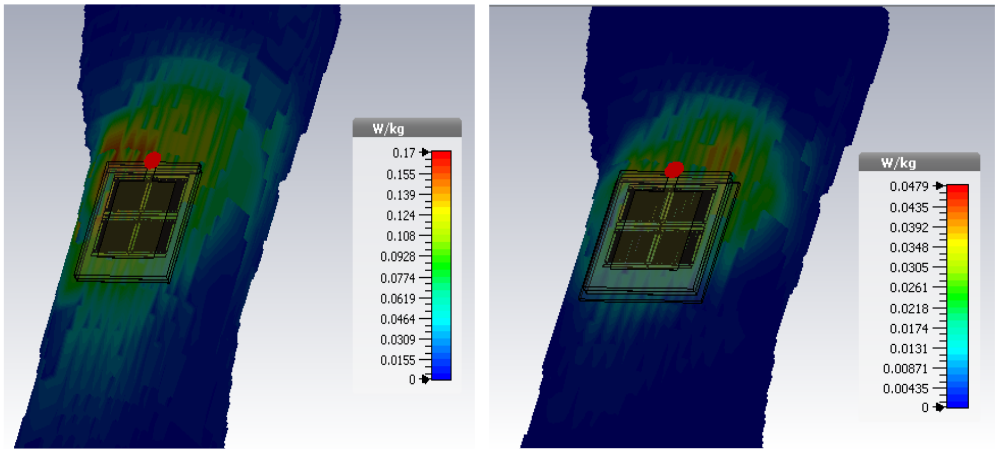

(a) (b)

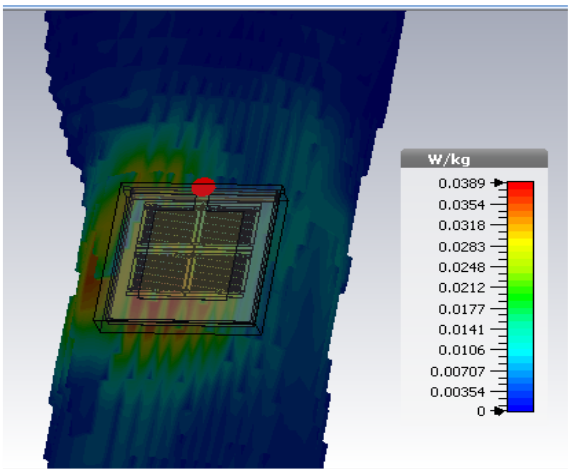

(c)

Figure 4.35 Simulated SAR values on the wrist of Gustav voxel model (a) SAR values of IDE antenna with a maximum of 0.17 W/kg, (b) SAR values of foam-backed IDE antenna with a maximum of 0.05 W/kg, (c) SAR values of full foam covered IDE antenna with a maximum of 0.04 W/kg

Table 4.4 Performance Comparison of the Proposed Antenna (work 1 – Simple IDE incorporated antenna and work 2 – Foam-backed IDE Incorporated antenna) with Few Standard Works in Free Space and On-body

Ref	Dimension (mm^3)	On air		On-body		
		Gain(dB)	%η	Gain (dB)	%η	SAR (W/kg)
[124]	40 x 40 x 5	-	-	1.4 @ 2.4 GHz	-	-
[125]	40 x 145 x 2	-	63	-	16	3.06 (10g) – hetro
[126]	40 x 50 x 5	4.39	69	- 0.89	26	-
[38]	62 x 42 x 4	5.9	59	5.8	-	0.66 (1g) – hetro
[87]	36 x 48 x 3.2	4.8	70	-	-	0.364 (1g) – homo
[130]	38 x 38 x 3	2.3	50	-	38	0.29 (1g) – hetro
This work-1	38 x 36 x 3.12	5.3	80	-	-	0.24 (1g) – homo 0.25 (1g) – hetro
This work-2	38 x 36 x 3.12	-	-	3.7 @ 2.4 GHz	50	0.09 (1g) – homo 0.12 (1g) – hetro

4.6 Conclusion

In this chapter, we proposed a novel interconnected, via-less, and compact inter-digital EBG cell. A lumped circuit model of the unit cell based on surface current flow has been developed and is then validated by the reflection phase diagram obtained using full-wave analysis. The IDE unit cell shows stability to polarization change in incident TEM wave. Besides, the stability of the IDE cell to obliquely incident TE-TM wave has also been presented with the help of the reflection phase diagrams. Then we designed an array consisting of 2x2 unit cells for the incorporation with a monopole antenna. It has been shown that the surface wave rejection ability of the array in the MBAN region is reasonable and provides suppression of -15dB. The EBG incorporated monopole antenna shows significant performance improvement in terms of matching, frequency coverage, and radiation parameters. Furthermore, a set of

measurements inside an anechoic chamber and indoor environment for on-body foam-backed EBG incorporated antenna gives a maximum gain of 3.7 dB at 2.4 GHz with a radiation efficiency of more than 50% and this again is a substantial improvement in the existing state-of-the-art. Moreover, the maximum measured gain and efficiency of the IDE cell incorporated antenna in the air is 5.1 dBi and 80%, respectively. Finally, the received power, SAR values, and compactness demonstrate the usefulness of the proposed design in wrist-worn devices.

Chapter 5

Conformal EBG Surfaces

This chapter is based on the following research paper:

- D. Rano, M.S. Hashmi, and M.A. Chaudhary, "A Geometrical Approach to Determine Shift in Reflection Phase of Conformal Electromagnetic Band Gap/High Impedance Surface for an Oblique Incident EM Wave," *IET Microwaves, Antennas & Propagation* (Accepted for publication).

In this chapter, we present a simple approach to determine the shift in in-phase reflection frequency of three standard conformal EBG/HIS. The planar EBG unit cells are simulated numerically, and reflection phases are recorded. Subsequently, the unit cells are bent along *x*- and *y*-axes under radii (*r*) of 40, 50, and 60 mm. In our approach when an EBG unit cell of a given dimension is drawn on a circle of desired radius (*r*), the new path traveled by the reflected and incident EM wave at the edges in terms of an electrical length (βl) results in a maximum shift in reflection phase. Moreover, we also extended the proposed theory to analyze three conformal EBG arrays consisting of 2x2 and 3x3 unit cells. In the first step of validation of our proposed approach, we simulated three conformal EBG unit cells for unit cell boundary condition (UC-BC) under TE^z-TM^z wave incidence and as well as for magnetic-electric BC (ME-BC) under TEM wave. Finally, an array of 3x3 unit cells is prototyped, and the reflection phase under TEM wave incidence for the array bent along *x*-and *y*-axes is recorded**.** The close agreement between the theoretical, simulated, and measured results justifies the significance of the proposed work.

5.1 Background and Related work

An essential feature of wearable devices is conformability for the comfort of users. It necessitates the design of conformal antennas suitable for placement on shoulders, biceps, wrists, and legs [37]–[39], [92]. These aspects create increased interest in the development of conformal EBG. Figure 5.1 shows two scenarios in which conformed antenna for WBAN applications are placed on wrist and triceps.

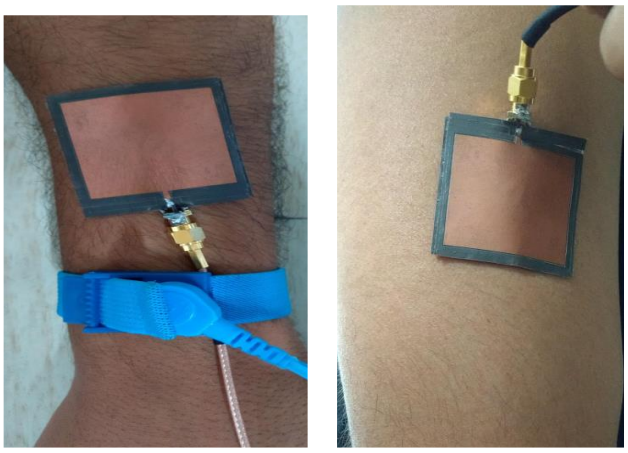

(a) (b)

Figure 5.1 (a) Conformed antenna on the wrist (b) Conformed antenna on triceps

The fundamental challenge in the design of conformal structures is that the bending leads to alteration of the in-phase property and hence changes in the performance of the conformed antenna [51]. Therefore, either unit cell of larger width is required so that even after bending, the desired band is covered [38] – [39], or appropriate prior analysis is carried out for phase compensated design [52]. However, increased cell width is often not feasible, considering that wearable applications require miniaturization. Furthermore, the determination of in-phase property in simulation is a complex process as the meshing of conformal EBG unit cell, or EBG array is critical. The discontinuity in the edges might appear while conforming to a unit cell or array, and hence increase in the number of mesh cells is needed to smoothen the computational area [53]. As a consequence, it increases the simulation time and,

consequently, memory allocation for the entire UC/array. We have explained here the concept, as mentioned above, with the help of an example. We have also explained the term in-phase frequency and its shift, which have been used throughout this chapter.

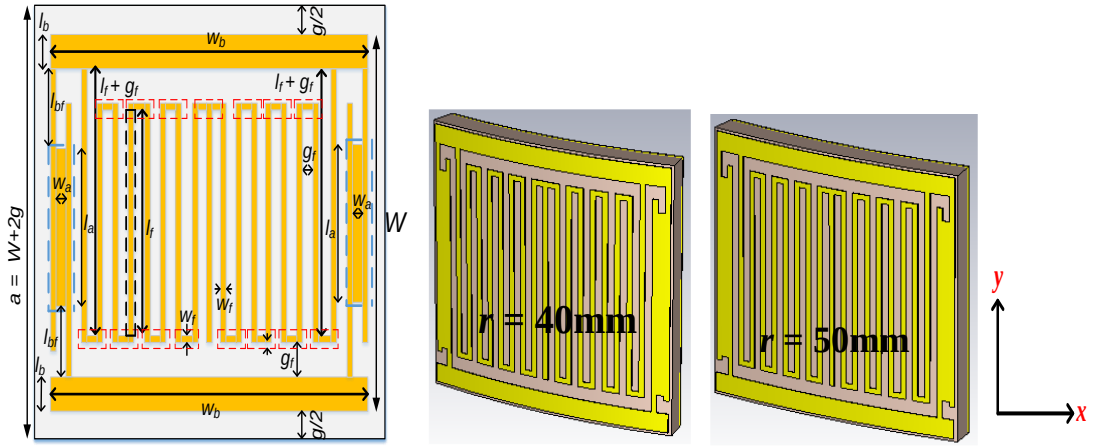

(a) (b) (c)

Figure 5.2 (a) IDE UC with all dimensions given in Figure 4. (b) Conformed IDE unit cells along *x*-axis (b) *r* = 40mm (c) *r* = 50mm

Figure 5.2 (a) shows the unit cell we proposed in Chapter 4. The dimensions of the unit cell and the substrate details are given in Chapter 4. The conformed unit cells along the *x*-axis (radius of curvatures are 40 and 50mm) are shown in Figures 5.2 (a) and (b). The reflection phase plots of the planar and conformal unit cell when terminated by unit cell boundary condition and excited by a TE wave, are shown in Figure 5.3(a). Point A, B, and C represent the in-phase frequency points of the planar and conformal unit cells. It is because, at these points, the reflected wave is in phase with the incident wave falling on the surface of a unit cell. The planar cell, as we discussed in Chapter 4, exhibits in-phase resonance at 2.38 GHz and has a total bandwidth of approximately 40MHz (covering MBAN band from 2.36 – 2.4 GHz, frequencies between $\pm 90^{o}$). However, the conformed unit cells resonate at 2.4 GHz and 2.41 GHz for ***r*** = 50mm, and 40mm, respectively. Besides, the bandwidth of the conformed unit cells, as apparent from Figure 5.3(a), is out of the desired band (2.38 – 2.42 GHz for *r* = 40mm and 2.4 – 2.44 GHz for *r* = 50mm).

We have seen in chapter 4 that the performance of an antenna heavily relies on the band of operation of an EBG cell. Therefore, this frequency shift deteriorates the overall performance of the antenna. For example, the planar antenna designed in section 4.6 when conformed along the *x*-axis, the gain drops from 5.3dBi to 4.7 dBi, and 3.7 dBi in *xz*-plane for the radius of 50mm and 40mm, respectively, as shown in Figure 5.3(b). Similarly, gain drops from 5.5 dBi to 4.6 dBi and 3.7dBi in *yz*-plane for the radius of 50mm and 40mm, respectively, as shown in Figure 5.3(c). It is important to note that the shift in in-phase frequency does not have an impact on the bandwidth of the EBG unit cell. Therefore, if the proposed EBG unit cell is designed in a way such that it takes into account the shift prior, then the degradation in the performance of an antenna can be avoided.

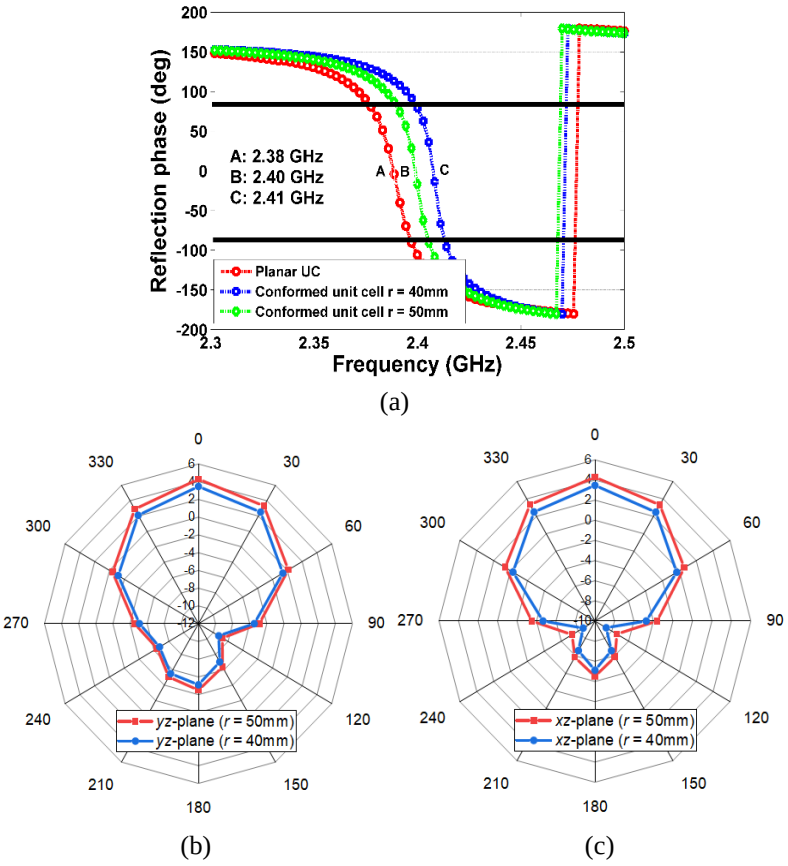

(a)

(b) (c)

Figure 5.3 (a) Reflection phases of planar and conformal IDE cell (b) Radiation pattern of the conformal antenna along *yz*-plane (c) Radiation pattern of the conformal antenna along *xz*-plane

We have now further explained the theory mentioned above with the help of another standard EBG unit cell in [39], as shown in Figure 5.4(a). The unit cell is designed on RO5880 with ε_r and h of 2.2 and 5mm. For the dimensions of the unit cells, as given in Figure 5.4(a), it operates in the ISM band from 2.4–2.4835 GHz. The planar and the conformed geometries of the unit cells are shown in Figure 5.4(b)-(c).

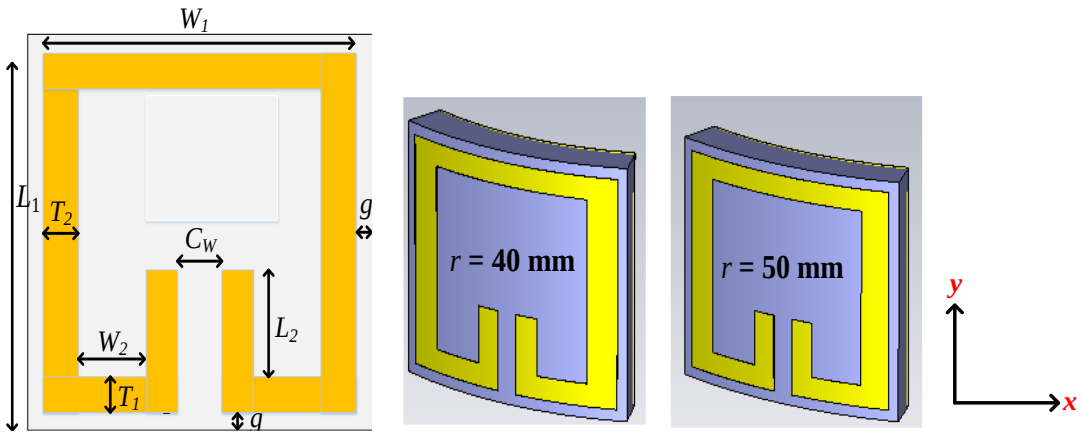

(a) (b) (c)

Figure 5.4 (a) Geometry of the unit cell in [15] with overall dimensions: W_1 = 27.83mm, W_2 = 6.4mm, L_1 = 25.3mm, L_2 = 6.32mm, T_1 = 2.53mm, T_2 = 3.34mm, C_W = 2.78mm, and g = 1.25mm, Conformed unit cells on a cylinder along x-axis (b) r = 40mm (c) r = 50mm

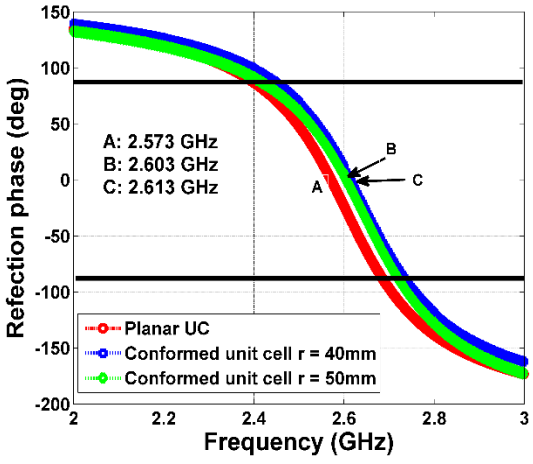

Figure 5.5 Reflection phases of the planar and conformal unit cell in Figure 5.4 (a) – (c)

Subsequently, we simulated the designs for the unit cell boundary condition to obtain the reflection phase plots, as shown in Figure 5.5. Once again, the points A, B, and C signify the in-phase frequency points of the planar and conformal unit cells. It is apparent from the plots that though the conformal geometries exhibit shift in in-phase frequency, the intended band (i.e., ISM band) is still covered. It is because the operational bandwidth of the planar EBG unit cell is from 2.39 – 2.65 GHz (approximately seven times more than the proposed unit cell in Figure 5.2). A shift of 30MHz (for 50mm) and 40 MHz (40mm) in in-phase frequency points as apparent from Figure 5.5 does not have a significant impact on antenna operation. We know from chapter 4 that bandwidth of an EBG unit cell is inversely proportional to the capacitance developed between the top metallic patch and the ground plane. Since the patch at the top is separated from the ground plane by 5mm in [39], which is approximately 3.5 times the proposed EBG unit cell, therefore, the operational bandwidth of unit cell in [39] is wider than the unit cells shown in Figure 5.2.

We can infer the following from the above discussion.

1) Determination of shift in in-phase frequency of a conformal EBG unit cell can aid in getting better performance from an EBG backed antenna. Having prior knowledge of frequency shift in in-phase points of a conformal EBG cell can help a designer to modify the circuit in such a way that the intended band of operation is covered. From the WBAN perspective, the determination of this shift is of utmost importance. It is because body-worn antennas need to conformal for suitable placement on wrist, biceps, legs, or shoulders. As EBG surfaces are used to enhance the performance of such antennas in the presence of lossy tissues [37] – [38], [92], out of band operation might result in link failure with an external node.

2) Thicker substrates can help to tackle the shift in the in-phase frequency of an EBG surface. However, from the WBAN perspective, the body-worn antennas need to be low profile and compact. Moreover, thicker PCBs are hard to bend, and this may damage the patch surface due to the application of high force.

After an extensive literature survey, we found out two works in this direction that analytically computes the reflection phase of a conformal EBG/HIS surfaces [51] – [52]. In [52], the reflection phase of a curved HIS/EBG surface is obtained from the scattered fields. Scattered fields, in turn, can be obtained from the proposed analytical model or full-wave solution simulator like HFSS. The technique also incorporated surface wave effects to strengthen the theory further. The analytically obtained results were in good agreement with the measured values. In [51], a phase compensated metasurface is designed for the Fabry-Perot cavity antenna. In this method group of 25 wire antennas are placed over a metallic cylinder. Then each antenna is excited by a phase shift that compensates the phase lag from the planar surface. The proposed method, when applied on a conformal PRS, shows improvement in gain w.r.t. uncompensated antenna. However, both techniques have some drawbacks from the WBAN perspective. These are as follows.

1) The analytical formulations derived in [52] to determine the reflection phase of a curved surface assumed the scattered field from an infinitely long cylinder. Since WBAN devices are miniature in size and compact such formulation may not be useful.

2) The radius of curvature assumed in [51] to develop the phase compensation between the antenna elements considered the radius of curvature of 152mm. It is impractically larger from the WBAN perspective.

3) Both works have analyzed only symmetrical HIS/EBG unit cells.

4) The size of the array used to analyze the proposed method in [52] uses 20x20 unit cells. Once again, the size of the EBG array is impractically larger from the WBAN perspective. A maximum of 3x3/2x2 EBG/HIS unit cells is designed for an incorporated antenna.

5) The effect of surface waves becomes dominant once the overall size of the array reduces. It requires to demonstrate the mutual coupling among the elements of the EBG array through transmission characteristics.

Therefore, the following steps have been adopted in this dissertation to address the above concerns.

1) Both symmetrical and asymmetrical structures have been considered to determine a shift in in-phase reflection frequency of EBG unit cells and array.

2) Both TE-TM and TEM mode of polarization of EM wave has been considered here for unit cell and magnetic-electric boundary condition. However, owing to the practical size of conformal arrays, therefore, only the TEM mode of incidence is considered under magnetic-electric boundary conditions.

3) Mutual coupling among the unit cells in an array has been demonstrated with the help of the dispersion diagram, and transmission characteristics. The results show that the level of mutual coupling between two adjacent unit cells is significantly less and hence can be ignored from the analysis.

4) Since the proposed work only focuses on EBGs/HIS designed for on-body application, therefore, the radius of cylinder (***r***) on which unit cells and array are conformed is taken to be 40, 50, and 60mm which almost covers dimension of wrist and biceps of all age groups. Moreover, the effectiveness of the proposed theory is presented only on unit cells designed primarily for on-body applications.

5) Only obliquely incident EM wave on conformal EBG unit cell and the array has been employed for both the proposed theory and the simulation setup.

5.2 Proposed Geometrical Approach for EBG Unit Cells

In this section, we present a geometrical approach to determine the in-phase frequency shift of a conformal EBG unit cell. The proposed method is implemented on three different EBG unit cells to predict the respective change in reflection frequencies bent along either *x*- or *y*-axes.

5.2.1 Proposed Approach

A Planar EBG unit cell (P-EBG UC) and the corresponding conformal (C-EBG UC) geometry on a circle of radius ***r*** (represented by an arc) are depicted in Figure 5.6 (a). The P-EBG UC is separated from C-EBG UC and is shown on top of it. The center of the circle is O, whereas A, B, and C are the extreme and mid-points of the arc. The angle subtended by the arc AB about O is θ while the angle formed between the arc AC/BC and O is $\theta/2$.

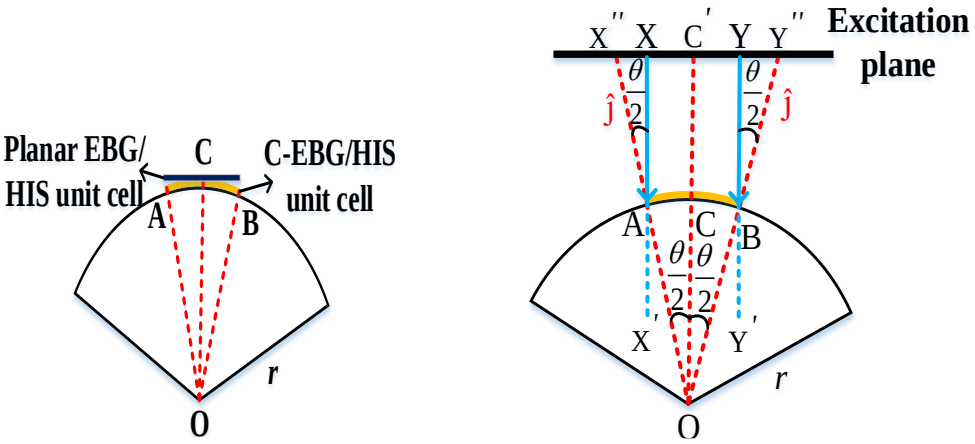

(a) (b)

Figure 5.6 (a) Planar and conformed EBG/HIS unit cell of radius *r* with extreme points A, B and mid-point C (Where P-and C-EBG signifies planar and conformal EBG) (b) Arc representing C-EBG cell with incident EM wave making an angle $\theta/2$ at the two extreme points A and B w.r.t. normal vector ĵ

For the proposed approach, the incident waves XA, YB (in light blue), and C′C (in dotted red) on C-EBG UC, along with the excitation plane, are shown in Figure

5.6(b). The term ĵ is normal to A and B on the arc of the circle and intersects the excitation plane at X″ and Y″ respectively. As we saw in Chapter 4 that to obtain the reflection phase of an EBG cell, the excitation plane is placed at a distance equivalent to the height by which an antenna is separated from, so is here as shown in Figure 5.6(b). Here, the height is not specified; however, it is assumed that the excitation plane is away from the C-and P-EBG UC by some length. XAX′, YBY′, and C′CO are parallel to each other as only obliquely incident waves on C-EBG UC are considered in this dissertation. Two transversal OX intersects these parallel lines″, and OY″ and therefore it can be deduced from elementary geometry that ∠AOC = ∠X″ AX and ∠ BOC = ∠Y″ BY as expressed in (5.1).

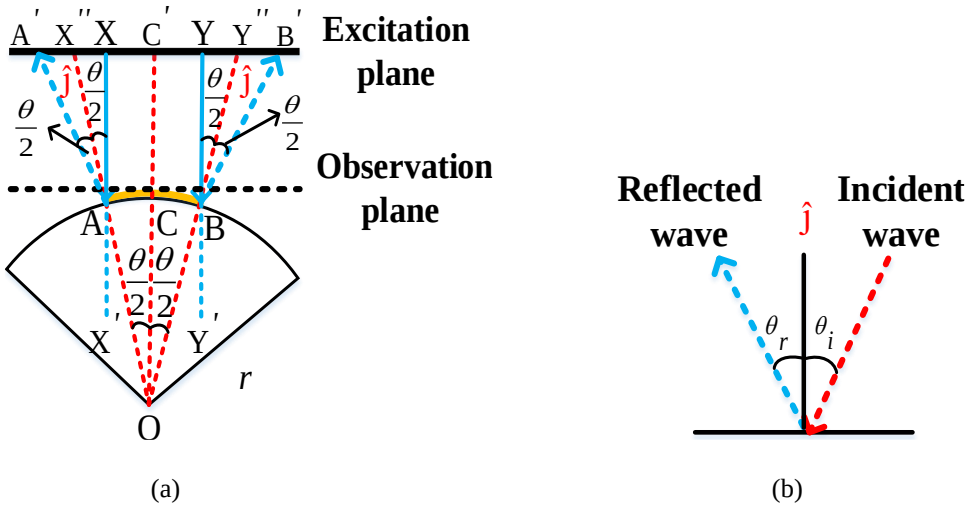

(a) (b)

Figure 5.7 (a) Law of reflection on a planar surface (Here, ĵ is normal to the interface) (b) Reflection of EM wave on C-EBG cell (the dotted line represents observation plane)

For an incident EM wave, we can obtain the in-phase reflection of a P-EBG UC by positioning the observation plane at its surface, as depicted in Figure 5.7(a) (from chapter 4). We know from the law of reflection, as shown in Figure 5.7(b) that *the angle of incidence* (***θ*ᵢ**) *on an interface is equal to the angle of reflection* (***θ*ᵣ**). This concept is applied for the C-EBG UC in Figure 5.7(a) where incident waves XA and YB make angle ***θ/2*** about the normal ĵ (AX″ and BY″) and are reflected by an identical angle (AA′ and BB′) as expressed by (5.2). Apparently, both the extreme regions A

and B of C-EBG UC behave identically for an incident EM wave.

$$\angle AOC' = \angle XAX'' = \angle BOC' = \angle YBY' = \boldsymbol{\theta/2} \tag{5.1}$$

$$\angle XAX'' = \angle YBY'' = \angle X''AA' = \angle Y''BB' = \boldsymbol{\theta/2} \tag{5.2}$$

We can determine angle $\boldsymbol{\theta}$ subtended by arc AB about the center O, as shown in Figure 5.7(a) using (5.3). Here, W is the width of the EBG cell, $\boldsymbol{r}$ is the radius of the circle, and 360^o is the total angle at the center. W is identical for both the C-EBG UC and P-EBG UC because the conforming of a P-EBG cell on a conformal platform does not change its physical dimension.

$$W = \frac{\boldsymbol{\theta}}{360^o} \times 2\pi \boldsymbol{r} \Rightarrow \boldsymbol{\theta} = \frac{W \times 360^o}{2\pi \boldsymbol{r}} \tag{5.3}$$

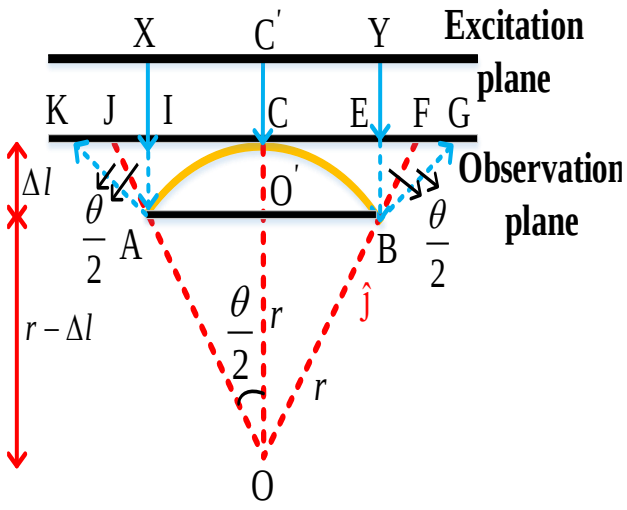

Figure 5.8. Magnified representation of reflection at C-EBG surface along with the path lag an EM wave experiences while interacting with C-EBG cell

We can infer from Figure 5.8, that the incident EM waves (IA/EB) while interacting with the C-EBG UC experiences path lag due to reflected waves AK and BG instead of reflection AX and BY to be seen in P-EBG UC. Similarly, path lag can

be experienced by incident waves IA and EB, as shown in Figure 5.8, because IE lies on the observation plane for P-EBG UC. In contrast, AB is separated from the observation plane by $\Delta \boldsymbol{l}$ for C-EBG UC. The equivalent phase shift in terms of electrical length for the incident wave IA ($\Delta \boldsymbol{l}$) and reflected wave AK in Figure 5.8 is expressed in (5.4). Here, β is wavenumber at the operating frequency of the P-EBG UC; $\Delta \boldsymbol{l}$ and AK are the path delays due to incident and reflected wave. Now, the use of the Pythagorean Theorem in Δ IAK and Δ OO′A allows the determination of AK in terms of $\Delta \boldsymbol{l}$ given in (5.5) and $\Delta \boldsymbol{l}$ in terms of $\boldsymbol{r}$ given in (5.6). Then the sum of individual phase lagged due to incident and reflected waves give the net shift in the in-phase reflection of C-EBG UC. Then the total change in radians, given by (5.7), is twice that value, considering that similar phenomenon occurs at point B.

$$\Delta \boldsymbol{\theta}_{\text{incident}} = \beta \times (\text{IA}) = \beta \Delta \boldsymbol{l} \tag{5.4}$$

$$\Delta \boldsymbol{\theta}_{\text{reflected}} = \beta \times \text{AK} \tag{5.5}$$

$$\cos\left(\text{IAK}\right) = \cos\boldsymbol{\theta} = \frac{\Delta \boldsymbol{l}}{\text{AK}} \quad \Rightarrow \quad \text{AK} = \frac{\Delta \boldsymbol{l}}{\cos\boldsymbol{\theta}} \tag{5.6}$$

$$\cos\frac{\boldsymbol{\theta}}{2} = \frac{\text{OO}'}{\text{OA}} = \frac{\boldsymbol{r} - \Delta l}{\boldsymbol{r}} \quad \Rightarrow \quad \Delta \boldsymbol{l} = \boldsymbol{r} - \boldsymbol{r}\cos\frac{\boldsymbol{\theta}}{2} \tag{5.7}$$

$$\boldsymbol{\theta}_{\text{shift}} = 2 \cdot \left(\Delta \boldsymbol{\theta}_{\text{incident}} + \Delta \boldsymbol{\theta}_{\text{reflected}} \right) = 2 \cdot \left(\beta \Delta \boldsymbol{l} + \frac{\beta \Delta \boldsymbol{l}}{\cos\boldsymbol{\theta}} \right) \tag{5.8}$$

We can see there is no path lag for EM wave falling on point C of the observation plane. In this dissertation, only the maximum shift in the in-phase reflection for the unit cells is considered, and hence only the extreme points are chosen to determine corresponding $\boldsymbol{\theta}_{\text{shift}}$.

5.2.2 Unit Cell (UC-1)

The first P-EBG cell called here UC-1, along with its geometrical dimensions, to be analyzed in this chapter is shown in Figure 5.9(a) [39]. It is shown in [39] that

the P-EBG UC exhibits an in-phase reflection frequency of 2.45 and 1.413 GHz, which results in β of 51.3 and 29.6 rad/m *y*- and *x*-polarized EM wave respectively. Due to asymmetry in the structure, the polarization stability of the UC is low and in-phase frequencies are far apart from each other, as explained in chapter 4. The polarization of EM wave plays a critical role in the determination of $\boldsymbol{\theta}_{\mathbf{shift}}$ of a UC for *x*- or *y*-bend because for *x*-bend, the plane of incidence of EM wave coincides with the *y*-axis, and makes *y*-polarization suitable. Similarly, for *y*-bend, the plane of incidence of EM wave coincides with *the x*-axis and makes *x*-polarization convenient.

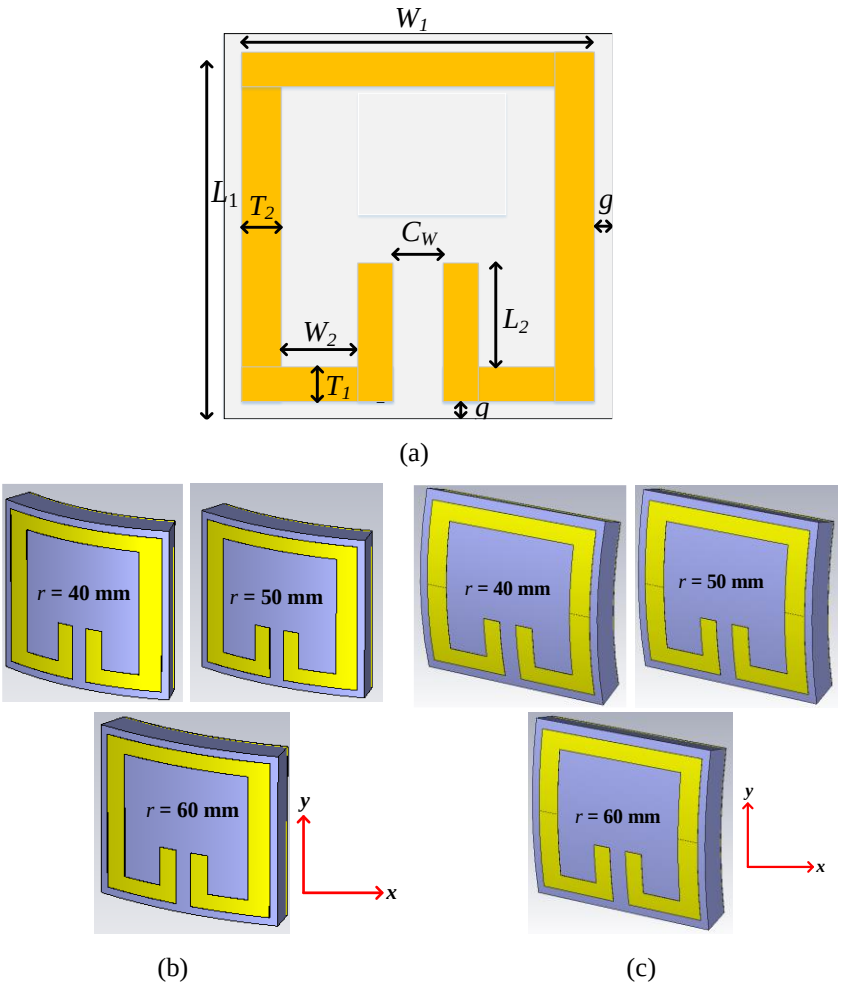

Figure 5.9 (a) Geometry of the unit cell in [39] with overall dimensions: W_1 = 27.83mm, W_2 = 6.4mm, L_1 = 25.3mm, L_2 = 6.32mm, T_1 = 2.53mm, T_2 = 3.34mm, C_W = 2.78mm, and g = 1.25mm, Conformed unit cells on cylinder of radii r = 40, 50 and 60mm (b) along *x*-axis (c) along *y*-axis

5.2.2.1 Conformal UC-1 Along the *x*-axis

The conformal UC-1 along *x*-axis on a cylindrical platform of radii $\boldsymbol{r}$ = 40, 50 and 60mm are depicted in Figure 5.9(b). A cylindrical platform is chosen, considering that it readily portrays the shape of body parts like a bicep, wrist, leg, and many more in WBAN. As a case study, we determine here $\boldsymbol{\Theta}_{\mathbf{shift}}$ of the C-EBG UC-1 using the proposed formulations in section 5.2 for $\boldsymbol{r}$ = 50mm. For this we substitute $W_1 + 2g$ = 30.33mm (from Figure 5.9(a)) and $\boldsymbol{r}$ = 50mm in (5.3) resulting in $\boldsymbol{\Theta} = 34.75^0$. Then $\Delta\boldsymbol{l}$ = 2.28mm is obtained for this value of $\boldsymbol{\Theta}$ in (5.6). Placing the values of $\boldsymbol{\Theta}$, $\Delta\boldsymbol{l}$, and β in (5.7) results in $\boldsymbol{\Theta}_{\mathbf{shift}}$ of 0.54 rad or 31.3^0. The calculated values of $\boldsymbol{\Theta}_{\mathbf{shift}}$ for the other two radii are listed in Table 5.1. It is apparent that the decrement in the radius of curvature results in a gradual increase in $\boldsymbol{\Theta}_{\mathbf{shift}}$. It is obvious because as $\boldsymbol{r}$ decreases (60mm → 50mm → 40mm), it leads to longer path delay $\Delta\boldsymbol{l}$ due to incident and reflected waves, as shown in Figure 5.8.

5.2.2.2 Conformal UC-1 Along the *y*-axis

The conformed UC-1 along the *y*-axis on a cylindrical platform of radii $\boldsymbol{r}$ = 40mm, 50mm, and 60mm are depicted in Figure 5.9(c). Here, the overall width now becomes $L_1 + 2g$ is 27.8mm, and the EM wave is *x*-polarized. Following the steps, as mentioned in section 5.2.2.1, we determined $\boldsymbol{\Theta}_{\mathbf{shift}}$ for this case, as listed in Table 5.1. The value of β used in this case is 29.6 rad/m. Once again, the $\boldsymbol{\Theta}_{\mathbf{shift}}$ reduces with the decrease in radii $\boldsymbol{r}$ due to longer path delay $\Delta\boldsymbol{l}$.

TABLE 5.1 Conformed UC-1 Parameters Determined by Proposed Method for *y*- and *x*-Polarized EM Wave

Pol.	$\boldsymbol{r}$ (mm)	$\boldsymbol{\Theta}$ (deg)	$\Delta\boldsymbol{l}$ (mm)	$\Delta\boldsymbol{\Theta}_{\mathbf{reflected}}$ (rad)	$\Delta\boldsymbol{\Theta}_{\mathbf{incident}}$ (rad)	$\Delta\boldsymbol{\Theta}_{\mathbf{shift}}$ (rad)	$\boldsymbol{\Theta}_{\mathbf{shift}}$ (deg)
y –	40	43.44	2.84	0.211	0.153	0.728	41.71
	60	28.96	1.91	0.118	0.103	0.442	25.32
x –	40	39.82	2.39	0.098	0.075	0.346	19.80
	50	31.86	1.92	0.078	0.066	0.287	16.48
	60	26.54	1.60	0.056	0.050	0.212	12.17

5.2.3 Unit Cell (UC-2)

The second P-EBG UC, called UC-2 in this work, with all the dimensions, is shown in Figure 5.10(a) [38]. It exhibits an in-phase reflection frequency of 2.46 and 5.04 GHz for *y*- and *x*-polarized EM waves, respectively, and this results in β of 51.6 and 105.5 rad/m. Once again, asymmetry in the design of UC results in considerable variation in in-phase frequency points, as demonstrated in chapter 4. The corresponding C-EBG UC-2 on cylinder along *x*- and *y*-axes of radii $\boldsymbol{r}$ = 40, 50 and 60mm are shown in Figs. 5.10(b)–(c).

Once again, the proposed formulations are used to determine the respective shifts $\boldsymbol{\Theta}_{\mathbf{shift}}$, as given in Table 5.2. The widths of the C-EBG UC-2 in this case are $L_1 + 2L_1 + 2g_1$ = 29.21mm and $W_2 + 2g_2$ = 18.49mm along *y*-and *x*-axes respectively. We can infer from Table 5.2 that the phase shift obtained for *y*-bend (*x*-pol) is more when compared to the *x*-bend (*y*-pol). It can be attributed to the fact that the width for the *x*-polarized wave ($L_1 + 2L_1 + 2g_1$ = 29.21mm) is more than the width for the *y*-polarized wave ($W_2 + 2g_2$ = 18.49mm). As a consequence, the path delay between the observation plane and point of incidence increases, and that, in turn, increases the phase delay. Once again, as the radius of curvature increases (40mm → 50mm → 60mm), the $\boldsymbol{\Theta}_{\mathbf{shift}}$ decreases, as evident from Table 5.2. It is attributed to the fact explained in section 5.2.2.1.

TABLE 5.2 Conformed UC-2 Parameters Determined by Proposed approach for *y*- and *x*-polarized EM wave

Pol.	***r*** **(mm)**	***Θ*** **(deg)**	**Δ*l*** **(mm)**	**$\Delta\boldsymbol{\Theta}_{\mathbf{reflected}}$** **(rad)**	**$\Delta\boldsymbol{\Theta}_{\mathbf{incident}}$** **(rad)**	**$\Delta\boldsymbol{\Theta}_{\mathbf{shift}}$** **(rad)**	**$\boldsymbol{\Theta}_{\mathbf{shift}}$** **(deg)**
	40	26.48	1.06	0.061	0.055	0.233	13.34
y –	50	21.20	0.85	0.047	0.044	0.183	10.46
	60	17.63	0.71	0.038	0.037	0.151	8.64
	40	41.84	2.63	0.374	0.278	1.304	73.70
x –	50	33.47	2.12	0.268	0.224	0.984	56.40
	60	27.90	1.77	0.211	0.187	0.797	45.66

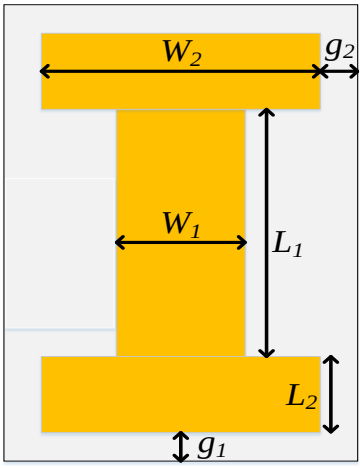

(a)

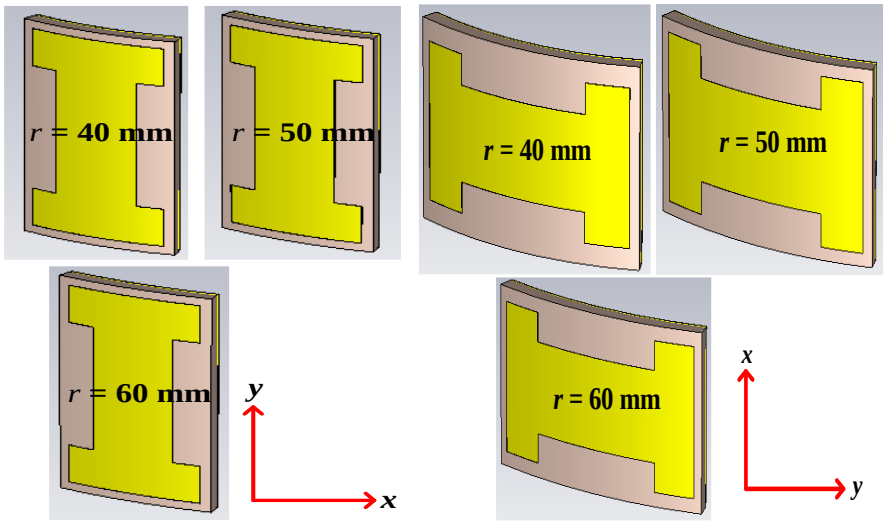

(b) (c)

Figure 5.10 (a) Geometry of the UC in [38] with dimensions: W_1 = 9.75mm, W_2 = 16mm, L_1 = 16.86mm, L_2 = 5.1mm, g_1 = 1.075mm, g_2 = 1.245mm, Conformed UCs-2 on cylinder of radii r = 40, 50 and 60mm (b) along *x*-axis (c) along *y*-axis

5.2.4 Unit Cell (UC-3)

The third P-EBG UC, called UC-3, with all the dimensions, is shown in Figure 5.11(a). This unit cell is proposed by us and is explained in detail in Chapter 6. The P-

EBG UC is designed on RO5880 with permittivity and thickness of 2.2 and 0.381mm. The in-phase reflection frequencies of 2.372 and 2.39 GHz for *y*- and *x*-polarized EM wave respectively are obtained. Due to symmetry in the dimension of the UC, the in-phase frequencies are comparatively closer than the previous two designs. It results in β of approximately 50 rad/m for both the polarization. The corresponding conformed UCs along *x*- and *y*-axes are depicted in Figures 5.11(b)-(c).

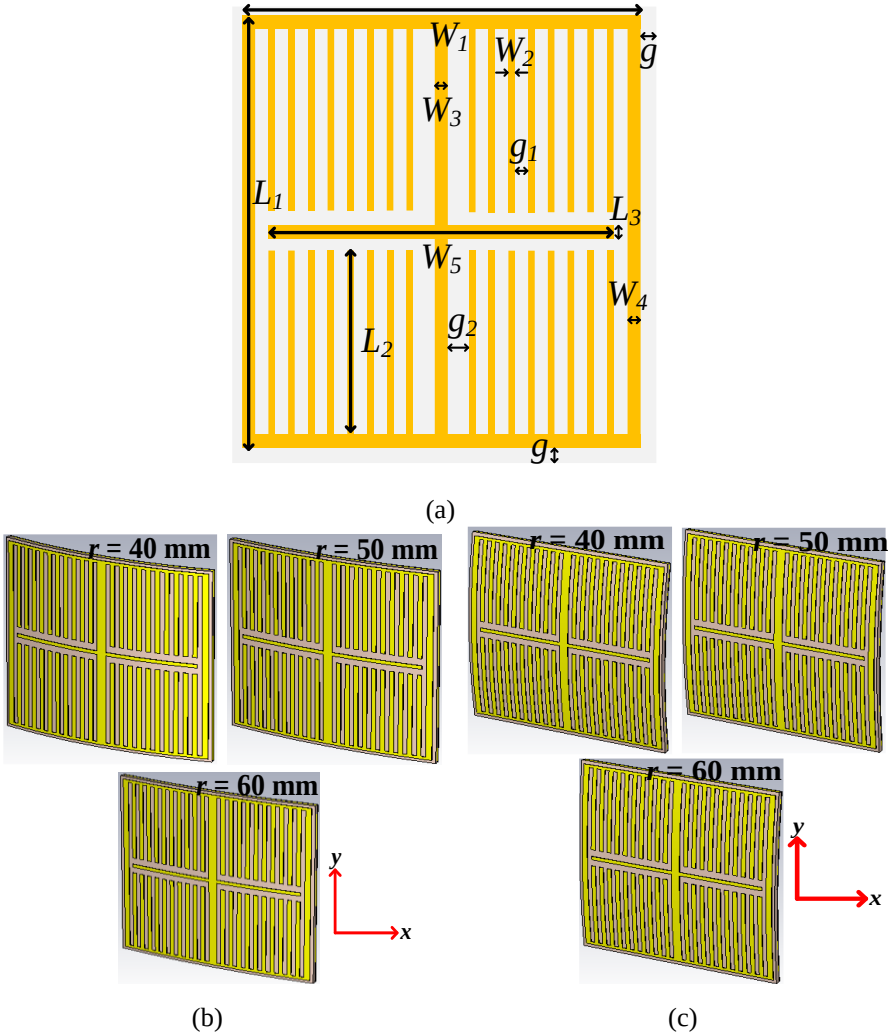

Figure 5.11 (a) Geometry of the unit cell with overall dimensions: W_1 = 13.8mm, W_2 = 0.3mm, W_3 = 0.4mm, W_4 = 0.45mm, W_5 = 11.8mm, L_1 = 13.4mm, L_2 = 6mm, L_3 = 0.4mm, g_1 = 0.4mm, g_2 = 1.245mm g = 0.5mm Conformed unit cells on cylinder of radii r = 40, 50 and 60mm (b) along *x*-axis (c) along *y*-axis

Once again, the proposed theory is applied to C-EBG UC-3 to determine $\boldsymbol{\theta}_{\mathbf{shift}}$ in reflection frequency. Substituting the respective widths of 13.8mm and 13.4mm along the *x*-and *y*-axes in (5.1) – (5.8), the $\boldsymbol{\theta}_{\mathbf{shift}}$ the UCs bent along *x*-and *y*-axes are given in Table 5.3. It can be inferred from the results that $\boldsymbol{\theta}_{\mathbf{shift}}$ obtained for both the polarizations are very close to each other. It is because the UC is approximately symmetrical about both *x*-and *y*-axes and therefore resulting in a similar path and phase delays.

TABLE 5.3 Conformed UC-3 parameters determined by proposed approach for *y*- and *x*-polarized EM wave

Pol.	r (mm)	θ (deg)	Δl (mm)	$\Delta\theta_{\text{reflected}}$ (rad)	$\Delta\theta_{\text{incident}}$ (rad)	$\Delta\theta_{\text{shift}}$ (rad)	θ_{shift} (deg)
	40	19.77	0.59	0.0315	0.0297	0.122	7.02
y –	50	15.80	0.47	0.0246	0.0237	0.097	5.54
	60	13.18	0.39	0.0206	0.0198	0.081	4.62
	40	19.19	0.56	0.0297	0.0280	0.115	6.61
x –	50	15.35	0.45	0.0232	0.0224	0.091	5.23
	60	12.80	0.37	0.0192	0.0187	0.076	4.34

5.2.5 Mutual Coupling Among the UCs

Mutual coupling among the UCs plays a significant role in altering the reflection phase [51]. Typically, EBG UCs are parallel resonant circuits represented by lumped inductors and capacitors formed due to metallic strips and gaps between the adjacent cells [43]–[45]. Therefore, the surface impedance of the UC at resonant frequency becomes infinity, and the structure behaves as a band-stop filter [43]–[45]. It results in no propagation of the surface wave (surface current) in the substrate ideally and hence indicates no coupling among the UCs as well [41] – [48], [92]. However, the practical EBG UCs always have some surface currents propagating through the surface. We can say that better is the rejection of surface waves, lesser is the

interference of surface currents on in-phase frequency. We obtained the band-gap of the UCs in CST with the help of Eigen-mode solver, as shown in Figures 5.12.

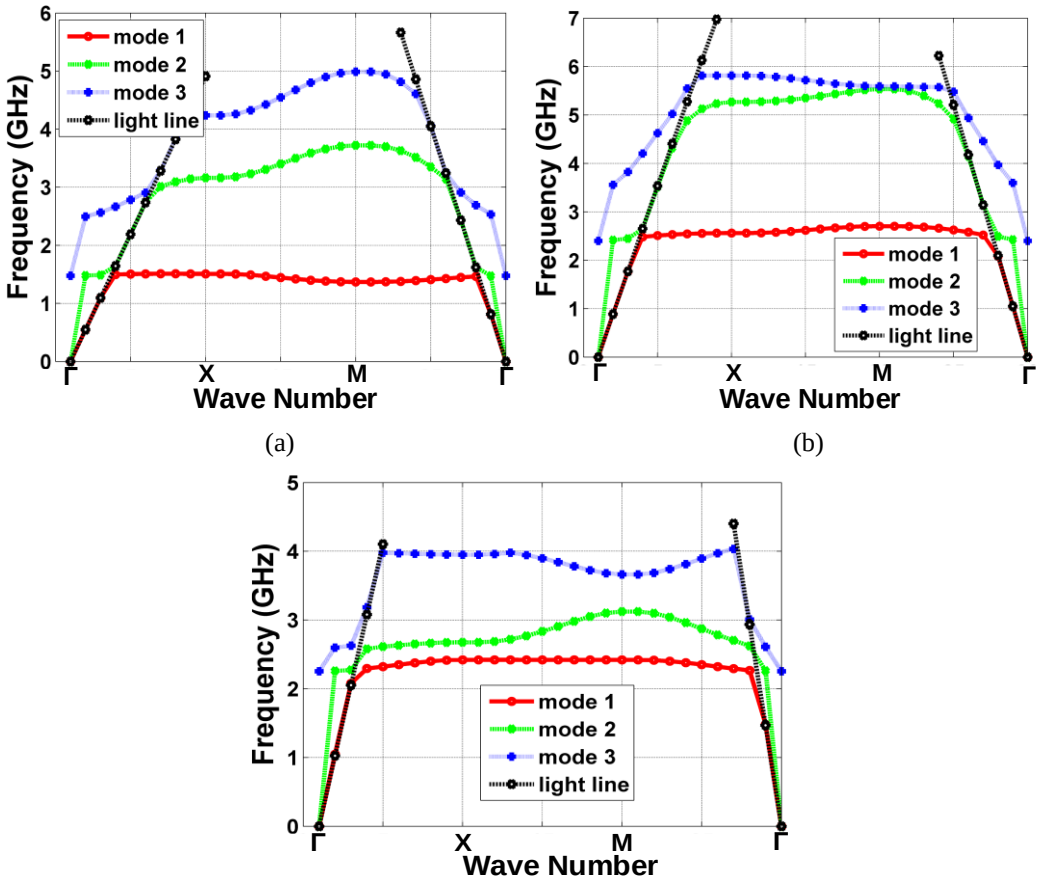

Figure 5.12 (a) Dispersion diagram of UC-1 with bandwidth = 1.45 – 3.2 GHz *(b)* Dispersion diagram of UC-2 with bandwidth = 2.45 – 5.4 GHz *(c)* Dispersion diagram of UC-3 with bandwidth = 2.35 – 2.45 GHz [Γ, X and M are points in Brillouin zone]

Mode 1 represents the first-order surface wave that is the TM mode without a cut-off frequency. The second-order surface wave is the TE mode depicted by mode 2 in Figures 5.12. The gap between the subsequent modes indicates the absence of surface waves in the substrate and hence signifies the band-gap. The in-phase resonance frequencies of all three UCs for both the polarizations fall in the band-gap region between mode one and mode two, and therefore, in the absence of surface wave,

mutual coupling among the UCs has not been considered in the above analysis. Furthermore, we have also demonstrated the mutual coupling among the UCs in finite-sized array in section 5.3 with the help of transmission characteristics. In general, every HIS/EBG UC exhibits band-stop and band-gap feature at the resonant frequency, therefore, mutual coupling effects can be ignored in overall.

5.3 Proposed Geometrical Approach for EBG Array

In this section, we extend the proposed approach for UC to an array. For this, the array of three UCs presented in section 5.2 has been analyzed.

5.3.1 Proposed Approach

A planar array (P-array) and conformed array (C-array) on a cylindrical platform of radius $\boldsymbol{r}$ of EBG unit cells are shown in Figure 5.13(a). The proposed method we divide the conformal surface into seven points A, E, F, C, H, G, and B, to find out the individual phase shifts and then sum them together to determine the eventual $\boldsymbol{\theta}_{\mathbf{shift}}$ of C-array. Subsequently, the addition of $\boldsymbol{\theta}_{\mathbf{shift}}$ with the reflection phase of P-array gives the in-phase property of C-array. In this work, the simulated values of reflection phases of P-array are used as a reference. The points A, E, F, C, H, G, and B are arranged along the conformal or planar surface in a way such that CF = CH, CE = CG, CA = CB. This implies that CF = FE = EA = CH = HG = GB = AB/6. $2\boldsymbol{\theta}_{\mathbf{1}}$, $2\boldsymbol{\theta}_{\mathbf{2}}$, and $2\boldsymbol{\theta}_{\mathbf{3}}$ are subtended by the arcs AB, EG, and FH at the center O, as shown in Figure 5.13(b). It can also be seen in Figure 5.13(a) that the obliquely incident EM waves A˝A and B˝B, E˝E and G˝G, F˝F and H˝H form $\boldsymbol{\theta}_{\mathbf{1}}$, $\boldsymbol{\theta}_{\mathbf{2}}$ and $\boldsymbol{\theta}_{\mathbf{3}}$ respectively w.r.t. to the corresponding transversals OA′ and OB′, OE′ and OG′, OF′ and OH′.

To show the path delays due to incident and reflected waves, the points A″–A′, E″–E′, F″–F′, H″–H′, G″–G′, B″–B′ in Figure 5.13(a) are brought to the observation plane shown in Figure 5.14(a). The reflection of the incident wave at the interfaces A and B (dotted green) is shown in Figure 5.14(a). Expressions (5.8)-(5.10) are written for these interfaces according to the law of reflection. Subsequently, $2\boldsymbol{\theta}_{\mathbf{1}}$, $2\boldsymbol{\theta}_{\mathbf{2}}$, and $2\boldsymbol{\theta}_{\mathbf{3}}$ subtended by the arcs AB, EG, and FH at the center O, given in (5.11), are

determined using Figure 5.14(b). At the same time, the path delays $\Delta \boldsymbol{l_1}$, $\Delta \boldsymbol{l_2}$, and $\Delta \boldsymbol{l_3}$ associated with the incident and reflected waves at the interfaces A, E, and F are expressed in (5.12). Therefore, $\boldsymbol{\theta_{shift}}$ due to points A, E, F, H, G, and B are evaluated using (5.13). Here, β is wavenumber at the operating frequency of the P-array. Once again, the reflection at point C is neglected as it lies on the observation plane. In (5.13), the first and last three terms signified phase shift due to the incident and reflected waves, respectively.

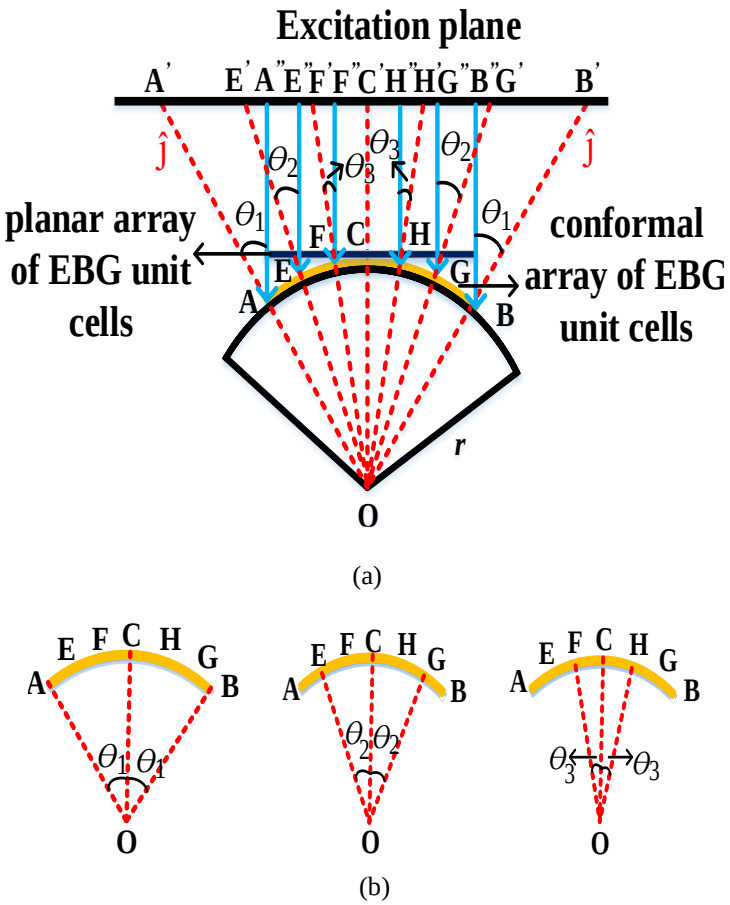

Figure 5.13 (a) P- and C-array of EBG unit cells with incident EM wave making angles $\boldsymbol{\theta_1}$, $\boldsymbol{\theta_2}$ and $\boldsymbol{\theta_3}$ at the extreme and intermediate points A, B, E, F, H and G w.r.t. normal vectors ĵ (b) Angles $\boldsymbol{\theta_1}$, $\boldsymbol{\theta_2}$ and $\boldsymbol{\theta_3}$ formed between arcs AB, EG, and FH at the center O

$$\angle A'AX'' = \angle A''AA' = \angle B'BK'' = \angle B''BB' = \boldsymbol{\theta_1} \qquad (5.8)$$

$$\angle E'EY'' = \angle E''EE' = \angle G'GJ'' = \angle G''GG' = \boldsymbol{\theta_2} \quad (5.9)$$

$$\angle F'FZ'' = \angle F''FF' = \angle H'HI'' = \angle H''HH' = \boldsymbol{\theta_2} \quad (5.10)$$

$$2\boldsymbol{\theta}_m = \frac{W_j \times 360^o}{2\pi r} \text{ (Where, } m = 1\ldots3 \text{ and } j = 1\ldots3) \quad (5.11)$$

$$\Delta \boldsymbol{l}_k = \boldsymbol{r} - \boldsymbol{r}\cos\boldsymbol{\theta}_m \quad \text{(Where, } k = 1\ldots3 \text{ and } m = 1\ldots3) \quad (5.12)$$

$$\boldsymbol{\theta}_{\text{shift}} = 2 \cdot \left(\beta\Delta \boldsymbol{l}_1 + \beta\Delta \boldsymbol{l}_2 + \beta\Delta \boldsymbol{l}_3 + \frac{\beta\Delta \boldsymbol{l}_1}{\cos 2\boldsymbol{\theta}_1} + \frac{\beta\Delta \boldsymbol{l}_2}{\cos 2\boldsymbol{\theta}_2} + \frac{\beta\Delta \boldsymbol{l}_3}{\cos 2\boldsymbol{\theta}_3} \right) \quad (5.13)$$

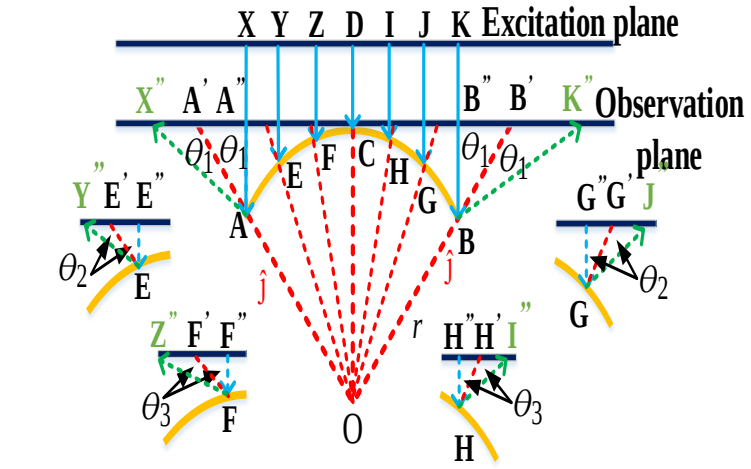

(a)

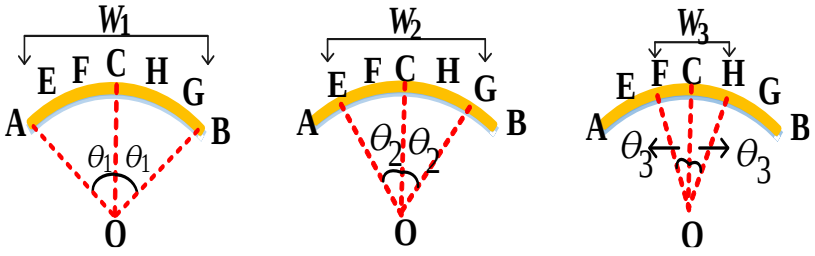

(b)

Figure 5.14 (a) Reflection of EM wave on the interfaces of C-array (b) C-array with respective arc lengths W_1, W_2 and W_3 are lengths of the arc AB, EG, FH

5.3.2 Array of UC-1

We employ the concept mentioned above on the 2x2 P-array of UC-1, as shown in Figure 5.15(a). The P-array is then conformed on a cylinder of $\boldsymbol{r}$ = 40mm along *x*- and *y*-axes, as shown in Figures 5.15(b)-(c). Just to reiterate, the C-array along the *x*-axis is excited by *y*-polarized EM wave, whereas *x*-polarization is employed for the C-array along the *y*-axis. For the determination of $\boldsymbol{\theta}_{\mathbf{shift}}$ for C-array in Figure 5.15(b), we divide the computational domain into six sections as per the concept in Figure 5.13(a). It gives CF = CH = 10.11mm, CE = CG = 20.22mm and CA = CB = 30.33mm respectively and these are then used to compute the values of $\boldsymbol{\theta}_1$, $\boldsymbol{\theta}_2$, $\boldsymbol{\theta}_3$ and $\Delta\boldsymbol{l}_1$, $\Delta\boldsymbol{l}_2$, $\Delta\boldsymbol{l}_3$, listed in Table 5.4, using (5.11)–(5.12).

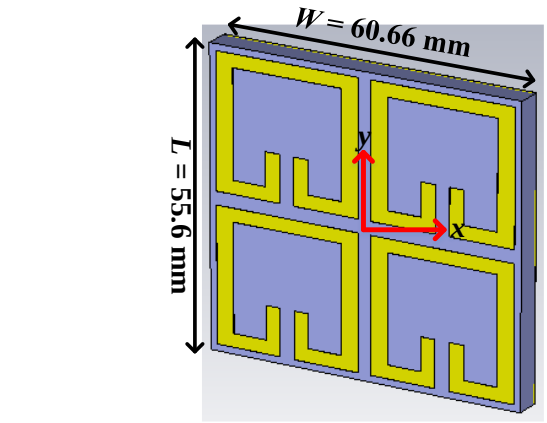

(a)

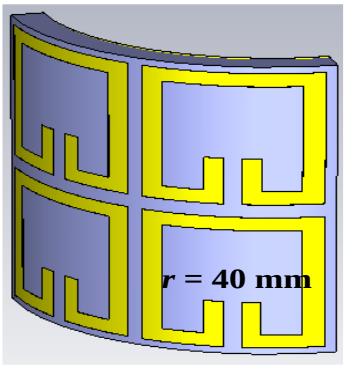

(b)

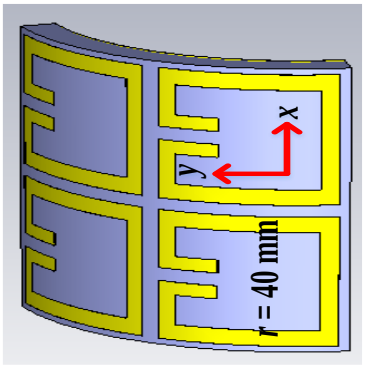

(c)

Figure 5.15 (a) Geometry of the planar array with overall dimensions: *W* = 60.66 mm and *L* = 55.6 mm, Conformed array of UC-1 on cylinder of radii *r* = 40mm along (b) *x*-axis (c) *y*-axis

The respective phase shifts for the incident and reflected EM waves on the interfaces evaluated using (5.13) are also included in Table 5.4. Although, $\Delta\boldsymbol{\theta}_{\mathbf{reflected}}$ and $\Delta\boldsymbol{\theta}_{\mathbf{incident}}$ of 1247.56^0 and 74.78^0 give $\boldsymbol{\theta}_{\mathbf{shift}}$ of 1322.34^0. However, $\boldsymbol{\theta}_{\mathbf{shift}} = 62.34^0$ is mentioned because the reflection phase of an EBG cell or array is recorded between $\pm 180^0$, and any value beyond this range needs adjustment. Therefore $\boldsymbol{\theta}_{\mathbf{shift}} = 1322.34^0$ is adjusted to $\boldsymbol{\theta}_{\mathbf{shift}} = 62.34^0$ by deducting 1260^0 ($7*180^0$) to fit it in the $\pm 180^0$ range. A similar approach when adopted for the C-array in Figure 5.15(c) results in a width of 55.6mm and hence the arc length CF/CH of 9.27mm (55.6/6) after rounding off up to two places after the decimal point. CE/CG and CA/CB become 18.54 and 27.81mm. These are then used in (5.13)–(5.14) to determine the parameters, and hence the $\boldsymbol{\theta}_{\mathbf{shift}}$ has given in Table 5.4.

5.3.3 Array of UC-2

Figure 5.16(a) depicts the 2x2 P-array of UC-2 and the corresponding C-arrays along *x*- and *y*-axes. Then to determine $\boldsymbol{\theta}_{\mathbf{shift}}$ of the C-array in Figure 5.16(b), the width 36.98mm is divided into seven segments resulting in CF/CH, CE/CG, and CA/CB of 6.16, 12.32 and 18.48mm respectively. These values are then used in (5.11)-(5.13) to determine all the parameters and the $\boldsymbol{\theta}_{\mathbf{shift}}$ given in Table 5.4. $\boldsymbol{\theta}_{\mathbf{shift}}$ lies within $\pm 180^{0,}$ and this can be attributed to the smaller width *W* when compared to the earlier two cases.

A similar approach is adopted for the determination of $\boldsymbol{\theta}_{\mathbf{shift}}$ for the C-array in Figure 5.16(c). In this case, the respective arc lengths CF/CH, CE/CG, and CA/CB are 9.74, 19.48, and 29.22mm for the overall width of 58.42mm. These values, in conjunction with (5.11), give $\boldsymbol{\theta}_{\mathbf{shift}}$ of $75.48^{0,}$ as mentioned in Table 5.4.

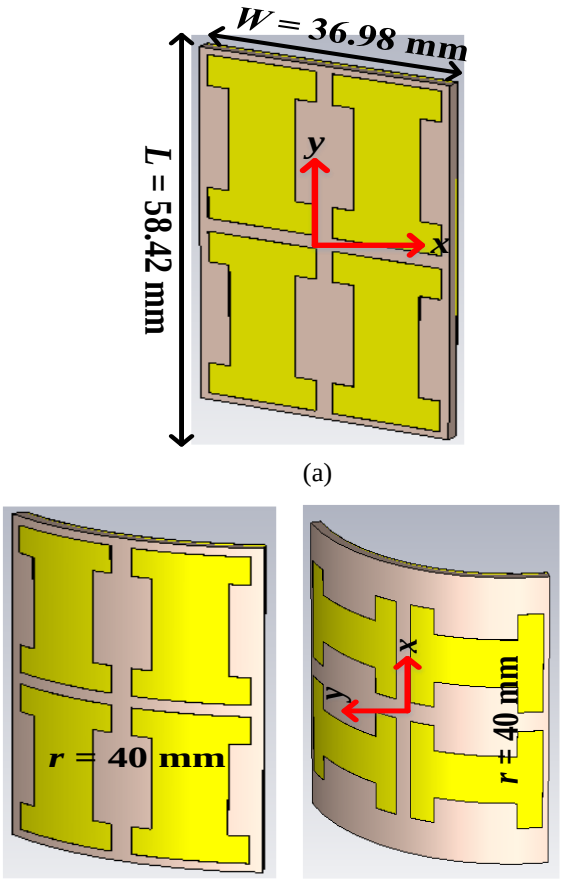

Figure 5.16 (a) Geometry of the planar array with dimensions: *W* = 36.98 mm and *L* = 58.42 mm, Conformed array of UC-1 on cylinder of radii *r* = 40mm (b) along *x*-axis (c) *y*-axis

5.3.4 Array of UC-3

Finally, Figure 5.17 depicts the P- and C- array of 3x3 UC-3 along *x*-and *y*-axes. $\boldsymbol{\theta}_{\mathbf{shift}}$ of the C-array shown in Figure 5.17(b) is obtained by dividing the width of 44.36 into seven points that result in CF/CH, CE/CH, and CA/CB of 7.39mm, 14.78mm and 22.17mm respectively. Substitution of these values in (5.11)-(5.13) all parameters along with $\boldsymbol{\theta}_{\mathbf{shift}}$ are computed as given in Table 5.4. Similarly, diving the length 42.8mm in seven points, the CF/CH, CE/CH, and CA/CB comes out to be 7.13mm, 14.26mm, and 21.39 mm, respectively. Once again, substituting these values in (5.11)-(5.13), $\boldsymbol{\theta}_{\mathbf{shift}}$ with other parameters is calculated as given in Table 5.4. Since the present

array is not as asymmetrical as the previous two arrays; therefore, $\boldsymbol{\Theta}_{\mathbf{shift}}$, in this case, is almost identical for both the polarizations (*x*-and *y*-).

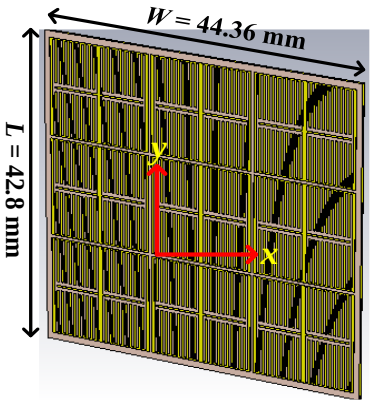

(a)

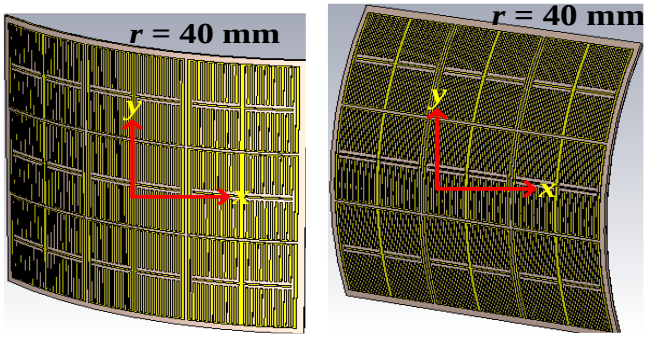

(b) (c)

Figure 5.17 (a) Geometry of the planar array with dimensions: W = 44.36 mm and L = 42.8 mm, Conformed array of UC-1 on cylinder of radii r = 40mm (b) along *x*-axis (c) *y*-axis

TABLE 5.4 Parameters of C-array Determined by Proposed Approach for *y*- and *x*- Polarized EM Wave

Type of UC	*Pol*	r (mm)	$2\Theta_1$ (deg)	$2\Theta_2$ (deg)	$2\Theta_3$ (deg)	Δl_1 (mm)	Δl_2 (mm)	Δl_3 (mm)	$\Delta\Theta_r$ (deg)	$\Delta\Theta_i$ (deg)	Θ_{shift} (deg)
UC-1	*y* –	40	28.9	57.9	86.8	1.2	5.0	10.9	1247.5	74.7	62.3
	x –	40	26.3	52.7	79.0	1.0	4.1	9.1	190.7	48.7	59.4
UC-2	*y* –	40	17.6	35.2	52.9	0.4	1.8	4.1	57.3	38.6	95.9
	x –	40	27.9	55.8	83.7	1.1	4.2	8.6	444.8	170.6	75.4
UC-3	*y* –	40	21.1	42.3	63.5	0.6	2.7	6.0	101.8	48.2	150
	x –	40	20.4	40.8	61.3	0.6	2.5	5.6	89.3	40.6	130

5.3.5 Mutual Coupling

Surface waves (SW) in the form of array guided surface waves (AGSW) propagate through a finite periodic structure and primarily responsible for mutual coupling among the array elements [51]. However, for an infinite regular system, SW vanish and are replaced by floquent current. Since the practically realizable arrays are always finite in size as shown in previous sub-sections, therefore, mutual coupling effects among the elements have been studied in this sub-section. Mutual coupling among the array elements can be demonstrated with the help of transmission characteristics [92] – [93], [132]. For this, a transmission line of 50Ω and EBG array is designed on the top and bottom plane of a PCB, as shown in Figure 5.18. Subsequently, either of the ports (as shown in Figure 5.18) of the transmission line is fed with input power and received at the other. We fed power of 0dB at port 1, and received power is obtained at port 2. The range of frequency (bandwidth) for which the level of S_{21} is lesser than -15 to 20dB, indicates the mutual coupling effects can be ignored [92]-[93], [132]. The width of the 50Ω line for the simulation arrangements of arrays in Figures 5.18 (a), (b), and (c) are 14, 4.8, and 1.1mm, respectively.

The transmission characteristic of all three arrays are shown in Figures 5.19 (a), (b), and (c). It is apparent from the results that for S_{21} of -20dB, the in-phase reflection frequency of all three arrays lies in the bandwidth, and hence, mutual coupling effects can be ignored from the analysis.

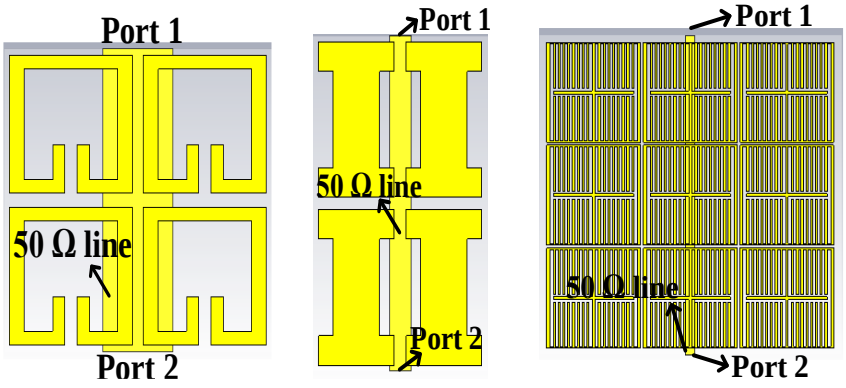

(a) (b) (c)

Figure 5.18 Simulation setup of arrays to obtain S_{21} from port 1 to 2 in arrays (a) UC-1 (b) UC-2 (c) 3x3 array of UC-3

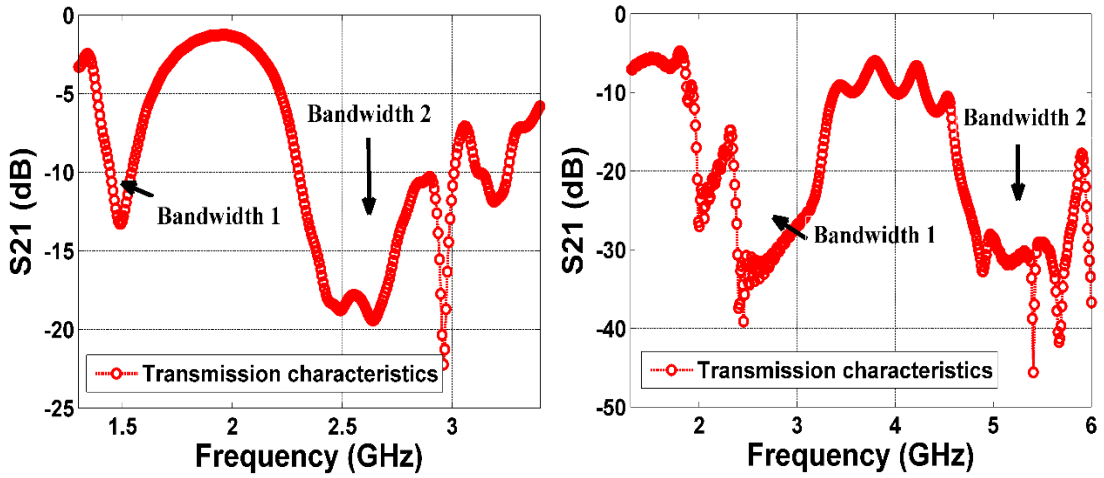

(a) (b)

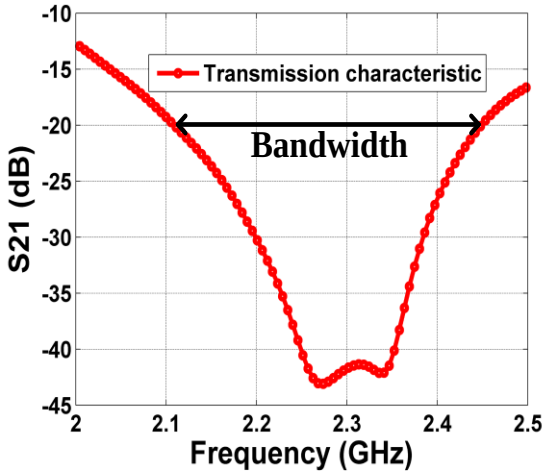

(c)

Figure 5.19 (a) S_{21} at port 2 for array of UC-1 (Bandwidth 1 = 1.45 – 1.51 GHz, Bandwidth 1 = 2.34 – 3 GHz) (b) S_{21} at port 2 for array of UC-2 (Bandwidth 1 = 2.35 – 3.2 GHz, Bandwidth 1 = 4.6 – 5.8 GHz) (c) S_{21} at port 2 for array of UC-3 (Bandwidth 1 = 2.15 – 2.45 GHz)

5.4 Results and Analysis

In this section, we compare the theoretically obtained results for the P-/C-EBG UC and arrays with the results obtained using the simulation tool, CST. For this, the unit cells in Figures 5.9, 5.10, and 5.11 are designed and simulated in CST under UC-

BC, and the in-phase reflection frequencies are located on reflection phase plots in Figures 5.20, 5.21 and 5.22. Then the UCs are incident with both TM and TE mode of excitation of EM wave. For *x*-bend, TM, and *y*-bend, TE mode of polarization is employed to simulate a P-EBG UC. Subsequently, the frequency points (2, 3, and 4) related to $\boldsymbol{\theta}_{\mathbf{shift}}$ obtained in Tables 5.1-5.3 are also located on the plot for the respective UCs and polarizations. These points indicate the shift in frequency to be obtained after conforming to a P-UC for a given $\boldsymbol{r}$. Afterward, we design the C-EBG UCs on a cylindrical platform of $\boldsymbol{r}$ = 40, 50, and 60mm and simulated under UC-BC and again the in-phase frequency points (5, 6, and 7) are located on the reflection phase diagrams as depicted in Figure 5.20, 5.21 and 5.22. This time, the in-phase frequencies are of C-EBG UCs.

The percentage variation in the shift between the simulated and theoretically obtained results for the C-EBG UCs bent along *x*- and *y*- axes are given in Table 5.5. It is apparent from Table 5.5 that the acquired frequency points (2, 3, and 4) indicated due to $\boldsymbol{\theta}_{\mathbf{shift}}$ on reflection phase of P-EBG UCs are close to the in-phase frequency points of C-EBG UCs (5, 6, and 7) and this demonstrates the effectiveness of the proposed method.

Next, the theoretical results are compared with another type of BC, i.e., ME-BC. For this, TEM wave polarized along both *x*-and *y*-axes with magnetic (along the *x*-axis) and electric (along the *y*-axis) truncation at the boundaries is employed for the simulating a P- and C- EBG UC. The orientation of the UCs to the polarized EM wave is identical to the condition mentioned in section 5.2.2. Figures 5.23, 5.24, and 5.25 depicts the simulated plots of the reflection phase of the UCs under the TEM mode of excitation. The in-phase frequency points of a C-EBG UC (5, 6, and 7) are then compared with that of the P-EBG UC obtained by locating $\boldsymbol{\theta}_{\mathbf{shift}}$ (2, 3, and 4) as mentioned in Tables 5.1-5.3.

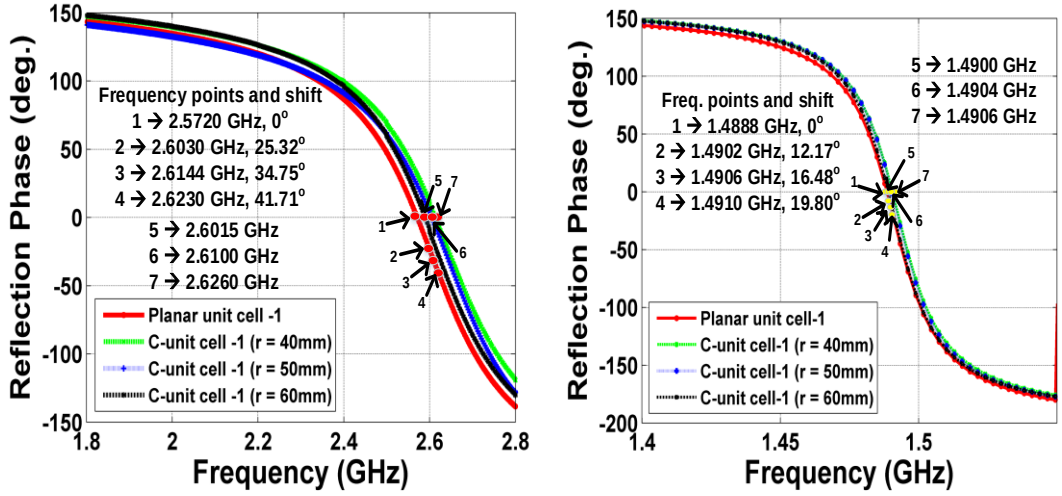

(a) (b)

Figure 5.20 Reflection phases of P-EBG UC-1 with Θ_{shift} indicated by points 2, 3, 4 and C-EBG UC-1 with in-phase points 5, 6, 7 under UC-BC and TE and TM mode of EM wave incidence (a) *x*-bend (b) *y*-bend

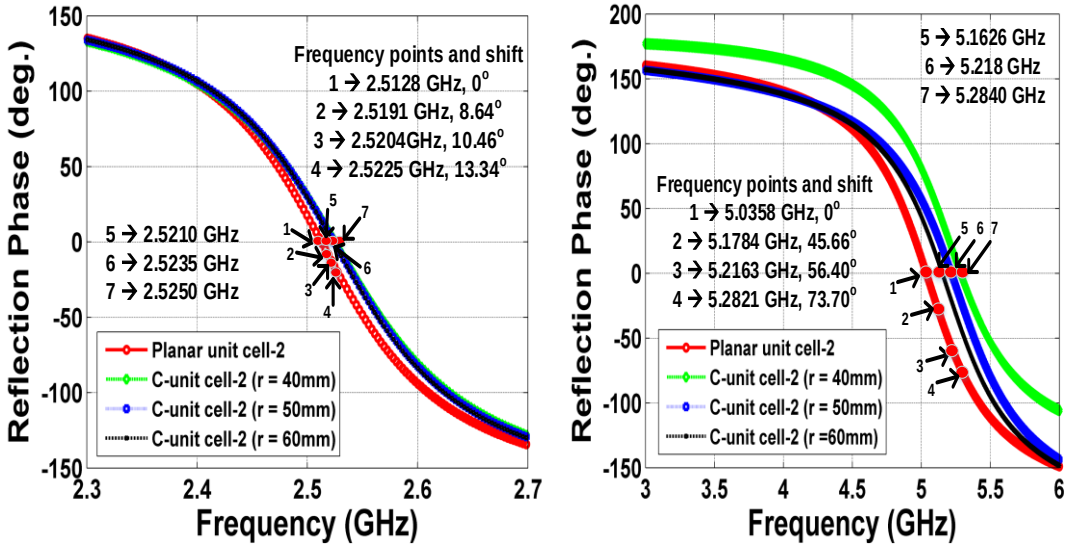

(a) (b)

Figure 5.21 Reflection phases of P-EBG UC-2 with Θ_{shift} indicated by points 2, 3, 4 and C-EBG UC -2 with in-phase points 5, 6, 7 under UC-BC and TE and TM mode of EM wave incidence (a) *x*-bend (b) *y*-bend

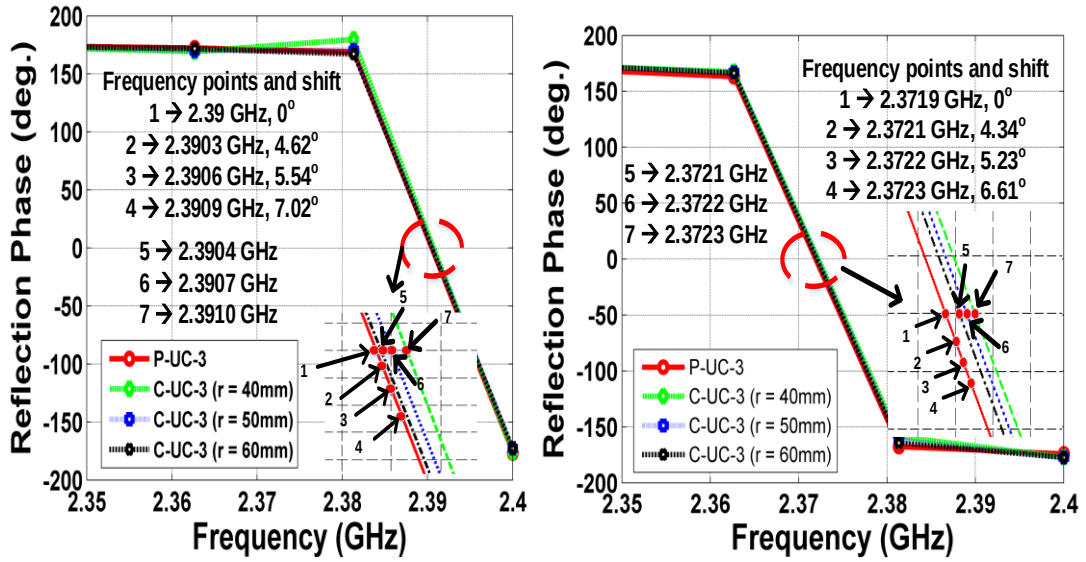

(a) (b)

Figure 5.22 Reflection phases of P-EBG UC-3 with Θ_{shift} indicated by points 2, 3, 4 and C-EBG UC-3 with in-phase points 5, 6, 7 under UC-BC and TE and TM mode of EM wave incidence (a) *x*-bend (b) *y*-bend

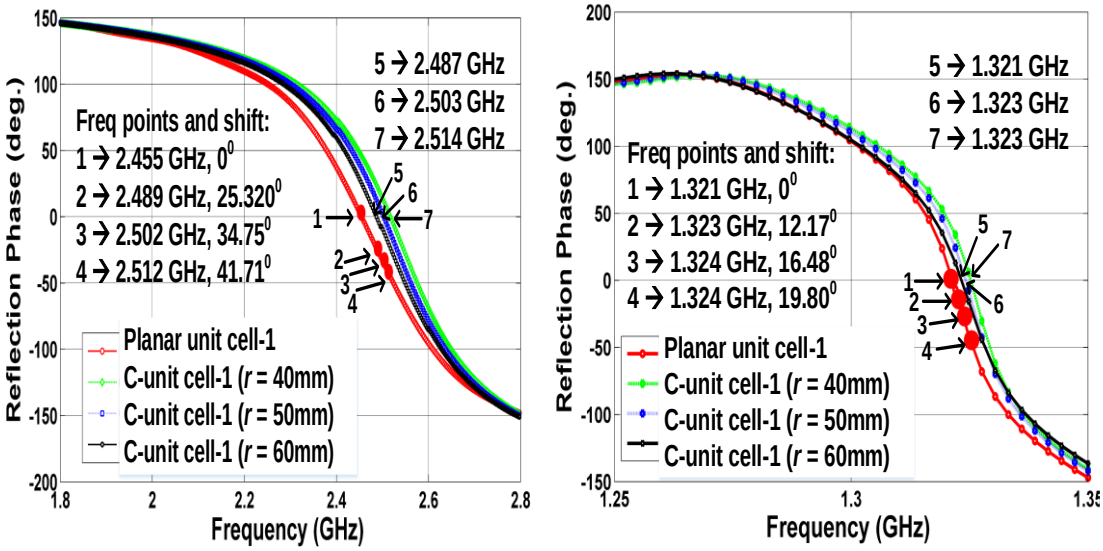

(a) (b)

Figure 5.23 Reflection phases of P-EBG UC-1 with Θ_{shift} indicated by points 2, 3, 4 and C-EBG UC-1 with in-phase points 5, 6, 7 under ME-BC and TEM mode of EM wave incidence (a) *x*-bend (b) *y*-bend

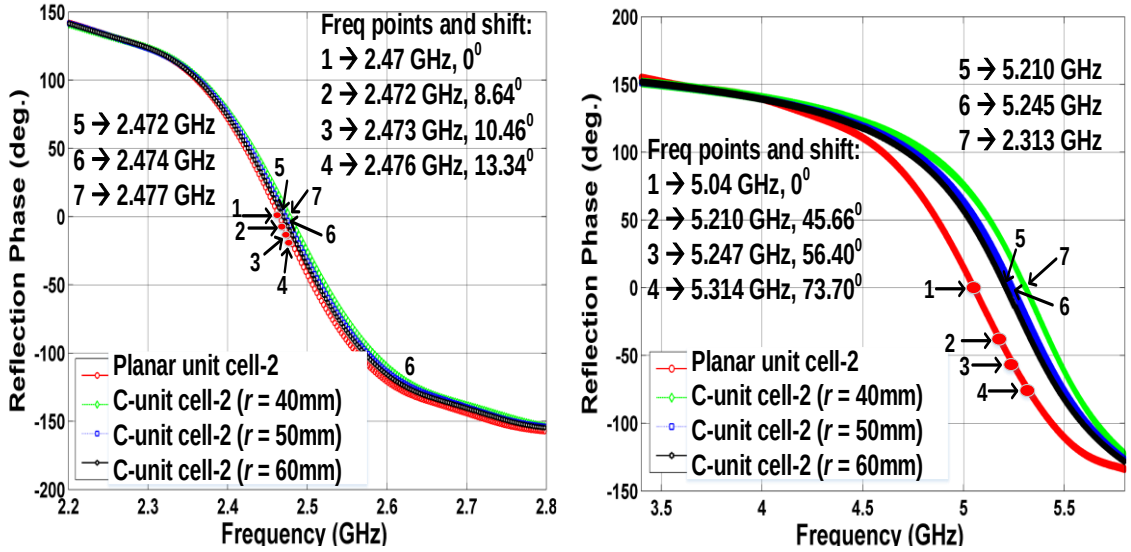

(a) (b)

Figure 5.24 Reflection phases of P-EBG UC-2 with Θ_{shift} indicated by points 2, 3, 4 and C-EBG UC-2 with in-phase points 5, 6, 7 under ME-BC and TEM mode of EM wave incidence (a) *x*-bend (b) *y*-bend

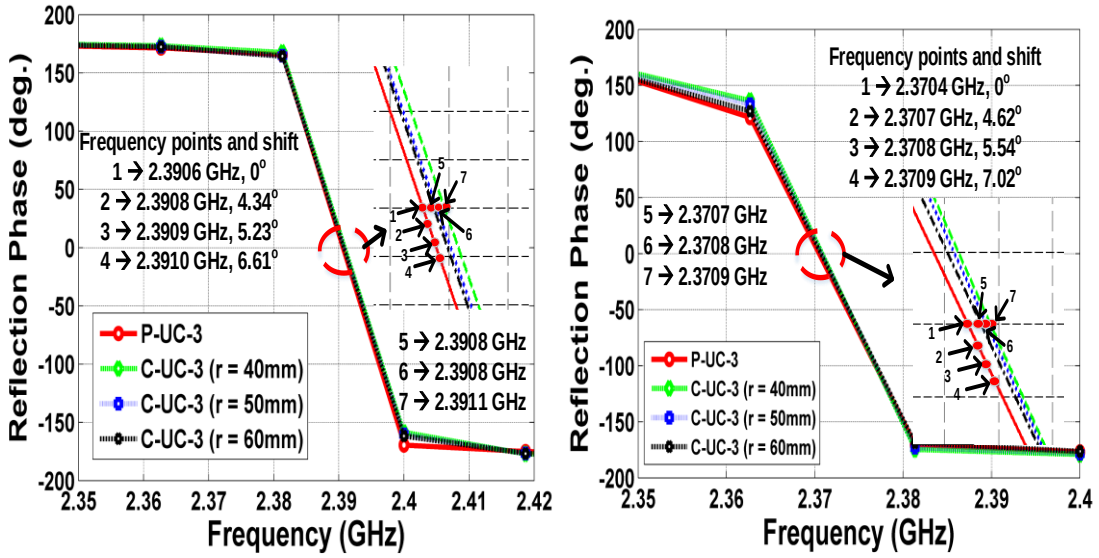

(a) (b)

Figure 5.25 Reflection phases of P-EBG UC-3 with Θ_{shift} indicated by points 2, 3, 4 and C-UC-3 with in-phase points 5, 6, 7, under ME-BC and TEM mode of EM wave incidence (a) *x*-bend (b) *y*-bend

After comparing the simulated and theoretically obtained results and their variations as listed in Table 5.5, it is evident that the simulated in-phase frequency points of C-EBG UCs are in close agreement with the P-EBG UCs incorporated with $\boldsymbol{\theta}_{\mathbf{shift}}$ in the reflection phase diagram. Interestingly, P-/C-EBG UC-3 does not show substantial variation in simulated and theoretical results. It is due to the compact size of the UC that the $\boldsymbol{\theta}_{\mathbf{shift}}$ itself is very small. Besides, due to the symmetrical geometry of the UC-3, the variations along *x*- and *y*-bend are almost identical. We can conclude from the Figures 5.20-5.25 that the proposed geometrical approach to predict the $\boldsymbol{\theta}_{\mathbf{shift}}$ of C-UC is independent of boundary conditions and polarization. It implies that the proposed system in this chapter can expect $\boldsymbol{\theta}_{\mathbf{shift}}$ that is applicable for any type of boundary condition and polarization as well.

TABLE 5.5 Percentage Variation of Results between the Theoretical and Simulated Values

UC	radius (mm)	percentage variation		percentage variation (*TEM*)	
		TM	*TE*	(*x*-bend)	(*y*-bend)
1	40	0.114	0.027	0.080	0.075
	50	0.168	0.013	0.040	0.075
	60	0.057	0.013	0.080	0.152
2	40	0.010	0.036	0.040	0.018
	50	0.123	0.032	0.040	0.038
	60	0.075	0.030	0	0
3	40	0.004	0.008	0.004	0
	50	0.004	0	0.004	0
	60	0.004	0	0	0

Then, we demonstrate the efficacy of the proposed method to determine $\boldsymbol{\theta}_{\mathbf{shift}}$ of C-array. First, the 2x2 P- and C-arrays in Figures 5.15 and 5.16 are simulated under TEM excitation with ME-BCs as practical arrays are finite in dimension, and UC-BC cannot be applied. It leads to increases in mesh cell size drastically due to the large computational area. The simulated reflection phases of P- and C-arrays of both the UCs excited by *y*- and *x*- polarized TEM waves are given in Figure 5.26. The corresponding variation in the shifts for the C-array bent along *x*- and *y*-axes are 0.04

%, 0 % and 0 %, 0 % for ***r*** = 40mm. Once again, the closeness of the frequency points obtained in simulation and using the proposed technique proves the effectiveness of the presented approach for arrays as well.

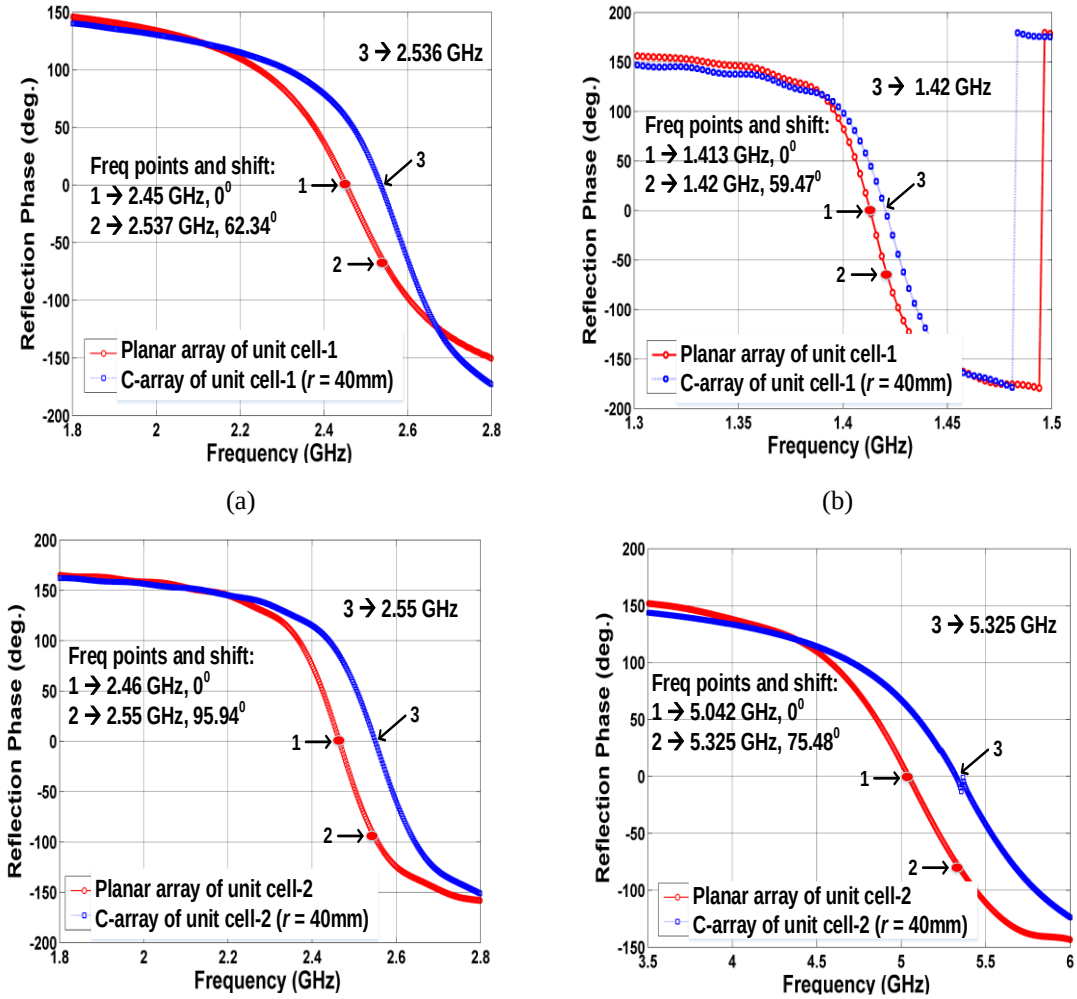

Figure 5.26 Reflection phases of P-arrays 1-2 with Θ_{shift} shown by point 2 and C-arrays 1-2 with in-phase reflection points 3 under ME-BC with TEM excitation (a) x-bend (Array-1) (b) y-bend (Array-1) (c) x-bend (Array-2) (d) y-bend (Array-2)

To further demonstrate the effectiveness of the proposed approach, we prototyped an array of 3x3 UC-3 (proposed by us), as shown in Figure 5.17. The prototyped array is shown in Figure 5.27(a). The array is designed on RO5880 with *h*

and ε_r of 0.381mm and 2.2, respectively. The gap among the UCs is 0.6mm along *x*- and *y*-axes. For convenience in the measurement of the reflection phase, P-and C-arrays are attached to a polystyrene sheet. Two-antenna arrangement one acting as a transmitter and other as the receiver is used to measure the phase of S_{21} in VNA. Both the transmitter and receiver antennas are separated by an approximate distance of $\lambda/2$ = 62mm, corresponding to an in-phase reflection frequency of 2.372 and 2.39GHz. Since the reflection phase of a UC or array is measured at the surface, therefore, the phase of 180^o ($\beta l = \pi$) was subtracted from the measured phase of S_{21}.

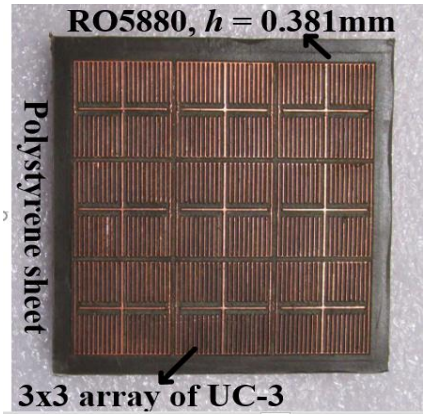

(a)

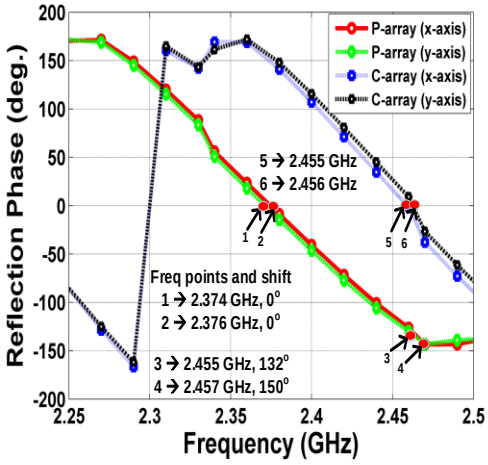

(b)

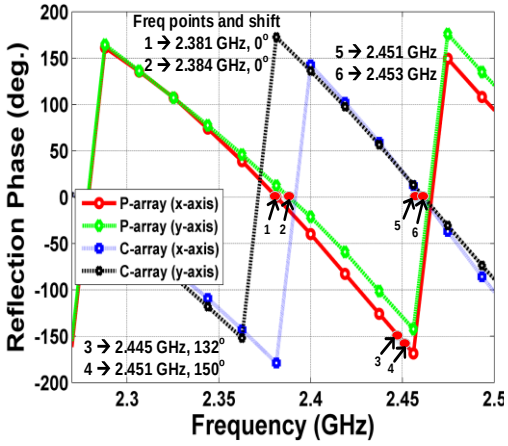

(c)

Figure 5.27 Prototyped array of UC-3 along with the simulated and measured reflection phase diagrams (a) Prototyped array on RO5880 (b) Simulated reflection phases of P-and C-array excited with TEM wave (c) Measured reflection phases of P-and C-array with TEM wave

A similar setup for the simulation of P- and C-arrays is designed in CST as well in which the array has open boundaries rather than ME-BC. The simulated and measured reflections phases of the P- and C-arrays are depicted in Figure 5.27(b) and (c). The variation in the shifts for the simulated and measured C-array bent along *x*- and *y*-axes are 0.163% and 0.122%, respectively. The variation in measured and simulated in-phase reflection frequencies of P-array incident with *x*- and *y*-polarized TEM waves are 0.3% and 0.33%, respectively. Slight increase of %variation of measurement results in comparison to simulated is because the conformal array had some irregularity at the edges, this might have generated leaky waves, which in turn couples with the incident EM wave and shifts the reflection phase diagram. Once again, the closeness of the frequencies in simulation and measurement proves the effectiveness of the proposed geometrical approach.

5.5 Conclusion

In this chapter, we presented a geometrical approach to determine the shift in the reflection phase of C-EBG UC and C-array. The technique makes use of the law of reflection of EM wave and elementary geometry to predict the change in the angle of reflection after conforming to a P-EBG and P-array. In the proposed method, the computational domain of a unit cell consists of two sections, whereas the array consists of six sections. The results obtained using simulation under UC and ME-BC and from the proposed technique are in excellent agreement. We know that the meshing of C-UC/C-array in the simulation environment is critical because discontinuity in the edges might appear while conforming the cell or array, and hence increase in the number of mesh cells is needed to smoothen the computational area. However, it comes at the cost of increased simulation time of the entire UC/array. On the other hand, the proposed method can predict the in-phase reflection point conveniently in very less time. Due to the unavailability of materials for in-house fabrication of arrays consisting of two other UCs, the proposed approach is validated with the only third type of UC. Since the only oblique incidence of EM wave on unit cell and the array is considered in this work, we would like to investigate the working of the presented theory for different incidence angles of EM wave.

Chapter 6

Conformal EBG Backed Antenna for WBAN Applications

This chapter is based on the following research paper:

- D. Rano, M.S. Hashmi, and M.A. Chaudhary, "Design and Experimental Investigation of Conformal Compact and Low-profile Antenna for Wireless Body Area Network Application," *IEEE Transaction on Biomedical Circuits and Systems*. (Under review).

In this dissertation, so far, we have discussed the significance of EBG structures in enhancing the properties of a low profile antenna. The structure we presented in chapter 4 was an EBG backed antenna with a minimal footprint, low profile, and suitable for smartwatch applications in WBAN. However, the incorporated antenna was not conformal and found limited usefulness in body-worn applications. Therefore, in this chapter, we propose a design of a conformal, low-profile, and compact EBG backed monopole antenna operating at the MBAN band (2.36 – 2.4 GHz). We designed the antenna and the EBG unit cell on the RO5880 board. The respective dimensions of the antenna and the unit cells are 44.36 x 42.8 x 0.832 mm^3 and 13.8 x 13.4 x 0.381 mm^3. We have also presented the polarization stability of the proposed unit cell to the incident TE and TM modes at angles 15^o, 30^o, 45^o, 60^o, and 75^o. A close symmetry of the proposed unit cell along *x*-and *y*-axes results in excellent polarization stability for the conditions mentioned above. We also observed an excellent agreement between the resonant frequency (f_r) achieved from the developed equivalent circuit

model of the unit cell, f_r = 2.38GHz, and the full-wave analysis using CST, f_r = 2.37, and 2.39 GHz, for TE and TM modes respectively.

We have also designed an array of unit cells arranged in a 3x3 pattern, acting as an antenna reflector. The array exhibits in-phase reflection frequency at 2.38 GHz by the terminating the boundaries along *x*–and *y*–axes by magnetic-electric walls. We then incorporated the developed EBG array to the low-profile monopole antenna for performance improvement. The low profile nature of the standalone antenna and the EBG array provides the conformability feature, and it is demonstrated by bending it for three distinct radii (*r*) of 40, 50 and 60mm. We measured the performance of the EBG incorporated conformal antenna on the body at the wrist and shoulders. The design exhibits excellent agreement between the measured and simulated results, whereby it achieves band-gap, gain, and efficiency of 2.34 – 2.65 GHz, 5.5dB, and 72%, respectively.

6.1 Background and Related work

The proliferation of wireless health monitoring in the last decade has led to an improved scenario of health standards. It facilitates remote tracking of essential physiological parameters such as glucose content, temperature, blood pressure, and many more [1]–[3], [115]. It necessitates the sensor nodes placed on-body to be compact, conformal, low-profile, and operate at low power [115]. An antenna is an integral part of these devices to establish a link between sensor nodes either along the body (on-body) or away from the body (off-body) [5] – [6], [17] – [18], [23] – [25]. As a consequence, such antennas need to be compact, low-profile, and optimum in performance in terms of gain, efficiency, human body loading, and specific absorption rate (SAR) [18] – [23]. However, the gain and efficiency of such antennas drop considerably, and SAR near the adjacent tissues increases with the size reduction. Besides, antennas operating close to the body adversely affect the matching and resonant frequency (f_r) as well. Another critical feature of WBAN devices is their ability to conform to body parts like wrists, biceps/triceps, legs, shoulders, ears, and many more. However, conformability adds a challenge to the overall design. The

bending leads to alteration of electrical length, and hence resonance might occur at a different frequency than the desired one, as we observed in Chapter 5.

It has been established that the radiation property and SAR values of an antenna can be improved substantially by incorporating EBG/HIS in the ground plane [41]–[48]. We have already discussed the advantages of the EBG surfaces when incorporated with a low-profile antenna in Chapter 4 in detail. However, for understanding, we have again presented here a brief of EBG surfaces and their applications. EBG surfaces are the artificially engineered structures that exhibit in-phase reflection for an incident EM wave (through reflection phase diagram) and band-gap property (through dispersion diagram) [41]–[48]. In-phase reflection results in constructive interference of reflected and incident electric field from an antenna at the far-field hence assist in enhancing the radiation properties [48]. Besides, the band-gap feature rejects the propagation of surface waves along the substrate (reduces diffraction at the edges) and hence minimizes SAR [41]–[43]. However, the design of compact, conformal, polarization stable, and surface wave rejection is tough to achieve from the same EBG unit cell. We discuss these terms and complexity involved in achieving them from the WBAN perspective with the help of a few standard EBG cells proposed in the literature.

Compactness and Conformability: In general, thinner substrates are natural to conform to any conformal surface like a cone or cylinder [33] – [37]. It is the only reason the textile fabric has attracted researchers in the first place for the design of the WBAN antenna. However, in doing so, the overall size of the EBG unit cells increases. For example, the IDE cell in Chapter 4 has a thickness of 1.524mm and has been designed on an unbendable RO4350B PCB, as shown in Figure 6.1(a). But if the same EBG unit cell is designed on RO4350B but with a thickness of 0.381mm (one of the standard thickness manufactured by Rogers Corporation), it is evident that it achieves bendable property. However, the in-phase frequency now shifts to a higher value, as evident from the reflection phase plot in Figure 6.1(b) (under TM mode of excitation). The original in-phase frequency can be restored by increasing the width of the IDE unit cell. Consequently, it leads to an increase in the overall size of the antenna.

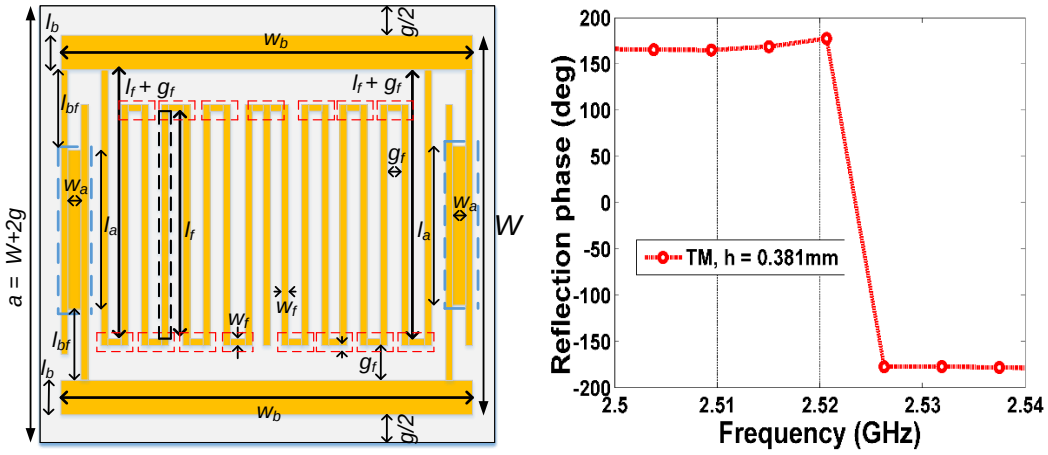

(a) (b)

Figure 6.1 (a) The geometry of the IDE unit cell (b) Reflection diagram of an IDE unit designed on RO4350B board with thickness od 0.381mm

Polarization Stability: This is another critical aspect involved in the design of an EBG unit cell. It is explained here with the help of two standard unit cells presented in [38] and [39]. Figure 6.2(a) shows an asymmetrical EBG unit cell designed on RO4003C [38]. For the dimensions given in Figure 6.2(a), the unit cell exhibits separate in-phase frequencies when excited under TE and TM modes of EM wave, as shown in Figure 6.2(b). It indicates poor polarization stability of the unit cell. Another EBG cell designed on foam and proposed in [39] is almost symmetrical about *x*-and *y*-axes, as shown in Figure 6.3(a). However, the in-phase frequency points of the unit cells under the TE and TM mode of excitation are different, as shown in Figure 6.3(b). Once again, the unit cell indicates poor polarization stability.

We know from Chapter 4 that the EBG ground plane is separated from a low profile antenna by a minimal height [43], [46] – [48], [92] – [93]. We also know from the cavity model of patch antenna that although TM mode is the dominant mode of propagation, however, TE mode can also exist in the region very close to it [58]. It is then imperative that the EBG cell must exhibit the same band of operation for both the TE and TM modes. We can, therefore, conclude that the design of a polarization stable unit cell is very crucial.

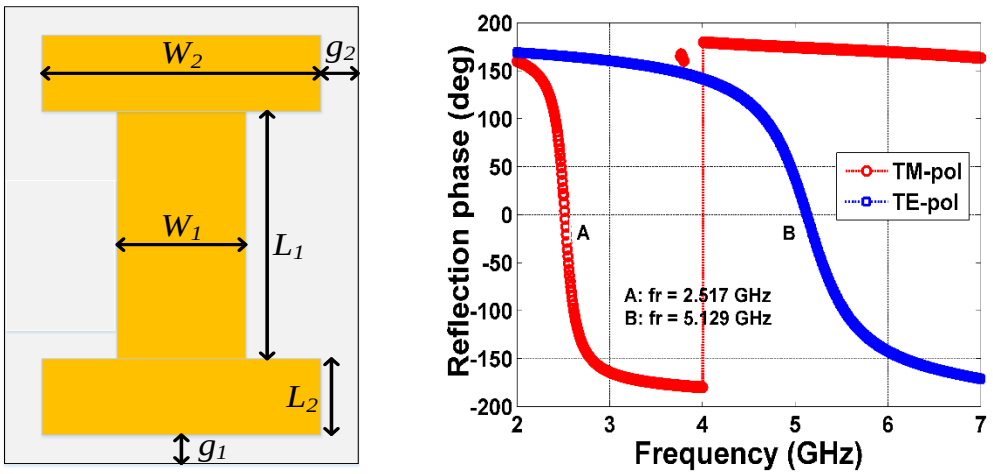

(a) (b)

Figure 6.2 (a) Geometry of the unit cell in [38] with dimensions: W_1 = 9.75mm, W_2 = 16mm, L_1 = 16.86mm, L_2 = 5.1mm, g_1 = 1.075mm, g_2 = 1.245mm, height of substrate = 2mm (b) Reflection phase plot of the unit cell under TE and TM mode of incidence

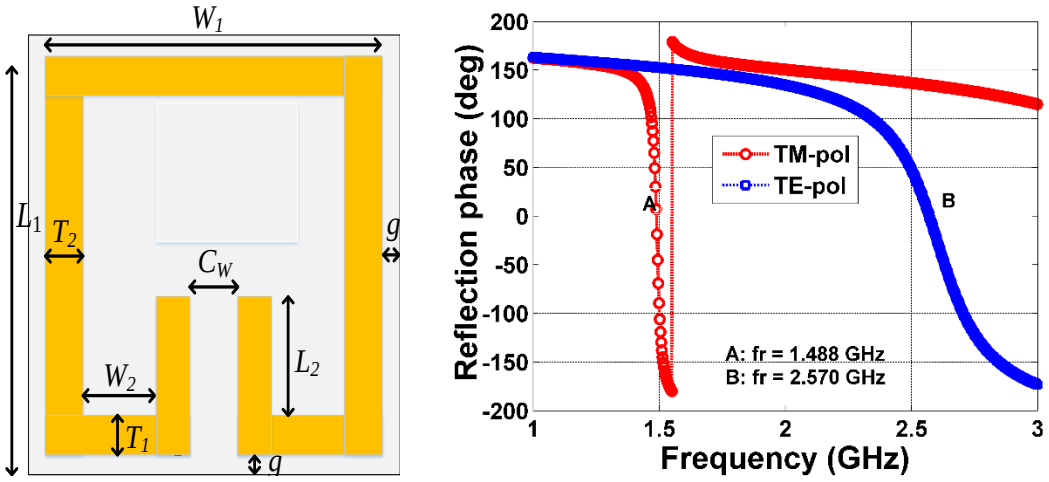

(a) (b)

Figure 6.3 (a) Geometry of the unit cell in [39] with overall dimensions: W_1 = 27.83mm, W_2 = 6.4mm, L_1 = 25.3mm, L_2 = 6.32mm, T_1 = 2.53mm, T_2 = 3.34mm, C_W = 2.78mm, and g = 1.25mm, height of substrate = 5mm (b) Reflection phase plot of the unit cell under TE and TM mode of incidence

Surface wave rejection: Another essential aspect of EBG surfaces is their ability to discard the propagation of surface waves. This feature helps in reducing the diffraction of surface currents at the edges of PCB and minimizes back lobes [43] – [45]. We explain here the surface wave rejection ability of an EBG array with the help of the simulation setup we devised in Chapter 4 and an example (unit cell designed in Figure 6.3(a)).

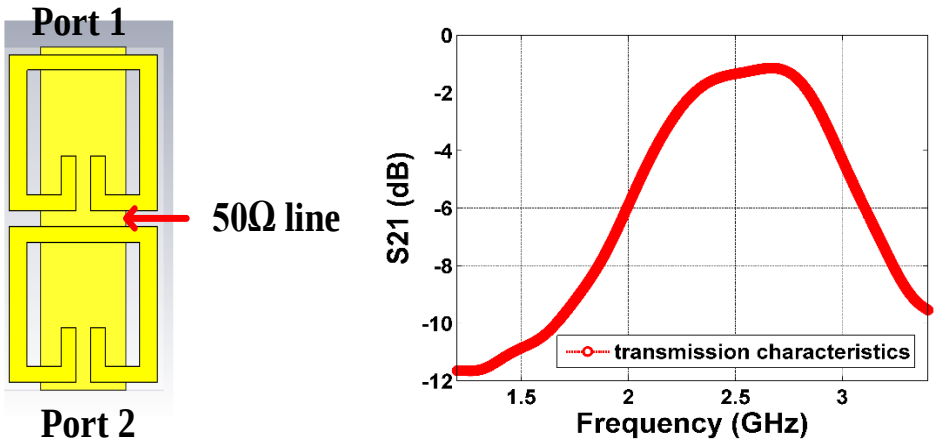

(a) (b)

Figure 6.4 (a) 2x1 arrangement of EBG unit cells in [39] with 50Ω at the back (b) Simulated transmission result of the array

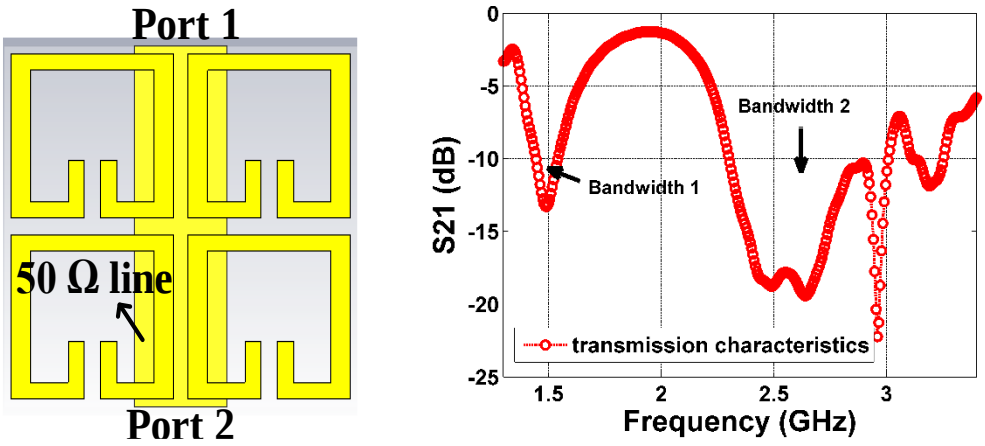

(a) (b)

Figure 6.5 (a) 2x2 arrangement of EBG unit cells in [39] with 50Ω at the back (b) Simulated transmission result of the array

Figure 6.4 (a) shows a 2x1 array of unit cells proposed in [39]. To extract, the level of surface wave rejection of the arrangement in Figure 6.4(a), a 50Ω line of 14 mm is printed at the back of the PCB. Next, an RF power of 0dBm is fed into port 1 and received at port 2, as shown in Figure 6.4(b). It is evident from the plot that the array is unable to suppress surface waves at the operational frequency of the unit cells, as shown in Figure 6.3(b). However, if an array of 2x2 unit cells, as shown in Figure 6.5(a), are used instead of 2x1 arrangement, a clear band-gap appears at the desired frequencies, as depicted in Figure 6.5(b). It indicates that the selection of array arrangement in suppressing surface waves is very tricky, and it might increase the overall size of the antenna in doing so.

In this context, several EBG/HIS incorporated antenna (EIA) meeting the desired performance for WBAN has been reported. For example, a conformal and dual-band EBG array of size 150x170mm^2 exhibits in-phase reflection at 2.4–2.7GHz and 5.04–6.04GHz [33]. This design is suitable for ISM bands (2.4 and 5.8GHz) but suffers from sensitivity to TE and TM modes incident at different angles. Besides, the prototyping of the EBG unit cell in that design is problematic as it involves laser micromachining. Designs based on textile fabrics are an excellent candidate for body-worn antennas as they possess suitable conformability [17]–[21], [25]–[27]. However, due to the low dielectric constant and thinner material, often the size of the overall EIA is huge [33] – [34]. Also, the conductive material needs to tack to the surface of the textile with the help of adhesives. It certainly changes the dielectric constant of the system, and operational bandwidth may change. Besides, inscribing intricate designs of EBG cells, as proposed in Chapter 4 on textile materials, is very challenging.

A dual-band textile monopole antenna backed by an array of 3x3 EBG unit cells successfully suppresses surface wave propagation and hence significantly reduces SAR values [34]. However, this design has a large footprint (150x150 mm^2) and achieves an on-body gain of -5dBi. It also includes a large unit cell of dimensions 50x50 mm^2 when compared to previous work [33]. Similarly, a CPW fed conformal monopole antennas backed by 3x3 and 4x4 array of EBG UC exhibit respective gain of 8.55 and 6.4 dBi [35]–[36]. Once again, these designs suffer from a large footprint

area (124x124 and 120x120mm^2). These designs also do not discuss the polarization stability feature under TE–TM mode of incidence and surface wave suppression ability of the UC. Furthermore, the design in [35] was hand cut or tacked together using spray adhesive, and as a consequence, there may be discontinuity on the surfaces when conformed on cylindrical/conical platform, which might alter the desired performance.

Another EIA of a comparatively smaller size than [33] – [36], i.e., 100x100 mm^{2,} exhibits gain of 2.5dBi at 2.45 GHz and 4dBi at 5GHz when operated close to the human body [37]. However, this design doesn't provide conformability analysis (measured) and surface wave rejection ability of the UC/array. Furthermore, polarization stability analysis is also not provided in the given work. It is important to note that the compactness of antennas is critical in WBAN applications. This aspect is addressed by the compact conformal monopole antennas backed by 2x1 (68x38 mm^2) and 2x2 (62x42 mm^2) EBG arrays in [38]–[39]. However, these designs find limited usefulness due to the high dependence of unit cells on the polarization of incident EM wave, as shown in Figures 6.2(b) and 6.3(b). The unit cells used in both the works are highly asymmetrical, which leads to poor polarization stability to obliquely incident TE and TM waves as well. Moreover, the asymmetry also creates distinct in-phase f_r for *x*- and *y*-polarized TEM waves for the respective UC (2.57 and 2.52 GHz for *x*-pol and 1.5 and 5.1 GHz for *y*-pol) as evident from Chapter 5.

After an extensive literature survey provided above, the following inference can be made.

1) Textile based antennas and EBG surfaces are an excellent candidate for conformability. However, due to the smaller thickness and low dielectric constant, the overall size of the antenna is impractically larger from the WBAN perspective.

2) The design of polarization stable unit cells is crucial from the antenna's performance point of view, which has been ignored in previous researches.

3) Surface wave rejection ability to reduce diffraction at the edges and

minimize back lobes contributing to high SAR values has also been ignored by most of the previous researches.

An IDE EBG unit cell proposed by us in Chapter 4 addresses many of the above concerns associated with the antennas for WBAN. In this design, antenna, and UC, possesses the most compact dimension of 36x38 mm^2 and 14.3x14.5 mm^2. The design shows excellent polarization stability of the UC to incident TE-TM (at a different angle) and TEM (*x*-and *y*-pol) wave. The EIA exhibits an on-body gain of 3.7 dBi and an efficiency of 50%. However, this design doesn't report conformability features on a cylindrical surface and, therefore, may not be appropriate for numerous applications within the realm of WBAN.

Therefore, in this chapter, the design of a conformal and compact EBG backed monopole antenna for WBAN application (specifically in MBAN band) is proposed. The unit cell proposed in this chapter is of dimension 13.4x13.8 mm^2 and is the smallest reported so far and is almost symmetrical. The proposed UC display excellent stability to TE-TM and TEM wave incident obliquely owing to their symmetric designs. Besides, the proposed UC exhibits excellent surface wave rejection ability, which is analyzed by the dispersion diagram with the help of Eigenmode solver [53], [92] – [93]. The work presented in this chapter also elaborates on the mutual coupling or surface wave rejection ability of the proposed array with the help of transmission property. The conformability of the proposed EIA is shown through the conformal platform of radii r = 40, 50 and 60mm. Finally, the SAR values are measured on the skin and homogeneous liquid phantoms developed by us in Chapter 5 by incorporating the EIA on an elliptical container holding them. The EIA for a 3x3 EBG backed antenna achieves superior gain, SAR values, efficiency, and conformability.

6.2 Blocking EBG Unit Cell

In this section, we present a new EBG unit cell called *Blocking Type*. We derived the physical parameters of the unit cell from the equivalent circuit model proposed in Chapter 4. We did a parametric variation of a few parameters to obtain the desired

resonance at 2.38 GHz. The proposed circuit model is validated through full-wave analysis in CST. We used TE, TM, and TEM modes of excitation to check the stability of the unit cell as well as the appropriateness of the circuit model. Furthermore, the polarization stability of the unit cell is assessed in this section with the help of TE and TM modes incident at different angles. Finally, the ability of the unit cell to suppress surface wave propagation is shown with the help of a dispersion diagram in CST.

6.2.1 Unit Cell and *LC*-Circuit Model

The proposed UC, with all the dimensions, is shown in Figure 6.6(a). It consists of fingers running from the top and bottom of the base metal and has disjoint at the center, as shown in dotted red in Figure 6.6 (a). The circuit modeling approach adopted here is identical to that used in chapter 4. For an incident *y*-polarized EM wave, the surface current takes the path through the metallic strips, as depicted in Figure 6.6(b). At the center of the bottom strip, the surface current splits equally and takes the path, as shown in dotted blue and red lines in their respective halves in Figure 6.6(b). Finally, the surface current from both the sections meet at the central strip shown in dotted green. Interestingly, due to the disconnection between the fingers and the central horizontal stripe, the flow of surface current is discontinuous, as apparent from Figure 6.6(b) and hence is called *Blocking Type* EBG (B-UC).

We know from previous works that the metallic portions through which the surface current flows imitate as inductors *L* and discontinuous areas (gap) as capacitors *C* [18]-[20]. It results in the distribution of *L* and *C* along the B-UC, as shown in Figure 6.7(a). The splitting of the surface current at the bottom results in two parallel branches of inductors. Moreover, post splitting the surface current flows in series (shown in blue and red in their respective halves), and the inductors L_2, L_3, and L_4 are in series as well. Another set of parallel inductors L_5 due to fingers are connected to L_6 through C_g. For clarity, the distribution of L_5, L_6, and C_g are only shown for a single quadrant. Similarly, distribution is expected for the other three quadrants as well. Eventually, the parallel branches terminate in series connection with L_1. Here, C_{c1} and C_{c2} are the coupling capacitance among the adjacent B-UC and are given by (6.1).

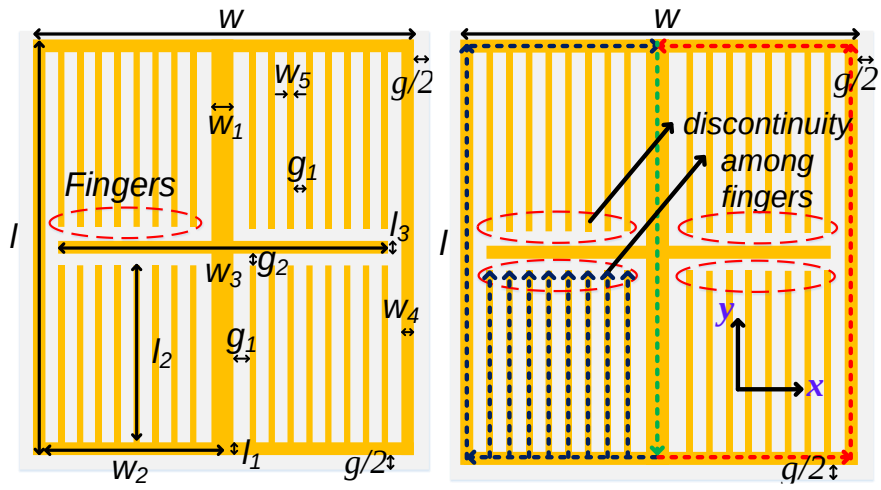

(a) (b)

Figure 6.6 (a) UC of B-type EBG with dimensions [*w*: width of the patch, *l*: length of the patch, *g/2*: gap on either side of the patch (top and bottom) (b) Surface current flow through metallic portion for *y*- polarized EM wave

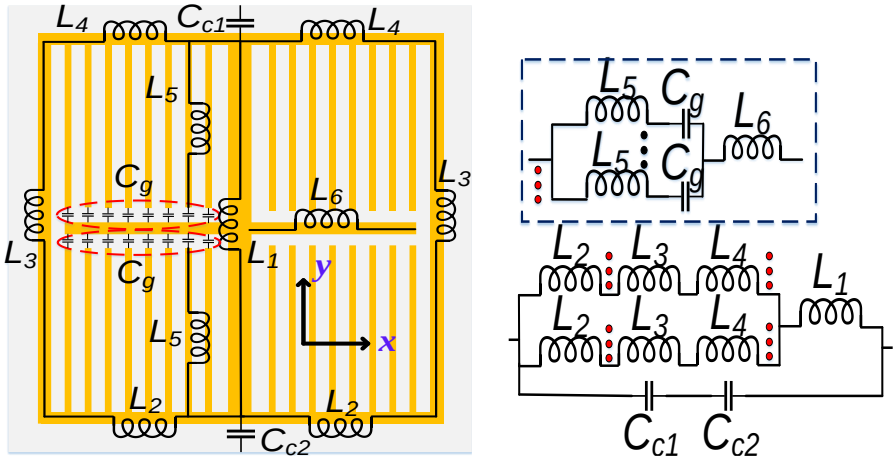

(a) (b)

Figure 6.7 (a) Distribution of inductances and capacitances due to surface current flow across the UC (b) *LC* modeling to extract f_r

$$C_{c1} = C_{c2} = \frac{17 \times \varepsilon_o \times w \times (\varepsilon_r + 1)}{\pi} \times \cosh^{-1}\left(\frac{w+g}{g}\right) \qquad (6.1)$$

Here, w is the width of the B-UC, g is the gap width, while ε_o and ε_r are the permittivity of the air and substrate, respectively. Now, it is essential to mention that the distribution mentioned above of lumped elements is applicable only for the *y*-polarized EM wave. The distribution of *LC* components can change for an *x*-polarized wave. The equivalent circuit model of the UC to extract f_r is shown in Figure 6.7 (b). It consists of two parallel branches of series inductors L_2–L_3–L_4 and finally connected to a vertical strip of inductance L_1 identical to Figure 6.7 (a). The branches of parallelly connected L_5 and C_g (equivalent to the number of fingers) with a series connection of L_6 are shown separately in the dotted blue box in Figure 6.7 (b). This set of the branch appears four times after L_2 and L_4 in the top and bottom of the respective halves, as shown in dotted red in Figure 6.7 (b).

To evaluate the inductances of the B-UC in Figures 6.6 and 6.7, the dimensions parallel to the electric field forms length l, l_1, l_2, l_3, whereas dimensions orthogonal to the electric field forms width w, w_1, w_2, w_3, w_4, w_5. Similarly, for an *x*-polarized EM wave, the dimensions are reversed, for example, l … l_3 becomes width and w … w_5 becomes the length of the strips. We took this idea from Chapter 4 when we obtained the inductances of an IDE cell.

Expression (6.2) relates L_1 with strip's length and width l and w_1 respectively for *y*-polarized wave. Here, k_g is the correction factor due to the presence of a full ground plane and is given by (6.3). Here, h is the height of the substrate. Subsequently, L_2 … L_6 can also be determined using (6.2) by the substitution of corresponding length and width of the strips. We can observe from Figures 6.1 and 6.2 that $L_2 = L_4$. It is because the dimension of the strips (l_1 and w_2) are identical for both the cases. Furthermore, later in the section, it becomes apparent that the impedance offered by C_g given by (6.4) is so large that the branch shown in dotted blue acts as an open circuit, and hence the overall equivalent circuit in Figure 6.7(b) reduces to Figure 6.8(a). Here, A and g_2 are the areas of overlap and gap between the fingers and the horizontal strip, respectively. Since C_{c1} and C_{c2} in Figures 6.7(b) and 6.8(a) are in series, therefore resultant capacitance in (1) becomes $C_c = C_{c1}/2 = C_{c2}/2$. The net impedance Z_{eq} of the circuit shown in Figure 6.8(a) is given by (6.5). Here, L_{eq} is the total inductance of

series and parallelly connected L_1, L_2, and L_3. Subsequently, we obtain the f_r/stop-band frequency of the circuit as expressed in (6.6) by equating the denominator of (6.5) to 0 for parallel resonance.

$$L_1 = 0.25\times10^{-7}\times l\left[\ln\frac{l}{w_1}+1.193+0.25\frac{w_1}{l}\right]k_g \tag{6.2}$$

$$k_g = 0.57-0.145\ln\frac{w_1}{h} \tag{6.3}$$

$$C_g = \frac{\varepsilon_0\varepsilon_r A}{g_2} \tag{6.4}$$

$$Z_{eq} = \frac{j\omega L_{eq}}{\left(1-\omega^2 L_{eq}C_c\right)} \tag{6.5}$$

$$f_r = \frac{1}{2\pi}\sqrt{\frac{1}{L_{eq}C_c}} \tag{6.6}$$

Now we present a design example. For this, B-UC on RO5880 with height h = 0.381mm and permittivity ε_r = 2.2 is designed. The optimized dimensions of the B-UC operating at 2.38 GHz are given in Table 6.1. Tables 6.1 also lists the essential circuit parameters required to obtain the f_r. It has an overall dimension of 13.4x13.6mm^2, which is the smallest of all the previous works without involving via geometry [33]–[40], [92] – [93], [132]. Next, we substitute the values of L_1, L_2, L_3, and C_c in Figure 6.8(a) to plot f_r using (5), as shown in Figure 6.8(b). The value of C_c used to plot f_r in Figure 6.8(b) is for g = 0.6mm. It is evident from the plot that the B-UC offers very high rejection at the desired frequency, which is an essential condition of an EBG cell. Furthermore, Figure 6.8(b) conveys that the substitution of L_5, L_6, and C_g in the equivalent model of Figure 6.7(b) brings no change in f_r. It is because impedance offered by C_g at 2.38GHz is approximately 900Ω (obtained after putting the values of A and g_2 in 6.4 and $Z = j/\omega C_g$). It enforces the branch shown in dotted blue in Figure 6.7(b) to behave as an open circuit.

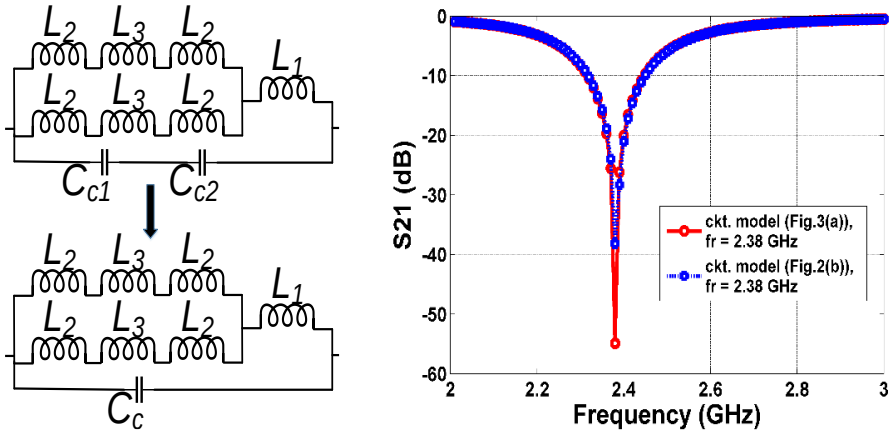

(a) (b)

Figure 6.8 (a) Simplified equivalent circuit model of the B-UC (b) Resonant/stop-band frequency of the B-UC for optimum dimension and g = 0.6mm

Table 6.1 Optimum Unit Cell Parameters

Parameter	Value (mm)	Parameter	Value
l	13.6	L_1	0.7500 nH
l_1	0.30	L_2	0.0038 nH
l_2	6.00	L_3	0.7000 nH
l_3	0.40	L_5	0.3100 nH
w	13.4	L_6	0.0036 nH
w_1	0.40	$C_{c1} = C_{c2}$	4.0500 pF
w_2	6.25	C_g	0.0805 pF
w_3	11.8	$g/2$ (g)	0.3 mm (0.6mm)
w_4	0.45	g_1	0.4 mm
w_5	0.30	g_2	0.4 mm

Next, we assessed the variations in g, w_1, and w_4 on f_r obtained by the circuit model. At first, the gap (g) between the B-UC is varied from 0.4–0.7mm while keeping all other parameters constant, as given in Table 6.1. The gap width of less than 0.4mm has not been considered in this dissertation due to the in-house fabrication tolerances. Table 6.2 lists the obtained C_C and f_r from (6.1) and (6.6). The swept plot of f_r for the gap widths is depicted in Figure 6.9(a). It is apparent from the plot that only the gap width of 0.6mm satisfies the desired resonance. The impact of variation in w_1 from 0.3–0.5 mm on L_1 and f_r obtained using (6.2) and (6.6) is given in Table 6.2. The plot

in Figure 6.9(b) depicts f_r for all the variations in w_1. The optimum w_1 of 0.4mm achieves the desired resonance in this case. Finally, w_4 is varied from 0.25–0.45mm and the obtained L_3 and f_r are listed in Table 6.2. The plot in Figure 6.9(c) depicts this variation on f_r, and clearly, w_4 of 0.45mm achieves the desired band.

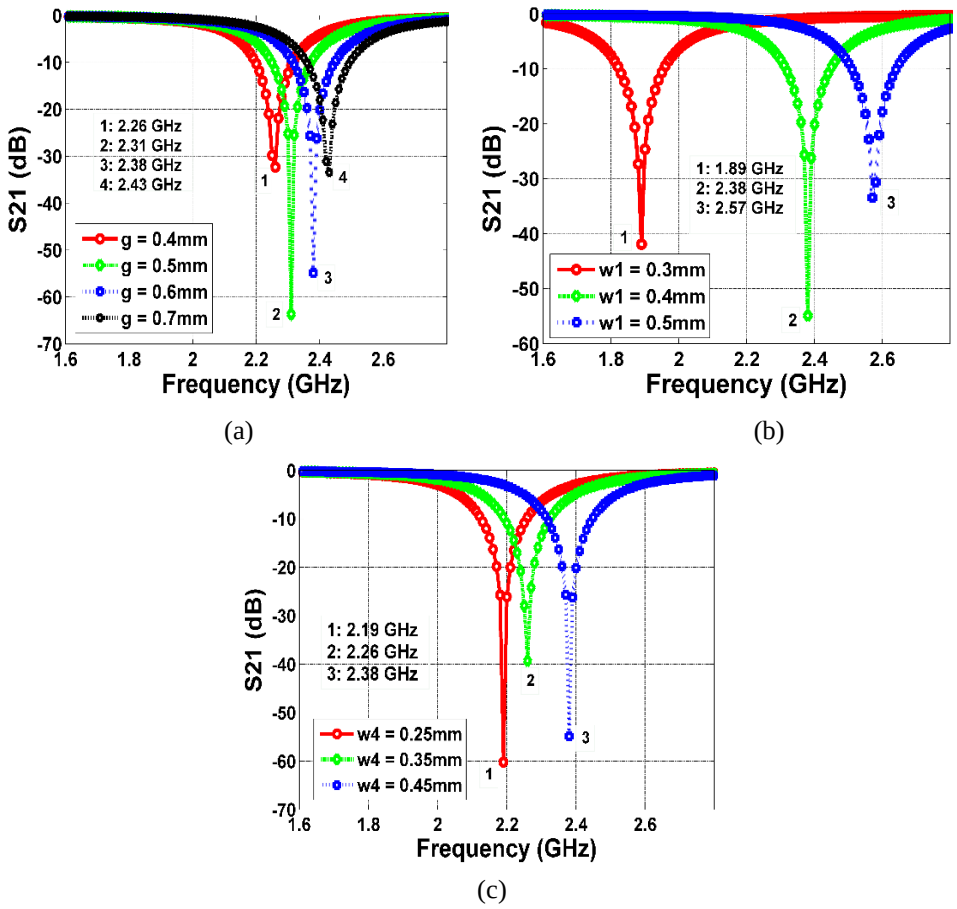

Figure 6.9 Resonant frequencies obtained from the equivalent circuit model (a) Due to variation in gap width *g* (b) Due to variation in w_1 and (c) Due to variation in w_4

Table 6.2 Parameter Variation and Resonant Frequency

g (mm)	C_c (pF)	f_r (GHz)	w_1 mm	L_1 (nH)	f_r (GHz)	w_4 (mm)	L_3 (nH)	f_r (GHz)
0.4	4.55	2.26	0.3	1.40	1.89	0.25	1.10	2.19
0.5	4.30	2.31	0.4	0.75	2.38	0.35	0.94	2.26
0.6	4.05	2.38	0.5	0.59	2.57	0.45	0.70	2.38
0.7	3.92	2.43						

6.2.2 Reflection Phase

In this sub-section, we validate the circuit model presented in the previous section through the reflection phase diagram to record in-phase frequency (IPF)/f_r with the help of CST. The B-UC, as shown in Figure 6.6(a) with all dimensions provided in Table 6.1, is designed in CST. The boundaries of the B-UC is terminated with the unit cell boundary condition. Then both TE and TM mode of EM wave is incident on the B-UC. For a horizontally polarized patch antenna, TM mode ($W>L$ or $L>W$) is the only dominant mode of propagation [58], but as the distance of separation between the antenna and the EBG ground plane is so small that both TE and TM modes of incidence on the EBG plane are considered in this work to record IPF.

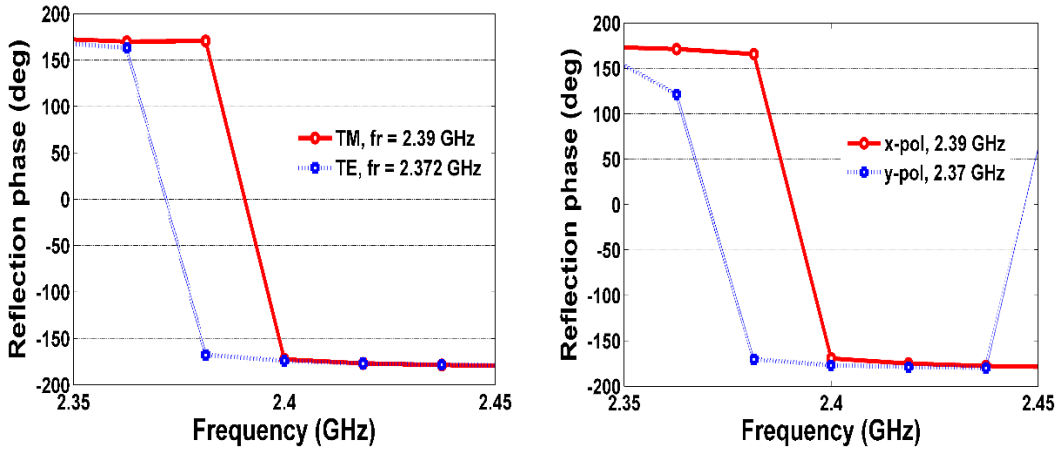

(a) (b)

Figure 6.10 (a) Reflection phase of B-UC for TE and TM incidence (b) Reflection phase of B-UC under *x*-and *y*-polarized TEM wave

The reflection phases of the B-UC for both the polarizations depicted in Figure 6.10(a) show that the IPF/f_r for TE and TM incidence lie in the MBAN band and closely match the circuit modeling results in Figure 6.8(a). Furthermore, the respective bandwidths of the proposed B-UC (±90^o) are 2.367–2.377GHz and 2.385–2.395 GHz for TE and TM modes. However, due to the smaller thickness of the substrate layer, the capacitance developed between the top and bottom metal layers, as given by (6.7) of the proposed B-UC is very large when compared to the previously reported works

[36]–[39], [92]. It contributes to the smaller bandwidth for the B-UC in this work [45].

$$BW \propto \sqrt{\frac{L_{eq}}{C_{gd}}} \tag{6.7}$$

Now, we plot the reflection phase of the B-UC under *x*–and *y*–polarized TEM wave in CST, as shown in Figure 6.10(b). In this case, the B-UC is terminated with a magnetic-electric boundary condition (ME-BC). It is apparent from the plots in Figures 6.10(a-b) and Figure 6.8(b) that they possess remarkable resemblance, and this once again proves the effectiveness of the developed circuit model.

It is pertinent to mention that irrespective of the type of polarization of EM wave, the excitation plane in simulation is positioned at 0.381mm above the B-UC. It is because the EBG ground plane in EBG incorporated antenna (EIA) is separated by the thickness of the antenna's substrate layer, which is 0.381mm for the present case. In general, the EBG layer forms the ground plane for an EIA [46] – [48]. Therefore, incoming radiation from the antenna has to pass through its substrate layer before meeting the EBG layer. It implies that to design a B-UC in simulation, the effective permittivity of the multiple dielectric layers need to be taken into account. For the present case, since the antenna and the EBG structure both are designed on RO5880, the effective permittivity (ε_r) comes out to be 2.27 using the formulations done by us in Chapter 2. This value has been used to design B-UC/array in simulation. Besides, $\varepsilon_r = 2.27$ was also used in the determination of C_C, C_g, and f_r in the previous sub-section as well.

6.2.3 Polarization Stability

The reflection phases of the B-UC shown in Figures 6.10(a) and (b) are for normal incidence (incidence angle of 0^o) of TE-TM and TEM wave. Since the proposed B-UC possess slight asymmetry in the geometry, therefore in this sub-section, we check the polarization sensitivity of the proposed unit cell to obliquely incident TE and TM. Besides, the separation distance of the antenna and EBG plane

is so small that it does not lie in the far-field region. It implies that the angle at which TE/TM wave falling on the EBG surface may not always be $0^{o,}$ and other angles have to be investigated as well. For this, TE and TM wave at angles 15^{o}, 30^{o}, 45^{o}, $60^{o,}$ and 75^{o} are incident on the B-UC, and the corresponding reflection phases are plotted as shown in Figures 6.11 (a)-(b). The results convey that the proposed B-UC exhibits a stable phase relationship for all considered incident angles of TE and TM wave with complete MBAN coverage.

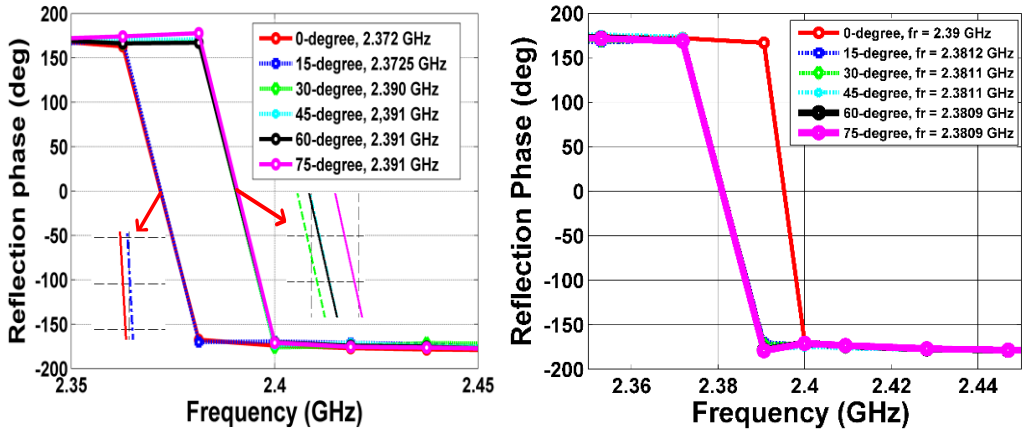

(a) (b)

Figure 6.11 (a) Reflection phases of the unit cell for TE wave incidence at 0^{o}, 15^{o}, 30^{o}, 45^{o}, 60^{o} and 75^{o} (b) Reflection phases of the unit cell for TM wave incidence at 0^{o}, 15^{o}, 30^{o}, 45^{o}, 60^{o} and 75^{o}

6.2.4 Parametric Variation and Band Gap

In this sub-section, we present the variation of parameters g, w_1, w_4, g_1, l_2, g_2 on IPF obtained with the help of CST. For this, the B-UC in Figure 6.6(a) is considered, and the reflection phases are plotted in Figure 6.12(a)–(e). The variations in g, w_1, and w_4 are identical to what we carried out in section 6.2.1. It is evident from the Figures 6.12(a)–(c) that the IPF points possess perfect similarity with that of f_r obtained through the modeled circuit in Figure 6.9(a)–(c). Once again, optimum g, w_1, w_4 of 0.6, 0.4, and 0.45mm respectively are the only suitable values to get desired resonance.

It appeared from the circuit model that g_1, g_2, and l_2 had negligible or no effect

on f_r. However, we have shown here that the IPF of the B-UC does vary. For this, g_1 is altered from the optimum value of 0.4mm to either 0.3mm or 0.5mm. Consequently, the number of fingers changes from 8 to 9 (0.3mm), then to 7 (0.5mm). Consequently, the IPF points of the B-UC shifts, as indicated in Figure 6.12(d). It is apparent that except g_1 = 0.4mm, none of the other gaps satisfy the condition of resonance. Similarly, finger length, l_2, is also varied from 6mm to 5mm with a step size of 0.5mm. The reflection phase plots for all three variations are shown in Figure 6.12(e). We can observe from the plot that only l_2 of 6mm is capable of achieving the desired resonance. For the variation in l_2, g_2 has been maintained to 0.4mm throughout the simulation. It means that for l_2 = 5mm, the g_2 is still 0.4mm. Consequently, it increases l_3 from its initial value of 0.4mm to 0.9mm (0.4mm+0.5mm).

Next, we present the surface wave rejection ability of the proposed B-UC with the help of a band-gap diagram. For this, the proposed B-UC is terminated with periodic boundary condition (PBC), and the computation domain is divided into Brillouin zone $\Gamma \rightarrow X$, $X \rightarrow M$ and $M \rightarrow \Gamma$ [48]. The Eigen frequencies of the surface wave are solved in CST, and the dispersion diagram is plotted, as shown in Figure 6.12(f). A band-gap between 2.355–2.5GHz appears between the fundamental mode (mode 1) and the next higher mode (mode 2). In general, the fundamental occurs from DC value and has no cut-off. The higher modes of the surface waves depend on the geometry of the substrate. It is also known that the dominant mode of an MPA is also TM_0. Therefore, getting band-gap between the fundamental mode and the next higher mode ensures no coupling between them and also significantly less propagation along the substrate [43] – [48]. It proves the effectiveness of the proposed B-UC to eliminate undesired surface waves accounting for increased SAR values.

We made a comparison between the proposed B-UC and the earlier designs in terms of band-gap, height, and size in Table 6.3. The proposed B-UC is the smallest reported design operating at MBAN frequency. Moreover, the proposed B-UC is smaller than the IDE cell presented in Chapter 4. Besides, B-UC can also be conformed on any conformal platform with ease due to the small thickness of the substrate layer. The via-less geometry makes the proposed UC convenient for use in WBAN.

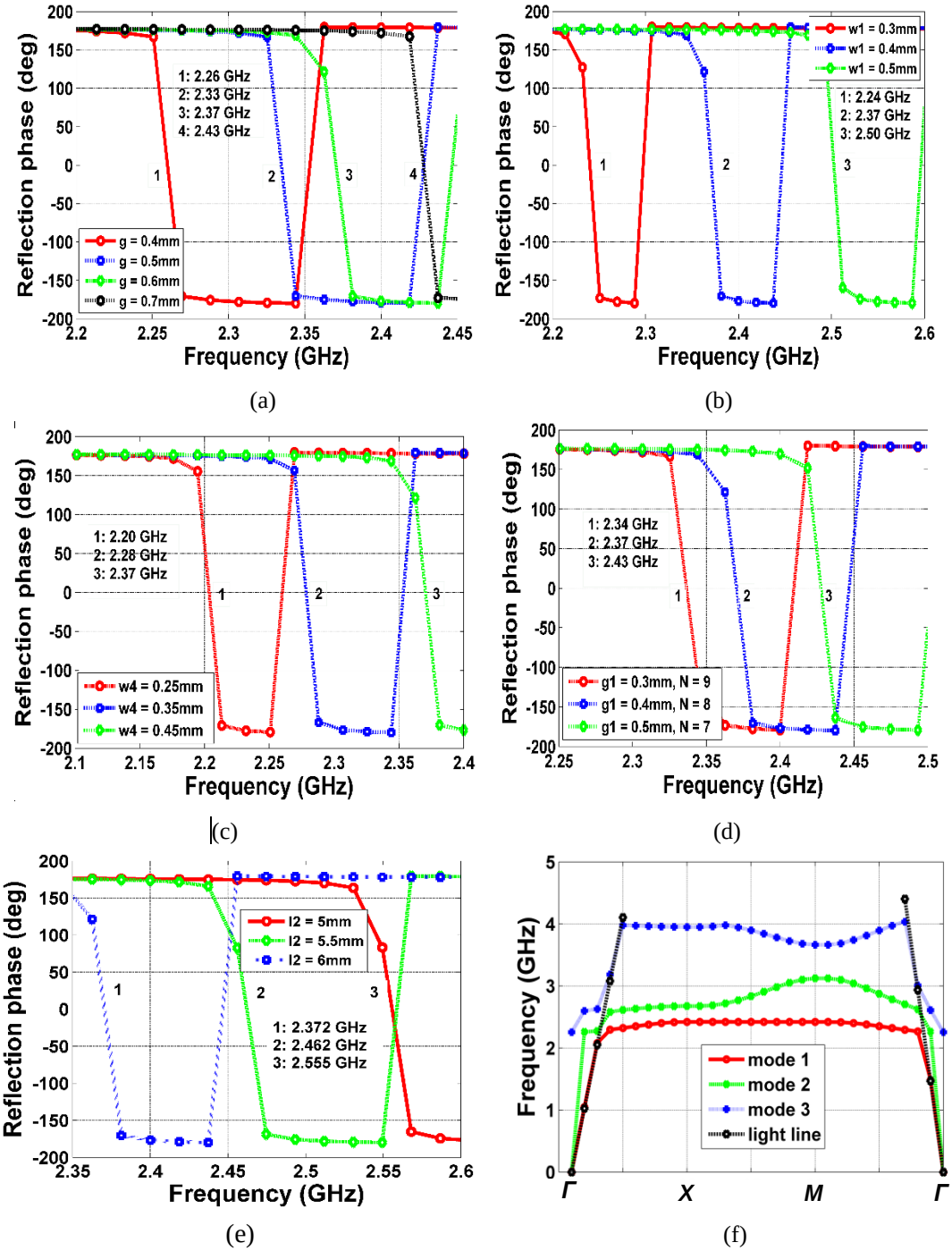

Figure 6.12 Reflection phase plots of B-UC with in-phase frequency (a) in gap width *g* (b) in w_1 (c) in w_4 (d) in g_1 or number of fingers and (e) in l_2 (f) Dispersion diagram exhibiting band gap between mode 1, mode 2, and mode 3

Table 6.3 Comparison of the Proposed B-UC with State-of-the-Art Works Working at MBAN and Wi-Fi

Ref.	Size (lxb) (mm^2)	*g* (mm)	*h* (mm)	Band-gap (GHz)	Size Comparison (%)
[34]	48.0*48.0	2.00	1.00	-	1246
[91]	34.0*34.0	0.40	0.10	-	625
[36]	31.0*31.0	-	1.52	-	520
[88]	27.6*27.6	1.20	0.70	.07	412
[39]	25.3*27.8	2.50	5.00	-	380
[87]	22.7*22.7	1.00	1.52	.02	278
[38]	27.0*16.0	2.15	2.00	-	234
[89]	20.0*20.0	1.00	2.00	-	216
[90]	20.0*18.0	1.50	3.00	-	194
[92]	14.3*14.5	0.4	1.52	0.35	112
B-UC	13.8*13.4	0.6	0.38	0.15	100

[Where, %size comparison = {size (lxb) [Ref] / size (lxb) (Proposed B-UC)} x 100)] (*h is the height of the dielectric layer)

6.3 Design and Analysis of Array

In this section, we design an array of 3x3 B-UCs, as shown in Figure 6.13, to serve as a reflector for an antenna. Then the array (B-array) is thoroughly analyzed using the reflection phase and band-gap. The B-UCs are arranged in a way such that the reflection phase of the array falls in the MBAN band. The gap between the elements is fixed at 0.6mm obtained in the last section. However, a parametric study is performed for the variables g_1 and g_2, and the achieved values are 2.4 and 2.1mm, respectively. The overall dimension of the array then becomes 42.8x44.36 mm^2.

The plot in Figure 6.14(a) shows the reflection phases of the array under *x*- and *y*-polarized TEM waves. Here, ME-BC is used to truncate the boundaries of the B-array along *x*-and *y*- axes while keeping the excitation plane at the earlier identified

distance of 0.381mm. It can be observed that the reflection phase of the array falls in the MBAN region with IPF points in close agreement with that of the B-UC. Furthermore, Figure 6.14(b) also shows the variation in IPF by altering *g* from 0.5–0.7mm for the *y*-polarized TEM wave. It is clear from the plot that the only *g* of 0.6mm provides the desired resonance.

Subsequently, we have shown the surface wave rejection ability of the designed array with the help of the transmission parameter. For this, the array with given dimensions is prototyped, as shown in Figure 6.15(a). A 50Ω transmission line is etched at the ground plane, as shown in Figure 6.15(b). The dimension of the 50Ω line for the substrate used in this work is 1.1mm. Afterward, RF power of 0dBm is fed into any of the two ports and then received in the form of S_{21} with the help of a VNA. The measurement setup for this arrangement is shown in Figure 6.16(a). The measured and simulated S_{21} of the array, along with the band-gap region, is shown in Figure 6.16(b). The surface wave rejection of more than -20dB is possible in the MBAN region for the proposed B-array. The remarkable resemblance between the measured and simulated results justifies the effectiveness of the proposed design. It is essential to mention that the open boundary condition is taken in simulation instead of ME-BC.

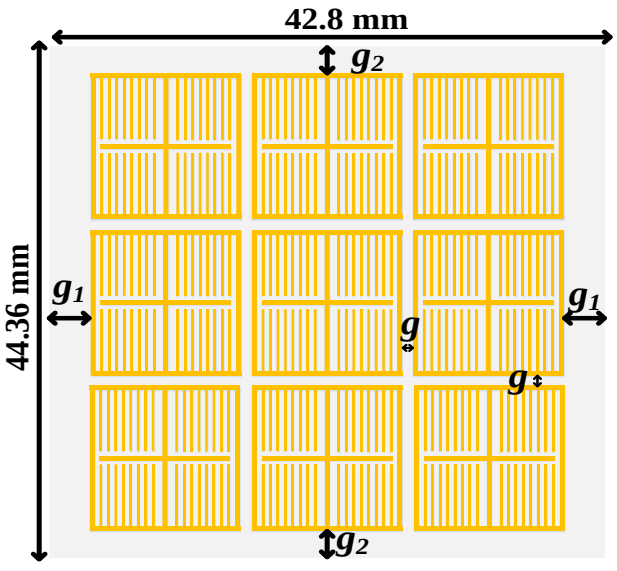

Figure 6.13 Array of 3x3 B-EBG unit cells [g_1 = 2.4 mm, g_2 = 2.1 mm, g = 0.6 mm]

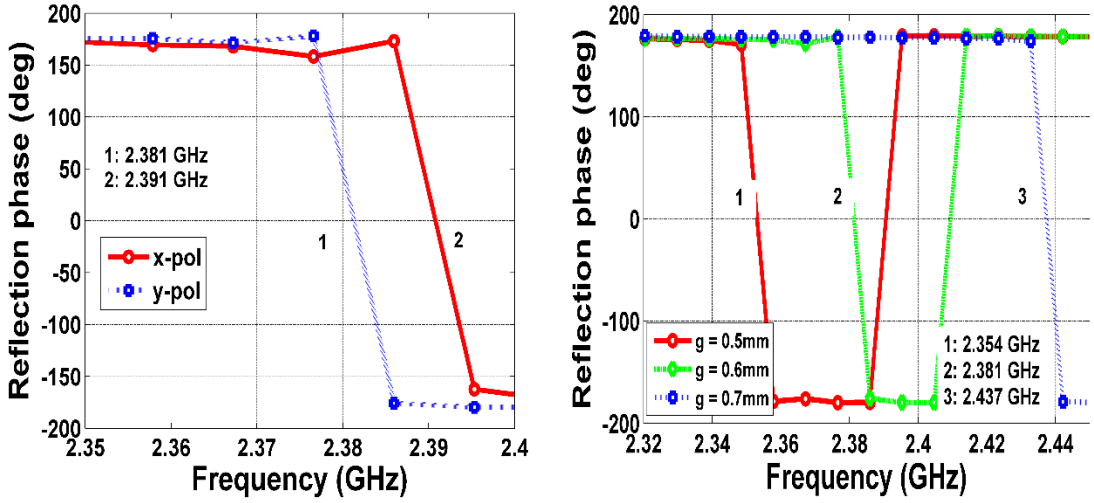

(a) (b)

Figure 6.14 (a) Reflection phase of the array with 3x3 UCs (b) Variation in in-phase frequency of array with a change in the gap with *g*

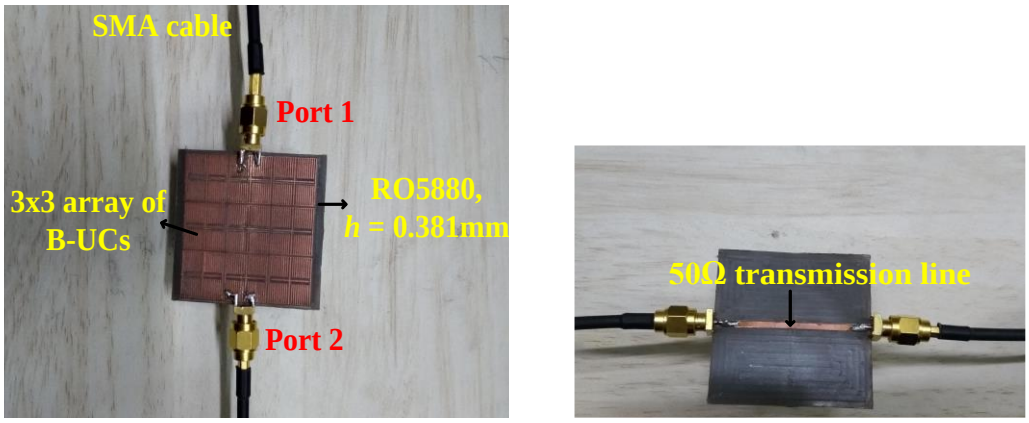

(a) (b)

Figure 6.15 (a) Prototyped EBG array to demonstrate band-gap (b) 50Ω line at the bottom of the prototyped array

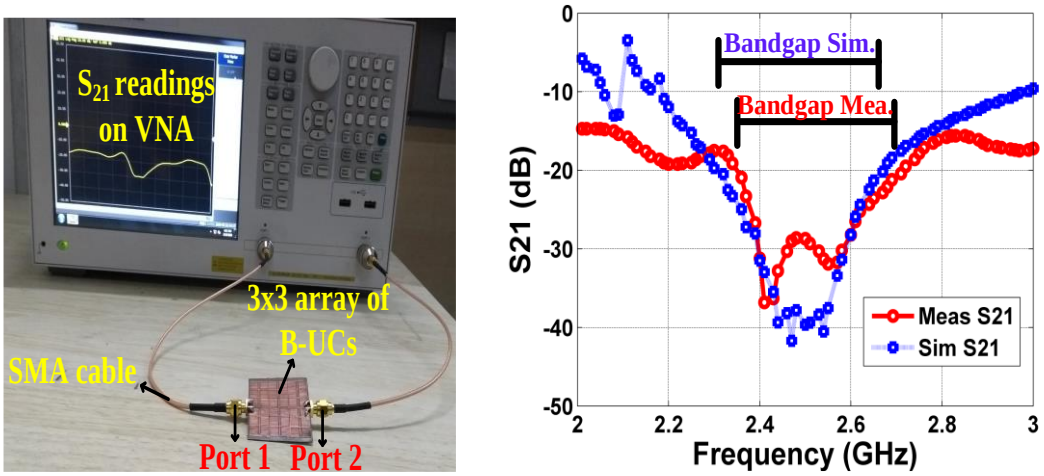

(a) (b)

Figure 6.16 (a) Measurement setup to extract band-gap (b) Measurement result

6.4 EBG Incorporated Monopole Antenna (EIA)

In this section, we incorporate a monopole antenna (EIA) with the EBG array designed in the previous section to enhance the performance. The EIA is designed in CST, as shown in Figure 6.17. The top and bottom of the EIA consist of a monopole antenna with partial ground plane and the EBG array, respectively. The optimized physical parameters L_{gnd}, L_{gap}, W_F, L_F, W_P, and L_P of the EIA are given in Table 6.4. We left no gap between the antenna and the arrays in this work in contrast to previous designs [38] – [39].

The prototyped monopole antenna with all the parameters given in Table 6.4 is shown in Figure 6.18(a). The front and side view of the prototyped EIA is depicted by Figures 6.18(b)–(c). The layers of the antenna and the EBG array are attached with the help of low permittivity RTV coating (ε_r = 1.22). We have taken proper care to avoid the formation of a gap between the subsequent layers. However, due to the minimal thickness of the substrate layers, the gap does form, as can be seen in Figure 6.18(c). For the appropriate placement of the SMA connector, the antenna is slightly shifted upwards, as shown in Figures 6.17 and 6.18(b)–(c). The parameter L_{gap} plays a crucial role in providing a good match at the f_r. For example, it has been observed that when

L_{gap} decreases, the f_r shift to higher values but improves matching. Therefore, we took proper care to tune the value of L_{gap} such that an optimum matching and desired resonance both can be achieved.

Table 6.4 Design parameters (in mm) of the EBG integrated monopole antenna

L_P	W_P	L_F	W_F	L_{gnd}	L_{gap}
38.5	38	7	1.8	4	0.74

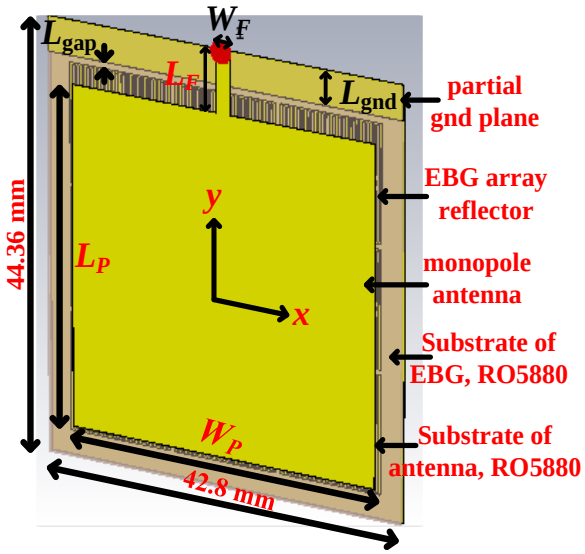

Figure 6.17 EBG backed monopole antenna

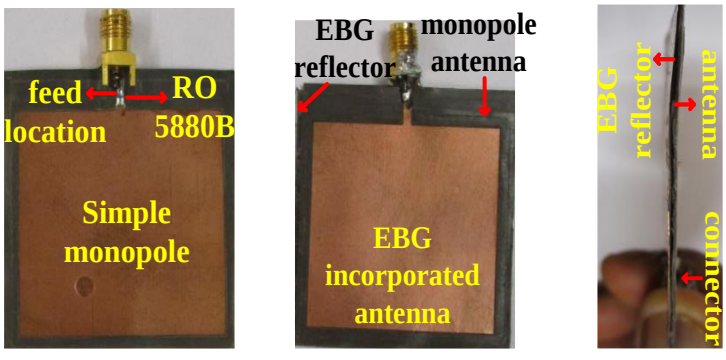

(a) (b) (c)

Figure 6.18 Prototyped antennas (a) monopole (b) EBG array incorporated antennas (front view) (c) EIA (side view)

The simulated and measured return losses (S_{11}) of the simple monopole antenna and EIA are shown in Figures 6.19(a) and (b). The prototyped EIA demonstrates its operation for the entire MBAN band having resonance at 2.38GHz. Besides, the measured S_{11} of the EIA exhibits better band coverage (100MHz) than the simulated one. It is attributed to the overall reduction in quality factors from ohmic (soldering) and dielectric losses (due to the gap) [38].

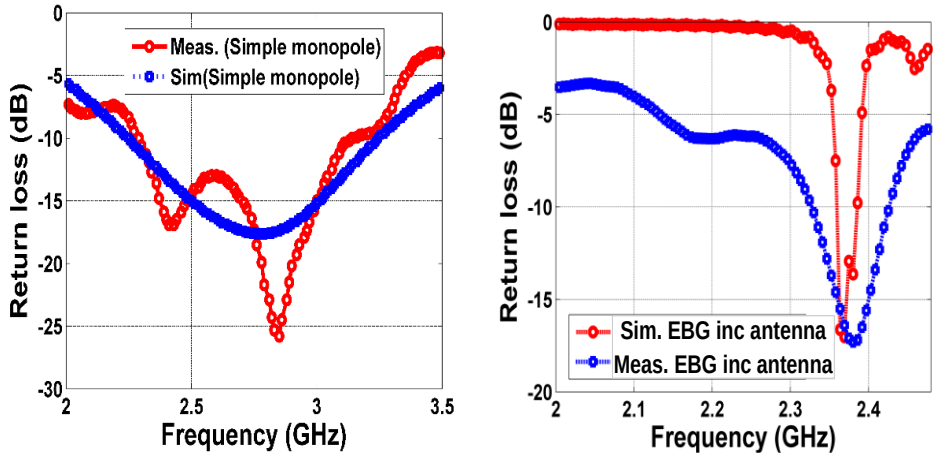

(a) (b)

Figure 6.19 Simulated and measured return losses of (a) simple monopole (b) EIA

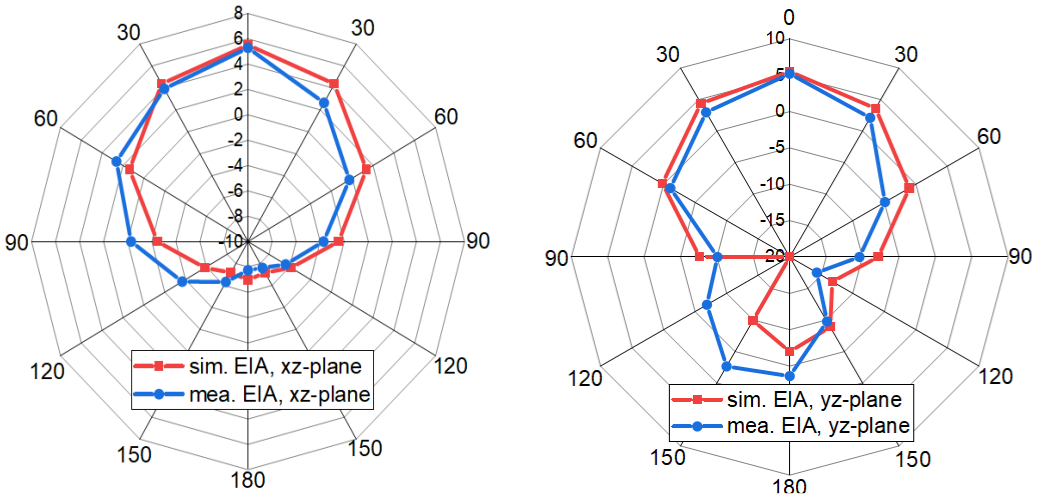

(a) (b)

Figure 6.20 Simulated and measured radiation patterns of EBG incorporated antenna along (a) *xz* plane (b) *yz* plane

Next, we measure and simulate the radiation pattern of the EIA along *xz* and the *yz* plane. We obtained a measured gain of 5.3dBi and 5.2dBi from the fabricated EIA along *xz* and *yz* planes, as shown in Figures 6.20(a)-(b). When we compare it with the simulated gain resulting in 5.51dBi in both the planes as evident from plots in Figures 6.20(a)-(b) shows perfect agreement. Slight variation in the back lobes of the simulated and measured plots in Figures 6.20(a) and (b) can be accounted for the formation of the gap between the layers.

6.5 Conformal B-Array and Incorporated Antenna

Conformability is an essential requirement of an antenna designed for wearable applications due to its operation near leg, wrists shoulder, bicep, and many more [33] – [37]. For this purpose, the incorporated antenna is conformed on a cylinder along *x*- and *y*-axes of radii (*r*) 40, 50, and 60mm, respectively, as shown in Figures 6.21. We have already presented the stability in the performance of the proposed unit cell and the array when bent along *x*-and *y*-axes designed in this chapter in Chapter 5 (UC-3). Both unit cell and array covered the MBAN band for the conformal radii of 40, 50, and 60mm.

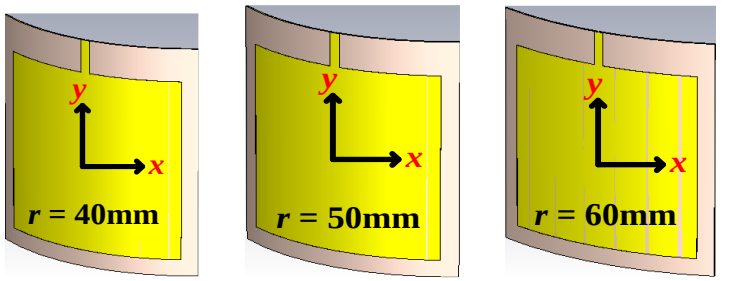

(a)

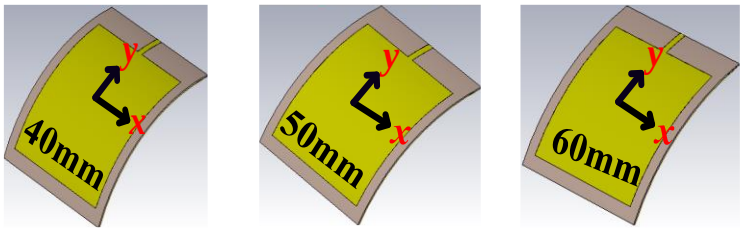

(b)

Figure 6.21 Conformal EIA bent on a cylindrical platform of radii 40, 50 and 60 mm along (a) *x*-axis (b) *y*-axis

The prototyped EIA as shown in Figures 6.18 is bent under similar conditions as mentioned above. As an example, EIA bent along *x*- and *y*-axes for *r* = 60 mm is depicted in Figure 6.22 (a)-(b). The measured S_{11} plots vs frequency for *r* = 60 mm are shown in Figures 6.24 (a)-(b). The measured S_{11} for the other two cases (*r* = 40 and 50 mm) are also shown in Figures 6.24 (a)-(b). Apparently, the measured results achieve the desired band coverage for all three bend radii. Besides, EIA bent along the *y*-axis is more prone to frequency shift than the bend along the *x*-axis as evident from Figures 6.24 (a)-(b).

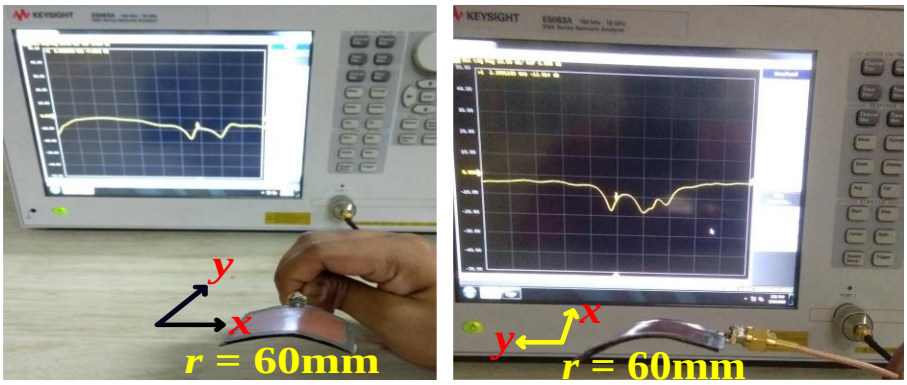

(a) (b)

Figure 6.22 Measurement return loss of prototyped conformal EIA bent along (a) *x*-axis (b) *y*-axis

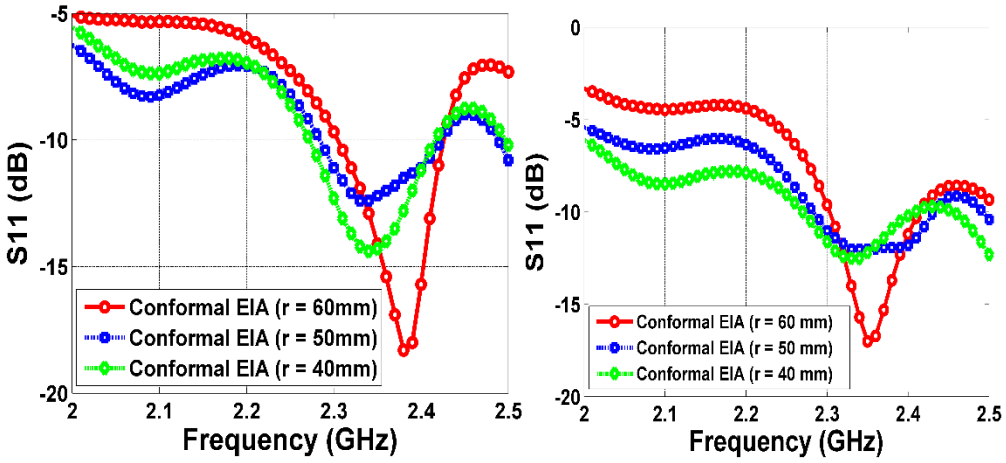

(a) (b)

Figure 6.23 Measured return losses of the conformal EIA bent along (a) *x*-axis (b) *y*-axis

Next, the simulated and measured radiation patterns of the EIA along *xz* and *yz* planes are plotted and depicted in Figures 6.24 and 6.25. The measured values are once again superior to the simulated ones. It is because of the reason mentioned above. Finally, Table 6.5 lists the summary of simulated and measured gain and efficiency of the EIA for all the three conformal radii.

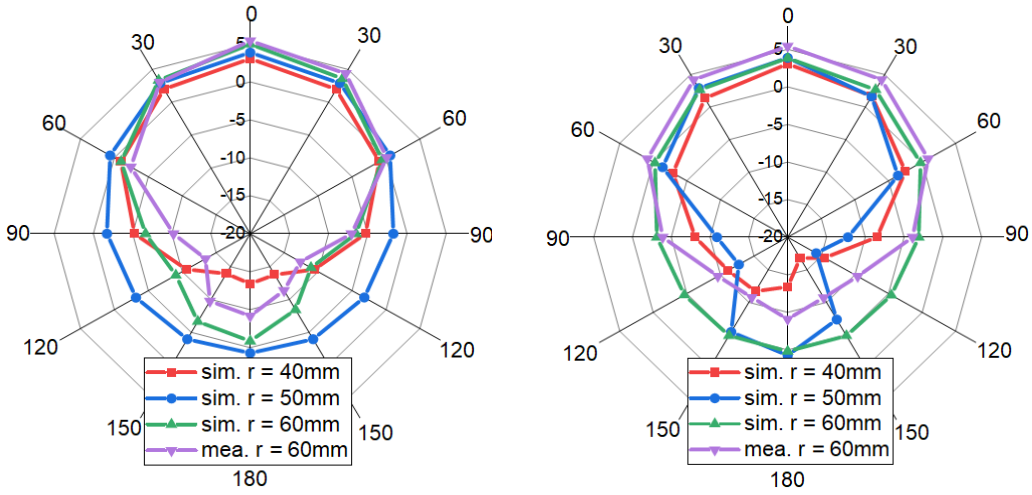

(a) (b)

Figure 6.24 Simulated and measured radiation patterns of the conformed EIA along *x*-axis about (a) *xz* plane (b) *yz* plane

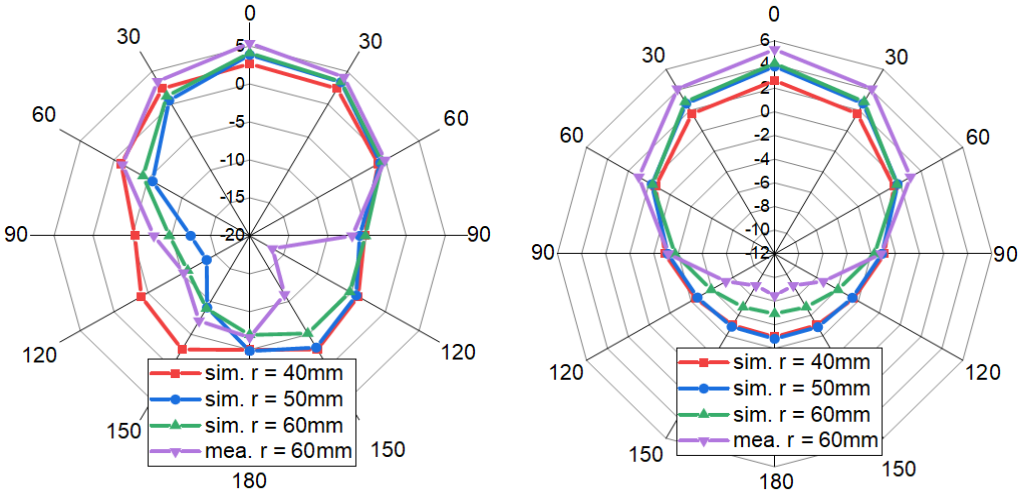

(a) (b)

Figure 6.25 Simulated and measured radiation patterns of the conformed EIA along *y*-axis about (a) *xz* plane (b) *yz* plane

Table 6.5 Summarized Values of Measured and Maximum Simulated Gain and Efficiency of the Conformal EIA

Bend	Radii (mm)	Gain (dBi) Sim. (Meas.)	Efficiency Sim. (Meas.)
	40	3.94	66.90
x-axis	50	4.07	66.90
	60	4.26 (5.37)	68 (71.45)
	40	2.66	57.08
y-axis	50	3.85	64.08
	60	4.09 (5.28)	62.34 (72)

6.6 On-body Performance

In this section, we present the performance of the proposed antenna when placed on-body. The on-body analysis is essential because body-worn devices operate very close to the body, and hence loading effects may change the impedance matching and radiation properties of an antenna. Therefore, the prototyped EIA is placed on the wrist, and shoulders, as shown in Figure 6.26(a)-(b). The return loss of the EIA placed on-body is plotted against frequency, as depicted in Figure 6.27. It is apparent from the plots that placing the EIA close to the body affects the matching and resonance as well. However, for all the cases, the EIA covers the desired band, i.e., MBAN. It proves the effectiveness of the proposed design. Furthermore, for the conformal EIA placed on-body, the shift in f_r is more than the planar geometry, as apparent from the previous section.

The radiation property of the antenna operating close of the human body is evaluated by considering three models, namely planar wrist, conformal wrist, and numerical phantom (Gustav in CST), as depicted in Figure 6.28. The planar model is typically a four-layer model consisting of skin, fat, muscle, and bone, as we discussed in Chapter 4. The electrical properties (ε_r and σ_d) at 2.4 GHz and thickness are mentioned in Figure 6.28 (a). The conformal model consists of an elliptical cylinder

similar to the wrist having a radius of 30mm and 20mm along semi-major and minor axes, respectively. The composition of layers filling the conformal geometry is identical to the planar model. Finally, one of the numerical phantoms (Gustav) in CST is used for accurate and realistic determination of the radiation performance of the EIA, as shown in Figure 6.28(a).

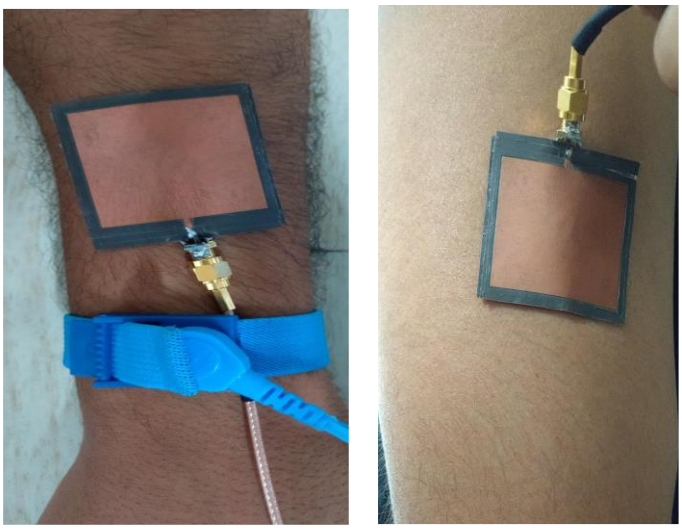

(a) (b)

Figure 6.26 Placement of prototyped EIA on (a) wrist (b) triceps

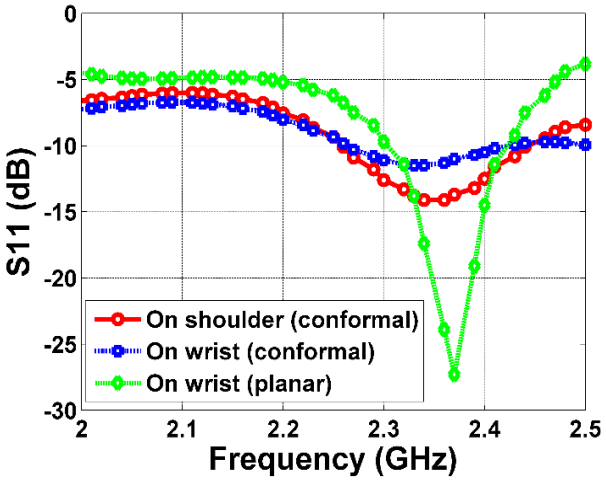

Figure 6.27 Measured return losses of the EIA at wrist planar, wrist conformal and shoulder conformal

The radiation pattern of the antenna along *xz* and *yz* planes for all three models are shown in Figure 6.29. A simulated maximum gain of 4.93 dBi (planar), 4.24 dBi (elliptical), and 4.78 dBi (on-wrist, Gustav) are obtained for the respective models. It is apparent from the gain values in Figure 6.29 that the performance of EIA is stable while operating close to the body.

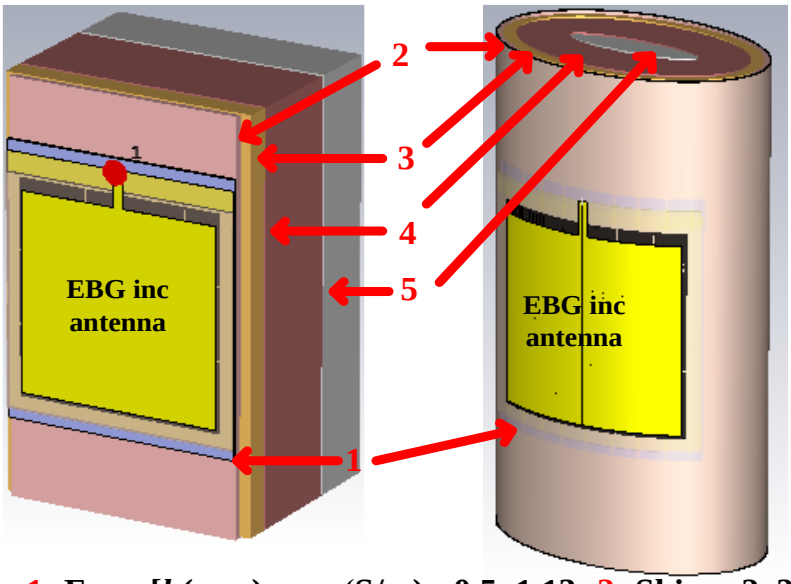

1: Foam[*h*(mm), ε_r, σ(S/m)= 0.5, 1.13; 2: Skin = 2, 38, 1.44
3: Fat = 5, 5.3, 0.12; 4: Muscle = 20, 52.8, 1.7 ; 5: Bone = 13, 18, 0.82

(a)

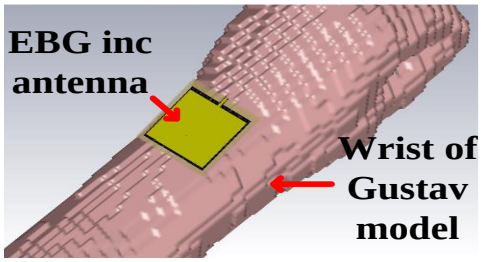

(b)

Figure 6.28 Simulated EIA backed by body models (a) planar (b) conformal, (c) Gustav model in CST

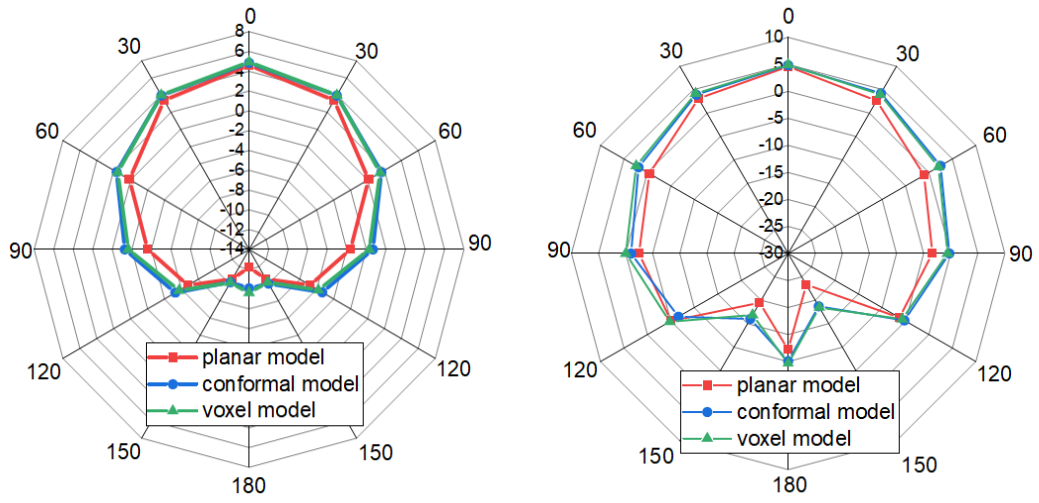

Figure 6.29 Simulated radiation patterns of the EIA backed by body models about (a) *xz* plane (b) *yz* plane

6.7 SAR Analysis

The SAR measures the amount of radiation absorbed near the adjacent tissue when exposed to RF sources like mobile handsets and body-worn devices. In this section, SAR analysis of the EIA backed by a foam layer (as shown in Figure 6.28), and the simple monopole antenna has been carried out. The SAR analysis is done with the help of a homogenous, heterogeneous (as shown in Fig. 6.28) and Gustav models in CST. Besides, both planar and conformal platforms are used to determine SAR to mimic portions where body-worn antennas are placed more commonly such as wrist and triceps.

The SAR of EIA backed by foam, EIA w/o foam, and a simple monopole antenna is determined for an equivalent homogeneous model of the body. Both planar and conformal geometries of the homogeneous model of the body are used for the determination of SAR as shown in Figure 6.30. The electrical properties of the model are given in Figure 6.30. The physical parameters of both the flat and conformal models are identical to the heterogeneous model as depicted in Figure 6.28.

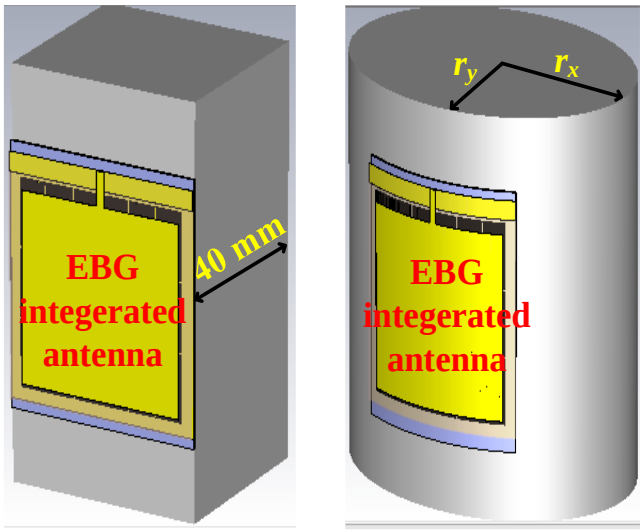

Planar and Elliptical container with homogeneous model

$\varepsilon_r = 40$, $\sigma_d = 1.22$ S/m, $r_x = 25$ mm, $r_y = 20$ mm

Figure 6.30 EIA backed by planar and conformal homogeneous models of body

For an input power of 1 mW and 10 g of averaging mass, the simulated SAR of EIA at 2.38 GHz backed by a foam layer and w/o a foam layer on flat homogeneous body models are depicted in Figures 6.31 (a) and (b). The power input of 1 mW is chosen because in general, the devices operate at this power level in the MBAN band. It is apparent from the plots that due to the presence of a foam layer beneath EIA, the SAR values in Figure 6.31 (a) is smaller than the EIA w/o foam. Similarly, SAR is determined on the conformal homogeneous model with identical power levels and averaging mass as shown in Figures 6.32 (a) and (b). It is apparent from the plots in Figures 6.31 and 6.32 that for identical power levels and averaging mass the SAR values are approximately equal for both flat and conformal homogeneous body models.

Table 6.6 provides a comparison between the SAR values of the EIA (with and w/o foam) and monopole antenna at five different frequencies on the flat and conformal platforms for input power and averaging mass of 1 mW and 10 g respectively. The SAR values of the EIA are substantially better than the standalone

monopole antenna. However, it is important to mention here that because of the slight larger dimension of the conformal model (along the *x*-axis = diameter of major axis = 50 mm) than the flat one (43 mm), Table 6.6 indicates a drop in the value of SAR at some frequency points.

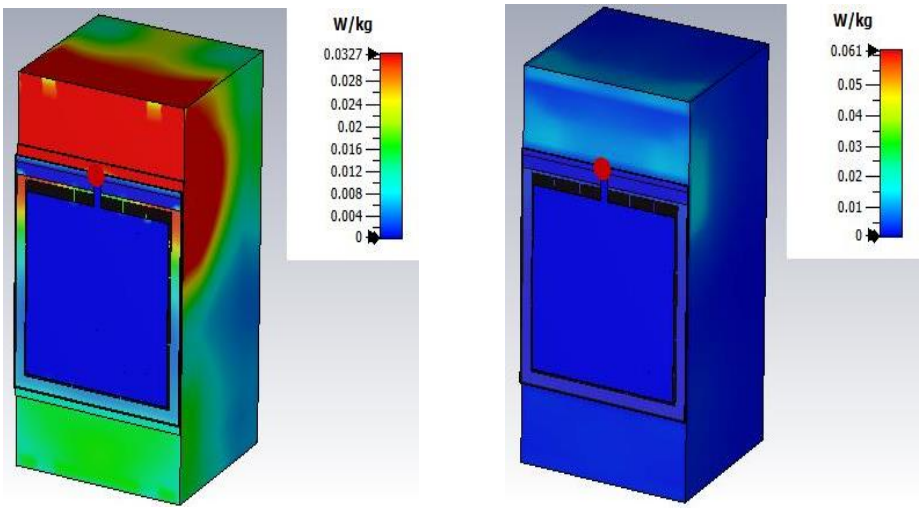

(a) (b)

Figure 6.31 Simulated SAR of EIA on the flat homogeneous model at 2.38 GHz (a) with foam (b) w/o foam

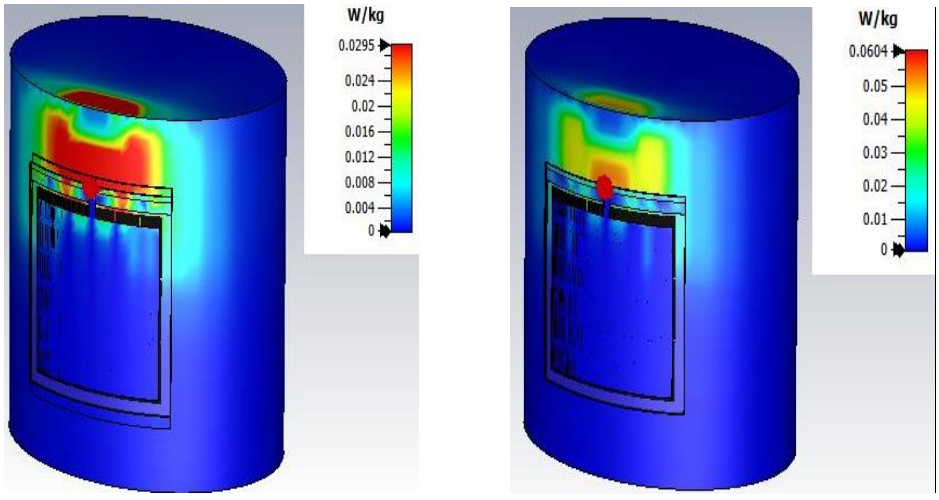

(a) (b)

Figure 6.32 Simulated SAR of EIA on the conformal homogeneous model at 2.38 GHz (a) with foam (b) w/o foam

Table 6.6 Summarized Values of SAR for Homogeneous Model of Body

Freq. (GHz)	SAR (W/Kg)_Planar			SAR (W/Kg)_Conformal		
	w/o foam	with foam	mono. antenna	w/o foam	with foam	mono. antenna
2.30	0.008	0.042	1.330	0.038	0.005	1.227
2.35	0.041	0.049	1.366	0.044	0.024	1.260
2.40	0.050	0.056	1.385	0.048	0.026	1.276
2.45	0.070	0.062	1.410	0.054	0.032	1.293
2.50	0.081	0.070	1.430	0.058	0.033	1.310

Furthermore, SAR of EIA with foam, w/o foam, and monopole antenna on a flat and conformal heterogeneous body models are also determined. For this, the models as shown in Figure 6.28 are used to simulate the designs. For an input power of 1 mW and averaging mass of 10 g, the simulated SAR values of EIA on the flat model with foam and w/o foam at 2.38 GHz are depicted in Figures 6.33. Once again, due to the presence of an additional layer (foam) SAR values in Figure 6.33 (a) is smaller than that of w/o foam in Figure 6.33 (b).

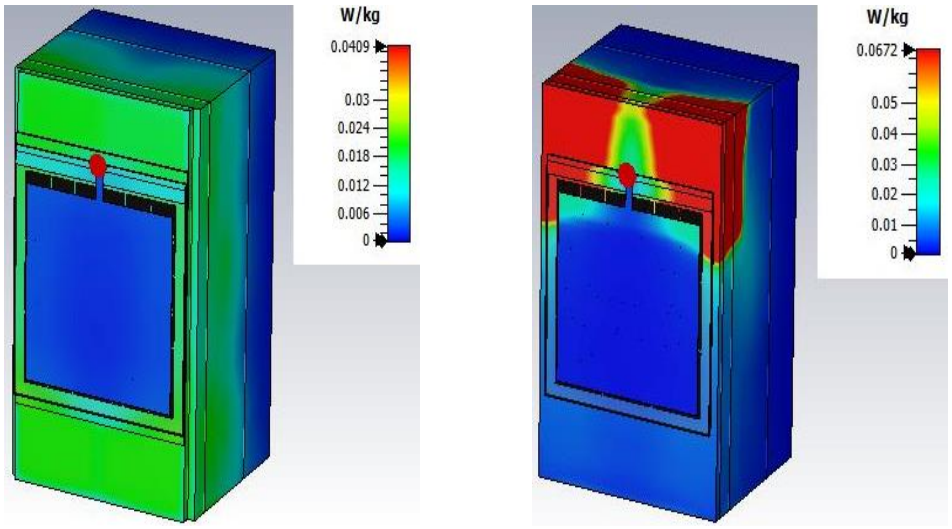

(a) (b)

Figure 6.33 Simulated SAR of EIA on the flat heterogeneous model at 2.38 GHz (a) with foam (b) w/o foam

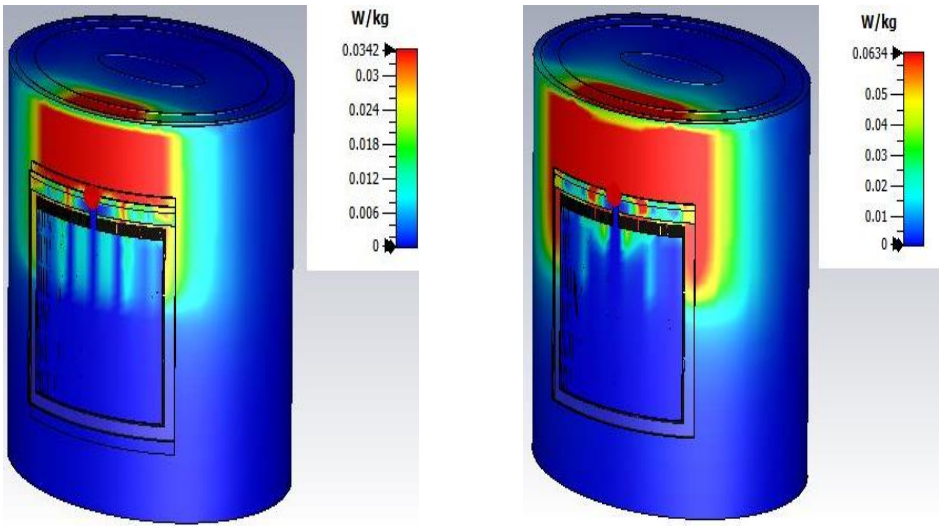

(a) (b)

Figure 6.34 Simulated SAR of EIA on the conformal heterogeneous model at 2.38 GHz (a) with foam (b) w/o foam

Table 6.7 Summarized Values of SAR for Heterogeneous Model of Body

Freq. (GHz)	SAR (W/Kg)_Planar			SAR (W/Kg)_Conformal		
	w/o foam	with foam	mono. antenna	w/o foam	with foam	mono. antenna
2.30	0.043	0.008	1.120	0.038	0.012	0.930
2.35	0.067	0.041	1.132	0.050	0.027	1.170
2.40	0.081	0.050	1.818	0.047	0.037	1.260
2.45	0.094	0.070	2.040	0.065	0.045	1.328
2.50	0.012	0.081	2.260	0.081	0.047	1.404

Similarly, the simulated SAR of EIA backed by the conformal heterogeneous model for identical power levels and averaging mass, are depicted in Figure 6.34. Once again, a comparison between the SAR values of three different kinds of antennas is provided in Table 6.7 at five different frequencies. Apparently, the SAR values of EIA are substantially lesser when compared to the simple monopole antenna. Moreover, the SAR values of the conformal model are slightly lesser than the flat model as evident from the previous sub-section. It is important to mention here that due to the higher dielectric conductivity of heterogeneous model (σ_d = 1.44, first layer from

Figure 6.28) than the homogeneous model (σ_d = 1.22, from Fig. 31) SAR levels of the former are lesser than that of the later one.

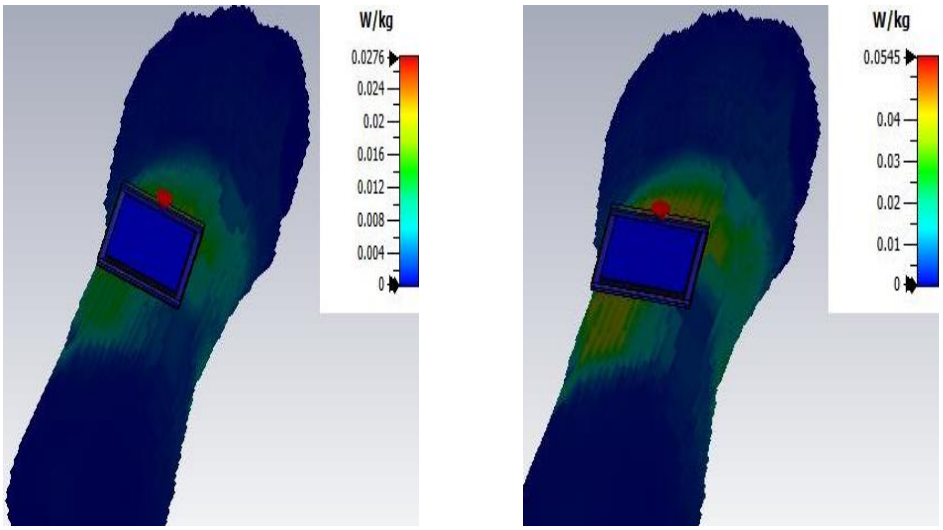

(a) (b)

Figure 6.35 Simulated EIA backed by Gustav model in CST

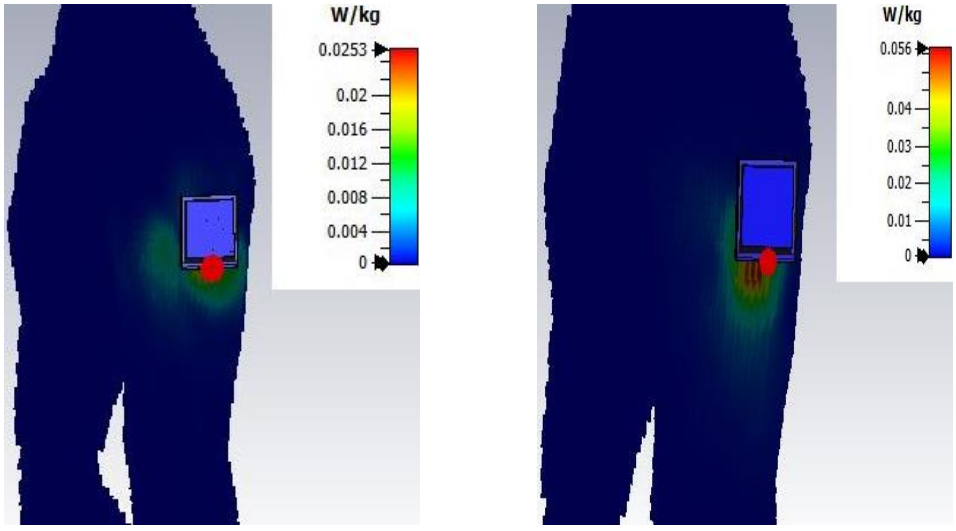

(a) (b)

Figure 6.36 Simulated EIA backed by Gustav model in CST

Next, SAR analysis of the proposed EIA is done on a more realistic human model i.e, the Gustav in CST. For the determination of SAR, the wrist and triceps region of the model is selected, and EIA with foam and w/o foam are simulated with an input power of 1 mW and averaging mass of 10 g. The simulated SAR at these two locations for EIA with foam and w/o foam are depicted in Figure 6.35 and 6.36. It is apparent from the results that the results of the numerical phantom are approximately similar to the flat and conformal models used in this work. The SAR values of the numerical phantom are even smaller than the approximate models.

Table 6.8 Performance Comparison of the Proposed EIA with State-of-the-art Works in Free Space and On-Body at 2.4 GHz

Ref	Dimension (mm^2)	*h* (mm)	On air		On-body			S (mm)	Size comp (%)
			Gain (dBi)	%η	Gain (dBi)	%η	SAR (W/kg)		
[34]	150 × 150	3.00	- 4.00	---	- 4.00	---	0.016 (1 g – hetro)	1.0	1185
[35]	120 × 120	3.30	6.40		4.39		0.079 (1 g – hetro)	5.3	758
[133]	81 × 81	4.00	6.00	70.0	---	---	0.554 (1 g – hetro) 0.23 (10 g – hetro)	6.0	346
[125]	40 × 145	2.00	---	63.0	---	16.0	3.06 (10 g – hetro)	0.0	305
[134]	72 × 72	0.10	1.25	82.3	- 4.10	12.9	2.48 (1 g - hetro)	5.0	273
[40]	65.7 × 65.7	1.50	4.80	---	---	---	0.638 (1 g - hetro)	1.7	227
[38]	62 × 42	4.00	6.20	---	5.80	---	0.480 (1 g – hetro)	5.0	137
[39]	68 × 38	6.57	6.00	76.0	6.25	60.0	0.244 (1 g - muscle)	2.0	136
[135]	50 × 50	5.00	5.20	75.0	4.80 (wrist)	68.0	0.18 (1g - hetro)	4.0	132
This work	44.36 × 42.8	0.762	5.50	80 (Sim.) 78 (Meas)	4.93 (wrist)	70	0.012 (1 g – homo) 0.029 (1 g – hetro) 0.026 (1 g - Gustav)	0.0	100

[Note: '---' indicates not given in the report/paper, 'S' - Separation between the antenna and body model, '*h*' – Height of substrate, %η – Radiation efficiency, % size comparison = {size (l×b) [Ref] / size (l×b) (This work)} × 100)]

Finally, Table 6.8 lists a comparison of the proposed EIA with a few state-of-the-art works in terms of size, gain, efficiency, and SAR values. It is apparent from Table 6.8 that although the gain of the proposed antenna is smaller than [35], [38], [39], and [133], still the SAR values are substantially better. Besides, the gain of an

antenna is directly proportional to its ground plane size [58]. Since the dimensions of antennas are larger than the proposed work in the above-mentioned references, reduction in gain can be accounted for due to this. Moreover, the on-body radiation efficiency of the proposed antenna is better than most of the works mentioned in Table 6.8. This once again justifies the effectiveness of the proposed EIA from the WBAN perspective.

6.8 Conclusion

In conclusion, we proposed a new compact and conformal blocking EBG UC for WBAN (especially for MBAN) applications in this chapter. The design of the proposed B-UC is supported by a newly developed equivalent circuit model and validated through the use of the reflection phase diagram obtained with the help of full-wave analysis in CST. We then demonstrated the excellent stability of the proposed B-UC to polarization change for obliquely incident TE and TM waves at 15^{o}, 30^{o}, 45^{o}, 60^{o}, and 75^{o}. Also, for an *x*- and *y*-polarized TEM wave, the B-UC demonstrates an in-phase band within the MBAN frequency band. The band stop nature of the proposed B-UC is demonstrated with the help of the dispersion diagram. A B-array consisting of 3x3 B-UCs is also proposed as a reflector for enhancing the performance of the monopole antenna. The B-array exhibits excellent surface rejection ability and provides suppression of more than -25dB in the MBAN frequency band. A monopole antenna incorporated with the B-array shows superior performance in terms of matching and bandwidth. The antenna exhibits a measured gain of 5.3 and 5.2 dBi along *xz* and *yz* planes. Subsequently, the proposed EIA is evaluated for conformability by bending it on a cylindrical platform along *x*- and *y*-axes of radii 40, 50 and 60mm. The conformed EIA again exhibits excellent performance in terms of matching and radiation. Finally, SAR analysis using the homogeneous, heterogeneous, and Gustav model is carried out. The obtained SAR values are substantially better than the previous works. Also, SAR values of EIA are significantly superior when compared to the values obtained by simulating a simple monopole antenna under similar conditions.

Chapter 7

Conclusion and Future Work

7.1 Conclusion

With the growing demand of WSN for constant monitoring and tracking of health, there is a need for compact, conformal, light-weight, and low-profile antenna. Despite tremendous achievement in this direction in the last decade, still, issues like large antenna size at MBAN and Wi-Fi bands, significant radiation towards the body, non-conformability, and reduction in performance in the presence of body require further investigations. In our preliminary work [70], we designed a planar dipole antenna (MPA) operating in the MBAN band and observed its performance on-air and on-body. The results were encouraging; however, the design lacked several aspects from the WBAN perspective, as listed below in the following points.

a) The size of the dipole antenna (80x62 mm^2) is considerable compared to a standard body-worn antenna.

b) Reduction in the gain and efficiency of the MPA when placed on the body indicating sound coupling.

c) A shift in resonant frequency was observed when covered with a protective textile layer.

d) SAR values showed tremendous improvement from a single antenna to an array. It is due to the presence of a large ground plane that gradually attenuates surface wave propagating through the surface wave. However, the size of the overall array antenna (120x60 mm^2) is enormous from the WBAN perspective and certainly requires miniaturization.

From that point, we moved in three distinct directions. First is the design of compact, conformal, and low-profile EBG surfaces to be integrated with the body-worn antenna so that despite the compact size, performance improves. EBG surfaces have shown a significant improvement in radiation properties and miniaturization of antenna used in WBAN applications.

Secondly, for reliable communication between an external node and an on-body antenna covered with multiple textile layers, we proposed a CM based approach and an iterative model to determine the effective dielectric constant of an MPA not only covered with multiple textile layers but also with dielectric layers.

Thirdly, the development of real phantoms with straightforward and cost-effective methods to measure maximum point SAR. The present SAR measurement techniques like electric field probe scanning, thermographic method, temperature rise method are indeed very accurate but involve a much more sophisticated process. These measurement setups are also costly and often not assessable to all.

In summary, this dissertation presents two novel, compact, conformal, low-profile, and polarization stable EBG surfaces. These surfaces, when integrated with a monopole antenna, enhances the performance in terms of gain, bandwidth, efficiency, and SAR values. One of the designs is perfectly suitable for smart-watch applications. Next, we have also proposed an iterative model and modified expressions based on CM to accurately determine the effective dielectric constant of an MPA covered with either single or multiple dielectric layers. We have also validated our approach and formulations on textile layers like polyester, Rayon, terry wool, jean cotton, pure cotton, and others. Furthermore, we have also developed two straightforward and cost-effective approaches to design liquid phantoms (homogeneous and skin) and measure maximum point SAR.

7.2 Summary of Contribution

7.2.1 Determination of Effective Dielectric Constant and Resonant Frequency of an MPA Covered with Multiple Dielectric Layers

In chapter 2, we propose new empirical relations based to determine the effective dielectric constant of an MPA covered with either PCB or textile layers. The chapter also presents a unique iterative model that fragments a superstrate layer into multiple sub-layers and then computes ε_{eff} and f_r of the whole arrangement. This chapter finds its usefulness from the WBAN scenario, where sensor networks operate beneath multiple layers of protective clothing. The theoretically obtained results, when compared with the measured and simulated values, exhibits remarkable resemblance and, in this way, advances the current state-of-the-art.

7.2.2 Development of Liquid Phantoms and SAR Measurement

In chapter 3, we developed a homogeneous and skin equivalent liquid phantoms with the help of low-cost materials such as salt, sugar, glycerine, and water. Two different techniques to determine the crucial parameters of the phantom ε_r and σ_d with the use of just VNA are presented instead of the complicated and expensive setup, such as a dielectric probe tool kit. The effectiveness of the presented approaches are verified by simulation, and measurement of point SAR on liquid phantoms developed. Once again, expensive and sophisticated tools like a thermographic camera and electric field probe scanner are not required to perform the measurements.

7.2.3 Design of Compact, Conformal, Polarization stable and Via-less EBG surfaces for Antenna in WBAN Applications

A novel, interconnected, via-less, and compact IDE EBG UC operating in the MBAN band is proposed in chapter 4. The IDE EBG UC shows stability to polarization change in incident TEM and TE-TM waves. The dimension of the EBG incorporated monopole antenna perfectly fits for the integration into present smart-watches. The integrated antenna demonstrates significant performance improvement

in terms of matching, bandwidth, and radiation parameters whereby maximum on-body gain of 3.7 dB at 2.4 GHz with a radiation efficiency of more than 50% can be achieved, and it is a substantial improvement in the existing state-of-the-art.

In chapter 6, we proposed a new compact and conformal blocking EBG UC (B-EBG UC) for the MBAN band. We demonstrated the excellent stability of the proposed B-UC to polarization change for obliquely incident TE and TM waves at 15^o, 30^o, 45^o, 60^o, 75^o, and also, for an *x*- and *y*-polarized TEM wave. The proposed EIA exhibits a measured gain of 5.3 and 5.2 dBi along *xz* and *yz* planes. Subsequently, we evaluated the antenna for conformability by bending it on a cylindrical platform along *x*-and *y*-axes of radii 40, 50, and 60mm. The low profile nature of the material used in the design allows for terrific conformability along *x*-and *y*-axes. Finally, SAR analysis using the proposed conformed antenna is carried out on skin and homogeneous liquid phantoms resulting in values of 0.357 W/Kg and 0.535 W/Kg, respectively. These are significantly superior when compared to the values obtained by measuring a simple monopole antenna (1.33 and 1.11 W/Kg) under similar conditions.

7.2.4 Conformability Analysis of EBG Surfaces used in WBAN Applications

In chapter 5, we presented a geometrical approach to determine the shift in the reflection phase of C-EBG UC and C-array. The technique makes use of the law of reflection of EM wave and elementary geometry to predict the change in the angle of reflection after conforming to a P-EBG and P-array. The proposed method can predict the in-phase reflection point conveniently in very less time in comparison to a full-wave analysis simulation tool like CST. Furthermore, the proposed techniques fit particularly well for the determination of in-phase reflection frequency of a conformal EBG unit cell or array designed from the WBAN perspective.

7.3 Future Work

The work done in this dissertation has primarily covered various aspects of on-body to off-communication like the compact and conformal EBG integrated antenna

design, communication through multiple dielectric layers, phantom generation, and measurement of SAR. However, the two other scenarios of the WBAN, i.e., on-body to on-body and in-body to on-body communication has not been pursued here. Therefore, I would like to pursue research on these two scenarios in the future. The following points present a glimpse of the future research direction.

7.3.1 Design of Compact and Conformal End-fire Antenna

For on-body to on-body communication, the antenna needs to radiate along the body rather than away from the body. It necessitates the use of vertically polarized antenna instead of horizontal polarization, due to less coupling with the body while propagation [24], [28]. However, vertically polarized antenna like a vertical dipole or monopole has protrusion away from the surface. This arrangement is highly undesirable for a body-worn antenna as it is not aesthetically pleasing. Moreover, conforming such a design on body parts like biceps, wrists, and shoulders might break the antenna. Planar end-fire antenna with horizontal polarization is best suited for this scenario [23] – [29]. The planar Yagi-Uda antenna has shown promises in this direction to achieve the desired radiation feature [25] – [29]. However, the existing works suffer from a large footprint [26], low gain when placed nearby body [25], infeasible or inconvenient design (no substrate, substrate as air) [27], large thickness (non-conformal) [23]. Therefore, I would like to continue my research in pursuit of compact, conformal, and efficient EBG incorporated planar Yagi-Uda antenna.

7.3.2 Localization of Implant in WCE

In the future, I would like to investigate the localization of WCE. WCE is an implant technology that inspects abnormality in the gastrointestinal (GI) tract of the human body without the use of optical fibers, sedation, discomfort, and pain. For this, an ingestible pill like wireless device is swallowed and later on retrieved. It uses an embedded camera inside the pill to capture the images of the GI tract, which is very hard to be accessed by routine endoscopy and an RF source for the accurate

localization of the capsule. If an anomaly is detected, corrective surgery is performed at a precise location to get rid of it.

The radio frequency-based localization uses the angle of arrival (AOA), received signal strength indicator (RSSI), and time of arrival. Although each technique has its advantages and disadvantages, the technique which I plan to work in the future is localization based on RSSI. For this, at first, there is a need to develop tissue-mimicking liquids or gels that exactly resembles the GI tract. In this regard, the technique we proposed to develop liquid phantoms in chapter 3 can be used. The other constituent of the GI tract through which radio waves travel can also be developed by varying the weight percentage of salt, sugar, glycerine, and water in LUTs developed in Chapter 3. The development of phantom for other layers like skin, fat, bones, etc. is under progress. The technique presented in this thesis is just a preliminary approach to the model skin layer. In the future, a more sophisticated model representing all other layers of the body along with skin can be developed by varying the percentage of water in glycerine and using a solidifying agent to have boundaries between the layers. Next, for the estimation of the position of the implant inside the body, an RF source (compact and conformal antenna) travels inside the liquid phantom. A series of a conformal body-worn antenna placed around the stomach measures the S_{21} parameter by connecting one port of the RF source and another to the receiver antenna. From the received power, the distance of separation between the implant and the on-body antenna can be computed using expression (3.7). After the determination of the distance of the WCE from the receiver, a trilateration method can be used to determine the coordinates of the capsule.

The present localization technique can detect the RF source inside the body within an error of 1 cm of the actual position. It is a significant development in the context of engineering systems but is constrained for real-time medical applications. I intend to increase the accuracy to mm.

References

[1] C. Rotariu, H. Costin, G. Andruseac, R. Ciobotariu, and F. Adochiei, "An integrated system for wireless monitoring of chronic patients and elderly people," in *Proc. 15th Int. Conf. Sys.Theory, Control and Computing*, 2011.

[2] L. Wolf, and S. Saadaoui, "Architecture concept of a wireless body area sensor network for health monitoring of elderly people," *in Proc. 4th IEEE Consumer Communicat and Networking Conference,* 2007, pp. 722-726.

[3] S. Armstrong, "Wireless connectivity for health and sports monitoring: a review," in *British Journal of Sports Medicine*, vol. 41, no. 5, pp. 285-289, Jan. 2007.

[4] H. Sjoland, and et. al., "A receiver architecture for devices in wireless body area networks," *IEEE Jour. Emerging Sel. Top. Circ. Sys.*, vol. 2 no. 1, pp. 82-95, March 2012.

[5] I. M. Saied, S. Chandran, and T. Arslan, "Integrated flexible hybrid silicone-textile dual-resonant sensors and switching circuit for wearable neurodegeneration monitoring systems," *IEEE Trans. On Bio Circuits Systems*, vol. 13, no. 6, Dec. 2019.

[6] H. Cao, V Leung, C. Chow, and H. Chan, "Enabling technologies for wireless body area networks: A survey and outlook," *IEEE Comm. Mag.*, vol. 47, no. 12, pp. 84-93, Dec. 2009

[7] E. Y. Chow, A. L. Chlebowski, and Pedro P. Irazoqui, "A Miniature-implantable RF-wireless active glaucoma intraocular pressure monitor," *IEEE Trans. On Bio Circuits Systems.*, vol. 4, no. 6, pp. 340–349, Dec. 2010.

[8] K. M. S. Thotahewa, J. M. Redoutè, and M. R. Yuce, "Propagation, Power Absorption, and Temperature Analysis of UWB Wireless Capsule Endoscopy Devices Operating in the Human Body" ," *IEEE Trans. on Antennas Propag*, vol. 63, no.11, pp. 3823 – 3833, Nov. 2015.

[9] J. Faerber, and et. al., "In Vivo Characterization of a Wireless Telemetry Module for a Capsule Endoscopy System Utilizing a Conformal Antenna," *IEEE Trans. On Bio Circuits Systems.*, vol. 12, no. 1, pp. 95–105, Feb. 2018.

[10] I. De Falco, G. Tortora, P. Dario, and A. Menciassi, "An Integrated System for Wireless Capsule Endoscopy in a Liquid-Distended Stomach," *IEEE Trans. On Biomed. Eng.*, vol. 61, no. 3, pp. 794–804, March 2014.

[11] G. Pan and L. Wang, "Swallowable Wireless Capsule Endoscopy: Progress and Technical Challenges," *Hindawi Gastroenterology Research and Practice*, vol. 2012, article 841691, pp. 1–9, Dec 2011.

[12] [Online]: https://www.lairdconnect.com/resources/white-papers/fcc requirements-for-medical-body-area-networks, downloaded December, 2017.

[13] "World Population Ageing: 1950-2050," A Report, Department of Economic and Social Affairs, Population Division, United Nations.

[14] 47 CFR Parts 2 and 95, [ET Docket No. 0859; FCC 1254], Medical Body Area Network, Federal Register, Rules and Regulations, vol. 77, No. 176, 11 Sept., 2012

[15] European Telecommunication Standards Institute website: https://www.etsi.org/.

[16] European Telecommunications Standards Institute, ETSI EN 301 839- 1 V1.3.1:Electromagnetic compatibility and Radio spectrum Matters (ERM); Short Range Devices (SRD); Ultra Low Power Active Medical Implants (ULP-

AMI) and Peripherals (ULP-AMI-P) operating in the frequency range 402 MHz to 405 MHz; Part 1: Technical characteristics and test methods, 2009.

[17] C. Hertleer, H. Rogier, L. Vallozzi, and L. Van Langenhove, "A Textile Antenna for Off-Body Communication Integrated Into Protective Clothing for Firefighters," *IEEE Trans. Antennas Propagat*., vol. 57, no. 4, pp. 919- 925, April 2009.

[18] J. Carter, J. Saberin, T. Shah, P.R. Sai Ananthanarayanan, and C. Furse, "Inexpensive fabric antenna for off-body wireless sensor communication," in *Proc. IEEE Antennas Propagat. Soc. Int. Symp., APSURSI*, Toronto, July 2010.

[19] Q. Bai, Hyung-Joo Lee, K.L. Ford, R.J. Langley, "Switchable textile microstrip antenna for on/off-body communications and shape distortion study," in *IEEE Asia-Pacific Conf. Antennas Propagat*., pp. 114- 115, Aug. 2012.

[20] W. El Hajj, C. Person, and J. Wiart, "A novel investigation of a broadband integrated inverted-F antenna design; application for wearable antenna," *IEEE Trans. Ant. Propag.*, vol. 62, no. 7, pp. 3843–3846, July 2014.

[21] S. J. Ha, Y. B. Jung, D. H. Kim, *et al.*, "Textile patch antennas using double layer fabrics for wrist-wearable applications," *Microw. Opt. Technol. Lett.*, vol.54, no. 12, pp. 2697–2702, sept. 2012.

[22] M. N. Suma, P. C. Bybi, and P. Mohanan, "A wideband printed monopole antenna for 2.45 GHz WLAN applications," *Microw. Opt. Technol. Lett.,* vol. 48, no. 5, pp. 871–873, March 2006.

[23] G.A. Conway, and W.G. Scanlon, "Antennas for Over-Body-Surface Communication at 2.45 GHz," *IEEE Trans. Antennas Propagat*., vol. 57, no. 4, pp. 844-855, Apr. 2009.

[24] R. Chandra, “Antennas, Wave Propagation, and Localization in Wireless Body Area Networks,” PhD Dissertation, Department of Electrical and Information Technology, Lund University, 2014.

[25] K. Agarwal, Y. Guo, and B. Salam, “Wearable AMC Backed Near-Endfire Antenna for On-Body Communications on Latex Substrate,” *IEEE Trans. on Components, Packaging and Manu. Techn.*, vol. 6, no. 3, pp. 346–358, March 2016.

[26] B. S. Abirami and E. F. Sundarsingh, “EBG-Backed Flexible Printed Yagi–Uda Antenna for On-Body Communication,” *IEEE Trans. Ant. Propag.*, vol. 65, no. 7, pp. 3762–3765, July 2017.

[27] C. Lin, K Saito, M. Takahashi, and K. Ito, “A Compact Planar Inverted-F Antenna for 2.45 GHz On-Body Communications,” *IEEE Trans. Ant. Propag.*, vol. 60, no. 9, pp. 3762–3765, Sept 2012.

[28] M. Koohestani, J. F. Zurcher, A. A. Moreira, and A. K. Skrivervik, “A novel, low-profile, vertically-polarized UWB antenna for WBAN,” *IEEE Trans. Antennas Propag.*, vol. 62, no. 4, pp. 1888–1894, Apr. 2014.

[29] J. Tak and J. Choi, “An all-textile antenna with EBG structure for on-body communication”, in *proc. IEEE International Workshop on Antenna Technology*, 2015, pp. 30 – 33.

[30] K. Gosalia, G. Lazzi, and M. Humayun, “Investigation of a microwave data telemetry link for a retinal prosthesis,” *IEEE Trans. Microwave Theory Techniq.*, vol. 52, no. 8, pp. 1925-1933, Aug. 2004.

[31] J.J. Struijk, “An Inductive Tongue Computer Interface for Control of Computers and Assistive Devices,” *IEEE Trans. Biomed. Engg.*, vol. 53, no. 12, pp. 2594-2597, Dec. 2006.

[32] H. Park, and et. al., “A Wireless Magnetoresistive Sensing System for an Intraoral Tongue-Computer Interface,” *IEEE Trans. on Biomed. Circuits Sys.*, vol. 6, no. 6, pp. 571-585, Dec. 2012.

[33] M. Mantash, M. E. de Cos, A-C. Tarot, S. Collardey, K. Mahdjoubi, and F. Las-Heras, “Dual-band textile hexagonal artificial magnetic conductor for WiFi wearbale applications,” in *Proc. Europ. Conf. on Ant. And Prop.*, 2012, pp. 1395-1398.

[34] S. Velan, E. F. Sundarsingh, M. Kanagasabai, A. K. Sarma, C. Raviteja R. Sivasamy, and J. K. Pakkathillam, “Dual-band EBG integrated monopole antenna deploying fractal geometry for wearable applications,” *IEEE Antennas Wireless Propag. Lett.* vol. 14, pp. 249–252, Sept. 2015.

[35] S. Zhu and R. Langley, “Dual-band wearable textile antenna on an EBG substrate,” *IEEE Trans. Antennas Propag.*, vol. 57, no. 4, pp. 926–935, April 2009.

[36] A. Alemaryeen, S. Noghanian, and R. F. Rezai, “EBG integrated textile monopole antenna for space health monitoring application” in *Proc. IEEE AP-S Int. Symp. Dig.*, 2015, pp. 1209-1210.

[37] S. Yan, P. J. Soh, and G. A. E. Vandenbosch, “ Low-profile dual-band textile antenna with artificial magnetic conductor plane,” *IEEE Trans. Antennas Propag.*, vol. 62, no. 12, pp. 6487–6490, Dec. 2014.

[38] Z. H. Jiang, D. E. Brocker, and P.E. Sieber, “A compact, low-profile meta-surface-enabled antenna for wearable medical body-area network devices”, *IEEE Trans. Antennas Propag*. vol. 62, no.8, pp. 4021–4030, Aug. 2014.

[39] M. A. B. Abbasi, S. Nikolaou, M. A. Antoniades, M. N. Stevanovic, and P. Vryonides, “Compact EBG- backed planar monopoles for BAN wearable applications”, *IEEE Trans. Antennas Propag.*, vol. 65, no. 2, pp. 453–463, Feb. 2017.

[40] H. R. Raad, A. I. Abbosh, H. M. Al-Rizzo, and D. G. Rucker, "Flexible and compact AMC based antenna for telemedicine applications," *IEEE Trans. Antennas Propag.*, vol. 61, no. 2, pp. 524–531, Feb. 2013.

[41] F. Yang and Y. Rahmat-Samii, "Microstrip antennas integrated with electromagnetic band-gap (EBG) structures: A low mutual coupling design for array applications," *IEEE Trans. Antennas Propag.*, vol. 51, pp. 2939–2949, Oct. 2003.

[42] D. Sievenpiper and E. Yablonovitch, "Circuit and method for eliminating surface currents on metals," U.S. Patent 60/079953, 30, 1998.

[43] D. F. Sievenpiper, "High impedance electromagnetic surfaces," Ph.D. dissertation, University of California, Los Angeles, 1999.

[44] F. Yang and Y. Rahmat-Samii, "Mutual coupling reduction of microstrip antennas using electromagnetic band-gap structure," in *Proc. IEEE AP-S Int. Symp. Dig.*, vol. 2, pp. 478–481, 2001.

[45] D. Sievenpiper and E. Yablonovitch, "Circuit and method for eliminating surface currents on metals," U.S. Patent 60/079953, 30, 1998.

[46] F. Yang and Y. Rahmat-Samii, "Reflection phase characterization of an electromagnetic band-gap (EBG) surface," in Proc. *IEEE AP-S Dig.*, 2002, pp. 744-747.

[47] F. Yang and Y. Rahmat-Samii, "Reflection phase characterizations of the EBG ground plane for low profile wire antenna applications," *IEEE Trans. Antennas Propag.*, vol. 51, no. 10, pp. 2691–2703, Oct. 2003.

[48] F. Yang and Y. Rahmat-Samii, *Electromagnetic Band Gap structures in Antenna Engineering*. New York, NY, USA: Cambridge Univ. Press, 2009.

[49] M. Rahman and M. Stuchly, “Wide-band microstrip patch antenna with planar PBG structure,” in *Proc. IEEE AP-S Int. Symp. Dig.*, 2001, pp. 486–489.

[50] W. Akaram, D. Rano, M. S. Hashmi, A. Q. Ansari, “Design of a new uc-planar EBG cell and its application in performance enhancement of microstrip patch antenna/antenna array,” in *Proc. Asia Pacific Microwave Conf.*, 2016, pp. 1-4.

[51] A.C. Durgun, C. A. Balanis and C.R. Birtcher, “Reflection Phase Characterization of Curved High Impedance Surfaces” *IEEE Trans. Antennas Propag*. vol. 61, pp. 6030–6038, Sept. 2013.

[52] D. Germain, D. Seetharamdoo, S.N. Burokur and A. de Lustrac, “Phase-compensated met surface for a conformal microwave antenna” *Appl. Phys. Lett.*, vol. 103, 1 – 4, Sept 2013.

[53] CST Microwave Studio. CST, Framingham, MA, USA, 2012. [Online]. Available: http://www.cst.com/.

[54] J. Scavina, “Analysis of multilayer microstrip lines by a conformal mapping method,” *IEEE Trans. Microw. Theory Tech.*, vol. 40, pp. 769–772, April 1992.

[55] S. S. Zhong, G. Liu, and G. Qasim, “Closed form expressions for resonant frequency of rectangular patch antennas with multi-dielectric layers,” *IEEE Trans. Ant. Prop.*, vol. 42, pp. 1360–1363, Sept. 1994.

[56] J. T. Bernhard and C. J. Tousignant, “Resonant frequencies of rectangular microstrip antennas with flush and spaced dielectric superstrates,” *IEEE Trans. Ant. Prop.*, vol. 47, pp. 302–308, Feb. 1999.

[57] J. Scavina, “A simple quasi-static determination of basic parameters of multilayer microstrip and coplanar waveguide,” *IEEE Microw. Guided Lett.* vol. 2, no. 10, pp. 385–387, Oct. 1992.

[58] C. A. Balanis, “Antenna Theory Analysis and Design” 3rd ed., New York, NY, USA: Wiley, 1997.

[59] R. Garg, *Microstrip Antenna Design Handbook*. Norwood, MA, USA: Artech House, 2001.

[60] G. Kumar and K. P. Ray, *Broadband Microstrip Antennas*. Norwood, MA, USA: Artech House, 2003.

[61] A. Bhattacharyya and T. Tralman, “Effects of dielectric superstrate on patch antennas,” *Electron. Lett.* vol. 24, pp. 356–358, Mar. 1988.

[62] C. A. Balanis, “Antenna Theory Analysis and Design” 3rd ed., New York, NY, USA: Wiley, 1997.

[63] I. J. Bahl, P. Bhartia, and S. Stuchly, “Design of microstrip antennas covered with a dielectric layer,” *IEEE Trans. Ant. Prop.*, vol. 30, no. 2, pp. 314–318, Mar. 1982.

[64] R. Shavit, “Dielectric cover effect on rectangular microstrip antenna array,” *IEEE Trans. Ant. Prop.*, vol. 42, pp. 1180–1184, Aug. 1994.

[65] A. Verma and Z. Rostamy, “Resonant frequency of uncovered and covered rectangular microstrip patch using modified Wolff model,” *IEEE Trans. Microw. Theory Tech.*, vol. 41, pp. 109–116, Jan. 1993.

[66] J. P. Damiano and A. Papiernik, “A simple and accurate model for the resonant frequency and the input impedance of printed antennas,” *Int. J. Microw. Millimeter-Wave Comp.-Aided Eng.*, vol. 3, pp. 350–361, Oct. 1993.

[67] H.A. Wheeler, “Transmission-line properties of parallel wide strips by a conformal mapping approximation,” *IEEE Trans. Microw. Theory Tech.*, vol. 12, pp. 280–289, Mar. 1964.

[68] H.A. Wheeler, “Transmission-line properties of parallel strips separated by a dielectric sheet,” *IEEE Trans. Microw. Theory Tech.*, vol. 13, pp. 172–185, Mar. 1965.

[69] D. Rano and M. S. Hashmi, “Determination of effective dielectric constant and resonant frequency of microstrip patch antenna with multilayered superstrate structures,” in *Proc. EuMC*, 2019, pp. 81 – 84.

[70] D. Rano. M. S. Hashmi, “Design and analysis of wearable patch antenna array for MBAN applications,” in *Proc. National Conf. on Comm.(NCC)*, 2016, pp. 1-6.

[71] Y. Okano, “The comparison measurement for SAR by thermal evaluation and the electric field probe,” in *Int. Zurich Symposium on EMC*, 2007, pp. 147-150.

[72] SPEAG. Dielectric Assessment Kit. Accessed: Aug. 6, 2016. [Online]. Available: http://www.speag.com/products/dak/.

[73] K. Kiminami, T. Iyama, T. Onishi, and S. Uebayashi, “Novel Specific Absorption Rate (SAR) Estimation Method Based on 2-D Scanned Electric Fields,” *IEEE Trans. Electromagnetic Compatibility*, vol. 50, no. 4, pp. 828–836, Nov. 2008.

[74] N. Michishita, T. Watanabe, Y. Yamada, H. Arai, and T. Tanaka, “Simplified Local Specific Absorption Rate Measurement Method Using Lightweight Phantom Composed of Wave Absorber Embedded of Electric Field Probe,” *IEEE Trans. Electromagnetic Compatibility*, vol. 54, no. 1, pp. 181–187, Feb. 2012.

[75] Y. Okano, T. Sato, and Y. Sugama, “A Specific Absorption Rate Measurement Method Using Fiber Optic Thermal Sensors,” *IEEE Trans. Instr. Meas*, vol. 59, no. 6, pp. 1705–1714, June 2010.

[76] Y. Okano, K. Ito, I. Ida, and M. Takahashi, “The SAR evaluation method by a combination of thermographic experiments and biological tissueequivalent phantom,” *IEEE Trans. Microw. Theory Tech*., vol. 48, no. 11, pp. 2094–2103, Nov. 2000.

[77] H. Kawai and K. Ito, “Simple evaluation method of estimating local average SAR,” *IEEE Trans. Microw. Theory Tech*., vol. 52, no. 8, pp. 2021– 2029, Aug. 2004.

[78] Y. Okano, and H. Shimoji, “Comparison Measurement for Specific Absorption Rate With Physically Different Procedure,” *IEEE Trans. Instr. Meas,* vol. 61, no. 2, pp. 439–446, Feb. 2012.

[79] R. Shimofusa, and Y. Okano Broadband, “Measurement System for the Specific Absorption Rate above 300 MHz,” in Proc. *IEEE International Symposium on Radio-Frequency Integration Technology,* 2015, pp. 88 – 90.

[80] V. Karthik, and T. R. Rao, “Estimation of Specific Absorption Rate Using Infrared Thermography for the Biocompatibility of Wearable Wireless Devices” *Progress In Electromagnetics Research M,* vol. 56, pp. 101-109, 2017.

[81] J. C. Wang, E. G. Lim, M. Leach, Z. Wang, K. L. Man and Y. Huang, “Two Methods of SAR Measurement for Wearable Electronic Devices”, in *Proc of the International Multi Conference of Engineers and Computer Scientists,* 2016, pp. 1 – 4.

[82] S. C. Palacios, A. V. Lluch, C. G. Pardo, A. F. Leal and N. Cardona, “Formulas for easy to-prepare tailored phantoms at 2.4 GHz ISM band,” in *proc. International Symposium on Medical Information and Communication Technology*, pp. 27–31, 2017.

[83] C.-K. Chou, G.-W. Chen, A. W. Guy, and K. H. Luk, “Formulas for preparing phantom muscle tissue at various radiofrequencies,” *Bio electromagnetics*, vol. 5, no. 4, pp. 435–441, 1984.

[84] D. Popovic, L. McCartney, C. Beasley, M. Lazebnik, M. Okoniewski, S. C. Hagness, and J. H. Booske, "Precision Open-Ended Coaxial Probes for In Vivo and Ex Vivo Dielectric Spectroscopy of Biological Tissues at Microwave Frequencies" *IEEE Trans. Microw. Theory Tech*., vol. 53, no. 5, pp. 1713–1722, May 2005.

[85] D. Lee, R. Augustine, D. Nowinski Investigation of Skull Defect using Resistive Dipole Antenna on Cranial Surgery Phantom Model, in *Proc. of IEEE Conference on Antenna Measurements & Applications,* 2017, pp. 301 – 303.

[86] J. Garrett, and Elise Fear, "A New Breast Phantom With a Durable Skin Layer for Microwave Breast Imaging", *IEEE Trans. Ant. Prop.*, vol. 63, no. 4, pp. 1693–1700, April 2015.

[87] A.Y.I. Ashyap, Z. Z. Abidin, S. H. Dahlan, H. A. Majid, and F. C. Seman, "A Compact Wearable Antenna Using EBG for Smart-watch Applications" in *Proc. of IEEE Asia-Pacific Microwave Conference,* 2018, pp. 1477 – 1479.

[88] A.Y.I. Ashyap, et. al., "Highly Efficient Wearable CPW Antenna Enabled by EBG-FSS Structure for Medical Body Area Network Applications" *IEEE Access*, vol. 6, pp. 77529–77541, Dec. 2018.

[89] G. Gao, R. Zhang, C. Yang, H. Meng, W. Geng, B. Hu, "Microstrip monopole antenna with a novel UC-EBG for 2.4 GHz WBAN applications" *IET Microwave. Antennas Propag*. vol. 13, no. 13, pp. 2319-2323, August 2019.

[90] G. Gao, S. Wang, R. Zhang, C. Yang, and B. Hu, "Flexible EBG-backed PIFA based on conductive textile and PDMS for wearable applications" in *Wiley Microwave Optical Technology Letter*, vol. 62, 1733–1741, December 2020.

[91] S.A. Balakrishnan, and E.F. Sundarsingh, "Conformal self-balanced EBG integrated printed folded dipole antenna for wireless body area networks," *IET Microwave. Antennas Propag*. vol. 13, no. 14, pp. 2480-2485, August 2019.

[92] D. Rano and M.S. Hashmi, “Extremely Compact EBG-Backed Antenna for Smart-Watch Applications in Medical Body Area Network,” *IET Microwave. Antennas Propag*. vol. 13, pp. 1031-1040, December 2019.

[93] D. Rano and M.S. Hashmi, “A Modified Interdigital EBG Reflector for Wireless Body Area Network Applications,” in *Wiley Microwave Optical Technology Letter*, vol. 61, pp. 912–919, December 2019.

[94] D. Guha and J. Y. Siddiqui, “Resonant Frequency of Circular Microstrip Antenna Covered With Dielectric Superstrate,” *IEEE Trans. Ant. Prop.*, vol. 51, no. 7, pp. 1649–1652, July 2003.

[95] Y. Li, and Nicola Bowler, “Resonant Frequency of a Rectangular Patch Sensor Covered With Multilayered Dielectric Structures” *IEEE Trans. Ant. Prop.*, vol. 58, no. 6, pp. 1883–1889, June 2010.

[96] S. Banik, M. Biswas, and M. Sen, “Resonant frequency of a rectangular patch in multilayered dielectric media”, in *Proc. IEEE International Conference on Microwave and Photonics*, 2013, pp. 1 – 6.

[97] M. Kirschning, R. H. Jansen, and N. H. L. Koster, “Accurate model for open end effect of microstrip lines,” *Electron. Lett.* vol. 17, pp. 123–125, Feb. 1981.

[98] S. Sankaralingam and B. Gupta, “Determination of dielectric constant of fabric materials and their use as substrates for design and development of antennas for wearable applications” *IEEE Trans. on Instrument. Meas.*, vol. 59, no. 12, pp. 3122–3230, Dec. 2010.

[99] J. Tak, S. Lee, and J. Choi, “All-textile higher order mode circular patch antenna for on-body to on-body communications,” *IET Microw., Antennas Propag.*, vol. 9, no. 6, pp. 576–584, April 2015.

[100] D.T. Le, L. Hamada, S. Watanabe, and T. Onishi, “A Fast Estimation Technique for Evaluating the Specific Absorption Rate of Multiple-Antenna Transmitting Devices” *IEEE Trans. Ant. Prop.*, vol. 65, no. 4, pp. 1947–1957, April 2017.

[101] A. Gioia, E. Porter, I. Merunka, A. Shahzad, S. Salahuddin, M. Jones, and M. O’Halloran, “Open-Ended Coaxial Probe Technique for Dielectric Measurement of Biological Tissues: Challenges and Common Practices,” *MDPI, Diagnostics*, vol. 8, no. 40, pp. 1 – 38, June 2018.

[102] C. Gabriel, E.H. Grant, and I.R. Young, “Use of Time Domain Spectroscopy for Measuring Dielectric Properties with a Coaxial Probe,” *J. Phys. E* 19, pp. 843–846. Oct. 1986.

[103] T. Reinecke, L. Hagemeier, V. Schulte, M. Klintschar, and S. Zimmermann, “Quantification of Edema in Human Brain Tissue by Determination of Electromagnetic Parameters” In *Proc. of the IEEE Sensors*, 2013; pp. 1–4.

[104] A. Nicolson, and G.F. Ross, “Measurement of the Intrinsic Properties of Materials by Time-Domain Techniques.,” *IEEE Trans. Instrum. Meas.*, vol. 19, pp. 377–382, Nov. 1970.

[105] W.B. Weir “Automatic Measurement of Complex Dielectric Constant and Permeability” in *Proc. IEEE*, vol. 62, pp. 33–36, Jan. 1974.

[106] J. Jarvis, E.J Vanzura, and W.A Kissick, “Improved Technique for Determining Complex Permittivity with the Transmission/Reflection Method,” *IEEE Trans. Microw. Theory Tech.*, vol. 38, pp. 1096–1103, Aug. 1990.

[107] S. Kim, and J. Jarvis, “An Approximate Approach To Determining the Permittivity and Permeability near λ/2 Resonances in Transmission/Reflection Measurements” in *Prog. Electromagn. Res. B*, vol. 58, pp. 95–109, Dec 2014.

[108] E. Burdette, F. Cain, and J. Seals, “In Vivo Probe Measurement Technique for Determining Dielectric Properties at VHF through Microwave Frequencies”, *IEEE Trans. Microw. Theory Tech.*, vol. 28, pp. 414–427, April 1980.

[109] S. Gabriel, R.W. Lau, and C. Gabriel, “The Dielectric Properties of Biological Tissues: II. Measurements in the Frequency Range 10 Hz to 20 GHz”. *Phys. Med. Biol.*, vol. 41, pp. 2251–2269, 1996,

[110] D. Popovic, M. Okoniewski, D. Hagl, J.H. Booske, and S.C. Hagness, “Volume Sensing Properties of Open Ended Coaxial Probes for Dielectric Spectroscopy of Breast Tissue,” In *Proc of the IEEE Antennas and Propagation Society*, Boston, 2001, pp. 254–257.

[111] Keysight Technologies Dielectric Probr Kit. [Online]. Available: https://www.keysight.com/.

[112] N. K. Tiwari, A. Sharma, S. P. Singh, M. Jaleel Akhtar and A. Biswas, “Non-Invasive Dielectric Characterization of Chemical Solvents using Microstrip-Fed Dielectric Resonator based Sensor,” *Proc. URSI Asia-Pacific Radio Science Conference*, New Delhi, India, 2019, pp. 1-4.

[113] H. Kawabata, H. Tanpo, and Y. Kobayashi, “A rigorous analysis of a TM/sub 010/ mode cylindrical cavity to measure accurate complex permittivity of liquid,” *Proc. European Microwave Conference*, Munich, Germany, 2003, pp. 759-762.

[114] S. Datta and K. J. Vinoy, "Design of a Compact Radio Frequency Cavity Resonator as a Sensor for Dielectric Liquids," 2018 IEEE MTT-S International Microwave and RF Conference (IMaRC), Kolkata, India, 2018, pp. 1-3.

[115] P.S. Hall, Y. Hao: ‘Antenna and propagation for body-centric wireless comm.’, (Norwood: Artech House, 2016, 2nd edn. 2012)

[116] X. Gao, Z. Zhang, W. Chen, *et al.*: "A novel wrist wear dual-band diversity antenna", *Proc. IEEE Int. Symp. Antennas Propag. Soc.*, Charleston, SC, USA, 2009, pp. 1–4.

[117] S. Woo, J. Beak, H. Park, H., *et al.*: "Design of a compact UWB diversity antenna for WBAN wrist-watch applications", *Proc. IEEE Int. Symp. Antennas Propag.*, 2013, pp. 1304–1306.

[118] C.H. Wu, K.L. Wong, Y.C. Lin, *et al.*: "Conformal bluetooth antenna for the watch-type wireless communication device application" *Proc. IEEE Antennas Propag. Int. Symp.*, 2007, pp. 4156–4159.

[119] C.H. Wu, K.L. Wong, Y.C. Lin, *et al.*: "Internal shorted monopole antenna for the watch-type wireless communication device for Bluetooth operation", *Microwave Optical Technology Letter*, vol. 49, no. 4, pp. 942–946, Feb. 2007.

[120] V.K. Palukuru, A. Pekonen, V. Pynttari, *et al.*: "An inkjet-printed inverted-F antenna for 2.4-GHz wrist applications", *Microwave Optical Technolgy Letter*, vol. 51, no. 12, pp. 2936–2938, Sept. 2009.

[121] A. Zhao, A., J. Xue, C. Jing, *et al.*: "The use of Murata ceramic Bluetooth antenna for wrist device based on flexible printed circuit boards" *Proc. 1st European Wireless Technology Conference*, Amsterdam, Netherlands, 2008, pp. 334–337.

[122] J. Lee, S. Kwak, S. Lim, "Wrist-wearable zeroth-order resonant antenna for wireless body area network applications", *Electronics Letter*, vol. 47, no. 7, pp. 431–433, April 2011.

[123] K. Zhao, S. Zhang, C.Chiu, *et al.*: 'SAR study for smart watch applications'. *Proc. IEEE Int. Symp. Antennas Propag. Soc.*, 2014, pp. 1198–1199.

[124] S. Woo, J. Baek, H. Park, “Design of a compact UWB diversity antenna for WBAN wrist-watch applications” in *Proc. IEEE Int. Symp. Antennas Propag., Nanjing, China*, 2013, pp. 1304–1306.

[125] K. Zhao, Z. Ying, and S. He, “Antenna designs of smart watch for cellular communications by using metal belt,” *European Conference on Antenna and Prop.*, 2015, pp. 1–5.

[126] W.S. Su, Y.T. Hsieh, “Integerated metal-frame antenna for smartwatch wearable device,” *IEEE Trans. Antennas Propag*., vol. 65, no. 2, pp. 453–463, July 2015.

[127] S. E. Hong, J.H. Kwon, and H.D. Choi, “A study SARs for smart-watch model with monopole antenna,” *General Assembly and Scientific Symp. of the Int. Union of Radio Science*, 2017, pp. 1–3.

[128] L. Yang, et.al., “A novel compact electromagnetic-bandgap (EBG) structure and its applications for microwave circuits,” *IEEE Trans. Microw. Theory Techn.*, vol. 53, no. 1, pp. 183–190, Jan. 2005.

[129] D. Wen, Y. Hao, H. Wang, et al. “A wearable antenna design using a high impedance surface for all-metal smartwatch applications’. *Int. Workshop on Antenna Tech. Small Antennas, Inovative St. and Applications*, 2017, pp. 274–276.

[130] Y.S. Chen and T.Y. Ku, “A low profile wearable antenna using a miniature high impedance surface for smartwatch applications”, *IEEE Antennas Wireless Propag. Lett*., 14, pp. 1144–1147, Oct. 2015.

[131] S. Kim, Y.J. Ren, H. Lee, *et al*.: ‘Monopole antenna with inkjet printed EBG array on paper substrate for wearable applications’, *IEEE Antennas Wireless Propag. Lett*., vol. 11, pp. 663-666, June 2012.

[132] D. Rano and M. S. Hashmi, “Interdigital based EBG: compact and Polarization stable for MBAN and Wi-Fi” in *Proc. EuCAP*, 2018, pp. 1–5.

[133] G.-P. Gao, B. Hu, S.-F. Wang, and C. Yang, ‘‘Wearable circular ring slot antenna with EBG structure for wireless body area network,’’ *IEEE Antennas Wireless Propag. Lett*., vol. 17, no. 3, pp. 434–437, Mar. 2018.

[134] M. Wang et al., ‘‘Investigation of SAR reduction using a flexible antenna with metamaterial structure in wireless body area network,’’ *IEEE Trans. Antennas Propag*., vol. 66, no. 6, pp. 3076–3086, 2018.

[135] Z. H. Jiang, Z. Cui, T. Yue, Y. Zhu, and D. H. Werner, ‘‘Compact, highly efficient, and fully flexible circularly polarized antenna enabled by silver nanowires for wireless body area networks,’’ *IEEE Trans. Biomed. Circuits Syst*., vol. 11, no. 4, pp. 920–932, 2017.